Modeling and inverse problems in hemodynamics : towards augmented cardiovascular monitoring

Jessica Manganotti

INSTITUT POLYTECHNIQUE DE PARIS

NNT : 2022IPPAX123

Thèse de doctorat

Modeling and inverse problems in hemodynamics: towards augmented cardiovascular monitoring

Thèse de doctorat de l'Institut Polytechnique de Paris
préparée à l'École polytechnique

École doctorale n°626 École doctorale de l'Institut Polytechnique de Paris
(ED IP Paris)
Spécialité de doctorat : Mécanique des fluides et des solides, acoustique

Thèse présentée et soutenue à Palaiseau, le 12 Décembre 2022, par

JESSICA MANGANOTTI

Composition du Jury :

Abdul Barakat Directeur de recherche, LadHyX, École polytechnique	Président
Muriel Boulakia Professeure, Laboratoire de Mathématiques de Versailles, Université de Versailles Saint-Quentin	Rapporteuse
Alessandro Veneziani Professeur, Computational and Data Enabled Science group, Emory Center for Mathematics and Computing in Medicine	Rapporteur
Chloé Audebert Maitre de conférences, LCQB et LJLL, Sorbonne Université	Examinatrice
Alfonso Caiazzo Chercheur, Numerical Mathematics and Scientific Computing group, Weierstrass Institute	Examinateur
Alberto Figueroa Professeur, Computational Vascular Biomechanics Lab, University of Michigan	Examinateur
Philippe Moireau Directeur de recherche, MΞDISIM et LMS, Inria et École polytechnique	Directeur de thèse
Sébastien Imperiale Chargé de recherche, MΞDISIM et LMS, Inria et École polytechnique	Co-directeur de thèse
Fabrice Vallée Professeur-praticien hospitalier, APHP	Invité

Eva's only fault has been the one of wanting to know more, to experiment
and search with her own sources the laws of the Universe,
of her own body and to refuse the teachings from "above".
Eva, basically, represents the curiosity of science
against the passive acceptance that belongs to faith.
– Margherita Hack

Acknowledgements

Cette thèse a été une merveilleuse aventure de trois ans, au cours de laquelle j'ai eu la chance de grandir en tant que scientifique et en tant que personne, grâce à l'environnement accueillant de l'équipe MΞDISIM. Tout d'abord, je tiens à remercier mes encadrants, Sébastien Imperiale et Philippe Moireau, qui ont été une grande source d'inspiration pour moi. Merci Sébastien pour les nombreuses fois où j'ai perdu confiance dans le résultat de mon code et où tu as été capable de trouver l'erreur en une seconde. Toutes les discussions mathématiques autour du tableau vont me manquer. Merci Philippe pour ta patience, mais aussi pour ta détermination, j'ai pu enfin écrire plus que cent pages de manuscrit. Toutes nos conversations sur les perspectives de notre travail ont été un véritable moteur de motivation.

I would also like to thank the reviewers of my manuscript, Muriel Boulakia and Alessandro Veneziani. Thank you for taking the time to review my work and giving me interesting suggestions for further improvements. I would also like to thank Abdul Barakat for chairing my doctoral jury. Then, I thank the members of the jury, Chloé Audebert, Alfonso Caiazzo and Alberto Figueroa for the enriching exchanges and your interesting questions during the defense.

En plus de mes encadrants, je tiens à remercier d'autres personnes sans qui ce travail n'aurait pas été possible, Laurent Steff et Fabrice Vallée. Merci Laurent pour ton aide précieuse sur les aspects de codage de cette thèse, ce fut un plaisir de travailler avec toi et je garderai précieusement tes suggestions et enseignements pour l'avenir. Merci Fabrice d'avoir apporté ton expertise médicale à ce travail et de m'avoir donné la possibilité de comprendre à fond le contexte clinique de ma thèse. Les journées de travail au temple ont été très instructives. Je suis également très reconnaissant à Jérôme Diaz et François Kimmig, qui ont été à la fois des collègues et des guides pour moi. Merci Jérôme pour les pauses café indispensables pendant le stage et ton soutien avec la matrice de gradient. Merci François pour le temps passé à travailler ensemble sur l'article et nos efforts pour comprendre de plus en plus la physiologie de la circulation sanguine. Votre aide a été si précieuse et je vous suis reconnaissant pour votre gentillesse et l'aide que vous apportez toujours à tout membre de l'équipe.

Un merci tout particulier à tous les membres de l'équipe MΞDISIM, qui ont su créer un merveilleux environnement de travail. Les discussions scientifiques ont été une source précieuse de nouvelles connaissances et les événements sociaux un véritable cadeau pour l'âme. Je n'étais pas seule face aux défis du doctorat, comme dans une équipe sportive, toute amélioration a été le résultat de nombreuses contributions. Pour cela, je dois remercier encore une fois mes encadrants, Sébastien et Philippe, qui ont été les meilleurs coachs dont on puisse rêver, donnant toujours le meilleur d'eux-mêmes pour me préparer et me soutenant à tout moment de cette aventure. Jérôme et François, membres de l'équipe toujours prêts à donner un coup de main aux autres, et à préparer et partager de délicieux gâteaux, et tout le monde sait que le sucre est essentiel pour une bonne performance

sportive. Ringrazio Federica Caforio, la mia mentore durante lo stage, per la sua disponibilitá e il suo intramontabile sorriso, in grado di risollevare l'umore anche quando i risultati di pressione aortica non erano affatto rassicuranti. Ringrazio Francesco Regazzoni che ha condiviso con me la magia dello sciopero e i gilet gialli. Grazie Vincenzo Zarra per il tuo accento, la tua allegria e i tuoi suggerimenti musicali. Ultima ma non ultima di questa parentesi super italiana, vorrei ringraziare Giulia Merlini, il futuro italiano del team, conto su di te per portare avanti la tradizione. Ma gratitude va aux collègues de l'open space, à Cécile Patte pour sa sagesse et ses précieux conseils concernant tous les aspects du doctorat (et pas seulement !!) et à Maria Gusseva pour le déjeuner passé ensemble et son tempérament si paisible. La vie dans ce bureau n'aurait pas été la même sans le sourire de Guillaume Ballif, les tentatives de parler italien d'André Dalmora, les danses de Mathieu Barre et les nombreuses mésaventures de Tiphaine Delaunay. Je remercie également Chloé Giraudet pour son aide dans les cauchemars administratifs et Nicole Tueni, qui a partagé avec moi le lieu de travail et l'appartement (même lorsque le premier et le deuxième étaient la même chose). Ma gratitude va également à tous les autres membres et collaborateurs de l'équipe que j'ai eu la chance de rencontrer, Frédérique Clément, Radomír Chabiniok, Martin Genet, Patrick Le Tallec, Dominique Chapelle, Jean-Marc Allain, Matthieu Caruel, Miguel Fernández, Arthur Le Gall, Frédérique Robin, Florent Wijanto, Hajer Methenni, Mahdi Manoochehrtayebi, Alice Peyraut, Othmane Mouzhi, Gaël Le Ruz, Zineb Ramiche, Louis-Pirre Chaintron, Colin Laville, Anne-Gaelle Eveno, Anna Gaubert et Jona Joachim. Enfin, je tiens à remercier Bahar Carabetta pour son merveilleux travail et son aide précieuse.

Je veux remercier aussi l'ensemble des collègues du LMS, et tous ceux qui ont partagé l'activité d'enseignement et de médiation scientifique avec moi.

Vorrei inoltre ringraziare tutti i miei amici, quelli che hanno condiviso la mia avventura parigina, quelli che mi aspettano sempre a braccia aperte quando torno a casa e tutti quelli sparsi per l'Europa (e non solo). Sono grata alla mia famiglia, sempre presente a festeggiare i traguardi e a supportarmi di fronte alle difficoltá incontrate lungo percorso. Last but not least, ringrazio Thibault Camalon, che ha saputo supportarmi e sopportarmi durante il percorso di dottorato.

Contents

Introduction (English)

There is only one way to learn. It's through action.
Everything you need to know you have learned
through your journey.
— Paulo Coelho, *The Alchemist*

Clinical Context

In this section, we summarize some anatomical and physiological informations about the arterial circulation that will help in understanding the clinical environment of the thesis. However, further details about the physiology and anatomy of the cardiovascular system can be found in [Silverthorn et al., 2009; Tortora and Derrickson, 2008], about the mechanical characteristics of the vessels in [Redaelli and Montevecchi, 2012] and about the pressure and blood flow in [Caro et al., 1978; Esper and Pinsky, 2014; Mackenzie, 1902; Vlachopoulos et al., 2011].

The cardiovascular system

The cardiovascular system (or circulatory system) is composed by the heart, the blood and the vascular network.

- *The heart*, is the main organ of the system. It presents a muscular wall – the myocardium – which is provided by an electrical activity which triggers its pumping activity that causes the blood to circulate. In Figure 5 it is possible to observe its structure, it is made up by four chambers: left and right atria which are connected, respectively, to the left ventricle via the mitral valve and to the right ventricle through the tricuspid valve. The heart tissue generates the heartbeat by alterning contraction and relaxation. The activation of the contractile state is induced by automatic electrical impulses which generates in the myocardium. The electro-mechanical activity causes a series of pressure changes resulting in a movement of blood within the chambers thanks to the opening of one-way valves, that happens when the upstream pressure overcomes the downstream one. This process is known as the cardiac cycle and shows four different phases that happens almost simultaneously for the left and right part.

  - *The isovolumetric relaxation:* it is the beginning of the diastole. The atrio-ventricular valves – mitral and tricuspid – and the outlet valves – pulmonary and aortic – are closed and the pressure inside the ventricle is decreasing.
  - *The filling:* the atrio-ventricular valves are opened and the outlet valves are closed. The blood flows from the atria to the ventricles where the volume increases.
  - *The isovolumetric contraction:* it corresponds to the beginning of the systole. The valves are closed, the volume of blood is steady but the pressure within the ventricles increases.
  - *The ejection:* the outlet valves are opened, the blood is pushed into the circulation and the contraction continues, increasing the blood pressure.

- *The blood*, is a body fluid whose main mechanical property is viscosity. It is composed by plasma, red blood cells, white blood cells and platelets. It is responsible of the transport of oxygen, nutrients and waste products within the body, it regulates the temperature of the body and responds to infection and blood loss.

- *The vascular network* is composed by interconnected vessels that carry blood from and towards the heart throughout the whole body. Blood vessels are characterized by a circular empty area, that takes the name of lumen, and by three concentric layers that forms the wall: the tunica intima, media and externa. The vessels can be divided into three main families,

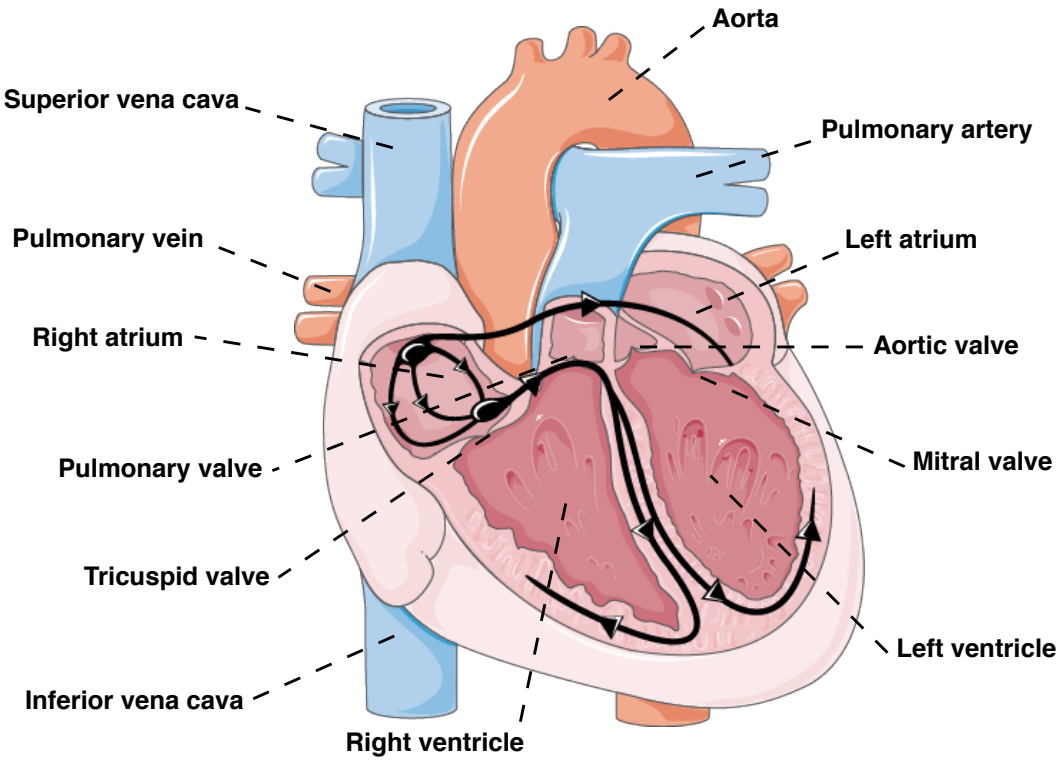

Figure 1 – Representation of the anatomy of the heart with its main important components. The path indicated by the black flashes represents the direction of the electric activation impulse. The Figure was partly generated using Servier Medical Art, provided by Servier, licensed under a Creative Commons Attribution 3.0 unported license.

- *arteries* receive oxygenated blood from the left ventricle and carry it to the body. They are characterized by an elastic muscular wall that makes them able to undergo the high pressure generated by the cardiac output (ejection of blood);
- *veins* are large vessels that return deoxygenated blood to the right atrium. Their wall lack in elasticity and smooth muscles as their functions do not require to withstand high pressures;
- *capillaries* are the smallest blood vessels. They form a connection between small arteries (arterioles) and veins (venules). Their thin wall allows for exchanges of oxygen and wastes with cells.

The function of the cardiovascular system is to send de-oxygenated blood from the cardiac cavity to the lungs, where blood gets oxygen, and then through arteries that run all over the body to oxygenate tissues, muscles and organs. Finally the veins bring back the deoxygenated blood to the heart and the process starts again.
The circulatory system can be seen as the sum of three circuits that form a closed loop (see Figure 6) for the blood to circulate

- *the systemic circuit*, or big circulation, carries oxygenated blood with nutrients and hormones from the left ventricle through the aorta – the main artery of the systemic circuit – to the rest of body. Then, the veins receive the waste of muscles, organs and tissues and return deoxygenated blood to the right atrium via the venae cavae;
- *the coronary circuit* is considered as a part of the systemic circulation. It provides oxygenated blood to the heart's tissue. Two coronary arteries branch out from the aorta and wrap the myocardium and supply it with oxygen. The oxygen-poor blood is then returned to the right heart by the coronary veins;
- *the pulmonary circuit*, or low pressure circuit, receives deoxygenated blood from the right ventricle through the pulmonary artery and it drives it to the lungs, where it is oxygenated and discharged of the body waste. Oxygenated blood is carried by the pulmonary veins and returns back to the left heart atrium.

In this work, we are mainly interested in the properties of the big arteries of the systemic circuit, and in particular the ones located in the upper limb. For this reason in the following paragraphs we focus on this specific component of the cardiovascular system.

The systemic arteries

The arteries of the systemic circulation have the important role to carry blood from the heart to the other organs of the body. There are many types of arteries characterized by a different lumen size. The first part of the circulation, connected with the left heart, is composed by large elastic arteries that branch into medium muscular arteries that reach various sectors of the human body. From these vessels arise even smaller arteries that in turn branch into smaller ones, called arterioles. Arterioles enter the different tissues and divide into the capillaries. Each type of vessel differs from another one also in the composition of the wall's middle layer, the tunica media, usually the thickest one. In the large arteries at the proximal sites – close to the aortic valve – the tunica media shows elastic fenestrated laminea in alternance with collagen fibers and smooth muscle cells, plus a high content of elastin that gives these vessels the name of elastic arteries. This mechanical feature is essential to store the volume of blood during systole and release it during diastole, creating a dumping effect on the pulsatile behavior of the blood flow. The

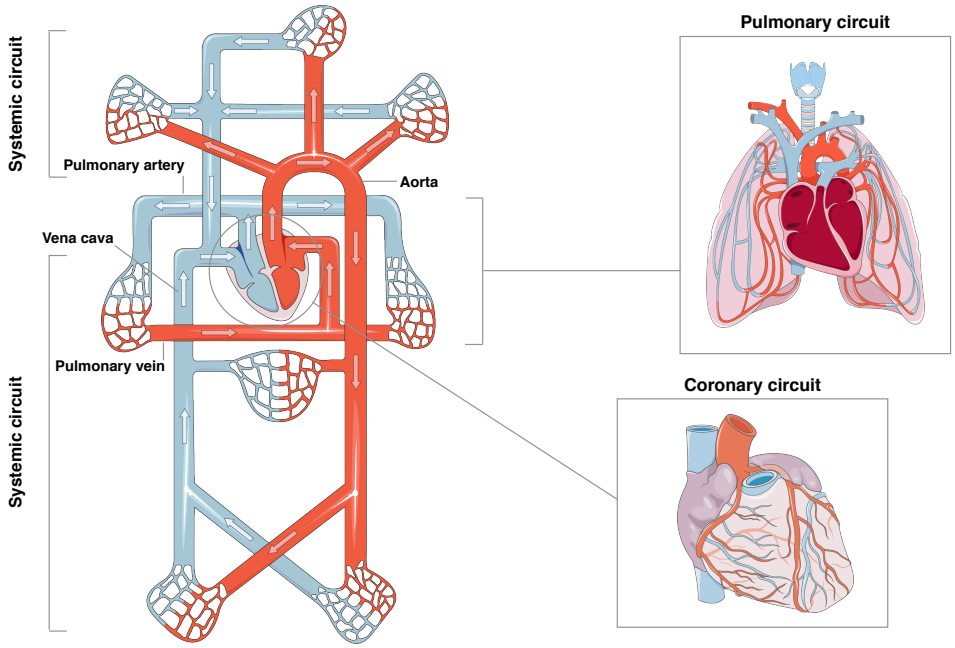

Figure 2 – Schematic representation of the cardiovascular circulation with its main components. The pulmonary and coronary circulation are zoomed to illustrate their anatomy. The Figure was partly generated using Servier Medical Art, provided by Servier, licensed under a Creative Commons Attribution 3.0 unported license.

presence of the muscle cells is of primary importance as these arteries, like the aorta, have to withstand very high pressure values. These cells are also the most important component in the tunica media of the smaller arteries, that contains also connective tissue, collagen and elastin. This composition gives the vessels the ability to regulate the flow by contracting or expanding the lumen, acting as resistors.

Anatomy of aorta and the main arteries of the upper limb

In Figure 7 it is possible to observe the anatomy of the arterial tree that covers the upper part of torso and the arms. The aorta is the main biggest artery that arise from the outlet of the left ventricle. In this vessel it is possible to distinguish four sections with a decreasing radius due to a tapering effect. From the aortic valve one can find the ascending aorta, followed by the typical curvature of the vessel, that takes the name of aortic arch, then there is the descending (or thoracic) aorta that ends around the level of the diaphragm and finally the abdominal aorta. The aortic arch presents three branches: the brachiocephalic trunk that divides into the right common carotid artery and the right subclavian artery, the left common carotid artery and the left subclavian artery. The subclavian arteries is one of the five main vessels of the upper limb, followed anatomically by the axillary artery and the brachial artery that branches into the radial and ulnar arteries that end at the level of the hand. The arteries of the upper limb are of primary importance in the clinical practice as they are used to access pressure measurements as we will see in details in the next section.

Pressure and blood flow in arteries

Blood Pressure is the force responsible for the blood to flow, more precisely thanks to the pressure gradients within the circulation. In Figure 8 it is possible to observe

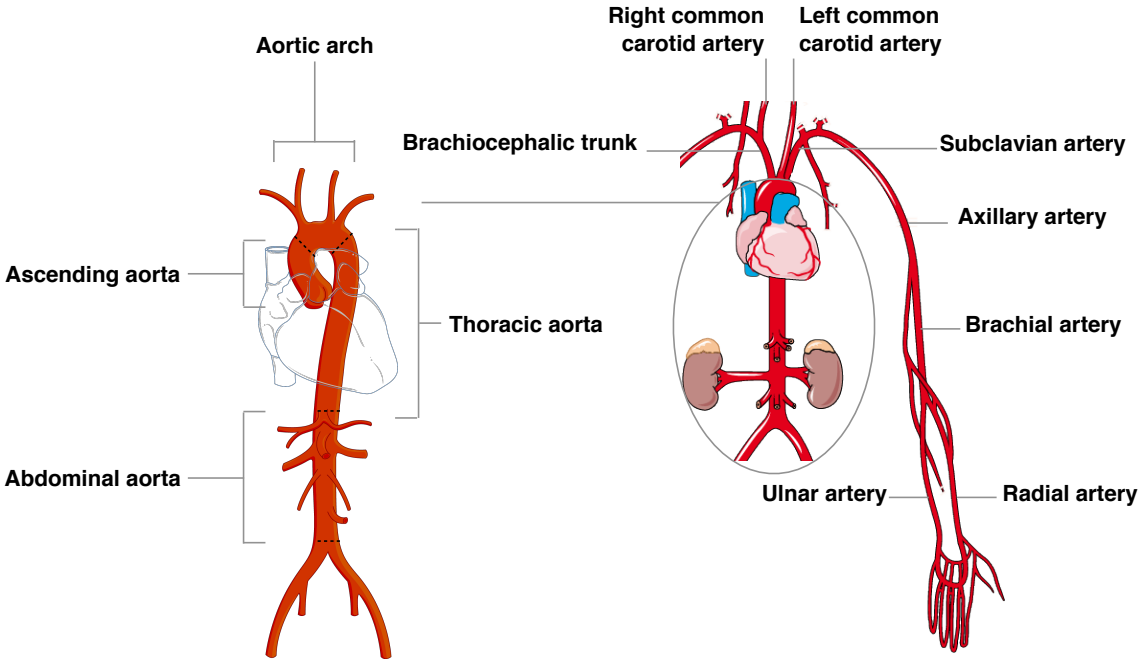

Figure 3 – Anatomy of the arterial circulation perfusing the torso and the arm. A focus on the aortic vessel is illustrated to show its sections. The Figure was partly generated using Servier Medical Art, provided by Servier, licensed under a Creative Commons Attribution 3.0 unported license.

how pressure varies inside the heart and throughout the arterial network: the more the lumen of the vessel decrease the more the pressure is dissipated to drive blood into the microcirculation. However, if we analyze the pressure curve at two close points on the axis of a vessel, for example the aorta, we can observe that the shape is almost unchanged but the one more far from the aortic valve has a delay with respect to the closer one. This suggests an important aspect of the pressure, that once it is generated as a pulse by the ventricle then travels along the vessels as a wave, and is reflected when encounters a barrier (e.g. a branching point). As blood pressure is unsteady, it is important to have a closer look at its shape in time. The blood pressure in the systemic arteries is directly coupled with the left ventricular contraction. During systole the left ventricular pressure rises and overcomes the aortic pressure, the aortic valve opens and the ejection starts. This marks the beginning of the positive slope in the blood pressure inside the aorta, known as the systolic period, in this phase ventricular and aortic pressure have similar values and shape. This first phase of the aortic pressure waveform is highly patient-specific and it is sensitive to the resistance that the left ventricle has to deal with as a pump. The pressure inside the vessel increases due to the high volume of blood coming from the heart, it becomes greater than the ventricular pressure and reaches a peak – the systolic pressure – then it starts to fall and the downslope is interrupted by a notch – the dicrotic notch – that happens simultaneously to the aortic valve closure. After this point there is a small increase in pressure caused by the reflected dicrotic wave. With the aortic valve closure the connection between the heart and the vessel is interrupted and the ventricular pressure rapidly falls while the aortic pressure enters its diastolic phase, characterized by a slow downslope thanks to the elasticity of its wall that acts as a reservoir and push back the blood stored during systole, and finally reaches its minimum value, known as diastolic pressure. The description given in this paragraph about the shape of the pressure wave is quite general and can apply to almost every large arteries of the systemic circulation.

However, the systolic and diastolic pressure as well as the dicrotic notch vary depending on the elastic properties of the vessel and the distance from the aortic valve, where the pressure pulse is first generated. For example, it is worth mentioning that, with respect to the aortic pressure waveform, the arteries of the upper limb present a sharper shape with a higher systolic peak. In particular, it is possible to observe a higher systolic peak and increased pulse pressure [Hamilton et al., 1936] while there is a small decrease in the diastolic and mean pressure [Kroeker and Wood, 1955].

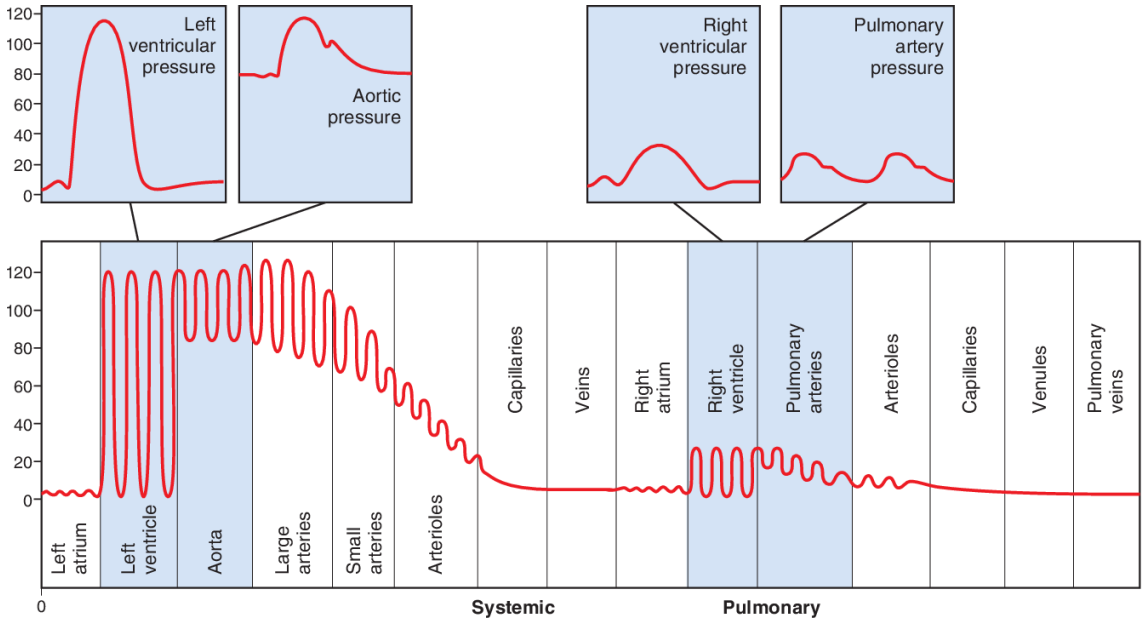

Figure 4 – Changes in the blood pressure inside the four heart chambers and throughout the different vessels of the cardiovascular circulation. Figure taken from Hall [2015].

Blood flow is a measure of the volume of blood that flows, in our case, through an artery in a determined time period. It is an unsteady motion driven by the pressure gradient and the resistance opposed by vessels due to the friction between blood and vessel wall. The shape of the ventricular ejection is determinant for the pattern of the flow wave in the very first part of the circulation, the aorta. This strong relation is also observed when it comes to heart rate. In fact, with a normal heartbeat, the forward flow corresponds to the $25-30\%$ of the cardiac cycle, this percentage rises up to the 50% with an increased heart frequency (e.g. during exercise) [Caro et al., 1978]. The positive trend of the blood flow curve starts with the opening of the aortic valve and the consequent ventricular ejection. The blood flow wave shows a rapid increase, up to a peak, and then decreases slowly and in certain cases a small back flow appears after the aortic valve closure with the relaxation of the ventricle [Nara et al., 2014]. In the previous paragraph it is mentioned that the flow is governed by the pressure, for this reason it is quite evident that the two phenomena are time-related. At the very beginning of the systolic period they rise in phase with each other, while in the late systole the reflected pressure waves breaks this synchrony.

Pathological cases: markers

In the previous sections we have highlighted the strong influence of vessel wall elasticity on the arterial waveforms. In fact, the elasticity allows the vessel to store the energy during the systolic phase and slowly return it during the diastole decreasing the systolic pressure

and increasing the diastolic one [Chassot, 2015]. As a consequence, when the arterial wall looses its elasticity, for example with aging, it is possible to observe an increase in the systolic peak and a decrease in the pressure return during diastole, as well as a decrease in the aortic blood velocity peak. In elder people large arteries are not able to dampen the pulsatile behavior of the heart and this causes damages to the cardiovascular system. Stiffness increases the afterload that the heart has to overcome, incrementing its work, it influences the flow in the coronaries and the perfusion of organs [Kannangara et al., 2015; O'Rourke, 2008]. The lack in elasticity, which might occurs also in presence of stents, increases the wave travel velocity and the peripheral resistance that the waves encounter. This causes the reflected wave to merge with the incident wave earlier, increasing even more the systolic peak and, in the worst scenario, generating a double peak. This particular waveform was found to be related to coronary artery diseases by Weber et al. [2004]. Another common pathology of arteries that locally affect vascular properties is arterial stenosis, that involves the reduction of the lumen of the vessel. This disease is related to flow waves of lower amplitude that show a tiny back flow, sometimes not present at all. The pressure wave remains mainly unchanged above the obstacle but has a reduced amplitude below. Vasodilation and vasoconstriction can be detected by looking at the dicrotic notch. In case of high vasodilation the notch appears at a lower value than the diastolic pressure wave [Murray and Foster, 1996]. On the other hand, vasoconstriction causes the increase of the dicrotic notch pressure value [Politi et al., 2016]. Even if changes in pressure and blood flow waves are mainly linked to variations in the vascular properties, there are also some cardiac problems that can be recognized looking at the pressure and flow waveforms. In case of hypertrophic cardiomyopathy it is possible to observe a biphasic flow ejection that causes a biphasic pressure pulse. The same pressure pattern is found, together with an increase in blood velocity inside the aorta, when the aortic valve presents some stenosis. Finally, in case of weakness of the cardiac muscle tissue, it is possible to observe a shorter systolic period in the flow wave [Vlachopoulos et al., 2011].

Measurements

We refer to [Mynard et al., 2020; Papaioannou et al., 2009] for a deep analysis of the available methods for pressure and blood flow assessments.

Pressure

- *Non-invasive measurements*
  - *Applanation tonometry* involves the compression of a superficial artery against a bone with a pressure transducer. Radial artery is suitable for the application of this technique.
  - *Volume-clamp method* is applied to fingers arteries. It involves a finger cuff with a infrared transmission plethysmograph that calibrate the volume of the artery. When volume of blood tends to increase so does the pressure inside the cuff in order to clamp the volume.
- *Invasive measurements*
  - *Micromanometer-tipped catheters* requires the use of a intravascular catheter with a very small transducer at the tip of it.
  - *Fluid-filled catheter with external manometer* allows for a continuous pressure monitoring. A needle is placed into the artery and is connected to a fluid-filled system connected to a monitor.

Flow and velocity

- *Non-invasive measurements*
  - *Phase contrast-MRI* is based on the proportionality between changes in phase of proton and their velocity through a magnetic field. The average velocity is deduced from the MRI scan images and multiplied by the cross-section to obtain the volume flow.
  - *Pulsed Doppler ultrasound* allows to register a velocity spectrum over time and commercial software are able to extrapolate velocity waveforms from it.
- *Invasive measurements*
  - *Perivascular flow probes* relies on transit-time between two ultrasound beams, placed upstream and downstream of the same vessel [D'Ancona et al., 2000].
  - *Doppler 'flow-wires'* measure velocities, an example is the Philips Volcano ComboWire that gives also pressure measurements thanks to the inclusion of a micromanometer.

Recovery of the central pressure

The blood pressure inside the aorta, also known as central aortic pressure (CAP), is directly linked to the pressure inside the ventricle and provides vital information about the heart and the arterial circulation [Chen et al., 1996; Liu et al., 1986; Westerhof and O'Rourke, 1995]. However, as we have seen in the previous section, a direct access to measurements of the CAP requires invasive and expensive techniques, while less or non-invasive methods give the access to peripheral pressures [Chen et al., 1997]. Though, distal pressure, like in the brachial or radial artery, are not representative of the cardiovascular state [Chirinos et al., 2005; Jankowski et al., 2004]. Consequently, there has been efforts to find a way to use those accessible measurements of pressure to predict the cardiovascular conditions at the central sites. These efforts mainly converge towards the development of a transfer function that gives an estimate of the aortic pressure from measurements of the brachial or radial one [Chen et al., 1997; Karamanoglu et al., 1993; Sharman et al., 2006; Westerhof et al., 2008]. The use of the transfer function (TF) for this clinical application relies on the hypothesis that the relations between the pressure at two different sites and between pressure and flow are linear. For this reason, it is just after Womersley [1957] deduced that nonlinearities in the Navier-Stokes equations applied to the circulatory system could be neglected – because small with respect to the errors introduced by the measurement technique – that TFs started to draw the attention of physiologists [Gallagher et al., 2004]. McDonald and Taylor [1959] were the first to promote the use of TF to describe the circulation in terms of pressure-flow relationship. In order to do that they expressed pressure and flow waves in the frequency domain, representing them by the Fourier series and then relating them to each others. At the beginning their work encountered some resistance from the American Physiological Society, but was finally recognized [O'Rourke and Avolio, 2008]. The rise of accurate non-invasive technique to obtain distal pressure measurements (e.g. tonometry) brought scientists to use TFs to relate the CAP with the distal pressure of the upper limb [Gallagher et al., 2004]. First, O'Rourke [1970] exploited the TF in order to study the cardiovascular factors that change the relationship between the two pressures. Afterwords, some studies has been done to analyze the stability of the transfer function under different conditions [Karamanoglu et al., 1993; Stok et al., 2011]. Sometimes, using arterial models of the upper limb to introduce the wave propagation features [Karamanoglu

et al., 1995; Westerhof et al., 2007]. The restriction to the availability of aortic pressure measurements prevented this analysis to go further and moved some researchers to work on the carotid pressure [Karamanoglu et al., 1993; Karamanoglu and Feneley, 1996], or the brachial one [Bos et al., 1996]. Even though there exists work where the TF has been applied to link the femoral and aortic pressure [Fitchett, 1993], this is risky because of the changes in the aorta due to aging or disease [Vlachopoulos et al., 2011] that cannot be directly taken into account in the transfer function. A company (AtCor Medical Pty Ltd, Sydney, New South Wales, Australia) decided to exploit the generalized transfer function to build a commercial device, the *SphygmoCor*®, and the Food and Drug Administration allowed the incorporation of TF method into the device to generate CAP from calibrated radial pressure recorded with non-invasive techniques [O'Rourke and Avolio, 2008]. The commercialization of the *SphygmoCor*® interested the scientific community and its functioning was analyzed against other pressure monitoring techniques [Cloud et al., 2003; Pauca et al., 2001; Soderstrom et al., 2002]. In the years, several different strategies has been developed to retrieve a transfer function [Westerhof et al., 2007]. Some TF are obtained from a linear autoregressive model (ARX) [Chen et al., 1997; Joachim et al., 2017; Stok et al., 2011], that is based on a linear different equation that links the inputs and outputs of a system and depends on some parameters [Ljung, 1999]. This approach was compared by [Fetics et al., 1999] to the Fourier-based TF [Oppenheim and Schafer, 1975] proving that the ARX-based transfer functions showed a better performance. In other works, the transfer function is derived and calibrated using a model of the arteries concerned [Karamanoglu et al., 1995; Karamanoglu and Feneley, 1996, 1997; Westerhof et al., 2007].

Discussion

The monitoring of the cardiovascular conditions of a patient represents a major issue, in particular for anesthesiologists that have to prevent non-physiological circulatory behavior during general anesthesia, that could cause dangerous damages. As we have mentioned above, the CAP is a good marker for the cardiovascular system but it is not directly available without involving invasive procedure. The transfer functions were developed in the intent of relating the central pressure to the radial pressure in order to have acces to this information. Most of the work we have presented above relies on the assumption that the variations of the cardiovascular condition does not affect in a major way the upper limb and so the radial pressure is similar for different subjects [Millasseau et al., 2003]. However, the use of a general TF requires to assume that the relation between the aortic and peripheral pressure is the same for every subject in every clinical conditions. For this reason, as we have seen, some groups tried to overcome this limitation by using a model, calibrated in order to match the measurements, and then used to parametrize the transfer function [Karamanoglu and Feneley, 1996, 1997]. However, this strategy requires multiple steps for both the calibrations and demands the availability of the two pressures involved in the TF. Moreover, the TF is not able to give a good prediction of the dicrotic notch [Fetics et al., 1999], that we have seen is an important marker for the cardiovascular state. To conclude, in real condition it is not possible to take into account in the TFs the characteristics of the subject, like its age, or anatomical informations that are usually available in case of surgery (e.g. lumen and length of the vessels thanks to pre-operative imaging), and that are found to influence a lot the transfer function [Westerhof et al., 2007].

Challenges and objectives

Despite the encouraging outcomes of the transfer functions in retrieving the central aortic pressure from measurements of peripheral pressure waveform, there are still some aspects that should be addressed. The TF is not versatile in terms of adaptability to different subjects and it is not always able to reproduce all the important markers of the pressure wave. In this work we propose a strategy to recover the blood waveforms at the central sites by using distal pressure records. We place our work in the background of general anesthesia, in the perspective of developing a method to estimate the CAP by using available peripheral pressure waves, to move a step towards an augmented cardiovascular monitoring. Our approach is twofold:

I - Arterial circulation modeling

The first step is to develop a model that reproduce the portion of the arterial tree that links the central pressure to the measurements sites. The goal is to obtain a formulation that is able to catch all the important features of blood propagation. In this sense, we rely on a one-dimensional reduced-order model, suitable to describe wave propagation phenomena [Peiro et al., 2003]. Moreover, we derive an energy-preserving formulation for the arterial model, compatible with the coupling to a reduced cardiac model [Caruel et al., 2013] developed in the team MΞDISIM. This coupling is important to understand the behavior of the systemic circulation. Ideally, this coupled model should be used, together with a parameters estimation strategy [Arthurs et al., 2020], to guess directly the cardiac parameters of interest.

II - Inverse problem

In order to derive the inputs of the arterial model by using the output pressure measurements we deduce an inverse problem (IP) strategy, based on an incremental variational approach [Lawless et al., 2005]. The idea is to build a reliable IP that leans on an accurate mathematical analysis of its properties. The goal here is to develop a useful tool that exploits noisy data of distal pressure so as to retrieve input pressure or flow waves. As the IP is directly applied to arterial model we are able to take into account some subject characteristics. Moreover, to test our approach we use some *in vivo* pressure records as input for our IP. These data are kindly provided by the anesthetists of the Hôpital Lariboisière AP-HP, Paris (FR). Willingly, this approach should be coupled with a parameter estimation strategy, in a two-step procedure, to obtain a full patient-specific approach.

Structure of the manuscript

This thesis is composed by two main parts

- Part I concerns the first step of this work, being the modeling of the blood flow circulation in the arteries. It is composed by four chapters
  - Chapter 1: in this chapter we present an introduction on multiscale modeling, highlighting the reasons that motivates the choice of using one-dimensional models for our work. We describe the derivation of one-dimensional formulation of blood flow and its relation with lumped-parameter models. Finally, we present a brief overview of existing one-dimensional models of the circulation.

- Chapter 2: this chapter is constituted by a published article [Manganotti et al., 2021]. The focus is the derivation of a cardiovascular model which has a cardiac model [Caruel et al., 2013] coupled with a one-dimensional model of the aortic circulation. The coupled model relies on a discrete energy-preserving formulation, which required a novel formulation for the circulation model.
- Chapter 3: Chapter 3 represents an 'upgrade' of Chapter 2. The circulation model is extended to represent with one-dimensional segment the main arteries of the upper limb. The modeling choices and the branching conditions are described.
- Chapter 4: in this chapter we describe the main perspective of this work. Namely, the introduction of tapering, the development of a strategy to include losses of flow due to small side vessels without introducing additional one-dimensional segments and the development of a closed-loop model.

- Part II regards the data assimilation strategy derived to estimate central physiological markers by using peripheral measurements. It contains four chapters
  - Chapter 5: in this chapter we present the main methods employed in data assimilation problems and we give an overview of the existing work where these strategies have been employed for inverse problems with cardiovascular applications. Finally, we discuss the motivation of our work and of the choices made to build the inverse problems.
  - Chapter 6: this chapter embodies an article that has been submitted. In this article we derive and analyze an optimal control strategy based on a penalized 4D-Var approach. The objective is to estimate the cardiac output by using peripheral aortic pressure data. This is applied on a linearized model of the blood flow and represents a preliminary step for the following chapter.
  - Chapter 7: Chapter 7 presents the application of an iterative inverse problems, which involves at each iteration the optimal control problem described in the previous chapter, on a model configuration that reflects the set-up required by the clinical application pursued. The radial pressure data are used to retrieve the central pressure close to the heart. The iterative strategy is presented and the model formulation employed is described in all the details.
  - Chapter 8: this final chapter describes the following steps required for this work to meet a real clinical application. In particular, the coupling of the inverse problem strategy described with a parameters estimation problem to move towards patient-specific model. An on-going work on a Kalman filter to estimate vessel elasticity and peripheral impedance is presented.

Disseminations

Journal articles

- Manganotti, J., Caforio, F., Kimmig, F., Moireau, P., and Imperiale, S. (2021). Coupling reduced-order blood flow and cardiac models through energy-consistent strategies: modeling and discretization. Advanced Modeling and Simulation in Engineering Sciences, 8(1), 1-37.

- Imperiale, S., Manganotti, J., and Moireau P. *Submitted in 2022.* Inlet flow recovery from distal pressure in linearized hemodynamics: An optimal control approach. Submitted to Inverse Problems.

Oral presentation

- Virtual Physiological Human - VPH 2020 - online
  Poster presentation: *4D-Var input flux recovery in a hemodynamic problem.*
- Fédération Francilienne de Mécanique - F2M april 2021 - Journée thématique biomécanique et biomatériaux - online
  Oral presentation: *Coupling reduced-order blood flow and cardiac models through energy-consistent strategies: modeling and discretization.*
- Jean Mandel Symposium 2021 - Palaiseau (France)
  Oral presentation: *Flow recovery from distal pressure by optimal control strategy.*
- Colibri Workshop 2022 - Mathematical modeling and machine learning in computational medicine - Graz (Austria)
  Oral presentation: *Input waves recovery from distal pressure by optimal control strategy.*
- Jean Mandel Symposium 2022 - Palaiseau (France)
  Oral presentation in collaboration with F. Kimmig: *Energy preserving reduced-order cardiovascular models for augmented hemodynamics monitoring.*
- 7^{th} International Conference on Computational and Mathematical Biomedical Engineering - CMBE 2022 - Milan (Italy)
  Oral presentation: *4D-Var input waves estimation using non-tangent linear models.*
- 9^{th} World Congress of Biomechanics - WCB 2022 - Taipei (Taiwan)/online
  Oral presentation: *Input waves recovery from distal pressure by optimal control strategy.*

Software development The arterial model presented in Part I has been implemented in the MATLAB code *CardiacLab*, developed by the team MΞDISIM. Moreover, the same model has been implemented in C++ to be compatible with the application of the reduced-order Kalman filter method [Moireau and Chapelle, 2011] code AKILLΞS, developed in the team as well.

Bibliography

Arthurs, C. J., Xiao, N., Moireau, P., Schaeffter, T., and Figueroa, C. A. (2020). A flexible framework for sequential estimation of model parameters in computational hemodynamics. *Advanced Modeling and Simulation in Engineering Sciences*, pages 1–37.

Bos, W. J. W., van Goudoever, J., van Montfrans, G. A., van den Meiracker, A. H., and Wesseling, K. H. (1996). Reconstruction of brachial artery pressure from noninvasive finger pressure measurements. *Circulation*, 94(8):1870–1875.

Caro, C., Pedley, T., Schroter, R., and Seed, W. (1978). *The mechanics of circulation*. Cambridge.

Caruel, M., Chabiniok, R., Moireau, P., Lecarpentier, Y., and Chapelle, D. (2013). Dimensional reduction of cardiac models for effective validation and calibration. In *Functional Imaging and Modeling of the Heart*, pages 259–267. Springer Berlin Heidelberg.

Chassot, P.-G. (2015). *Précis d'anesthésie-réanimation en chirurgie cardiaque*. Université de Lausanne.

Chen, C.-H., Nevo, E., Fetics, B., Pak, P. H., Yin, F. C., Maughan, W. L., and Kass, D. A. (1997). Estimation of central aortic pressure waveform by mathematical transformation of radial tonometry pressure. *Circulation*, 95(7):1827–1836.

Chen, C.-H., Ting, C.-T., Nussbacher, A., Nevo, E., Kass, D. A., Pak, P., Wang, S.-P., Chang, M.-S., and Yin, F. C. (1996). Validation of carotid artery tonometry as a means of estimating augmentation index of ascending aortic pressure. *Hypertension*, 27(2):168–175.

Chirinos, J. A., Zambrano, J. P., Chakko, S., Veerani, A., Schob, A., Perez, G., and Mendez, A. J. (2005). Relation between ascending aortic pressures and outcomes in patients with angiographically demonstrated coronary artery disease. *The American Journal of Cardiology*, 96(5):645–648.

Cloud, G. C., Rajkumar, C., Kooner, J., Cooke, J., and Bulpitt, C. J. (2003). Estimation of central aortic pressure by *SphygmoCor*® requires intra-arterial peripheral pressures. *Clinical Science*, 105(2):219–225.

D'Ancona, G., Ricci, M., Bergsland, J., Salerno, T. A., and Karamanoukian, H. L. (2000). Graft patency verification in coronary artery bypass grafting: Principles and clinical applications of transit time flow measurement. *Angiology*, 51(9):725–731.

Esper, S. A. and Pinsky, M. R. (2014). Arterial waveform analysis. *Best Practice & Research Clinical Anaesthesiology*, 28(4):363–380. Hemodynamic Monitoring Devices.

Fetics, B., Nevo, E., Chen, C.-H., and Kass, D. (1999). Parametric model derivation of transfer function for noninvasive estimation of aortic pressure by radial tonometry. *IEEE Transactions on Biomedical Engineering*, 46(6):698–706.

Fitchett, D. H. (1993). Aortofemoral transfer function: a method to determine the instantaneous aortic valve gradient in aortic valve stenosis. *Journal of the American College of Cardiology*, 22(7):1909–1914.

Gallagher, D., Adji, A., and O'Rourke, M. (2004). Validation of the transfer function technique for generating central from peripheral upper limb pressure waveform. *American Journal of Hypertension*, 17(11):1059–1067.

Hall, J. E. (2015). Guyton and hall textbook of medical physiology.

Hamilton, W. F., Woodbury, R. A., and Harper, H. T., J. (1936). Physiologic relationship between intrathoracic, intraspinal and arterial pressures. *Journal of the American Medical Association*, 107(11):853–856.

Jankowski, P., Kawecka-Jaszcz, K., Czarnecka, D., Brzozowska-Kiszka, M., Styczkiewicz, K., Styczkiewicz, M., Pośnik-Urbańska, A., Bryniarski, L., and Dudek, D. (2004). Ascending aortic, but not brachial blood pressure-derived indices are related to coronary atherosclerosis. *Atherosclerosis*, 176(1):151–155.

Joachim, J., Vallée, F., Gall, A. L., Matéo, J., Lenck, S., Millasseau, S., Houdart, E., Mebazaa, A., and Gayat, E. (2017). Velocity–pressure loops for continuous assessment of ventricular afterload: influence of pressure measurement site. *Journal of Clinical Monitoring and Computing*, 32(5):833–840.

Kannangara, D. O., Davidson, S. M., Pretty, C. G., Kamoi, S., Corbett-Davies, J., Desaive, T., Shaw, G. M., and Chase, J. G. (2015). An assessment of the relationship between dicrotic notch timing and cardiac preload. In *2015 37th Annual International Conference of the IEEE Engineering in Medicine and Biology Society (EMBC)*, pages 1001–1004.

Karamanoglu, M. and Feneley, M. P. (1996). Derivation of the ascending aortic-carotid pressure transfer function with an arterial model. *American Journal of Physiology-Heart and Circulatory Physiology*, 271(6):H2399–H2404.

Karamanoglu, M. and Feneley, M. P. (1997). On-line synthesis of the human ascending aortic pressure pulse from the finger pulse. *Hypertension*, 30(6):1416–1424.

Karamanoglu, M., Gallagher, D. E., Avolio, A. P., and O'Rourke, M. F. (1995). Pressure wave propagation in a multibranched model of the human upper limb. *American Journal of Physiology-Heart and Circulatory Physiology*, 269(4):H1363–H1369.

Karamanoglu, M., O'Rourke, M. F., Avolio, A. P., and Kelly, R. P. (1993). An analysis of the relationship between central aortic and peripheral upper limb pressure waves in man. *European Heart Journal*, 14(2):160–167.

Kroeker, E. J. and Wood, E. H. (1955). Comparison of simultaneously recorded central and peripheral arterial pressure pulses during rest, exercise and tilted position in man. *Circulation Research*, 3(6):623–632.

Lawless, A., Gratton, S., and Nichols, N. (2005). An investigation of incremental 4d-var using non-tangent linear models. *Quarterly Journal of the Royal Meteorological Society*, 131(606):459–476.

Liu, Z., Brin, K. P., and Yin, F. (1986). Estimation of total arterial compliance: an improved method and evaluation of current methods. *American Journal of Physiology-Heart and Circulatory Physiology*, 251(3):H588–H600.

Ljung, L. (1999). *System Identification: Theory for the User*. Prentice Hall information and system sciences series. Prentice Hall PTR.

Mackenzie, J. (1902). The study of the pulse, arterial, venous, and hepatic, and of the movements of the heart. *The Indian Medical Gazette*, 37:287 – 287.

Manganotti, J., Caforio, F., Kimmig, F., Moireau, P., and Imperiale, S. (2021). Coupling reduced-order blood flow and cardiac models through energy-consistent strategies: modeling and discretization. *Advanced Modeling and Simulation in Engineering Sciences*, 8(1):1–37.

McDonald, D. and Taylor, M. (1959). 3 - the hydrodynamics of the arterial circulation. *Progress in Biophysics and Biophysical Chemistry*, 9:105–173.

Millasseau, S. C., Patel, S. J., Redwood, S. R., Ritter, J. M., and Chowienczyk, P. J. (2003). Pressure wave reflection assessed from the peripheral pulse. *Hypertension*, 41(5):1016–1020.

Moireau, P. and Chapelle, D. (2011). Reduced-order unscented kalman filtering with application to parameter identification in large-dimensional systems. *ESAIM: Control, Optimisation and Calculus of Variations*, 17(2):380–405.

Murray, W. B. and Foster, P. A. (1996). The peripheral pulse wave: Information overlooked. *Journal of Clinical Monitoring*, 12(5):365–377.

Mynard, J. P., Kondiboyina, A., Kowalski, R., Cheung, M. M. H., and Smolich, J. J. (2020). Measurement, analysis and interpretation of pressure/flow waves in blood vessels. *Frontiers in Physiology*, 11.

Nara, S., Kaur, M., and Verma, K. L. (2014). Novel notch detection algorithm for detection of dicrotic notch in ppg signals. *International Journal of Computer Applications*, 86(17):36–39.

Oppenheim, A. V. and Schafer, R. W. (1975). Digital signal processing(book). *Research supported by the Massachusetts Institute of Technology, Bell Telephone Laboratories, and Guggenheim Foundation. Englewood Cliffs, N. J., Prentice-Hall, Inc., 1975. 598 p.*

O'Rourke, M. F. (1970). Influence of ventricular ejection on the relationship between central aortic and brachial pressure pulse in man. *Cardiovascular Research*, 4(3):291–300.

O'Rourke, M. F. (2008). How stiffening of the aorta and elastic arteries leads to compromised coronary flow. *Heart*, 94(6):690–691.

O'Rourke, M. F. and Avolio, A. P. (2008). Arterial transfer functions: background, applications and reservations. *Journal of Hypertension*, 26(1):8–10.

Papaioannou, T., Protogerou, A., Stamatelopoulos, K., Vavuranakis, M., and Stefanadis, C. (2009). Non-invasive methods and techniques for central blood pressure estimation: Procedures, validation, reproducibility and limitations. *Current Pharmaceutical Design*, 15(3):245–253.

Pauca, A. L., O'Rourke, M. F., and Kon, N. D. (2001). Prospective evaluation of a method for estimating ascending aortic pressure from the radial artery pressure waveform. *Hypertension*, 38(4):932–937.

Peiro, J., Sherwin, S., Parker, K., Franke, V., Formaggia, L., Lamponi, D., and Quarteroni, A. (2003). Numerical simulation of arterial pulse propagation using one-dimensional models. *Wall-fluid interactions in physiological flows*, pages 1–36.

Politi, M. T., Ghigo, A., Fernández, J. M., Khelifa, I., Gaudric, J., Fullana, J. M., and Lagrée, P.-Y. (2016). The dicrotic notch analyzed by a numerical model. *Computers in Biology and Medicine*, 72:54–64.

Redaelli, A. and Montevecchi, F. (2012). *Biomeccanica. Analisi multiscala di tessuti biologici*. Patron Editore.

Sharman, J. E., Lim, R., Qasem, A. M., Coombes, J. S., Burgess, M. I., Franco, J., Garrahy, P., Wilkinson, I. B., and Marwick, T. H. (2006). Validation of a generalized transfer function to noninvasively derive central blood pressure during exercise. *Hypertension*, 47(6):1203–1208.

Silverthorn, D., Johnson, B. R., Ober, W., Garrison, C. W., and Silverthorn, A. C. (2009). *Human Physiology: an integrated approach*. Pearson.

Soderstrom, S., Nyberg, G., O'Rourke, M., Sellgren, J., and Pontén, J. (2002). Can a clinically useful aortic pressure wave be derived from a radial pressure wave? *British Journal of Anaesthesia*, 88(4):481–488.

Stok, W. J., Westerhof, B. E., Guelen, I., and Karemaker, J. M. (2011). Aortic pressure wave reconstruction during exercise is improved by adaptive filtering: a pilot study. *Medical and Biological Engineering and Computing*, 49(8):909–916.

Tortora, G. and Derrickson, B. (2008). *Principles of Anatomy and Physiology*. John Wiley & Sons.

Vlachopoulos, C., ORourke, M., and Nichols, W. W. (2011). *McDonalds Blood Flow in Arteries*. CRC Press.

Weber, T., Auer, J., O'Rourke, M. F., Kvas, E., Lassnig, E., Berent, R., and Eber, B. (2004). Arterial stiffness, wave reflections, and the risk of coronary artery disease. *Circulation*, 109(2):184–189.

Westerhof, B. E., Guelen, I., Stok, W. J., Lasance, H. A. J., Ascoop, C. A. P. L., Wesseling, K. H., Westerhof, N., Bos, W. J. W., Stergiopulos, N., and Spaan, J. A. E. (2008). Individualization of transfer function in estimation of central aortic pressure from the peripheral pulse is not required in patients at rest. *Journal of Applied Physiology*, 105(6):1858–1863.

Westerhof, B. E., Guelen, I., Stok, W. J., Wesseling, K. H., Spaan, J. A. E., Westerhof, N., Bos, W. J., and Stergiopulos, N. (2007). Arterial pressure transfer characteristics: effects of travel time. *American Journal of Physiology-Heart and Circulatory Physiology*, 292(2):H800–H807.

Westerhof, N. and O'Rourke, M. (1995). Haemodynamic basis for the development of left ventricular failure in systolic hypertension and for its logical therapy. *Journal of hypertension*, 13(9):943—952.

Womersley, J. R. (1957). The mathematical analysis of the arterial circulation in a state of oscillatory motion. Technical Report Wade-TR.:56–614.

Introduction (Français)

Il n'y a qu'une seule façon d'apprendre. C'est par l'action. Tout ce que vous devez savoir, vous l'avez appris au cours de votre voyage.
— Paulo Coelho, *L'Alchimiste*

Contexte clinique

Dans cette section, nous résumons quelques informations anatomiques et physiologiques sur la circulation artérielle qui aideront à comprendre l'environnement clinique de la thèse. Cependant, de plus amples détails sur la physiologie et l'anatomie du système cardiovasculaire peuvent être trouvés dans [Silverthorn et al., 2009; Tortora and Derrickson, 2008], sur les caractéristiques mécaniques des vaisseaux dans [Redaelli and Montevecchi, 2012] et sur la pression et le débit sanguin dans [Caro et al., 1978; Esper and Pinsky, 2014; Mackenzie, 1902; Vlachopoulos et al., 2011].

Le système cardiovasculaire

Le système cardiovasculaire (ou système circulatoire) est composé du cœur, du sang et du réseau vasculaire.

- *Le cœur*, est l'organe principal du système. Il présente une paroi musculaire – le myocarde – qui est pourvue d'une activité électrique qui déclenche son activité de pompage qui fait circuler le sang. Dans la Figure 5 il est possible d'observer sa structure, il est composé de quatre chambres : les oreillettes gauche et droite qui sont reliées, respectivement, au ventricule gauche par la valve mitrale et au ventricule droit par la valve tricuspide. Le tissu cardiaque génère le rythme cardiaque en alternant contraction et relaxation. L'activation de l'état contractile est induite par des impulsions électriques qui se produisent dans le myocarde. L'activité électromécanique provoque une série de changements de pression qui entraînent un mouvement du sang à l'intérieur des cavités grâce à l'ouverture de valves unidirectionelles, qui se produit lorsque la pression en amont l'emporte sur celle en aval. Ce processus est connu sous le nom de cycle cardiaque et présente quatre phases différentes qui se produisent presque simultanément pour les parties gauche et droite.

  - *La relaxation isovolumétrique:* c'est le début de la diastole. Les valves atrio-ventriculaires – mitrale et tricuspide – et les valves de sortie – pulmonaire et aortique – sont fermées et la pression à l'intérieur du ventricule diminue.
  - *Le remplissage:* les valves auriculo-ventriculaires sont ouvertes et les valves de sortie sont fermées. Le sang circule des oreillettes vers les ventricules où le volume augmente.
  - *La contraction isovolumétrique:* elle correspond au début de la systole. Les valves sont fermées, le volume sanguin est stable mais la pression à l'intérieur des ventricules augmente.
  - *L'éjection:* les valves de sortie sont ouvertes, le sang est poussé dans la circulation et la contraction continue, augmentant la pression sanguine.

- *Le sang*, est un fluide corporel dont la principale propriété mécanique est la viscosité. Il est composé de plasma, de globules rouges, de globules blancs et de plaquettes. Il est responsable du transport de l'oxygène, des nutriments et des déchets dans l'organisme, il régule la température du corps et réagit aux infections et aux pertes de sang.

- *Le réseau vasculaire* est composé de vaisseaux interconnectés qui transportent le sang depuis et vers le cœur dans tout le corps. Les vaisseaux sanguins sont caractérisés par une zone circulaire vide, qui prend le nom de lumen, et par trois couches concentriques qui forment la paroi : la tunica intima, media et externa. Les vaisseaux peuvent être divisés en trois grandes familles,

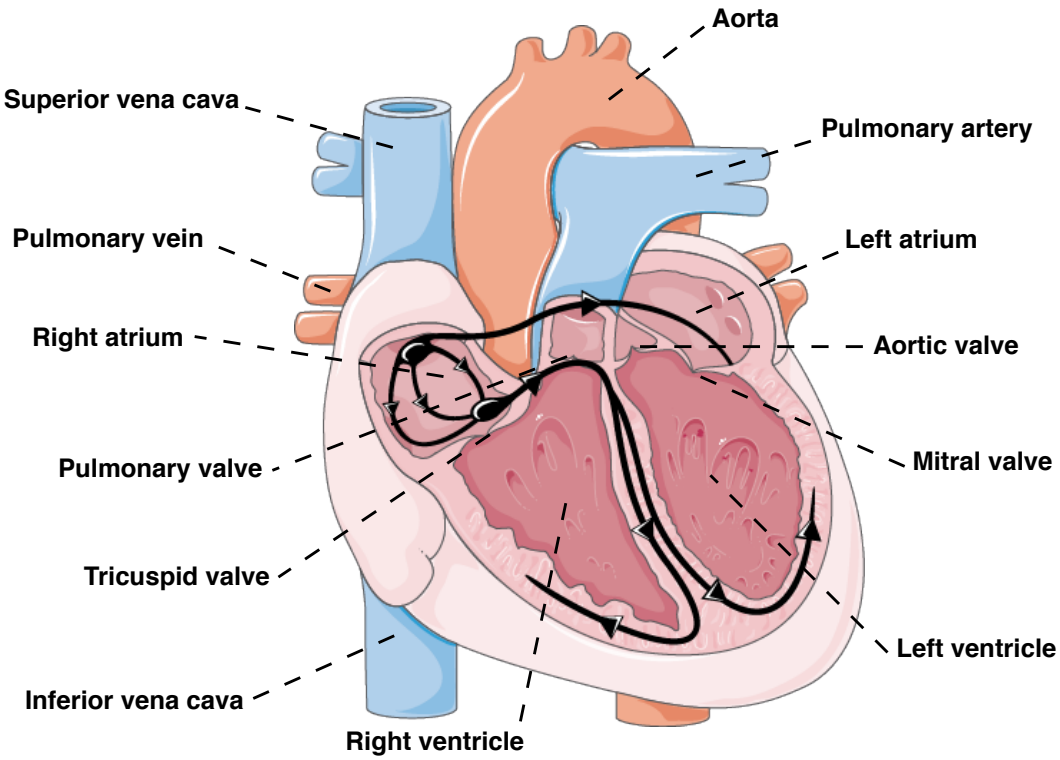

Figure 5 – Représentation de l'anatomie du cœur avec ses principaux composants importants. Le chemin indiqué par les flèches noirs représente la direction de l'impulsion électrique d'activation. La figure a été partiellement générée à l'aide de Servier Medical Art, fourni par Servier, sous licence Creative Commons Attribution 3.0 unported

.

- *Les artères* reçoivent le sang oxygéné du ventricule gauche et le transportent vers l'organisme. Elles sont caractérisées par une paroi musculaire élastique qui les rend capables de subir la forte pression générée par le débit cardiaque (éjection du sang) ;
- *Les veines* sont des vaisseaux de grande taille qui renvoient le sang désoxygéné vers l'oreillette droite. Leur paroi manque d'élasticité et de muscles lisses car leurs fonctions ne nécessitent pas de supporter des pressions élevées ;
- *Les capillaires* sont les plus petits vaisseaux sanguins. Ils forment une connexion entre les petites artères (artérioles) et les veines (veinules). Leur paroi fine permet les échanges d'oxygène et de déchets avec les cellules.

La fonction du système cardiovasculaire est d'envoyer le sang désoxygéné de la cavité cardiaque vers les poumons, où le sang s'oxygène, puis dans les artères qui parcourent tout le corps pour oxygéner les tissus, les muscles et les organes. Enfin, les veines ramènent le sang désoxygéné vers le cœur et le processus recommence. Le système circulatoire peut être considéré comme la somme de trois circuits qui forment une boucle fermée (voir Figure 6) pour que le sang circule

- *le circuit systémique*, ou grande circulation, transporte le sang oxygéné avec les nutriments et les hormones du ventricule gauche vers le reste du corps en passant par l'aorte – l'artère principale du circuit systémique. Ensuite, les veines reçoivent les déchets des muscles, des organes et des tissus et renvoient le sang désoxygéné vers l'oreillette droite via les veines caves ;

- *le circuit coronaire* est considéré comme une partie de la circulation systémique. Il fournit du sang oxygéné aux tissus du cœur. Deux artères coronaires se ramifient à partir de l'aorte, enveloppent le myocarde et l'alimentent en oxygène. Le sang pauvre en oxygène est ensuite renvoyé vers le cœur droit par les veines coronaires ;

- *le circuit pulmonaire*, ou circuit basse pression, reçoit le sang désoxygéné du ventricule droit par l'artère pulmonaire et le conduit vers les poumons, où il est oxygéné et débarrassé des déchets de l'organisme. Le sang oxygéné est transporté par les veines pulmonaires et retourne à l'oreillette du cœur gauche.

Dans ce travail, nous nous intéressons principalement aux propriétés des grandes artères du circuit systémique, et en particulier celles situées dans le membre supérieur. C'est pourquoi, dans les paragraphes suivants, nous nous concentrons sur cette composante spécifique du système cardiovasculaire.

Les artères systémiques

Les artères de la circulation systémique ont le rôle important de transporter le sang du cœur vers les autres organes du corps. Il existe de nombreux types d'artères caractérisées par une taille du lumen différente. La première partie de la circulation, reliée au cœur gauche, est composée de grandes artères élastiques qui se ramifient en artères musculaires moyennes qui atteignent divers secteurs du corps humain. De ces vaisseaux naissent des artères plus petites qui se ramifient à leur tour en artères encore plus petites, appelées artérioles. Les artérioles pénètrent dans les différents tissus et se divisent en capillaires. Chaque type de vaisseau diffère d'un autre également par la composition de la couche médiane de la paroi, la tunica media, généralement la plus épaisse. Dans les grosses artères proximales – près de la valve aortique – la tunica media présente des lamelles élastiques fenêtrées en alternance avec des fibres de collagène et des cellules musculaires lisses, ainsi

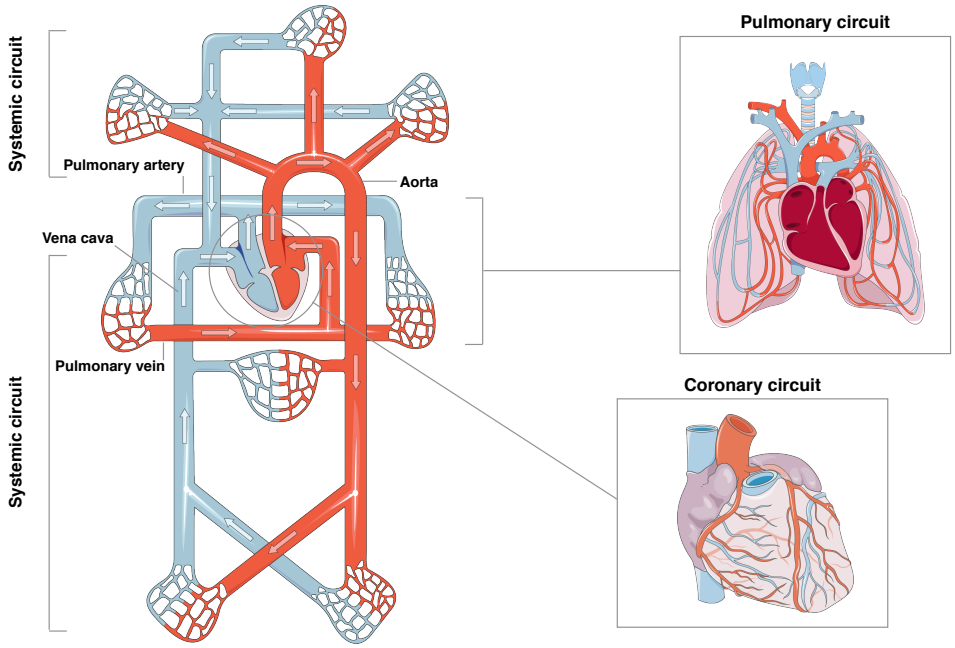

Figure 6 – Représentation schématique de la circulation cardiovasculaire avec ses principaux composants. Les circulations pulmonaire et coronaire sont zoomées pour illustrer leur anatomie. La figure a été partiellement générée à l'aide de Servier Medical Art, fourni par Servier, sous licence Creative Commons Attribution 3.0 unported.

qu'une forte teneur en élastine qui donne à ces vaisseaux le nom d'artères élastiques. Cette caractéristique mécanique est essentielle pour stocker le volume de sang pendant la systole et le libérer pendant la diastole, créant un effet de vidange sur le comportement pulsatile du flux sanguin. La présence des cellules musculaires est de première importance car ces artères, comme l'aorte, doivent supporter des valeurs de pression très élevées. Ces cellules sont également le composant le plus important de la tunica medi des petites artères, qui contient également du tissu conjonctif, du collagène et de l'élastine. Cette composition donne aux vaisseaux la capacité de réguler le flux en contractant ou en élargissant le lumen, agissant comme des résistances.

Anatomie de l'aorte et des artères principales du membre supérieur

La Figure 7 permet d'observer l'anatomie de l'arbre artériel qui couvre la partie supérieure du torse et les bras. L'aorte est la plus grande artère principale qui naît de la sortie du ventricule gauche. Dans ce vaisseau, il est possible de distinguer quatre sections dont le rayon diminue en raison d'un effet d'amincissement. À partir de la valve aortique, on trouve l'aorte ascendante, suivie de la courbure typique du vaisseau, qui prend le nom d'arc aortique, puis il y a l'aorte descendante (ou thoracique) qui se termine au niveau du diaphragme et enfin l'aorte abdominale. L'arc aortique présente trois branches : le tronc brachiocéphalique qui se divise en artère carotide commune droite et artère sous-clavière droite, l'artère carotide commune gauche et l'artère sous-clavière gauche. L'artère sous-clavière est l'un des cinq principaux vaisseaux du membre supérieur, suivi anatomiquement par l'artère axillaire et l'artère brachiale qui se ramifie en artères radiale et cubitale qui se terminent au niveau de la main. Les artères du membre supérieur sont de première importance dans la pratique clinique car elles sont utilisées pour accéder aux mesures de pression comme nous le verrons en détail dans la section suivante.

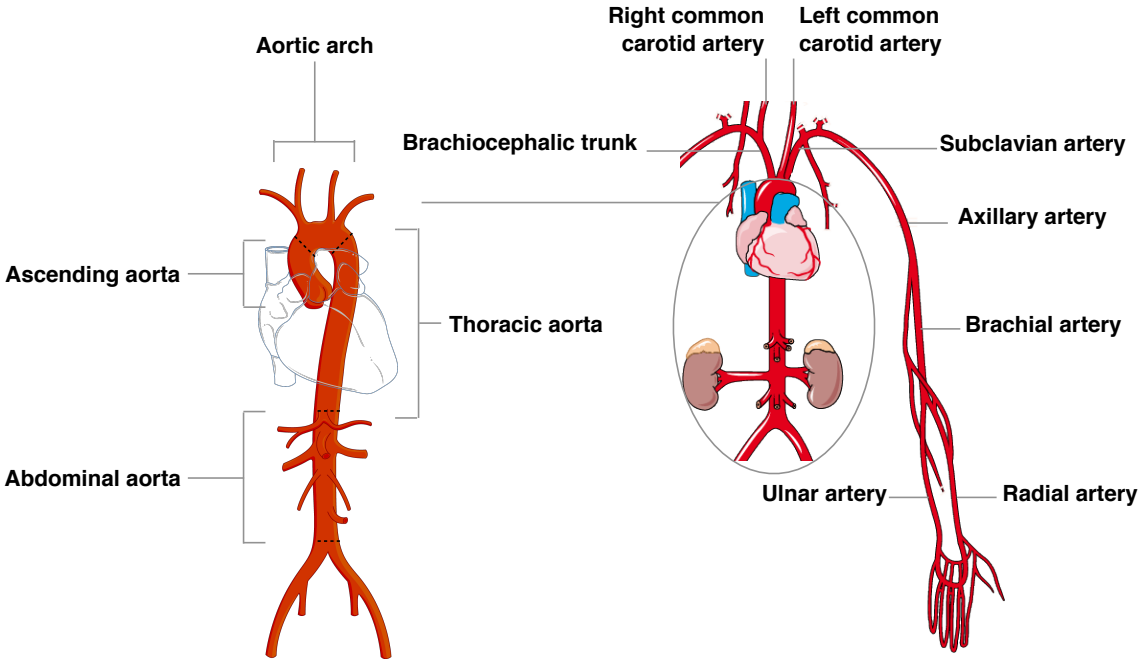

Figure 7 – Anatomie de la circulation artérielle irriguant le torse et le bras. Un focus sur le vaisseau aortique est illustré pour montrer ses sections. La figure a été partiellement générée à l'aide de Servier Medical Art, fourni par Servier, sous licence Creative Commons Attribution 3.0 unported.

Pression et débit sanguin dans les artères

La pression est la force responsable de l'écoulement du sang, plus précisément grâce aux gradients de pression au sein de la circulation. Dans la Figure 8, il est possible d'observer comment la pression varie à l'intérieur du cœur et dans tout le réseau artériel : plus le lumen du vaisseau diminue, plus la pression est dissipée pour conduire le sang dans la microcirculation. Cependant, si nous analysons la courbe de pression en deux points proches sur l'axe d'un vaisseau, par exemple l'aorte, nous pouvons observer que la forme est presque inchangée mais que celui qui est le plus éloigné de la valve aortique présente un retard par rapport à celui qui est le plus proche. Cela suggère un aspect important de la pression, à savoir qu'une fois qu'elle est générée sous forme d'impulsion par le ventricule, elle se déplace le long des vaisseaux sous forme d'onde, et est réfléchie lorsqu'elle rencontre une barrière (par exemple, un point de ramification). Comme la pression sanguine est instable, il est important d'examiner de plus près sa forme dans le temps. La pression sanguine dans les artères systémiques est directement couplée à la contraction du ventricule gauche. Pendant la systole, la pression du ventricule gauche augmente et dépasse la pression aortique, la valve aortique s'ouvre et l'éjection commence. Cela marque le début de la pente positive de la pression sanguine à l'intérieur de l'aorte, connue sous le nom de période systolique. Dans cette phase, les pressions ventriculaire et aortique ont des valeurs et une forme similaires. Cette première partie de l'onde de pression aortique est très spécifique au patient et elle est sensible à la résistance que le ventricule gauche doit surmonter en tant que pompe. La pression à l'intérieur du vaisseau augmente en raison du volume élevé de sang provenant du cœur, elle devient supérieure à la pression ventriculaire et atteint un pic – la pression systolique – puis elle commence à diminuer et la pente descendante est interrompue par une encoche – l'encoche dicrotique – qui se produit en même temps que la fermeture de la valve aortique. Après ce point, il y a une petite augmentation de la pression causée par l'onde dicrotique réfléchie. Avec la

fermeture de la valve aortique, la connexion entre le coeur et le vaisseau est interrompue et la pression ventriculaire chute rapidement tandis que la pression aortique entre dans sa phase diastolique, caractérisée par une lente descente grâce à l'élasticité de sa paroi qui agit comme un réservoir et repousse le sang stocké pendant la systole, pour finalement atteindre sa valeur minimale, appelée pression diastolique. La description donnée dans ce paragraphe sur la forme de l'onde de pression est assez générale et peut s'appliquer à presque toutes les grandes artères de la circulation systémique. Cependant, la pression systolique et diastolique ainsi que l'échancrure dicrotique varient en fonction des propriétés élastiques du vaisseau et de la distance par rapport à la valve aortique, où l'impulsion de pression est générée en premier. Par exemple, il convient de mentionner que, par rapport à la forme d'onde de la pression aortique, les artères du membre supérieur présentent une forme plus nette avec un pic systolique plus élevé. En particulier, il est possible d'observer un pic systolique plus élevé et une augmentation de la pression pulsée [Hamilton et al., 1936] alors qu'il y a une légère diminution de la pression diastolique et moyenne [Kroeker and Wood, 1955].

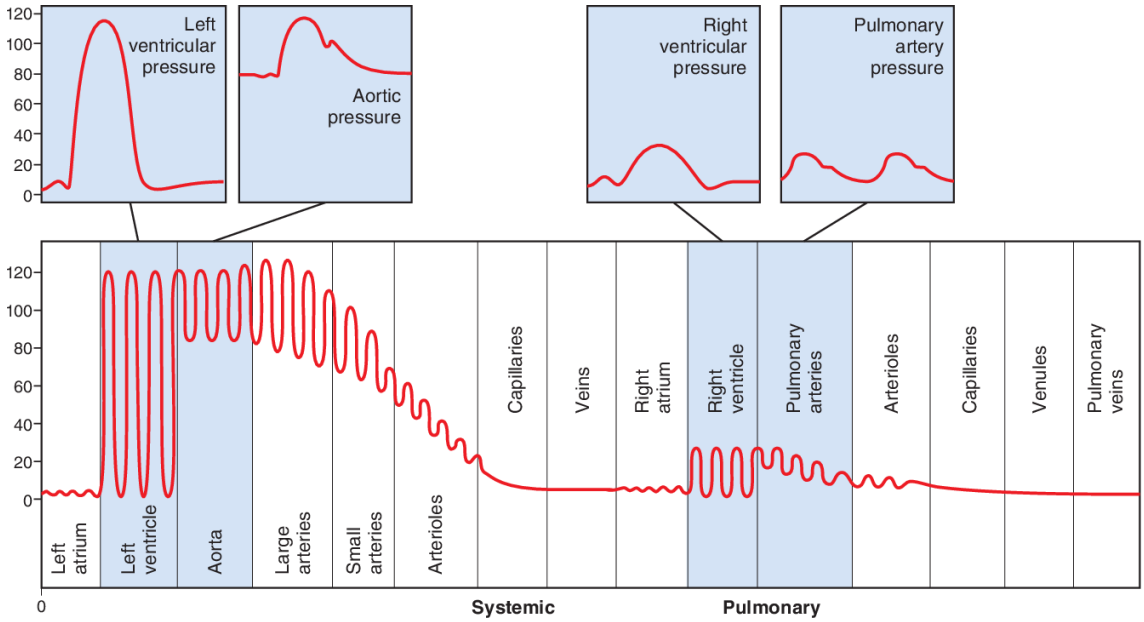

Figure 8 – Changements de la pression sanguine à l'intérieur des quatre cavités cardiaques et dans les différents vaisseaux de la circulation cardiovasculaire. Figure tirée de Hall [2015].

Le débit est une mesure du volume de sang qui circule, dans notre cas, dans une artère pendant une période déterminée. Il s'agit d'un mouvement instable entraîné par le gradient de pression et la résistance opposée par les vaisseaux en raison de la friction entre le sang et la paroi des vaisseaux. La forme de l'éjection ventriculaire est déterminante pour la configuration de l'onde d'écoulement dans la toute première partie de la circulation, l'aorte. Cette relation forte est également observée en ce qui concerne la fréquence cardiaque. En effet, lors d'un battement cardiaque normal, le flux vers l'avant correspond aux $25 - 30\%$ du cycle cardiaque, ce pourcentage s'élève jusqu'aux 50% avec une augmentation de la fréquence cardiaque (par exemple lors d'un exercice physique) [Caro et al., 1978]. La tendance positive de la courbe de débit sanguin commence avec l'ouverture de la valve aortique et l'éjection ventriculaire qui en résulte. L'onde de débit sanguin montre une augmentation rapide, jusqu'à un pic, puis diminue lentement et dans certains cas, un petit reflux apparaît après la fermeture de la valve aortique avec la relaxation du ventricule

[Nara et al., 2014]. Dans le paragraphe précédent, il est mentionné que le débit est régi par la pression, pour cette raison il est évident que les deux phénomènes sont liés en temps. Au tout début de la période systolique, ils s'élèvent en phase l'un avec l'autre, tandis que dans la systole tardive, les ondes de pression réfléchies brisent cette synchronisation.

Cas pathologiques: marqueurs

Dans les sections précédentes, nous avons souligné la forte influence de l'élasticité de la paroi vasculaire sur les formes d'onde artérielles. En effet, l'élasticité permet au vaisseau de stocker l'énergie pendant la phase systolique et de la restituer lentement pendant la diastole en diminuant la pression systolique et en augmentant la pression diastolique [Chassot, 2015]. En conséquence, lorsque la paroi artérielle perd son élasticité, par exemple avec le vieillissement, il est possible d'observer une augmentation du pic systolique et une diminution du retour de pression pendant la diastole, ainsi qu'une diminution du pic de vitesse du sang aortique. Chez les personnes âgées, les grosses artères ne sont pas en mesure d'amortir le comportement pulsatile du cœur, ce qui cause des dommages au système cardiovasculaire. La rigidité augmente la postcharge que le cœur doit surmonter, ce qui augmente son travail, elle influence le flux dans les coronaires et la perfusion des organes [Kannangara et al., 2015; O'Rourke, 2008]. Le manque d'élasticité augmente également la vitesse de déplacement des ondes et la résistance périphérique qu'elles rencontrent. Ainsi, l'onde réfléchie fusionne plus tôt avec l'onde incidente, ce qui augmente encore le pic systolique et, dans le pire des cas, génère un double pic. Cette forme d'onde particulière a été mise en relation avec les maladies des artères coronaires par Weber et al. [2004]. Une autre pathologie courante des artères qui affecte localement les propriétés vasculaires est la sténose artérielle, qui implique la réduction de le lumen du vaisseau. Cette maladie est liée à des ondes de flux de plus faible amplitude qui montrent un minuscule reflux, parfois inexistant. L'onde de pression reste essentiellement inchangée au-dessus de l'obstacle mais présente une amplitude réduite en dessous. La vasodilatation et la vasoconstriction peuvent être détectées en observant l'encoche dicrotique. En cas de forte vasodilatation, l'encoche apparaît à une valeur inférieure à celle de l'onde de pression diastolique [Murray and Foster, 1996]. D'autre part, la vasoconstriction provoque l'augmentation de la valeur de pression de l'encoche dicrotique [Politi et al., 2016]. Même si les changements dans les ondes de pression et de débit sanguin sont principalement liés aux variations des propriétés vasculaires, il existe également certains problèmes cardiaques qui peuvent être reconnus en regardant les formes d'ondes de pression et de débit. En cas de cardiomyopathie hypertrophique, il est possible d'observer une éjection biphasique du flux qui entraîne une impulsion de pression biphasique. On retrouve le même schéma de pression, accompagné d'une augmentation de la vitesse du sang à l'intérieur de l'aorte, lorsque la valve aortique présente une certaine sténose. Enfin, en cas de faiblesse du tissu musculaire cardiaque, il est possible d'observer une période systolique plus courte dans l'onde d'écoulement [Vlachopoulos et al., 2011].

Mesures

Nous renvoyons à [Mynard et al., 2020; Papaioannou et al., 2009] pour une analyse approfondie des méthodes disponibles pour les évaluations de la pression et du débit sanguin.

Pression

- *Mesures non invasives*

- *Tonométrie d'aplanissement* implique la compression d'une artère superficielle contre un os avec un capteur de pression. L'artère radiale se prête à l'application de cette technique.
- *Méthode de la pince à volume* est appliqué aux artères des doigts. Il s'agit d'un brassard de doigt muni d'un pléthysmographe à transmission infrarouge qui calibre le volume de l'artère. Lorsque le volume du sang a tendance à augmenter, la pression à l'intérieur du brassard augmente également, ce qui permet de maintenir le volume constant.

- *Mesures invasives*
  - *Cathéters munis d'un micromanomètre* nécessite l'utilisation d'un cathéter intravasculaire muni d'un très petit transducteur à son extrémité.
  - *Cathéter rempli de liquide avec manomètre externe* permet une surveillance continue de la pression. Une aiguille est placée dans l'artère et est reliée à un système rempli de fluide connecté à un moniteur.

Débit et vélocité

- *Mesures non invasives*
  - *L'IRM par contraste de phase* est basée sur la proportionnalité entre les changements de phase des protons et leur vitesse à travers un champ magnétique. La vitesse moyenne est déduite des images de l'IRM et multipliée par la section transversale pour obtenir le flux volumique.
  - *L'échographie Doppler pulsée* permet d'enregistrer un spectre de vitesse dans le temps et les logiciels commerciaux sont capables d'en extrapoler les formes d'onde de vitesse.

- *Mesures invasives*
  - *Sondes de débit périvasculaire* repose sur le temps de transit entre deux faisceaux d'ultrasons, placés en amont et en aval du même vaisseau [D'Ancona et al., 2000].
  - *Les fils de débit Doppler* mesurent les vitesses, un exemple est le Philips Volcano ComboWire qui donne également des mesures de pression grâce à l'inclusion d'un micromanomètre.

Récupération de la pression centrale

La pression sanguine à l'intérieur de l'aorte, également appelée pression aortique centrale (PAC), est directement liée à la pression à l'intérieur du ventricule et fournit des informations vitales sur le cœur et la circulation artérielle [Chen et al., 1996; Liu et al., 1986; Westerhof and O'Rourke, 1995]. Cependant, comme nous l'avons vu dans la section précédente, un accès direct aux mesures de la PAC nécessite des techniques invasives et coûteuses, alors que des méthodes moins ou non invasives donnent accès aux pressions périphériques [Chen et al., 1997]. Cependant, les pressions distales, comme dans l'artère brachiale ou radiale, ne sont pas représentatives de l'état cardiovasculaire [Chirinos et al., 2005; Jankowski et al., 2004]. Par conséquent, des efforts ont été faits pour trouver un moyen d'utiliser ces mesures accessibles de la pression pour prédire les conditions cardiovasculaires aux sites centraux. Ces efforts convergent principalement vers le développement d'une fonction de transfert qui donne une estimation de la pression aortique à partir des

mesures de la pression brachiale ou radiale [Chen et al., 1997; Karamanoglu et al., 1993; Sharman et al., 2006; Westerhof et al., 2008]. L'utilisation de la fonction de transfert (FT) pour cette application clinique repose sur l'hypothèse que les relations entre la pression à deux sites différents et entre la pression et le débit sont linéaires. Pour cette raison, c'est juste après que Womersley [1957] ait déduit que les non-linéarités dans les équations de Navier-Stokes appliquées au système circulatoire pouvaient être négligées – car faibles par rapport aux erreurs introduites par la technique de mesure – que les FT ont commencé à attirer l'attention des physiologistes [Gallagher et al., 2004]. McDonald and Taylor [1959] ont été les premiers à promouvoir l'utilisation des FT pour décrire la circulation en termes de relation pression-débit. Pour ce faire, ils ont exprimé les ondes de pression et de débit dans le domaine fréquentiel, les représentant par la série de Fourier et les mettant ensuite en relation les unes avec les autres. Au début, leurs travaux se sont heurtés à une certaine résistance de la part de l'American Physiological Society, mais ils ont finalement été reconnus [O'Rourke and Avolio, 2008]. L'apparition de techniques non invasives précises pour obtenir des mesures de pression distale (par exemple, la tonométrie) a amené les scientifiques à utiliser les FT pour mettre en relation la PAC avec la pression distale du membre supérieur [Gallagher et al., 2004]. Tout d'abord, O'Rourke [1970] a exploité la FT afin d'étudier les facteurs cardiovasculaires qui modifient la relation entre les deux pressions. Ensuite, des études ont été réalisées pour analyser la stabilité de la fonction de transfert dans différentes conditions [Karamanoglu et al., 1993; Stok et al., 2011]. Parfois, en utilisant des modèles artériels du membre supérieur pour introduire les caractéristiques de propagation des ondes [Karamanoglu et al., 1995; Westerhof et al., 2007]. La restriction de la disponibilité des mesures de pression aortique a empêché cette analyse d'aller plus loin et a poussé certains chercheurs à travailler sur la pression carotidienne [Karamanoglu et al., 1993; Karamanoglu and Feneley, 1996], ou brachiale [Bos et al., 1996]. Même s'il existe des travaux où la FT a été appliquée pour relier la pression fémorale et aortique [Fitchett, 1993], ceci est risqué à cause des changements dans l'aorte dus au vieillissement ou à la maladie [Vlachopoulos et al., 2011] qui ne peuvent être pris en compte dans la fonction de transfert de façon directe. Une société (AtCor Medical Pty Ltd, Sydney, Nouvelle-Galles du Sud, Australie) a décidé d'exploiter la fonction de transfert généralisée pour construire un dispositif commercial, le *SphygmoCor*®, et la Food and Drug Administration a autorisé l'incorporation de la méthode FT dans le dispositif pour générer la PAC à partir de la pression radiale calibrée enregistrée avec des techniques non invasives [O'Rourke and Avolio, 2008]. La commercialisation du *SphygmoCor*® a intéressé la communauté scientifique et son fonctionnement a été analysé par rapport à d'autres techniques de surveillance de la pression [Cloud et al., 2003; Pauca et al., 2001; Soderstrom et al., 2002]. Au cours des années, plusieurs stratégies différentes ont été développées pour récupérer une fonction de transfert [Westerhof et al., 2007]. Certaines FT sont obtenues à partir d'un modèle linéaire autorégressif (ARX) [Chen et al., 1997; Joachim et al., 2017; Stok et al., 2011], qui est basé sur une équation linéaire différente qui relie les entrées et les sorties d'un système et dépend de certains paramètres [Ljung, 1999]. Cette approche a été comparée par [Fetics et al., 1999] à la FT basée sur Fourier [Oppenheim and Schafer, 1975] prouvant que les fonctions de transfert basées sur ARX ont montré une meilleure performance. Dans d'autres travaux, la fonction de transfert est dérivée et calibrée en utilisant un modèle des artères concernées [Karamanoglu et al., 1995; Karamanoglu and Feneley, 1996, 1997; Westerhof et al., 2007].

Discussion

La surveillance des conditions cardiovasculaires d'un patient représente un enjeu majeur, en particulier pour les anesthésistes qui doivent prévenir un comportement circulatoire non physiologique pendant l'anesthésie générale, qui pourrait causer des dommages dangereux. Comme nous l'avons mentionné ci-dessus, le CAP est un bon marqueur du système cardiovasculaire, mais il n'est pas directement disponible sans impliquer une procédure invasive. Les fonctions de transfert ont été développées dans l'intention de relier la pression centrale à la pression radiale afin d'avoir accès à cette information. La plupart des travaux que nous avons présentés ci-dessus reposent sur l'hypothèse que les variations de la condition cardiovasculaire n'affectent pas de façon majeure le membre supérieur et que la pression radiale est donc similaire pour différents sujets [Millasseau et al., 2003]. Cependant, l'utilisation d'une FT générale nécessite de supposer que la relation entre la pression aortique et la pression périphérique est la même pour chaque sujet dans toutes les conditions cliniques. Pour cette raison, comme nous l'avons vu, certains groupes ont essayé de surmonter cette limitation en utilisant un modèle, calibré afin de correspondre aux mesures, et ensuite utilisé pour paramétrer la fonction de transfert [Karamanoglu and Feneley, 1996, 1997]. Cependant, cette stratégie nécessite plusieurs étapes pour les deux calibrations et exige la disponibilité des deux pressions impliquées dans la FT. De plus, la FT n'est pas capable de donner une bonne prédiction de l'encoche dicrotique [Fetics et al., 1999], dont nous avons vu qu'elle est un marqueur important de l'état cardiovasculaire. En conclusion, en condition réelle, il n'est pas possible de prendre en compte dans les FT les caractéristiques du sujet, comme son âge, ou les informations anatomiques qui sont habituellement disponibles en cas de chirurgie (par exemple le lumen et la longueur des vaisseaux grâce à l'imagerie préopératoire), et qui s'avèrent influencer beaucoup la fonction de transfert [Westerhof et al., 2007].

Défis et objectifs

Malgré les résultats encourageants des fonctions de transfert dans la récupération de la pression aortique centrale à partir des mesures de la forme d'onde de pression périphérique, certains aspects doivent encore être abordés. La FT n'est pas polyvalente en termes d'adaptabilité à différents sujets et elle n'est pas toujours capable de reproduire tous les marqueurs importants de l'onde de pression. Dans ce travail, nous proposons une stratégie pour récupérer les formes d'onde du sang aux sites centraux en utilisant les enregistrements de pression distaux. Nous plaçons notre travail dans le contexte de l'anesthésie générale, dans la perspective de développer une méthode pour estimer la PAC en utilisant les ondes de pression périphériques disponibles, afin de faire un pas vers un monitoring cardiovasculaire augmenté. Notre approche est double :

I - Modélisation de la circulation artérielle

La première étape consiste à développer un modèle qui reproduit la partie de l'arbre artériel qui relie la pression centrale aux sites de mesure. L'objectif est d'obtenir une formulation capable de saisir toutes les caractéristiques importantes de la propagation du sang. Dans ce sens, nous nous appuyons sur un modèle d'ordre réduit unidimensionnel, adapté à la description des phénomènes de propagation des ondes [Peiro et al., 2003]. De plus, nous dérivons une formulation préservant l'énergie pour le modèle artériel, compatible avec le couplage avec un modèle cardiaque réduit [Caruel et al., 2013] développé dans l'équipe MΞDISIM. Ce couplage est important pour comprendre le comportement de la circulation systémique. Idéalement, ce modèle couplé devrait être utilisé, avec une stratégie

d'estimation des paramètres [Arthurs et al., 2020], pour estimer directement les paramètres cardiaques d'intérêt.

II - Problème inverse

Afin de d'estimer les entrées du modèle artériel en utilisant les mesures de pression de sortie, nous déduisons une stratégie de problème inverse (PI), basée sur une approche variationnelle incrémentale [Lawless et al., 2005]. L'idée est de construire un PI fiable qui s'appuie sur une analyse mathématique précise de ses propriétés. L'objectif ici est de développer un outil utile qui exploite les données bruitées de la pression distale afin de récupérer les ondes de pression ou de débit d'entrée. Comme le PI est directement appliqué au modèle artériel, nous sommes en mesure de prendre en compte certaines caractéristiques du sujet. De plus, pour tester notre approche, nous utilisons des enregistrements de pression *in vivo* comme entrée pour notre PI. Ces données sont aimablement fournies par les anesthésistes de l'Hôpital Lariboisière AP-HP, Paris (FR). Cette approche devrait être couplée à une stratégie d'estimation des paramètres, dans une procédure en deux étapes, pour obtenir une approche complète et spécifique au patient.

Structure du manuscrit

Cette thèse est composée de deux parties principales

- Part I concerne la première étape de ce travail, à savoir la modélisation de la circulation du flux sanguin dans les artères. Elle est composée de quatre chapitres
  - Chapitre 1 : dans ce chapitre, nous présentons une introduction à la modélisation multi-échelle, en soulignant les raisons qui motivent le choix d'utiliser des modèles unidimensionnels pour notre travail. Nous décrivons la dérivation de la formulation unidimensionnelle du flux sanguin et sa relation avec les modèles à paramètres forfaitaires. Enfin, nous présentons un bref aperçu des modèles unidimensionnels existants de la circulation.
  - Chapitre 2 : ce chapitre est constitué d'un article publié [Manganotti et al., 2021]. L'accent est mis sur la dérivation d'un modèle cardiovasculaire qui comporte un modèle cardiaque [Caruel et al., 2013] couplé à un modèle unidimensionnel de la circulation aortique. Le modèle couplé repose sur une formulation discrète préservant l'énergie, ce qui a nécessité une nouvelle formulation pour le modèle de circulation.
  - Chapitre 3 : Le Chapitre 3 représente une "mise à niveau" du Chapitre 2. Le modèle de circulation est étendu pour représenter avec un segment unidimensionnel les artères principales du membre supérieur. Les choix de modélisation et les conditions de branchement sont décrits.
  - Chapitre 4 : dans ce chapitre, nous décrivons la perspective principale de ce travail. A savoir, l'introduction d'une géométrie fuselé, le développement d'une stratégie pour inclure les pertes de débit dues aux petits vaisseaux latéraux sans introduire de segments unidimensionnels supplémentaires et le développement d'un modèle en boucle fermée.
- Part II concerne la stratégie d'assimilation des données dérivée pour estimer les marqueurs physiologiques centraux en utilisant les mesures périphériques. Elle contient quatre chapitres

- Chapitre 5 : dans ce chapitre, nous présentons les principales méthodes employées dans les problèmes d'assimilation de données et nous donnons un aperçu des travaux existants où ces stratégies ont été employées pour des problèmes inverses avec des applications cardiovasculaires. Enfin, nous discutons de la motivation de notre travail et des choix effectués pour construire les problèmes inverses.
- Chapitre 6 : ce chapitre est constitué d'un article qui a été soumis. Dans cet article, nous dérivons et analysons une stratégie de contrôle optimal basée sur une approche 4D-Var pénalisée. L'objectif est d'estimer le débit cardiaque en utilisant les données de pression aortique périphérique. Cette approche est appliquée sur un modèle linéarisé du flux sanguin et représente une étape préliminaire pour le chapitre suivant.
- Chapitre 7 : Le Chapitre 7 présente l'application d'un problème inverse itératif, qui fait intervenir à chaque itération le problème de contrôle optimal décrit dans le chapitre précédent, sur une configuration de modèle qui reflète la mise en place requise par l'application clinique poursuivie. Les données de pression radiale sont utilisées pour retrouver la pression centrale près du cœur. La stratégie itérative est présentée et la formulation du modèle employé est décrite dans tous ses détails.
- Chapitre 8 : ce dernier chapitre décrit les étapes suivantes nécessaires pour que ce travail réponde à une application clinique réelle. En particulier, le couplage de la stratégie du problème inverse décrite avec un problème d'estimation des paramètres pour évoluer vers un modèle spécifique au patient. Un travail en cours sur un filtre de Kalman pour estimer l'élasticité des vaisseaux et l'impédance périphérique est présenté.

Bibliography

Arthurs, C. J., Xiao, N., Moireau, P., Schaeffter, T., and Figueroa, C. A. (2020). A flexible framework for sequential estimation of model parameters in computational hemodynamics. *Advanced Modeling and Simulation in Engineering Sciences*, pages 1–37.

Bos, W. J. W., van Goudoever, J., van Montfrans, G. A., van den Meiracker, A. H., and Wesseling, K. H. (1996). Reconstruction of brachial artery pressure from noninvasive finger pressure measurements. *Circulation*, 94(8):1870–1875.

Caro, C., Pedley, T., Schroter, R., and Seed, W. (1978). *The mechanics of circulation*. Cambridge.

Caruel, M., Chabiniok, R., Moireau, P., Lecarpentier, Y., and Chapelle, D. (2013). Dimensional reduction of cardiac models for effective validation and calibration. In *Functional Imaging and Modeling of the Heart*, pages 259–267. Springer Berlin Heidelberg.

Chassot, P.-G. (2015). *Précis d'anesthésie-réanimation en chirurgie cardiaque*. Université de Lausanne.

Chen, C.-H., Nevo, E., Fetics, B., Pak, P. H., Yin, F. C., Maughan, W. L., and Kass, D. A. (1997). Estimation of central aortic pressure waveform by mathematical transformation of radial tonometry pressure. *Circulation*, 95(7):1827–1836.

Chen, C.-H., Ting, C.-T., Nussbacher, A., Nevo, E., Kass, D. A., Pak, P., Wang, S.-P., Chang, M.-S., and Yin, F. C. (1996). Validation of carotid artery tonometry as a means of estimating augmentation index of ascending aortic pressure. *Hypertension*, 27(2):168–175.

Chirinos, J. A., Zambrano, J. P., Chakko, S., Veerani, A., Schob, A., Perez, G., and Mendez, A. J. (2005). Relation between ascending aortic pressures and outcomes in patients with angiographically demonstrated coronary artery disease. *The American Journal of Cardiology*, 96(5):645–648.

Cloud, G. C., Rajkumar, C., Kooner, J., Cooke, J., and Bulpitt, C. J. (2003). Estimation of central aortic pressure by *SphygmoCor*® requires intra-arterial peripheral pressures. *Clinical Science*, 105(2):219–225.

D'Ancona, G., Ricci, M., Bergsland, J., Salerno, T. A., and Karamanoukian, H. L. (2000). Graft patency verification in coronary artery bypass grafting: Principles and clinical applications of transit time flow measurement. *Angiology*, 51(9):725–731.

Esper, S. A. and Pinsky, M. R. (2014). Arterial waveform analysis. *Best Practice & Research Clinical Anaesthesiology*, 28(4):363–380. Hemodynamic Monitoring Devices.

Fetics, B., Nevo, E., Chen, C.-H., and Kass, D. (1999). Parametric model derivation of transfer function for noninvasive estimation of aortic pressure by radial tonometry. *IEEE Transactions on Biomedical Engineering*, 46(6):698–706.

Fitchett, D. H. (1993). Aortofemoral transfer function: a method to determine the instantaneous aortic valve gradient in aortic valve stenosis. *Journal of the American College of Cardiology*, 22(7):1909–1914.

Gallagher, D., Adji, A., and O'Rourke, M. (2004). Validation of the transfer function technique for generating central from peripheral upper limb pressure waveform. *American Journal of Hypertension*, 17(11):1059–1067.

Hall, J. E. (2015). Guyton and hall textbook of medical physiology.

Hamilton, W. F., Woodbury, R. A., and Harper, H. T., J. (1936). Physiologic relationship between intrathoracic, intraspinal and arterial pressures. *Journal of the American Medical Association*, 107(11):853–856.

Jankowski, P., Kawecka-Jaszcz, K., Czarnecka, D., Brzozowska-Kiszka, M., Styczkiewicz, K., Styczkiewicz, M., Pośnik-Urbańska, A., Bryniarski, L., and Dudek, D. (2004). Ascending aortic, but not brachial blood pressure-derived indices are related to coronary atherosclerosis. *Atherosclerosis*, 176(1):151–155.

Joachim, J., Vallée, F., Gall, A. L., Matéo, J., Lenck, S., Millasseau, S., Houdart, E., Mebazaa, A., and Gayat, E. (2017). Velocity–pressure loops for continuous assessment of ventricular afterload: influence of pressure measurement site. *Journal of Clinical Monitoring and Computing*, 32(5):833–840.

Kannangara, D. O., Davidson, S. M., Pretty, C. G., Kamoi, S., Corbett-Davies, J., Desaive, T., Shaw, G. M., and Chase, J. G. (2015). An assessment of the relationship between dicrotic notch timing and cardiac preload. In *2015 37th Annual International Conference of the IEEE Engineering in Medicine and Biology Society (EMBC)*, pages 1001–1004.

Karamanoglu, M. and Feneley, M. P. (1996). Derivation of the ascending aortic-carotid pressure transfer function with an arterial model. *American Journal of Physiology-Heart and Circulatory Physiology*, 271(6):H2399–H2404.

Karamanoglu, M. and Feneley, M. P. (1997). On-line synthesis of the human ascending aortic pressure pulse from the finger pulse. *Hypertension*, 30(6):1416–1424.

Karamanoglu, M., Gallagher, D. E., Avolio, A. P., and O'Rourke, M. F. (1995). Pressure wave propagation in a multibranched model of the human upper limb. *American Journal of Physiology-Heart and Circulatory Physiology*, 269(4):H1363–H1369.

Karamanoglu, M., O'Rourke, M. F., Avolio, A. P., and Kelly, R. P. (1993). An analysis of the relationship between central aortic and peripheral upper limb pressure waves in man. *European Heart Journal*, 14(2):160–167.

Kroeker, E. J. and Wood, E. H. (1955). Comparison of simultaneously recorded central and peripheral arterial pressure pulses during rest, exercise and tilted position in man. *Circulation Research*, 3(6):623–632.

Lawless, A., Gratton, S., and Nichols, N. (2005). An investigation of incremental 4d-var using non-tangent linear models. *Quarterly Journal of the Royal Meteorological Society*, 131(606):459–476.

Liu, Z., Brin, K. P., and Yin, F. (1986). Estimation of total arterial compliance: an improved method and evaluation of current methods. *American Journal of Physiology-Heart and Circulatory Physiology*, 251(3):H588–H600.

Ljung, L. (1999). *System Identification: Theory for the User*. Prentice Hall information and system sciences series. Prentice Hall PTR.

Mackenzie, J. (1902). The study of the pulse, arterial, venous, and hepatic, and of the movements of the heart. *The Indian Medical Gazette*, 37:287 – 287.

Manganotti, J., Caforio, F., Kimmig, F., Moireau, P., and Imperiale, S. (2021). Coupling reduced-order blood flow and cardiac models through energy-consistent strategies: modeling and discretization. *Advanced Modeling and Simulation in Engineering Sciences*, 8(1):1–37.

McDonald, D. and Taylor, M. (1959). 3 - the hydrodynamics of the arterial circulation. *Progress in Biophysics and Biophysical Chemistry*, 9:105–173.

Millasseau, S. C., Patel, S. J., Redwood, S. R., Ritter, J. M., and Chowienczyk, P. J. (2003). Pressure wave reflection assessed from the peripheral pulse. *Hypertension*, 41(5):1016–1020.

Murray, W. B. and Foster, P. A. (1996). The peripheral pulse wave: Information overlooked. *Journal of Clinical Monitoring*, 12(5):365–377.

Mynard, J. P., Kondiboyina, A., Kowalski, R., Cheung, M. M. H., and Smolich, J. J. (2020). Measurement, analysis and interpretation of pressure/flow waves in blood vessels. *Frontiers in Physiology*, 11.

Nara, S., Kaur, M., and Verma, K. L. (2014). Novel notch detection algorithm for detection of dicrotic notch in ppg signals. *International Journal of Computer Applications*, 86(17):36–39.

Oppenheim, A. V. and Schafer, R. W. (1975). Digital signal processing(book). *Research supported by the Massachusetts Institute of Technology, Bell Telephone Laboratories, and Guggenheim Foundation. Englewood Cliffs, N. J., Prentice-Hall, Inc., 1975. 598 p.*

O'Rourke, M. F. (1970). Influence of ventricular ejection on the relationship between central aortic and brachial pressure pulse in man. *Cardiovascular Research*, 4(3):291–300.

O'Rourke, M. F. (2008). How stiffening of the aorta and elastic arteries leads to compromised coronary flow. *Heart*, 94(6):690–691.

O'Rourke, M. F. and Avolio, A. P. (2008). Arterial transfer functions: background, applications and reservations. *Journal of Hypertension*, 26(1):8–10.

Papaioannou, T., Protogerou, A., Stamatelopoulos, K., Vavuranakis, M., and Stefanadis, C. (2009). Non-invasive methods and techniques for central blood pressure estimation: Procedures, validation, reproducibility and limitations. *Current Pharmaceutical Design*, 15(3):245–253.

Pauca, A. L., O'Rourke, M. F., and Kon, N. D. (2001). Prospective evaluation of a method for estimating ascending aortic pressure from the radial artery pressure waveform. *Hypertension*, 38(4):932–937.

Peiro, J., Sherwin, S., Parker, K., Franke, V., Formaggia, L., Lamponi, D., and Quarteroni, A. (2003). Numerical simulation of arterial pulse propagation using one-dimensional models. *Wall-fluid interactions in physiological flows*, pages 1–36.

Politi, M. T., Ghigo, A., Fernández, J. M., Khelifa, I., Gaudric, J., Fullana, J. M., and Lagrée, P.-Y. (2016). The dicrotic notch analyzed by a numerical model. *Computers in Biology and Medicine*, 72:54–64.

Redaelli, A. and Montevecchi, F. (2012). *Biomeccanica. Analisi multiscala di tessuti biologici*. Patron Editore.

Sharman, J. E., Lim, R., Qasem, A. M., Coombes, J. S., Burgess, M. I., Franco, J., Garrahy, P., Wilkinson, I. B., and Marwick, T. H. (2006). Validation of a generalized transfer function to noninvasively derive central blood pressure during exercise. *Hypertension*, 47(6):1203–1208.

Silverthorn, D., Johnson, B. R., Ober, W., Garrison, C. W., and Silverthorn, A. C. (2009). *Human Physiology: an integrated approach*. Pearson.

Soderstrom, S., Nyberg, G., O'Rourke, M., Sellgren, J., and Pontén, J. (2002). Can a clinically useful aortic pressure wave be derived from a radial pressure wave? *British Journal of Anaesthesia*, 88(4):481–488.

Stok, W. J., Westerhof, B. E., Guelen, I., and Karemaker, J. M. (2011). Aortic pressure wave reconstruction during exercise is improved by adaptive filtering: a pilot study. *Medical and Biological Engineering and Computing*, 49(8):909–916.

Tortora, G. and Derrickson, B. (2008). *Principles of Anatomy and Physiology*. John Wiley & Sons.

Vlachopoulos, C., ORourke, M., and Nichols, W. W. (2011). *McDonalds Blood Flow in Arteries*. CRC Press.

Weber, T., Auer, J., O'Rourke, M. F., Kvas, E., Lassnig, E., Berent, R., and Eber, B. (2004). Arterial stiffness, wave reflections, and the risk of coronary artery disease. *Circulation*, 109(2):184–189.

Westerhof, B. E., Guelen, I., Stok, W. J., Lasance, H. A. J., Ascoop, C. A. P. L., Wesseling, K. H., Westerhof, N., Bos, W. J. W., Stergiopulos, N., and Spaan, J. A. E. (2008). Individualization of transfer function in estimation of central aortic pressure from the peripheral pulse is not required in patients at rest. *Journal of Applied Physiology*, 105(6):1858–1863.

Westerhof, B. E., Guelen, I., Stok, W. J., Wesseling, K. H., Spaan, J. A. E., Westerhof, N., Bos, W. J., and Stergiopulos, N. (2007). Arterial pressure transfer characteristics: effects of travel time. *American Journal of Physiology-Heart and Circulatory Physiology*, 292(2):H800–H807.

Westerhof, N. and O'Rourke, M. (1995). Haemodynamic basis for the development of left ventricular failure in systolic hypertension and for its logical therapy. *Journal of hypertension*, 13(9):943—952.

Womersley, J. R. (1957). The mathematical analysis of the arterial circulation in a state of oscillatory motion. Technical Report Wade-TR.:56–614.

Part I

Arterial circulation modeling

CHAPTER 1

Introduction to one-dimensional modeling of the arterial circulation

Nothing in life is to be feared, it is only to be understood. Now is the time to understand more, so that we may fear less.

— Marie Curie

Contents

1.1 Cardiovascular reduced-order modeling

Cardiovascular modeling is about finding the compromise between computational cost and accuracy that best suits the application. This compromise is achieved by choosing a suitable model: higher order models (3D) comes with great accuracy but high computational cost while lower order models (0D) requires many simplifications but are computationally fast. Models can be divided in two main families: lumped parameter models, including the 0D models, or distributed models, that groups 3D, 2D, 1D and also some kind of 0D models. In the first category the spatial dependence is lost (infinite propagation velocity), while in the second one space is taken into account with different simplifications according to the model. Two, one and zero-dimensional distributed models represent a geometrical simplifications of anatomical three-dimensional models, these simplifications are performed when the geometry of the physical problem show some symmetries. The first class of models is described by a set of ordinary differential equation while the latter one by partial differential equations [Shi et al., 2011]. Each one of the model requires some assumption on the geometry and involves simplification in the mathematical formulation, therefore the choice of the model has to be in accordance with the requirements of the specific application [Rachid, 2018]. For the cardiovascular application, 3D models are usually involved to study fluid-structure interaction [Bennati et al., 2021; Bertoglio et al., 2013; Di Martino et al., 2001] and complex circulatory states that requires the representation of a complex geometry [Burton et al., 2006; Figueroa et al., 2006; Kim et al., 2010]. 2D models are mostly employed to model the circulation [Ghigo et al., 2017] with an attention on the shape of the velocity profile. 1D models are well establish in the blood flow modeling [Bollache et al., 2014; Formaggia et al., 2006; Matthys et al., 2007; Reymond et al., 2009] as their hyperbolic formulation enables to reproduce wave transmission within the cardiovascular network [Pythoud et al., 1995]. 0D distributed models are derived from the geometrical reduction of a spherical domain, the spatial dependence is linked only to the radius [Caruel et al., 2013]. Finally, lumped parameter models – mostly Windkessel models – are employed to reproduce the global response of a system [Korakianitis and Shi, 2006; Stergiopulos et al., 1999] or a restrained part of it [Segers et al., 2008], and they are suitable to be used as a boundary condition for distributed models [Quarteroni et al., 2001]. In cardiovascular modeling it is very common to couple models of different length-scales [Quarteroni et al., 2016], the reason for that is the nature of the cardiovascular system, meaning that local phenomena have a global effect on the whole system [Formaggia et al., 1999; Quarteroni et al., 2001]. Hence, it is necessary to account for the overall system, although with lower order models (e.g. lumped parameter models), even if the focus is restrained to a small part of it [Migliavacca et al., 2006]. This strategy enables to preserve the wholeness of the cardiovascular system and attains accurate results without dealing with high computational cost.

In our work, we are interested in the propagation of blood flow and pressure from the ascending aorta through the arterial network to the distal end of the radial artery. The application we pursue requires a simple model, easy to adapt and with a low computational cost, which is capable to describe and accurately reproduce the above mentioned wave propagation phenomena. In order to meet these requirements we choose to rely on a one-dimensional blood flow model. Moreover, lumped parameter models are employed as outlet boundary conditions. In what follows, we show how the one-dimensional mathematical formulations is derived and how it is related to the lumped parameter formulation. Finally, a review on the available one-dimensional models of the blood flow is presented to highlight its suitability to model the arterial circulation.

1.1.1 Derivation of 1D blood flow formulation

The one-dimensional formulation that describes the blood flow in a tube relies on some simplifications. Following the presentation of Wang [2014], we identify two main methods to derive the one-dimensional formulation currently used for blood flow modeling, one begins with Reynold transport equation [Formaggia et al., 2010; van de Vosse and Stergiopulos, 2011] and the second one, that we will pursue, from the Navier-Stokes equations [Barnard et al., 1966; Hughes and Lubliner, 1973; Čanić and Kim, 2003].
We start from the Navier-Stokes equations, that rely on the assumption of laminar flow of a Newtonian fluid, in their strong formulation and in cylindrical coordinates, we follow the procedure presented in [Rideout and Dick, 1967] and start from

$$\begin{cases} \rho\Big(\dfrac{\partial v_r}{\partial t} + v_r\dfrac{\partial v_r}{\partial r} + v_x\dfrac{\partial v_r}{\partial x}\Big) - \mu\Big[\dfrac{1}{r}\dfrac{\partial}{\partial r}(rv_r) + \dfrac{\partial^2 v_r}{\partial x^2}\Big] + \dfrac{\partial p}{\partial r} = 0, \\ \rho\Big(\dfrac{\partial v_x}{\partial t} + v_r\dfrac{\partial v_x}{\partial r} + v_x\dfrac{\partial v_x}{\partial x}\Big) + \mu\Big[\dfrac{1}{r}\dfrac{\partial}{\partial r}\Big(r\dfrac{\partial v_x}{\partial r}\Big) + \dfrac{\partial^2 v_x}{\partial x^2}\Big] + \dfrac{\partial p}{\partial x} = 0, \\ \dfrac{\partial v_r}{\partial r} + \dfrac{v_r}{r} + \dfrac{\partial v_x}{\partial x} = 0, \end{cases} \tag{1.1}$$

where v_x and v_r are respectively the axial and radial component of the velocity, p the pressure, ρ and ν the mass density of blood and its viscosity, x and r the distance along the axis and in the radial direction. One can note that System 1.1 describes a case where body forces are neglected and tangential motion is null (axisymmetric assumption). Moreover, the last equation of System 1.1, namely the continuity equation describing the mass conservation involves the assumption of blood incompressibility. However, in blood circulation applications, the terms $\frac{\partial^2 u_x}{\partial x^2}$ and $\frac{\partial^2 u_z}{\partial z^2}$ are small and will be neglected in what follows. Moreover, the pressure is assumed as constant along the radial direction, which implies that all the other terms of the first equation in System 1.1 vanish. We end up with a simplified system that reads

$$\begin{cases} \dfrac{\partial p}{\partial r} = 0, \\ \dfrac{\partial v_x}{\partial t} + v_r\dfrac{\partial v_x}{\partial r} + v_x\dfrac{\partial v_x}{\partial x} + \dfrac{1}{\rho}\dfrac{\partial p}{\partial x} = -\dfrac{\mu}{\rho}\dfrac{1}{r}\dfrac{\partial}{\partial r}\Big(r\dfrac{\partial v_x}{\partial r}\Big), \\ \dfrac{1}{r}\dfrac{\partial}{\partial r}(rv_r) + \dfrac{\partial}{\partial x}v_x = 0. \end{cases} \tag{1.2}$$

From this point on, we retrieve the formulation of [Wang, 2014] and follow the same procedure. System 1.2 is completed with no slip boundary condition, such that

$$v_x(R, x, t) = 0,$$

with R being the radius of the cylinder (or blood vessel). Moreover, we introduce an equation that describes the wall motion and constraints it along the r direction

$$v_r(R, x, t) = \frac{\partial R}{\partial t}.$$

Then, we multiply by $2\pi r$ and integrate along r the mass conservation equation in System 1.2, obtaining

$$2\pi\Big(\int_0^R \frac{\partial}{\partial r}(rv_r)dr + \int_0^R \frac{\partial v_x}{\partial r}rdr\Big) = 0.$$

Then, we apply the Reynold transport theorem on the term $v_x r$, such that

$$\frac{d}{dx}\int_0^R v_x r dr = \int_0^R \frac{\partial v_x}{\partial x}rdr + \frac{\partial R}{\partial x}v_x(R, x, t)R(x, t),$$

which, by using the no-slip condition, gives the integral form of the conservation equation

$$2\pi R v_r(R,x,t) + \frac{d}{dx}\int_0^R 2\pi v_x r dr = 0.$$

Moreover, as $v_r(R,x,t) = \frac{\partial R}{\partial t}$, and recalling that the cross-section of the vessel and the blood flow are defined as $A = \pi R^2$ and $Q = Av_x$, we can rewrite the previous equation as

$$\frac{\partial A}{\partial t} + \frac{\partial Q}{\partial x} = 0. \tag{1.3}$$

Finally, we multiply by $2\pi r$ and integrate over r the second equation of System 1.2

$$2\pi\int_0^R r v_r \frac{\partial v_x}{\partial r} dr = 2\pi\int_0^R \frac{\partial}{\partial r}(r v_r v_x) dr - 2\pi\int_0^R v_x \frac{\partial}{\partial r}(r v_r) dr,$$

knowing that $v_x(R) = 0$ and by using the mass continuity equation we obtain

$$\frac{\partial Q}{\partial t} + \frac{\partial}{\partial x}\Big(2\pi\int_0^R r v_x^2 dr\Big) + \frac{A}{\rho}\frac{\partial P}{\partial x} = 2\pi\nu\Big[r\frac{\partial v_x}{\partial r}\Big]_{r=R},$$

with $\nu = \mu/\rho$. Then, we introduce

$$\alpha = \frac{2\pi A}{Q^2}\int_0^R r v_x^2 dr = (2\pi)^2 \frac{\int_0^R r dr \int_0^R r v_x^2 dr}{\Big(\int_0^R r v_x dr\Big)^2},$$

the flux-momentum correction coefficient, and finally retrieve

$$\frac{\partial Q}{\partial t} + \frac{\partial}{\partial x}\Big(\alpha\frac{Q^2}{A}\Big) + \frac{A}{\rho}\frac{\partial P}{\partial x} = 2\pi\nu R\frac{\partial v_x}{\partial r}(R,x,t). \tag{1.4}$$

We can now put Eq. (1.3) and (1.4) together and obtain the following system

$$\begin{cases} \dfrac{\partial A}{\partial t} + \dfrac{\partial Q}{\partial x} = 0, \\ \dfrac{\partial Q}{\partial t} + \dfrac{\partial}{\partial x}\Big(\alpha\dfrac{Q^2}{A}\Big) + \dfrac{A}{\rho}\dfrac{\partial P}{\partial x} = 2\pi\nu R\dfrac{\partial v_x}{\partial r}(R,x,t). \end{cases} \tag{1.5}$$

In order to solve System 1.5 we need to define α and $\frac{\partial v_x}{\partial r}(R,x,t)$ which depend on the axial profile of the velocity. First, we set $v_x(r,x,t) = U(x,t)\Phi(r)$ where $U(x,t)$ is the average velocity, and $\Phi(r)$ is the velocity profile is constant along x. Moreover, we rewrite the friction term as $-kU$ or $-kQ/A$, where k depends on $\frac{\partial\Phi(R)}{\partial r}$. The profile is usually defined by means of $W_0 = R\sqrt{\frac{\varpi}{\nu}}$ – the Womersley number – which has a different value for different shape of the velocity, as shown in Figure 1.1. In particular, for the blood flow its value varies within a range

$$10^{-3} \leq W_0 \leq 15,$$

where the lower value is attained inside the capillaries and the higher one describes the aortic flow. However, two asymptotic values can be derived that are usually employed in one-dimensional blood flow modeling

$$\begin{cases} \alpha = 4/3 \quad \text{if} \quad W_0 << 1, \\ \alpha = 1 \quad \text{if} \quad W_0 >> 1. \end{cases}$$

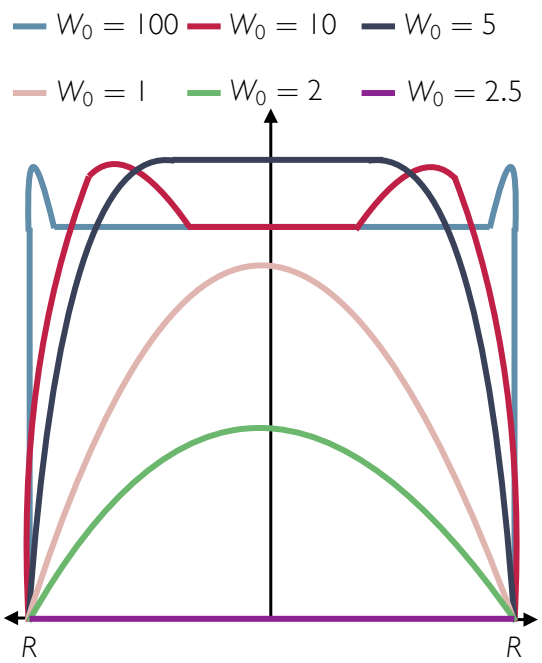

Figure 1.1 – Velocity profile in a tube in relation with the Reynolds number.

Moreover, we can define α by describing the velocity profile with a law, for example Φ_r can be defined as

$$\Phi(r) = 2\left[1 - \left(\frac{r}{R}\right)^2\right],$$

which describes a parabolic profile and involves $\alpha = 4/3$ [Formaggia and Veneziani, 2003]. However, the most common law in blood flow modeling is

$$\Phi(r) = \frac{\gamma + 2}{\gamma}\left[1 - \left(\frac{r}{R}\right)^\gamma\right],$$

allowing for variation in the velocity shape according to γ [Smith et al., 2002]. The choice of γ determines the profile of the axial velocity (e.g. with $\gamma = 2$ we obtain the parabolic profile as with the previous $\Phi(r)$ description), which is found to be rather flat for large arteries. This kind of profile is achieved by increasing the value of γ and by fitting with experimental data the best choice happens to be $\gamma = 9$ [Hunter, 1972], giving $\alpha = 1.1$ and $k = 22\pi\nu$. However, the correction coefficient is often approximated to $\alpha = 1$ as it simplifies the mathematical formulation [Formaggia and Veneziani, 2003]. Finally, to close System 1.5 we need to find a relation between the pressure P and the cross-section A – the so-called tube law. To retrieve this equation we follow the strategy of [Formaggia et al., 2003] which starts from a generalized string model [Quarteroni et al., 2000], of the form

$$\rho_w h \frac{\partial^2 \zeta}{\partial t^2} - \tilde{\gamma}\frac{\partial \zeta}{\partial t} - \tilde{a}\frac{\partial^2 \zeta}{\partial x^2} - \tilde{c}\frac{\partial^3 \zeta}{\partial t \partial x^2} + \tilde{b}\zeta = P - P_{ext}, \tag{1.6}$$

with $\zeta = R - R_0$ the displacement of the wall with respect to its reference configuration (R_0 being the reference radius), P and P_{ext} respectively the internal and external pressure, and their difference being the so-called transmural pressure. The first term is related to the inertia, the second one is a visco-elastic term (which we would retrieve by choosing a Kelvin-Voigt viscoelastic model), the third one takes into account a longitudinal pre-stress of the wall, the fourth one is again a visco-elastic term and the last one is related

to the elastic behavior of the wall. However, in classical application just the elastic and, sometimes, the Voigt-type viscoelastic term are kept. So we rewrite $\zeta = \frac{\sqrt{A}-\sqrt{A_0}}{\sqrt{\pi}}$ and define $\tilde{b}$ and $\tilde{\gamma}$ depending respectively on the elastic and viscoelastic properties of the wall, namely

$$\tilde{b} = \frac{\pi E h}{\kappa A_0}, \qquad \tilde{\gamma} = -\frac{\pi \phi h}{\kappa A_0},$$

where κ is usually chosen to be 1 or 3/4, that we will employ, formally depending on assumptions on the plane stress, E the young modulus of the wall and ϕ the viscosity coefficient. Eq (1.6) becomes

$$P = P_{ext} + \beta \frac{(\sqrt{A} - \sqrt{A_0})}{A_0} + \frac{\Gamma}{A_0\sqrt{A}}\partial_t A, \tag{1.7}$$

where

$$\beta = \frac{4\sqrt{\pi}Eh}{3} \qquad \text{and} \qquad \Gamma = \frac{2\sqrt{\pi}h\phi}{3}.$$

Finally, we can complete System 1.5 with Eq. (1.7) and obtain the one-dimensional formulation employed to model a one-dimensional vessel

$$\begin{cases} \dfrac{\partial A}{\partial t} + \dfrac{\partial Q}{\partial x} = 0, \\ \dfrac{\partial Q}{\partial t} + \dfrac{\partial}{\partial x}\left(\alpha \dfrac{Q^2}{A}\right) + \dfrac{A}{\rho}\dfrac{\partial P}{\partial x} = -k\dfrac{Q}{A}, \\ P = P_{ext} + \beta \dfrac{(\sqrt{A} - \sqrt{A_0})}{A_0} + \dfrac{\Gamma}{A_0\sqrt{A}}\partial_t A. \end{cases} \tag{1.8}$$

1.1.2 Relation between 1D and 0D model

The 0D models, or lumped parameters model, simplify the modeling of the blood flow by analogy with the electrical circuits. The pressure gradient drives the flow of blood inside the vessels, the same as current is driven by voltage difference inside the electrical network. Dissipations caused by viscosity generates a resistance against flux, playing a role similar to those of electrical resistances. The compliance of the vessels wall allows for blood storage, especially in the big elastic arteries, like capacitors store current. Finally, the inertia of the blood can be described as an inductor [Segers et al., 2008]. Moreover, the lumped parameter model can be derived as a first order discretization of a linearized one-dimensional model [Milišić and Quarteroni, 2004]. Following the procedure of Milišić and Quarteroni [2004] we show the proof of the above mentioned relation between distributed one-dimensional models and lumped parameter models. We start from System 1.8, neglecting the viscoelastic contribution in the tube law, we obtain

$$P(A) = \beta \frac{(\sqrt{A} - \sqrt{A_0})}{A_0}, \quad \text{with} \quad P(A) = P - P_{ext}.$$

Then, we rewrite System 1.8 to have P – instead of A – and Q as state variables, it reads

$$\begin{cases} \dfrac{\partial P}{\partial t} + \dfrac{\partial P}{\partial A}\dfrac{\partial Q}{\partial x} = 0, \\ \dfrac{\partial Q}{\partial t} + \dfrac{\partial}{\partial x}\left(\alpha \dfrac{Q^2}{A}\right) + \dfrac{A}{\rho}\dfrac{\partial P}{\partial x} = -k\dfrac{Q}{A}, \\ \dfrac{\partial P}{\partial A} = \dfrac{\beta}{2A_0\sqrt{A}}, \end{cases} \tag{1.9}$$

and we retrieve its non-conservative form

$$\frac{\partial}{\partial t}\begin{pmatrix} P \\ Q \end{pmatrix} + \begin{pmatrix} 0 & \frac{\partial}{\partial A}P \\ -\alpha\left(\frac{Q}{A}\right)^2 \frac{\partial}{\partial P}A + \frac{A}{\rho} & 2\alpha\frac{Q}{A} \end{pmatrix} \frac{\partial}{\partial x}\begin{pmatrix} P \\ Q \end{pmatrix} = \begin{pmatrix} 0 & 0 \\ 0 & -\frac{k}{A} \end{pmatrix}\begin{pmatrix} P \\ Q \end{pmatrix}. \tag{1.10}$$

We now define $u = Q/A$ and linearize around $(A, u) = (A_0, 0)$, obtaining

$$\begin{cases} \frac{\partial P}{\partial t} + \frac{\beta}{2A_0\sqrt{A}}\frac{\partial Q}{\partial x} = 0, \\ \frac{\partial Q}{\partial t} + \frac{A_0}{\rho}\frac{\partial}{\partial x}P = -k\frac{Q}{A}. \end{cases} \tag{1.11}$$

We introduce C', L' and R' such that

$$C' = \frac{2A_0\sqrt{A_0}}{\beta}, \qquad L' = \frac{\rho}{A_0}, R' = -\frac{\rho k}{A_0^2}.$$

Hence, System 1.11 can be rewritten as

$$\begin{cases} C'\frac{\partial}{\partial t}P + \frac{\partial}{\partial x}Q = 0, \\ L'\frac{\partial}{\partial t}Q + \frac{\partial}{\partial x}P = -R'Q. \end{cases} \tag{1.12}$$

Then, we integrate in space along x in $[0, l]$, where l is the distal end of a vessel, and define the resistance $R = R'l$, the inductance $L = L'l$ and the capacitance $C = C'l$, we retrieve

$$\begin{cases} C\frac{d}{dt}\bar{P}(t) + Q(l,t) - Q(0,t) = 0, \\ L\frac{d}{dt}\bar{Q}(t) + P(l,t) - P(0,t) = -R\bar{Q}(t), \end{cases} \tag{1.13}$$

where $\bar{P}(t) = \frac{1}{l}\int_0^l P(x,t)dx$ and $\bar{Q}(t) = \frac{1}{l}\int_0^l Q(x,t)dx$ represent respectively the mean pressure and blood flow along the vessel. We now make the hypothesis that we know $Q(0,t)$ and $P(l,t)$ (or $P(0,t)$ and $Q(l,t)$) and reduce the unknowns of System 1.13 to four. In order to divide the number of unknowns and solve the system, we suppose

$$\bar{P} \sim P(0,t), \qquad \bar{Q} = Q(l,t).$$

Finally, we have

$$\begin{cases} C\frac{d}{dt}\bar{P}(t) + \bar{Q}(t) - Q(0,t) = 0, \\ L\frac{d}{dt}\bar{Q}(t) + P(l,t) - \bar{P}(t) = -RQ(l,t), \end{cases} \tag{1.14}$$

which describes a lumped parameter model of the blood flow in a vessel, as shown in Figure 1.2.

1.2 One-dimensional modeling of the arterial network

In the following non exhaustive review of one-dimensional models for cardiovascular simulations, we start by following the historical sequence presented by Peiro et al. [2003]. The first work about one-dimensional models for the arterial circulation was presented by Euler

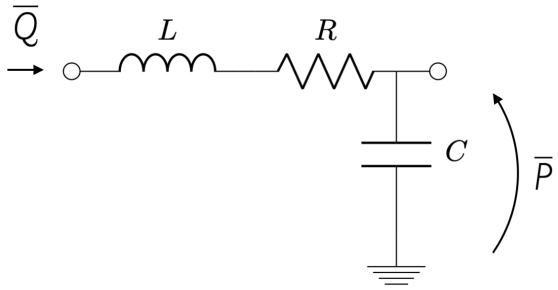

Figure 1.2 – Configuration of a classical $\mathcal{L}-$*circuit*. Inspired from [Milišić and Quarteroni, 2004]

in 1775 [Euler, 1862], the formulation was obtained by using the conservation of mass and momentum equations. Then, Young [1832] introduced the description of blood flow in arteries as a wave, deriving the wave propagation speed, before Moens [1877] and Korteweg [1878], by analogy with sound propagation. Then, the methods of the characteristic equations to formulate the blood flow was introduced by Riemann [1866]. Womersley [1957] obtained the solution to the wave problem by means of Fourier techniques after linearization of the 2D equations for the flow in an elastic pipe. Afterwords, the one-dimensional model became popular for the simulation of the blood flow, thanks to its low computational cost with respect to 3D models and its ability to reproduce wave propagation [Streeter et al., 1963]. This property of one-dimensional modeling was highlighted in [Guiot et al., 1990] by a comparison with the results of a lumped parameter model in describing blood flow in the coronaries. The outcomes of the one-dimensional blood flow simulations were also compared against *in vitro* [Alastruey et al., 2011; Boileau et al., 2015; Matthys et al., 2007; Muller and Toro, 2013], *in vivo* [Bertaglia et al., 2020; Bollache et al., 2014; Olufsen et al., 2000; Piccioli et al., 2022; Reymond et al., 2009, 2011] and *in silico* data [Boileau et al., 2015; Mynard and Nithiarasu, 2008; Xiao et al., 2013], showing good agreement. The promising accuracy of the results obtained with such reduced models encouraged the use of the one-dimensional model to simulate pathological conditions [Mynard and Nithiarasu, 2008; Reymond et al., 2012; Stergiopulos et al., 1992; Willemet and Alastruey, 2014] and the presence of endoprosthesis [Formaggia et al., 2002, 2003; Peiro et al., 2003; Pontrelli and Rossoni, 2003; Sherwin et al., 2003; Willemet and Alastruey, 2014]. One-dimensional model features are driven by two main factors: modeling and topological choices [Blanco et al., 2014]. Some works focused on the quantification of uncertainty due to modeling choices, for example concerning outflow boundary conditions [Chen et al., 2013] and material parameters [Alastruey et al., 2016], or the prescribed inlet flow [Brault et al., 2017]. The existing one-dimensional models show a huge variety of topological choices, ranging from anatomically detailed models of the arterial network [Alastruey et al., 2008; Formaggia et al., 2006; Guan et al., 2016; Matthys et al., 2007; Reymond et al., 2009; Piccioli et al., 2022; Willemet and Alastruey, 2014] taking into account an increasing number of vessel up to 2000 [Blanco et al., 2014] to models focusing on a single vessel or few of them [Bollache et al., 2014; Duanmu et al., 2019; Manganotti et al., 2021; Pontrelli, 2004]. Epstein et al. [2015] and Fossan et al. [2018] performed an analysis on the optimal number of vessels to take into account in order to encounter the ideal balance between increasing the anatomical accuracy and lowering the number of uncertain parameters introduced. The need for prescribed parameters and inflow/outflow conditions, together with the low computational cost of one-dimensional models made them the perfect candidate for data assimilation techniques, as we will see in Chapter 5.

Bibliography

Alastruey, J., Khir, A. W., Matthys, K. S., Segers, P., Sherwin, S. J., Verdonck, P. R., Parker, K. H., and Peiró, J. (2011). Pulse wave propagation in a model human arterial network: assessment of 1-d visco-elastic simulations against in vitro measurements. *Journal of biomechanics*, 44(12):2250–2258.

Alastruey, J., Parker, K. H., and Sherwin, S. J. (2008). Lumped parameter outflow models for 1-d blood flow simulations: Effect on pulse waves and parameter estimation. *Commun. Comput. Phys.*

Alastruey, J., Xiao, N., Fok, H., Schaeffter, T., and Figueroa, C. A. (2016). On the impact of modelling assumptions in multi-scale, subject-specific models of aortic haemodynamics. *Journal of The Royal Society Interface*, 13(119):20160073.

Barnard, A., Hunt, W., Timlake, W., and Varley, E. (1966). A theory of fluid flow in compliant tubes. *Biophysical journal*, 6(6):717–724.

Bennati, L., Vergara, C., Domanin, M., Malloggi, C., Bissacco, D., Trimarchi, S., Silani, V., Parati, G., and Casana, R. (2021). A computational fluid–structure interaction study for carotids with different atherosclerotic plaques. *Journal of Biomechanical Engineering*, 143(9).

Bertaglia, G., Navas-Montilla, A., Valiani, A., Monge García, M. I., Murillo, J., and Caleffi, V. (2020). Computational hemodynamics in arteries with the one-dimensional augmented fluid-structure interaction system: viscoelastic parameters estimation and comparison with in-vivo data. *Journal of Biomechanics*, 100:109595.

Bertoglio, C., Chapelle, D., Fernández, M., Gerbeau, J.-F., and Moireau, P. (2013). State observers of a vascular fluidâstructure interaction model through measurements in the solid. *Computer Methods in Applied Mechanics and Engineering*, 256:149–168.

Blanco, P. J., Watanabe, S. M., Passos, M. A. R., Lemos, P. A., and Feijóo, R. A. (2014). An anatomically detailed arterial network model for one-dimensional computational hemodynamics. *IEEE Transactions on biomedical engineering*, 62(2):736–753.

Boileau, E., Nithiarasu, P., Blanco, P. J., Müller, L. O., Fossan, F. E., Hellevik, L. R., Donders, W. P., Huberts, W., Willemet, M., and Alastruey, J. (2015). A benchmark study of numerical schemes for one-dimensional arterial blood flow modelling. *International Journal for Numerical Methods in Biomedical Engineering*, 31(10):e02732.

Bollache, E., Kachenoura, N., Redheuil, A., Frouin, F., Mousseaux, E., Recho, P., and Lucor, D. (2014). Descending aorta subject-specific one-dimensional model validated against in vivo data. *Journal of Biomechanics*, 47(2):424–431.

Brault, A., Dumas, L., and Lucor, D. (2017). Uncertainty quantification of inflow boundary condition and proximal arterial stiffness coupled effect on pulse wave propagation in a vascular network. *International Journal for Numerical Methods in Biomedical Engineering*, 33(10).

Burton, R. A., Plank, G., Schneider, J. E., Grau, V., Ahammer, H., Keeling, S. L., Lee, J., Smith, N. P., Gavaghan, D., Trayanova, N., and Kohl, P. (2006). Three-dimensional models of individual cardiac histoanatomy: Tools and challenges. *Annals of the New York Academy of Sciences*, 1080(1):301–319.

Čanić, S. and Kim, E. H. (2003). Mathematical analysis of the quasilinear effects in a hyperbolic model blood flow through compliant axi-symmetric vessels. *Mathematical Methods in the Applied Sciences*, 26(14):1161–1186.

Caruel, M., Chabiniok, R., Moireau, P., Lecarpentier, Y., and Chapelle, D. (2013). Dimensional reduction of cardiac models for effective validation and calibration. In *Functional Imaging and Modeling of the Heart*, pages 259–267. Springer Berlin Heidelberg.

Chen, P., Quarteroni, A., and Rozza, G. (2013). Simulation-based uncertainty quantification of human arterial network hemodynamics. *International journal for numerical methods in biomedical engineering*, 29(6):698–721.

Di Martino, E., Guadagni, G., Fumero, A., Ballerini, G., Spirito, R., Biglioli, P., and Redaelli, A. (2001). Fluidâstructure interaction within realistic three-dimensional models of the aneurysmatic aorta as a guidance to assess the risk of rupture of the aneurysm. *Medical Engineering Physics*, 23(9):647–655.

Duanmu, Z., Chen, W., Gao, H., Yang, X., Luo, X., and Hill, N. A. (2019). A one-dimensional hemodynamic model of the coronary arterial tree. *Frontiers in Physiology*, 10.

Epstein, S., Willemet, M., Chowienczyk, P. J., and Alastruey, J. (2015). Reducing the number of parameters in 1d arterial blood flow modeling: less is more for patient-specific simulations. *American Journal of Physiology-Heart and Circulatory Physiology*, 309(1):H222–H234.

Euler, L. (1862). Principia pro motu sanguinis per arterias determinando. *Opera Postuma 2*, pages 814–823.

Figueroa, C. A., Vignon-Clementel, I. E., Jansen, K. E., Hughes, T. J., and Taylor, C. A. (2006). A coupled momentum method for modeling blood flow in three-dimensional deformable arteries. *Computer methods in applied mechanics and engineering*, 195(41-43):5685–5706.

Formaggia, L., Lamponi, D., and Quarteroni, A. (2003). One-dimensional models for blood flow in arteries. *Journal of Engineering Mathematics*, 47(3):251–276.

Formaggia, L., Lamponi, D., Tuveri, M., and Veneziani, A. (2006). Numerical modeling of 1d arterial networks coupled with a lumped parameters description of the heart. *Computer Methods in Biomechanics and Biomedical Engineering*, 9(5):273–288.

Formaggia, L., Nobile, F., and Quarteroni, A. (2002). A one dimensional model for blood flow: Application to vascular prosthesis. In Babuška, I., Ciarlet, P. G., and Miyoshi, T., editors, *Mathematical Modeling and Numerical Simulation in Continuum Mechanics*, pages 137–153, Berlin, Heidelberg. Springer Berlin Heidelberg.

Formaggia, L., Nobile, F., Quarteroni, A., and Veneziani, A. (1999). Multiscale modelling of the circulatory system: a preliminary analysis. *Computing and Visualization in Science*, 2(2-3):75–83.

Formaggia, L., Quarteroni, A., and Veneziani, A. (2010). *Cardiovascular Mathematics: Modeling and simulation of the circulatory system*, volume 1. Springer Science & Business Media.

Formaggia, L. and Veneziani, A. (2003). Reduced and multiscale models for the human cardiovascular system. *Lecture notes VKI lecture series*, 7.

Fossan, F. E., Mariscal-Harana, J., Alastruey, J., and Hellevik, L. R. (2018). Optimization of topological complexity for one-dimensional arterial blood flow models. *Journal of The Royal Society Interface*, 15(149):20180546.

Ghigo, A. R., Fullana, J.-M., and Lagrée, P.-Y. (2017). A 2d nonlinear multiring model for blood flow in large elastic arteries. *Journal of Computational Physics*, 350:136–165.

Guan, D., Liang, F., and Gremaud, P. A. (2016). Comparison of the windkessel model and structured-tree model applied to prescribe outflow boundary conditions for a one-dimensional arterial tree model. *Journal of Biomechanics*, 49(9):1583–1592.

Guiot, C., Pianta, P., Cancelli, C., and Pedley, T. (1990). Prediction of coronary blood flow with a numerical model based on collapsible tube dynamics. *American Journal of Physiology-Heart and Circulatory Physiology*, 258(5):H1606–H1614.

Hughes, T. J. and Lubliner, J. (1973). On the one-dimensional theory of blood flow in the larger vessels. *Mathematical Biosciences*, 18(1):161–170.

Hunter, P. (1972). Numerical simulation of arterial blood flow. Master's thesis, The University of Auckland, Auckland.

Kim, H., Vignon-Clementel, I., Figueroa, C., Jansen, K., and Taylor, C. (2010). Developing computational methods for three-dimensional finite element simulations of coronary blood flow. *Finite Elements in Analysis and Design*, 46(6):514–525. The Twenty-First Annual Robert J. Melosh Competition.

Korakianitis, T. and Shi, Y. (2006). A concentrated parameter model for the human cardiovascular system including heart valve dynamics and atrioventricular interaction. *Medical Engineering Physics*, 28(7):613–628.

Korteweg, D. J. (1878). Ueber die fortpflanzungsgeschwindigkeit des schalles in elastischen roehren. *Annalen der Physik*, 241(12):525–542.

Manganotti, J., Caforio, F., Kimmig, F., Moireau, P., and Imperiale, S. (2021). Coupling reduced-order blood flow and cardiac models through energy-consistent strategies: modeling and discretization. *Advanced Modeling and Simulation in Engineering Sciences*, 8(1):1–37.

Matthys, K. S., Alastruey, J., Peiró, J., Khir, A. W., Segers, P., Verdonck, P. R., Parker, K. H., and Sherwin, S. J. (2007). Pulse wave propagation in a model human arterial network: Assessment of 1-d numerical simulations against in vitro measurements. *Journal of Biomechanics*, 40(15):3476–3486.

Migliavacca, F., Balossino, R., Pennati, G., Dubini, G., Hsia, T.-Y., de Leval, M. R., and Bove, E. L. (2006). Multiscale modelling in biofluidynamics: application to reconstructive paediatric cardiac surgery. *Journal of biomechanics*, 39(6):1010–1020.

Milišić, V. and Quarteroni, A. (2004). Analysis of lumped parameter models for blood flow simulations and their relation with 1d models. *ESAIM: Mathematical modelling and numerical analysis*, 38(4):613–632.

Moens, A. (1877). Over de voortplantingssnelheid von den pols. Technical report, Leiden.

Muller, L. and Toro, E. (2013). Well-balanced high-order solver for blood flow in networks of vessels with variable properties. *International Journal for Numerical Methods in Biomedical Engineering*, 29:n/a–n/a.

Mynard, J. P. and Nithiarasu, P. (2008). A 1d arterial blood flow model incorporating ventricular pressure, aortic valve and regional coronary flow using the locally conservative galerkin (lcg) method. *Communications in Numerical Methods in Engineering*, 24(5):367–417.

Olufsen, M. S., Peskin, C. S., Kim, W. Y., Pedersen, E. M., Nadim, A., and Larsen, J. (2000). Numerical simulation and experimental validation of blood flow in arteries with structured-tree outflow conditions. *Annals of biomedical engineering*, 28(11):1281–1299.

Peiro, J., Sherwin, S., Parker, K., Franke, V., Formaggia, L., Lamponi, D., and Quarteroni, A. (2003). Numerical simulation of arterial pulse propagation using one-dimensional models. *Wall-fluid interactions in physiological flows*, pages 1–36.

Piccioli, F., Valiani, A., Alastruey, J., and Caleffi, V. (2022). Assessment of cardiac function by pulse wave analysis. a computational study.

Pontrelli, G. (2004). A multiscale approach for modelling wave propagation in an arterial segment. *Computer Methods in Biomechanics and Biomedical Engineering*, 7(2):79–89.

Pontrelli, G. and Rossoni, E. (2003). Numerical modelling of the pressure wave propagation in the arterial flow. *International journal for numerical methods in fluids*, 43(6-7):651–671.

Pythoud, F., Stergiopulos, N., and Meister, J.-J. (1995). Forward and backward waves in the arterial system: nonlinear separation using riemann invariants. *Technology and Health Care*, 3(3):201–207.

Quarteroni, A., Ragni, S., and Veneziani, A. (2001). Coupling between lumped and distributed models for blood flow problems. *Computing and Visualization in Science*, 4(2):111–124.

Quarteroni, A., Tuveri, M., and Veneziani, A. (2000). Computational vascular fluid dynamics: problems, models and methods. *Computing and Visualization in Science*, 2(4):163–197.

Quarteroni, A., Veneziani, A., and Vergara, C. (2016). Geometric multiscale modeling of the cardiovascular system, between theory and practice. *Computer Methods in Applied Mechanics and Engineering*, 302:193–252.

Rachid, K. (2018). *Estimation de la pression aortique à l'aide de l'imagerie par résonance magnétique : développement d'un modèle biomécanique d'écoulement.* PhD thesis. 2018SACLS251.

Reymond, P., Bohraus, Y., Perren, F., Lazeyras, F., and Stergiopulos, N. (2011). Validation of a patient-specific one-dimensional model of the systemic arterial tree. *American Journal of Physiology-Heart and Circulatory Physiology*, 301(3):H1173–H1182.

Reymond, P., Merenda, F., Perren, F., Rüfenacht, D., and Stergiopulos, N. (2009). Validation of a one-dimensional model of the systemic arterial tree. *American Journal of Physiology-Heart and Circulatory Physiology*, 297(1):H208–H222.

Reymond, P., Westerhof, N., and Stergiopulos, N. (2012). Systolic hypertension mechanisms: effect of global and local proximal aorta stiffening on pulse pressure. *Annals of biomedical engineering*, 40(3):742–749.

Rideout, V. C. and Dick, D. E. (1967). Difference-differential equations for fluid flow in distensible tubes. *IEEE Transactions on Biomedical Engineering*, BME-14(3):171–177.

Riemann, G. (1866). Ein beitrag zu den untersuchungen uber die bewegung eines flussigen gleichartigen ellipsoides. Technical report, Gottingen.

Segers, P., Rietzschel, E., De Buyzere, M., Stergiopulos, N., Westerhof, N., Van Bortel, L., Gillebert, T., and Verdonck, P. (2008). Three-and four-element windkessel models: assessment of their fitting performance in a large cohort of healthy middle-aged individuals. *Proc Inst Mech Eng H*, 222(4):417–428.

Sherwin, S. J., Formaggia, L., Peiro, J., and Franke, V. (2003). Computational modelling of 1d blood flow with variable mechanical properties and its application to the simulation of wave propagation in the human arterial system. *International journal for numerical methods in fluids*, 43(6-7):673–700.

Shi, Y., Lawford, P., and Hose, R. (2011). Review of zero-d and 1-d models of blood flow in the cardiovascular system. *BioMedical Engineering OnLine*, 10(1):33.

Smith, N., Pullan, A., and Hunter, P. J. (2002). An anatomically based model of transient coronary blood flow in the heart. *SIAM Journal on Applied mathematics*, 62(3):990–1018.

Stergiopulos, N., Westerhof, B. E., and Westerhof, N. (1999). Total arterial inertance as the fourth element of the windkessel model. *American Journal of Physiology-Heart and Circulatory Physiology*, 276(1):H81–H88. PMID: 9887020.

Stergiopulos, N., Young, D., and Rogge, T. (1992). Computer simulation of arterial flow with applications to arterial and aortic stenoses. *Journal of biomechanics*, 25(12):1477–1488.

Streeter, V. L., Keitzer, W. F., and Bohr, D. F. (1963). Pulsatile pressure and flow through distensible vessels. *Circulation Research*, 13(1):3–20.

van de Vosse, F. N. and Stergiopulos, N. (2011). Pulse wave propagation in the arterial tree. *Annual Review of Fluid Mechanics*, 43(1):467–499.

Wang, X. (2014). *1D modeling of blood flow in networks: Numerical computing and applications*. PhD thesis, Université Pierre et Marie Curie-Paris VI.

Willemet, M. and Alastruey, J. (2014). Arterial pressure and flow wave analysis using time-domain 1-d hemodynamics. *Annals of Biomedical Engineering*, 43(1):190–206.

Womersley, J. R. (1957). An elastic tube theory of pulse transmission and oscillatory flow in mammalian arteries. Technical report, Aerospace Research Labs Wright-Patterson AFB OH.

Xiao, N., Alastruey, J., and Figueroa, C. A. (2013). A systematic comparison between 1-d and 3-d hemodynamics in compliant arterial models. *International Journal for Numerical Methods in Biomedical Engineering*, 30(2):204–231.

Young, T. (1832). Hydraulic investigations, subservient to an intended croonian lecture on the motion of the blood. *Abstracts of the Papers Printed in the Philosophical Transactions of the Royal Society of London*, 1:298–300.

CHAPTER 2

Coupling reduced-order blood flow and cardiac models through energy-consistent strategies: modeling and discretization

[...] all opening moves were the same, like in chess. You don't have to come up with anything new, there's no point, because you're both after the same thing anyway. The game soon finds its own way and it's only at that point that you need a strategy.
— Paolo Giordano, *The Solitude of Prime Numbers*

In this work we provide a novel energy-consistent formulation for the classical 1D formulation of blood flow in an arterial segment. The resulting reformulation is shown to be suitable for the coupling with a lumped (0D) model of the heart that incorporates a reduced formulation of the actin-myosin interaction. The coupling being consistent with energy balances, we provide a complete heart-circulation model compatible with thermodynamics hence stable numerically and informative physiologically. These latter two properties are verified by numerical experiments.
This chapter contains an accepted article, realized in collaboration with Federica Caforio, Sébastien Imperiale, François Kimmig and Philippe Moireau. My contributions include the mathematical formulation of the one-dimensional blood flow model and its discretization, the analysis of the energy properties, as well as the numerical strategy, the coupling with the existing cardiac model and the numerical results.

Contents

Coupling reduced-order blood flow and cardiac models through energy-consistent strategies: modeling and discretization

Jessica Manganotti[1,2], Federica Caforio[1,2,3], François Kimmig[1,2], Philippe Moireau[1,2] and Sebastien Imperiale[1,2]

[1]Inria, Team MΞDISIM, Inria Saclay-Ile-de-France, France
[2]LMS, Ecole Polytechnique, CNRS, Institut Polytechnique de Paris, 91128, Palaiseau, France
[3]University of Graz, Institute of Mathemtics and Scientific Computing, NAWI Graz, Graz, Austria

AMSES, DOI: 10.1186/s40323-021-00206-4

Abstract

In this work we provide a novel energy-consistent formulation for the classical 1D formulation of blood flow in an arterial segment. The resulting reformulation is shown to be suitable for the coupling with a lumped (0D) model of the heart that incorporates a reduced formulation of the actin-myosin interaction. The coupling being consistent with energy balances, we provide a complete heart-circulation model compatible with thermodynamics hence stable numerically and informative physiologically. These latter two properties are verified by numerical experiments.

Keywords— reduced-order models, cardiovascular modelling, energy-preserving time-scheme, shallow-water models, dicrotic notch

2.1 Introduction

The importance of reduced-order (RO) models in clinical applications has been extensively assessed in the last years. In particular, RO models are nowadays very widespread in the scientific literature [Formaggia et al., 1999; Quarteroni and Formaggia, 2004; Arts et al., 2005; Shi et al., 2011; Manzoni et al., 2018] concerning cardiovascular applications for patient-specific model predictions. Lumped-parameter zero-dimensional (0D) models – typically Windkessel models [Westerhof et al., 2009; Segers et al., 2003, 2008] – can provide a general view on the global response, *e.g.* in pressure and flow, of the whole cardiovascular system or a portion of it [Shi et al., 2011; Quarteroni et al., 2016]. Hence, RO models can be used as simplified limit conditions for a more detailed system, *e.g.* a full three-dimensional (3D) heart model [Sainte-Marie et al., 2006; Kerckhoffs et al., 2007; Augustin et al., 2016; Hirschvogel et al., 2017] and in practice they are often used to represent the circulation upstream and/or downstream of the domain of a higher-order model and to define the relationship between pressure and flow at its boundaries [Alastruey et al., 2008; Vignon-Clementel et al., 2012; Guan et al., 2016].

RO models used in cardiovascular applications are one-dimensional (1D) models of the blood circulation. The 1D formulation accounts for the effects due to pulse wave

transmission and thus enables to predict important markers such as pressure wave velocity. These models have been validated against *in vitro* [Matthys et al., 2007; Boileau et al., 2015] and *in vivo* [Reymond et al., 2009; Bollache et al., 2014] measurements and have proven to provide useful insights for the understanding of cardiovascular physiology and pathology. Further, 1D models may be preferred over 0D models when local vascular changes or distributed properties (*e.g.* tapering, branching, stenoses) are under study, and when the impact of physiological and disrupted wave transmission on the circulation (f.e. the origin and clinical relevance of the dicrotic notch, as in [Politi et al., 2016]) is investigated. Therefore, 1D models are ideal to simulate blood flow in a single arterial segment [Alastruey et al., 2008; Bollache et al., 2014; Pontrelli, 2004; Xiao et al., 2013] or a more structured tree of arteries [Guan et al., 2016; Matthys et al., 2007; Boileau et al., 2015; Willemet and Alastruey, 2014]. In addition, 1D models may also be used to take into account other components (*e.g.* coronary circulation) [Reymond et al., 2009] and be employed to simulate the global human circulation [Müller and Toro, 2014; Mynard and Smolich, 2015; Brault et al., 2017; Audebert et al., 2017] (in combination with lumped-parameter models for the heart dynamics [Formaggia et al., 2006], pulmonary circulation and microvascular beds).

In addition, RO models can also be employed to model the heart dynamics. The simplest approach to model the heart dynamics is based on the use of time-varying elastance heart dynamics models [Shishido et al., 2000]. More accurate RO approaches were also developed, see for instance [Lumens et al., 2009; Caruel et al., 2013]. In the 0D model proposed in [Caruel et al., 2013], the geometry of the left ventricle is considered to be a thick sphere and the dependence on space of the heart motion is only related to the radius of the sphere. In [Lumens et al., 2009], the mechanics of ventricular interaction is based on the assumption of a simplified ventricular composite geometry. In more detail, ventricular geometry is approximated by three thick-walled spherical segments encapsulating the LV and RV cavities.

Due to their reduced computational cost, RO models are well suited for real-time monitoring when coupled with data assimilation strategies [Lombardi, 2013; Caiazzo et al., 2017; Arthurs et al., 2020]. Furthermore, due to the reduced number of parameters used to describe the reduced dynamics (compared to full 3D models for instance), they are more adequate for the stable solution of inverse problems (IP). However, IP strategies and data assimilation strategies may fail if the forward problem lacks of appropriate stability properties. Typically, the forward model must provide a stable solution, especially when it is solved with various sets of parameters and (noisy) feedback terms. In this regard, energy-preserving schemes are ideal to discretize forward problems, since they are stable with respect to a variation of parameters and they ensure a reliable control on the behavior of the solution [Chapelle et al., 2012]. Moreover, energy balance and exchanges turn out to be important physiological markers that should be well approximated and be easily accessed, thus motivating once more the use of RO models that preserve the energy balance intrinsic to the considered modeled phenomena.

Several difficulties must be overcome when deriving energy-preserving RO models and their associated discretization. First at the continuous level, RO models do not necessarily come under a form that is obviously compliant with energy principles (appropriate energy balance may be lost during the model reduction). Hence, such RO models must be adapted or transformed. Then, it is also not obvious to construct a numerical scheme that preserves the continuous energy balance, since advanced RO models are often highly non-linear.

In this work, we extend the previous work of [Formaggia et al., 2006] by introducing a coupling strategy involving the heart model of [Caruel et al., 2013] and an arterial segment. On the one hand, we provide a novel energy-consistent formulation for the classical

1D formulation of blood flow in an arterial segment. Of note, although the application envisaged blood circulation, this energy-consistent mathematical framework and the formulation proposed are prone to extension to other non-linear hyperbolic 1D problems, like shallow water equations. The resulting reformulation is shown to be suitable for the coupling with the lumped (0D) model of the heart initially proposed in the work of [Caruel et al., 2013]. On the other hand, the novelty concerning the cardiac model is that we are able to prove the stability both in the continuous and discrete reduced order formulations, hence guaranteeing the consistency with the energy relation described by [Chapelle et al., 2012] for a 3D heart model. The coupling being consistent with energy balances, we finally provide a complete heart-circulation model compatible with thermodynamics hence stable numerically and informative physiologically.

The paper is structured as follows: first, in Section 2.2 we present the equations that describe, respectively, the 1D blood flow model, the 0D heart model and the valve dynamics, and we report their energy relation for all the compartments. Then, in Section 2.3 we detail the changes of variables that are performed in the blood flow model to obtain an energy-compliant formulation and we illustrate its non trivial numerical aspects. The key aspects of the discretization are presented in Section 2.4. Finally, in Section 2.5 we show the results of the numerical simulations and we draw the conclusions and perspectives.

2.2 Partial differential equations of the reduced models

2.2.1 One-dimensional blood flow model

Blood propagation in the aorta

Momentum and continuity equations in their one-dimensional formulation are widely used to model the arterial tree, or a portion of it, and to study pressure and blood flow [Reymond et al., 2009]. The standard formulation that describes blood flow propagation in a vessel is derived from the Navier-Stokes equation by an asymptotic analysis procedure [Formaggia et al., 2000; Quarteroni and Formaggia, 2004]. For all time $t > 0$ we look for a blood flow $Q(t, s)$ and a cross-section $A(t, s)$, along the axis s of the vessel, that are solution of

$$\begin{cases} \partial_t A + \partial_s Q = 0, \\ \partial_t Q + \alpha_{\text{vp}}\, \partial_s \dfrac{Q^2}{A} + \dfrac{A}{\rho} \partial_s P(A) + K_r \dfrac{Q}{A} = 0, \\ P(A) = P_{\text{ext}} + \psi_e(A) + \psi_v(A)\,, \end{cases} \tag{2.1}$$

where α_{vp} is a coefficient related to the a-priori assumption on the velocity profile in the vessel, $P(A)$ is the pressure, P_{ext} the exterior pressure, ρ the density of blood (considered as a constant value) and K_r the friction parameter. In this work we assume that the velocity profile is flat, therefore

$$\alpha_{\text{vp}} = 1.$$

The first equation of System (2.1) represents a reduced form of the continuity equation, whereas the second one corresponds to the momentum conservation and the last one is a relation that accounts for the vessel wall displacement. In particular, it links the change in pressure to the wall deformation and deformation rate, hence the change in the cross-section A. It reads:

$$\psi_e(A) = \beta \frac{\sqrt{A} - \sqrt{A_0}}{A_0} \quad \text{and} \quad \psi_v(A) = \frac{\Gamma}{A_0 \sqrt{A}} \partial_t A, \tag{2.2}$$

where $\beta = (4\sqrt{\pi}E\,h_0)/3$, with E the Young modulus of the vessel and h_0 its thickness, $\Gamma = (2\sqrt{\pi}h_0\nu)/3$, with ν viscosity of the wall and A_0 the reference area of the cross-section of the vessel. The analysis of ψ_v will be addressed in Section 2.3.8. Therefore, if not specified, in the following sections ψ corresponds to ψ_e.
System (2.1) should be completed with the initial condition $A(0,s) = A_0$ and $Q(0,s) = 0$ as well as boundary conditions that are the subject of the forthcoming sections. When Γ and K_r are considered equal to zero, System (2.1) is composed by non-linear hyperbolic equations and discontinuities may appear in time, *e.g.* shocks, even when smooth data are considered. However, the presence of viscosity smoothens the solution and it is reasonable to assume that its derivative with respect to s exists.

It is possible to show that, for smooth solutions, an energy relation holds. Surprisingly, such relation has not yet been used in the literature to deduce numerical models for the propagation of blood flow, although it is well known that energy-consistent methods provide great benefits in terms of stability, which is a key aspect in the context of multi-physics couplings.
Considering the continuous problem, if we take into account a vessel of length L, then we can define the energy related to (A, Q) – or to (A, u) where u is the blood velocity since $Q = Au$ – as

$$\mathcal{E}_{\text{ar}}(t) = \int_0^L e(t,\, s)\,\mathrm{d}s \tag{2.3}$$

with

$$e = \frac{\rho}{2}Au^2 + \Psi(A) \text{ and } \Psi(A(t,s)) = \int_{A_0}^{A(t,s)} \psi_e(a)\,\mathrm{d}a \geq 0. \tag{2.4}$$

Moreover, we define the instantaneous loss term as

$$\mathcal{D}_{\text{ar}}(t) = \rho\,K_r \int_0^L u^2\,\mathrm{d}s \;+ \frac{\Gamma}{A_0}\int_0^L \frac{|\partial_s(A\,u)|^2}{\sqrt{A}}\,\mathrm{d}s \;\geq 0\,.$$

Then, a straightforward extension of [Formaggia et al., 2000, Lemma 2.2] can be deduced.

Lemma 2.2.1 *Any smooth solution of System (2.1) satisfies the conservation property*

$$\frac{\mathrm{d}}{\mathrm{d}t}\mathcal{E}_{ar} + \mathcal{D}_{ar} + Q\big(P_{tot} - P_{ext}\big)\big|_0^L = 0, \tag{2.5}$$

with P_{tot} defined as

$$P_{tot} = P(A) + \frac{\rho}{2}\,u^2. \tag{2.6}$$

Outflow and inflow conditions

The energy balance (2.5) shows that the energy defined in (2.3) is a decreasing function of time if there is no blood flow imposed at the inlet and the outlet. But of course, System (2.1) should be completed with more realistic boundary conditions, typically relating the input flux (output flux, respectively) or the pressure described in (2.6) at the inlet (outlet, respectively) with the flux or pressure in other systems. In our case, a simple three-element Windkessel [Westerhof et al., 1969] is employed at the outlet, hence we introduce a new unknown, a pressure P_c, that satisfies

$$C_c\frac{\mathrm{d}}{\mathrm{d}t}P_c + \frac{P_c}{R_{\text{per}}} = Q(L), \quad (P_{\text{tot}} - P_{\text{ext}}) - P_c = R_c Q(L), \tag{2.7}$$

where C_c, R_{per} and R_c are positive parameters that correspond to a conductance and resistances in the Windkessel terminology. At the inlet, we have

$$P_{\text{ar}} = P_{\text{tot}}(0) - P_{\text{ext}}, \quad Q_{\text{ar}} = Q(0), \tag{2.8}$$

where P_{ar} and Q_{ar} stand for the arterial pressure and the arterial flux at the inlet of the aorta, respectively. One can then easily deduce from Lemma 2.2.1 an energy balance for the coupled equations (2.1) and (2.7).

Theorem 2.2.2 *Any smooth solution of Systems (2.1,2.7) satisfies the conservation property*

$$\frac{\mathrm{d}}{\mathrm{d}t}\Big(\mathcal{E}_{ar} + \mathcal{E}_w\Big) + \mathcal{D}_{ar} + \mathcal{D}_w = P_{ar}Q_{ar}, \tag{2.9}$$

where

$$\mathcal{E}_w = \frac{C_c}{2}P_c^2, \quad \mathcal{D}_w = \frac{P_c^2}{R_{per}} + R_c Q(L)^2.$$

In the next two subsections a non-linear reduced-model of the heart and cardiac valves is derived as an efficient parametrized generator of an inlet flow. This reduced model will then be adequately coupled to the one-dimensional model proposed in this work in order to preserve the energy balance.

2.2.2 Heart model

In this section, we describe the chosen reduced heart model proposed in [Caruel et al., 2013]. This model benefits from an appealing mathematical structure while producing accurate pressure-volume loops. It integrates in a system of ODEs a microscopical Huxley-like model of actin-myosin binding with a macroscopical cavity deformation formulation. The dimension reduction relies on a spherical hypothesis and a shell asymptotic derivation. Here, we will prove that an energy balance exists for the reduced model as it is the case for the three-dimensional formulation that is derived in [Chapelle et al., 2012]. This will allow us to derive a complete energy balance property when the 0D heart model is coupled to the 1D blood flow. Following [Caruel et al., 2013], we can derive by an asymptotic procedure a system of ODEs describing a lumped cardiac mechanical model that is geometrically represented by a thick sphere of radius R and thickness d – see Figure 2.2. The unknown displacement field is reduced to a radial lumped quantity y, that is a unique scalar variable such that the deformed radius of the sphere R, the thickness in the deformed configuration d and the volume of the deformed cavity V [Burtschell, 2016], shown in Figure 2.2, are given by

$$R(y) = R_0 + y, \quad d(y) = d_0\Big(1 + \frac{y}{R_0}\Big)^{-2} \text{ and } V(y) = \frac{4}{3}\pi\left(R(y) - \frac{d(y)}{2}\right)^3,$$

where R_0 and d_0 are the radius and the thickness of the sphere in the reference configuration, respectively. The system of ODEs also involves variables accounting for the modeling of heart contraction through the active deformation e_c and the active stress τ_c, which are linked to the global deformation with the rheology pictured in Figure 2.2 following the recent formulation proposed in Kimmig et al. [2019]. The system is loaded with the ventricular pressure P_v. The dynamics reads

$$\begin{cases} \rho_0|\Omega_0|\ddot{y} + \dfrac{|\Omega_0|}{R_0}k_s\Big(\dfrac{y}{R_0} - e_c\Big) + \dfrac{\partial \mathcal{W}_p}{\partial y}(y) + \mathcal{W}_v(y,\dot{y}) = P_v\dfrac{\partial V(y)}{\partial y}, \\ \mu\,\dot{e}_c - k_s\Big(\dfrac{y}{R_0} - e_c\Big) = -\tau_c, \end{cases} \tag{2.10}$$

where ρ_0 is the density in the reference configuration, μ a viscosity parameter, k_s a stiffness parameter accounting for passive components of the myosin filament – typically the passive stiffness of the filaments themselves plus the Z-disks and $|\Omega_0|$ is the volume of the myocardium in the reference configuration, which is given by

$$|\Omega_0| = \frac{4}{3}\pi\left[\left(R_0 + \frac{d_0}{2}\right)^3 - \left(R_0 - \frac{d_0}{2}\right)^3\right].$$

Moreover $\mathcal{W}_p(y)$ and $\mathcal{W}_v(y,\dot{y})$ are directly inferred from the passive potential and the viscous pseudo-potential of the connective tissue matrix [Caruel et al., 2013]. They are smooth functions that satisfy in particular

$$\mathcal{W}_p(y) \geq 0 \quad \text{and} \quad \mathcal{W}_v(y,\dot{y})\,\dot{y} \geq 0.$$

Choosing an isotropic transverse exponential law [Holzapfel and Ogden, 2009; Caruel et al., 2013] leads to

$$\mathcal{W}_p(y) = |\Omega_0|\left[C_0 e^{C_1\left[2\left(1+\frac{y}{R_0}\right)^2+\left(1+\frac{y}{R_0}\right)^{-4}-3\right]^2} + C_2 e^{C_3\left[\left(1+\frac{y}{R_0}\right)^2-1\right]^2}\right],$$
$$\mathcal{W}_v(y,\dot{y}) = 2\eta|\Omega_0|\left(1+\tfrac{y}{R_0}\right)^2\left[1+2\left(1+\tfrac{y}{R_0}\right)^{-12}\right]\dot{y},$$

where C_0 and C_2 are some parameters that describe the stiffness of the material and C_1 and C_3 are non-dimensional parameters, while η is the viscosity.

Assuming for now that the active stress τ_c is imposed, the dynamics described in System (2.10) gives a reduced heart dynamical systems of 2-state variables (y, e_c) for which we can derive the heart energy balance. We first introduce the energy

$$\mathcal{E}_{\text{hr}} = \frac{\rho_0|\Omega_0|}{2}\dot{y}^2 + \mathcal{W}_p + \frac{|\Omega_0|k_s}{2}\left(\frac{y}{R_0} - e_c\right)^2, \tag{2.11}$$

that is a combination of the kinetic energy $\rho_0|\Omega_0|\frac{\dot{y}^2}{2}$, the hyperelastic energy $\mathcal{W}_p$ and the elastic energy stored in the series element.Then, we introduce the dissipation term

$$\mathcal{D}_{\text{hr}} = \mathcal{W}_v(y,\dot{y})\dot{y} + \mu|\Omega_0|(\dot{e}_c)^2 \tag{2.12}$$

and state the following energy relation result.

Theorem 2.2.3 *Any smooth solution of System (2.10) satisfies the energy balance*

$$\frac{\mathrm{d}}{\mathrm{d}t}\mathcal{E}_{hr} + \mathcal{D}_{hr} = P_v\,\frac{\mathrm{d}}{\mathrm{d}t}(V(y)) - |\Omega_0|\tau_c\dot{e}_c, \tag{2.13}$$

where, at the right-hand side, we have the coupling term with the circulation and the microscopic active stress input.

Microscopic actin-myosin binding model

The chosen model of active contraction balances our need of reasonable complexity with physiological characteristics regarding pressure-volume loops [Bestel et al., 2001; Chapelle et al., 2012; Kimmig et al., 2019]. In more detail, the microscopic active stress τ_c is computed from the first two moments of a Huxley-like formulation of the actin-myosin

binding phenomenon. Introducing the active stiffness variable k_c, we have the following system

$$\begin{cases} \dot{\tau}_c = -(|\nu| + \alpha|\dot{e}_c|)\tau_c + n_0(e_c)\sigma_0|\nu|_+ + k_c\dot{e}_c, \\ \dot{k}_c = -(|\nu| + \alpha|\dot{e}_c|)k_c + n_0(e_c)k_0|\nu|_+, \end{cases} \tag{2.14}$$

where we use the symbol $|\cdot|_+$ to denote the positive part. The parameter k_0 denotes the maximum active stiffness parameter and σ_0 the corresponding maximum active stress, α is a time constant, $n_0(e_c)$ is a function with values in $[0, 1]$ accounting for the Frank-Starling mechanism, and $\nu(t) = \nu([\mathrm{Ca}^{2+}](t))$ is a function triggering the contraction, typically when $[\mathrm{Ca}^{2+}] > c_{\mathrm{th}}$, with c_{th} a given threshold, see Figure 2.1. The state variables (τ_c, k_c)

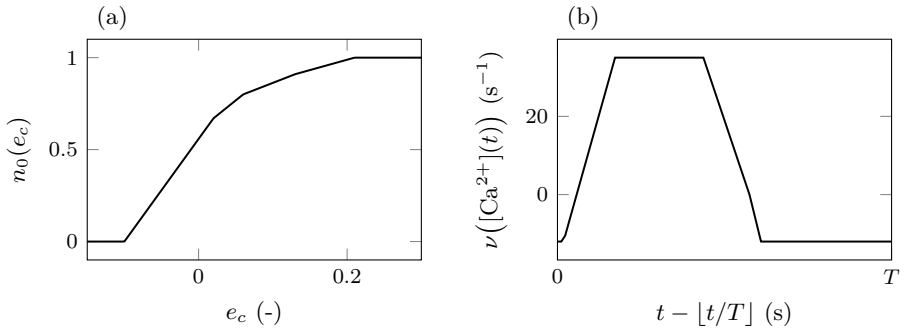

Figure 2.1 – (a) Definition of the function n_0. (b) Time evolution of contraction triggering function ν. We denote here by T the duration of a heartbeat.

of System (2.14) model the active contraction triggered by the input signal ν. For the energy balance, we introduce the energy stored in our homogenized model of actin-myosin bridges and a dissipative term [Chapelle et al., 2012]

$$\mathcal{E}_c = \frac{|\Omega_0|}{2}\frac{\tau_c^2}{k_c}, \quad \mathcal{D}_c = (|\nu| + \alpha|\dot{e}_c|)\mathcal{E}_c.$$

Theorem 2.2.4 *Any smooth solution of System (2.14) satisfies the energy balance*

$$\frac{\mathrm{d}}{\mathrm{d}t}\mathcal{E}_c + \mathcal{D}_c = |\Omega_0|\tau_c\dot{e}_c + \frac{|\Omega_0|n_0(e_c)\tau_c}{k_c}\Big(\sigma_0 - \frac{\tau_c k_0}{2k_c}\Big)|\nu|_+. \tag{2.15}$$

Combining (2.13) and System (2.15), we finally obtain the complete energy balance for the heart model

$$\frac{\mathrm{d}}{\mathrm{d}t}\Big[\mathcal{E}_{\mathrm{hr}} + \mathcal{E}_c\Big] + \Big[\mathcal{D}_{\mathrm{hr}} + \mathcal{D}_c\Big] = P_v\frac{\mathrm{d}}{\mathrm{d}t}(V(y)) + \frac{|\Omega_0|n_0(e_c)\tau_c}{k_c}\big(\sigma_0 - \frac{\tau_c k_0}{2k_c}\big)|\nu|_+,$$

where, from the point of view of the heart model, ν is an input signal and P_v an external loading.

Remark 2.2.5 *The energy relation in System (2.15) is deduced by introducing the variable $\lambda_c = \tau_c/\sqrt{k_c}$ [Chapelle et al., 2012]. Then, as an intermediate step it can be shown that λ_c satisfies the following ODE:*

$$\dot{\lambda}_c = -\frac{\dot{k}_c}{2\,k_c}\lambda_c + \frac{\dot{\tau}_c}{\sqrt{k_c}} = -(|\nu| + \alpha|\dot{e}_c|)\frac{\lambda_c}{2} + \frac{n_0(e_c)}{\sqrt{k_c}}\Big(\sigma_0 - \frac{k_0\,\lambda_c}{2\sqrt{k_c}}\Big)|\nu|_+ + \sqrt{k_c}\,\dot{e}_c. \tag{2.16}$$

The energy relation is finally obtained by multiplying (2.16) by $|\Omega_0|\,\lambda_c$.

2.2.3 Cardiac valve models and energy relation for the complete system

The inlet and outlet of the ventricular model are represented, respectively, by the atrioventricular and the aortic valve, as shown in Figure 2.2. To represent the fact that they may be open or closed, valves are modeled as diodes. Therefore, using Kirchhoff's circuit laws, we get

$$\begin{cases} C_{\text{mi}}\dot{P}_v - Q_v + \dfrac{|P_v - P_{\text{ar}}|_+}{K_{\text{ar}}} + \dfrac{|P_v - P_{\text{at}}|_+}{K_{\text{iso}}} - \dfrac{|P_{\text{at}} - P_v|_+}{K_{\text{at}}} = 0, \\ C_{\text{ar}}\dot{P}_{\text{ar}} - \dfrac{|P_v - P_{\text{ar}}|_+}{K_{\text{ar}}} + Q_{\text{ar}} = 0, \end{cases} \tag{2.17}$$

where the first equation is associated with the atrioventricular valve, whereas the second one relates to the aortic valve. In more detail, P_v, P_{at} and P_{ar} represent the pressure in the ventricle, in the atria and at the inlet of the aorta, respectively, whereas Q_v and Q_{ar} correspond to the ejected blood flow throughout the ventricle and at the inlet of the aorta, respectively. Finally, K_{ar}, K_{iso} and K_{at} represent the resistances of the valves [Chabiniok et al., 2017], as depicted in Figure 2.2.

It is worth mentioning, for what follows, that Q_v corresponds to the volume variation of the ventricle, so one can write

$$-\frac{\mathrm{d}}{\mathrm{d}t}\big(V(y)\big) = Q_v. \tag{2.18}$$

Now, if we multiply the first equation of System (2.17) by P_v, we multiply the second equation by P_{ar}, we sum them and we define

$$\mathcal{E}_v = \frac{C_{\text{mi}}}{2}P_v^2 + \frac{C_{\text{ar}}}{2}P_{\text{ar}}^2, \quad \mathcal{D}_v = \frac{|P_v - P_{\text{ar}}|_+^2}{K_{\text{ar}}} + \frac{|P_v - P_{\text{at}}|_+^2}{K_{\text{iso}}} + \frac{|P_{\text{at}} - P_v|_+^2}{K_{\text{at}}},$$

we can obtain an energy relation for the cardiac valve formulation.

Theorem 2.2.6 *Any smooth solution of System (2.17) satisfies the conservation property*

$$\frac{\mathrm{d}}{\mathrm{d}t}\mathcal{E}_v + \mathcal{D}_v = \frac{|P_{at} - P_v|_+ P_{at}}{K_{at}} - \frac{|P_v - P_{at}|_+ P_{at}}{K_{iso}} - P_v\frac{\mathrm{d}}{\mathrm{d}t}\big(V(y)\big) - P_{ar}Q_{ar}, \tag{2.19}$$

where we have, at the right-hand side, the input pressure term and the coupling term that take into account both the cardiac and the arterial contribution.

Finally, using Theorems 2.2.2 to 2.2.6, we are able to retrieve the global energy relation that takes into account the contribution of the heart (including the microscopic modeling of the actin-myosin binding), the valves and the arterial segment.

Corollary 2.2.6.1 *Any smooth solution of Systems (2.1, 2.7, 2.10, 2.14, 2.17) satisfies the conservation property*

$$\begin{aligned} &\frac{\mathrm{d}}{\mathrm{d}t}\Big(\mathcal{E}_{hr} + \mathcal{E}_c + \mathcal{E}_v + \mathcal{E}_{ar} + \mathcal{E}_w\Big) + \mathcal{D}_{hr} + \mathcal{D}_c + \mathcal{D}_v + \mathcal{D}_{ar} + \mathcal{D}_w \\ &\qquad = \frac{|\Omega_0|n_0(e_c)\tau_c}{k_c}\Big(\sigma_0 - \frac{\tau_c k_0}{2k_c}\Big)|\nu|_+ + \frac{|P_{at} - P_v|_+ P_{at}}{K_{at}} - \frac{|P_v - P_{at}|_+ P_{at}}{K_{iso}}. \end{aligned} \tag{2.20}$$

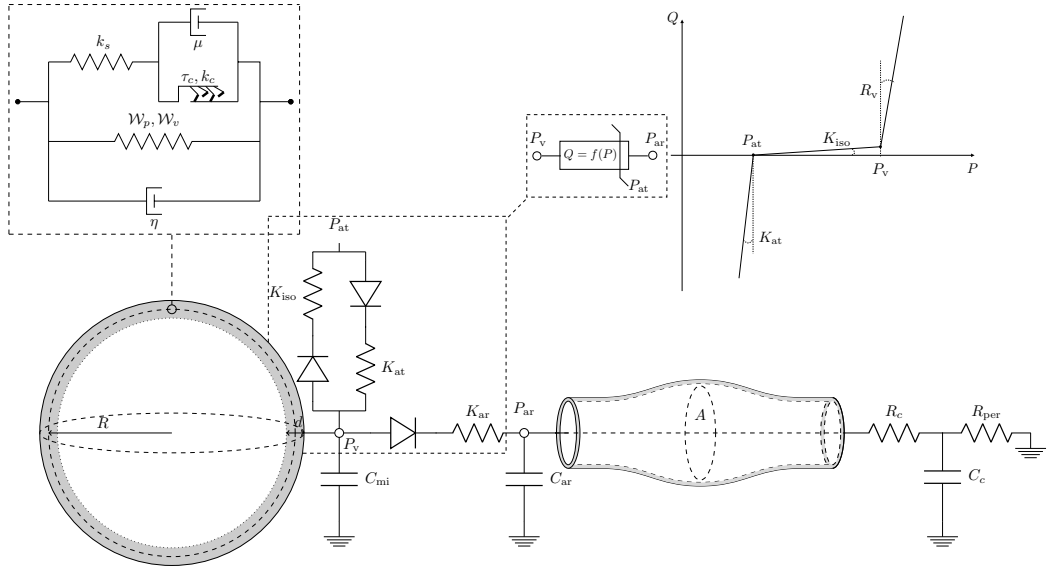

Figure 2.2 – Complete scheme of the coupled system including the heart, the cardiac valve and the arterial segment. Note that in the upper right plot we have $R_v := K_{\text{ar}} K_{\text{iso}}/(K_{\text{ar}} + K_{\text{iso}})$. This model will later be referred to as the *fully coupled model*.

2.3 An energy-compliant formulation for the blood flow model

In order to obtain an energy-preserving scheme for the blood flow model, which satisfies a discrete counterpart of Theorem 2.2.1, we will introduce three variational formulations. The first one corresponds to the standard formulation that one obtains directly from System (2.1). This formulation has A and u as principal unknowns, where A is the cross-section of the aorta defined as $A = Q/u$ and u is the blood velocity. Then, we introduce a second formulation that uses as a primary unknown the radius of the aorta $R = \sqrt{A}/\sqrt{\pi}$ and u. This formulation is straightforwardly deduced from the first one and is a convenient intermediate step, since it introduces several simplifications. From these intermediate changes we deduce the last formulation that is written in the unknowns

$$v := R\,u \quad \text{and} \quad \Phi := \varphi(R),$$

where $\varphi(R)$ is a smooth bijective function from $\mathbb{R}^+$ to $I \subset \mathbb{R}$ that we define later. This change of variables has the main advantage to provide an "energy-compliant" discretization, as it will be shown in the next chapter. As the reader will see, the energy is a quadratic functional of the new variables (Φ, v) .

2.3.1 Variational formulation in (A, u)

As a first step, we substitute Q with Au in (2.1) and assume that $\Gamma = 0$, hence $\psi_v = 0$. After some algebraic manipulations we obtain that (2.1) is equivalent to the system

$$\begin{cases} \partial_t A + \partial_s(Au) = 0, \\ \left(\frac{1}{2}(\partial_t A)\, u + A\partial_t u\right) + \left(\frac{1}{2}\, u^2\, \partial_s A + \frac{3}{2} A\, u\, \partial_s u\right) + \frac{A}{\rho}\partial_s P(A) + K_r u = 0. \end{cases} \tag{2.21}$$

Note that we have rewritten System (2.1) in a specific form adapted to the derivation of the energy balance (in fact System (2.21) is obtained following the proof of Lemma 2.2.1 provided in [Formaggia et al., 2000]). Indeed, multiplying the second equation of System (2.21) by u, one can see that

$$\left(\frac{1}{2}(\partial_t A)\, u + A\partial_t u\right) u = \frac{1}{2}\partial_t(Au^2), \qquad \text{and} \quad \left(\frac{1}{2}\, u^2\, \partial_s A + \frac{3}{2} A\, u\, \partial_s u\right) u = \frac{1}{2}\partial_s(Au^3). \tag{2.22}$$

These two equalities are, in fact, essential to prove the energy relation of Lemma 2.2.1. The objective is now to derive a weak formulation of System (2.21). Concerning the first equation, we multiply it by a space-dependent test function $\tilde{\Phi}$ and we integrate in space, obtaining

$$(\partial_t A, \tilde{\Phi}) + (\partial_s(Au), \tilde{\Phi}) = 0, \tag{2.23}$$

where $(\cdot, \cdot)$ is the L^2-scalar product in $(0, L)$. We now focus on the second equation of System (2.21) and we repeat the procedure performed above, multiplying each term by a space-dependent test function $\tilde{v}$. After some manipulations, we obtain

$$\left(\frac{\rho}{2}(\partial_t A)u + \rho A\partial_t u, \tilde{v}\right) + a(u; \tilde{v}, A) - (\partial_s(A\tilde{v}), \psi(A)) + \rho K_r(u, \tilde{v}) = g(\tilde{v}; A, u), \tag{2.24}$$

where $a(u; \cdot, \cdot)$ is bilinear in its two last arguments but non-linear in u and is given by

$$a(u; A, \tilde{v}) := \int_0^L \rho\left(\frac{1}{2}\, u^2\, \partial_s A + \frac{3}{2} A\, u\, \partial_s u\right) \tilde{v}\, \mathrm{d}s - \frac{\rho}{2} A\, u^2\, \tilde{v}\Big|_0^L, \tag{2.25}$$

and the non-linear functional g is defined as

$$g(A, u; \tilde{v}) := -\left(\frac{\rho}{2} A\, u^2\, \tilde{v} + A\, \tilde{v}\, \psi(A)\right)\Big|_0^L = -A\tilde{v}\,(P_{\text{tot}} - P_{\text{ext}})\,\Big|_0^L. \tag{2.26}$$

Observe that, by construction, g is linear in $\tilde{v}$ and includes only boundary terms. Up to this point, the weak formulation of the problem described in System (2.21) is

$$\begin{cases} (\partial_t A, \tilde{\Phi}) + (\partial_s(Au), \tilde{\Phi}) = 0, \\ \left(\frac{\rho}{2}(\partial_t A)u + \rho A\partial_t u, \tilde{v}\right) + a(u; A, \tilde{v}) - (\partial_s(A\tilde{v}), \psi(A)) + \rho K_r(u, \tilde{v}) = g(A, u; \tilde{v}). \end{cases} \tag{2.27}$$

Finally, observe that if we substitute

$$\tilde{\Phi} = \psi(A), \quad \tilde{v} = u,$$

in System (2.27), we can easily retrieve the energy relation presented in Lemma 2.2.1. Indeed, thanks to (2.22), one can see that

$$a(u; A, u) = 0. \tag{2.28}$$

Moreover, we recover the energy relation

$$\frac{\mathrm{d}}{\mathrm{d}t}\mathcal{E}_{ar}(t) + \mathcal{D}_{ar}(t) = g(A, u; u), \tag{2.29}$$

with

$$\frac{\mathrm{d}}{\mathrm{d}t}\mathcal{E}_{ar}(t) = \Big(\frac{\rho}{2}(\partial_t A)u + \rho A \partial_t u, u\Big) + (\partial_t A, \psi(A)) \quad \text{and} \quad \mathcal{D}_{ar}(t) = \rho K_r(u, u). \tag{2.30}$$

Here $\mathcal{E}_{ar}(t)$ is the total energy of the 1D model and $\mathcal{D}_{ar}(t)$ represents the dissipative term with $K_r \geq 0$.

2.3.2 An intermediate formulation in (R, u)

In order to obtain a formulation that leads to the achievement of the energy preservation at a discrete level, we construct an intermediate form of System (2.21). This formulation is obtained by replacing A with πR^2, where R represents the radius of the lumen. The unknowns become u and R. The first equation of System (2.21) is now described as

$$2\pi\big(R\,\partial_t R, \tilde{\Phi}\big) + \pi\big(\partial_s(R^2 u), \tilde{\Phi}\big) = 0. \tag{2.31}$$

Then, the first term in (2.24) can be rewritten, substituting $\tilde{v} \leftarrow \tilde{v}/R$, as

$$\Big(\frac{\rho}{2}(\partial_t A)u + \rho A \partial_t u, \frac{\tilde{v}}{R}\Big) = \pi\,\rho\,\big(u\,\partial_t R + R\partial_t u, \tilde{v}\big) = \pi\,\rho\,\big(\partial_t(Ru), \tilde{v}\big).$$

Moreover, one can see that

$$a\Big(u; A, \frac{\tilde{v}}{R}\Big) = \pi\rho \int_0^L \left(\frac{(Ru)^2}{R^2}\,\partial_s R + \frac{3}{2}(Ru)\,\partial_s \frac{Ru}{R}\right)\tilde{v}\,\mathrm{d}s - \pi\ \frac{\rho}{2}(Ru)^2\,\frac{\tilde{v}}{R}\Big|_0^L,$$

and

$$\Big(\partial_s\Big(A\frac{\tilde{v}}{R}\Big), \psi(A)\Big) = \pi(\partial_s(R\tilde{v}), \psi(\pi R^2)).$$

Note that the substitution $\tilde{v} \leftarrow \tilde{v}/R$ does not lead to any issue, since we consider solutions with $R > 0$ at any time and position. Finally, collecting the four expressions above, one can obtain a formulation with R and u as primary unknowns. It reads

$$\begin{cases} 2\pi\big(R\,\partial_t R, \tilde{\Phi}\big) + \pi\big(\partial_s(R^2 u), \tilde{\Phi}\big) = 0, \\ \pi\,\rho\,\big(\partial_t(Ru), \tilde{v}\big) + a\Big(u; \pi\,R^2, \dfrac{\tilde{v}}{R}\Big) \\ \qquad\qquad - \pi(\partial_s(R\tilde{v}), \psi(\pi R^2)) + \rho K_r\Big(u, \dfrac{\tilde{v}}{R}\Big) = g\Big(\pi R^2, u; \dfrac{\tilde{v}}{R}\Big). \end{cases} \tag{2.32}$$

It is worth noticing that the product Ru appears "almost" naturally and it is therefore tempting to define $v := Ru$ as a new variable. It becomes even more obvious that this choice is suitable by looking at the energy density, defined as

$$e = \frac{\rho}{2}Au^2 + \Psi(A) = \frac{\pi\rho}{2}(Ru)^2 + \Psi(\pi R^2). \tag{2.33}$$

This is precisely what motivates the introduction of the next formulation. Moreover, it is worth mentioning that now

$$\psi(\pi R^2) = \beta\frac{\sqrt{\pi}R - \sqrt{A_0}}{A_0}, \tag{2.34}$$

so $\psi(\pi R^2)$ is linear with respect to the unknown R and we will see in the next sections that $\Psi(\pi R^2)$ is a third-order polynomial and this will simplify its analysis.

Remark 2.3.1 *The change of variable $A = \pi R^2$ is still meaningful even if the 1D hemodynamic model does not assume a perfect circle for the geometry of the cross-section. What matters here is that the new variable R depends on the square root of A. Obviously, the introduction of the factor π is natural to obtain a physical meaning for this new variable since, in practice, arterial cross-sections are almost circular.*

2.3.3 Variational formulation in (Φ, v)

A change of variables has to be made in order to demonstrate that the scheme is energy-preserving after time discretization. More precisely, time discretization can easily deal with energies that involve quadratic terms of the unknowns. However, the energy density described in (2.33) is not a quadratic term of the unknowns (R, u), but we can see that the first contribution is a quadratic term of

$$v := Ru.$$

Therefore, we propose to use v as a main unknown. A first naive choice is then to set $\varphi(R)$ equal to $\sqrt{\Psi(\pi R^2)}$, where $\Psi(\pi R^2)$ is defined as

$$\Psi(\pi R^2) = \int_{A_0}^{A} \beta \frac{\sqrt{a} - \sqrt{A_0}}{A_0} da = \frac{\beta}{A_0}\Big[\frac{2}{3}\pi^{\frac{3}{2}} R^3 - \sqrt{A_0}\pi R^2 + \frac{1}{3}A_0^{\frac{3}{2}}\Big], \tag{2.35}$$

and set $\Phi \equiv \varphi(R)$ as the other main unknown. However, we show in Section 2.3.3 that this choice is not convenient, since $\varphi(\cdot)$ would not be a bijective function from $\mathbb{R}^+$ to $\mathbb{R}^+$. Instead, we define

$$\varphi(R) := \begin{cases} \sqrt{\Psi(\pi R^2)} & R \geq R_0, \\ -\sqrt{\Psi(\pi R^2)} & 0 \leq R < R_0, \end{cases} \quad \text{with} \quad R_0 = \frac{\sqrt{A_0}}{\sqrt{\pi}}. \tag{2.36}$$

Before studying in more detail the impact of the choice described in System (2.36) (in particular the bijectivity of the function φ), we formally give the variational formulation associated with the new couple of unknowns (v, Φ), where $\Phi := \varphi(R)$. Assuming for now that φ is bijective, we define the reciprocal function $r(\Phi) := \varphi^{-1}(\Phi)$. Then, each term of the second equation of System (2.32) can be modified as follows:

i) The term involving the time derivative reads

$$\pi\,\rho\,\big(\partial_t(Ru), \tilde{v}\big) = \pi\,\rho\,\big(\partial_t v, \tilde{v}\big). \tag{2.37}$$

ii) The non-linear transport term reads

$$\begin{aligned} a\Big(u; \pi R^2, \frac{\tilde{v}}{R}\Big) &= \tilde{a}\Big(\frac{v}{r(\Phi)}, v, \tilde{v}\Big) \\ &:= \frac{\pi\rho}{2}\int_0^L \Big(2\,\tilde{v}\,\frac{v}{r(\Phi)}\,\partial_s v + v\,\tilde{v}\,\partial_s\frac{v}{r(\Phi)}\Big)\,\mathrm{d}s - \frac{\pi\rho}{2}\tilde{v}\,v\,\frac{v}{r(\Phi)}\Big|_0^L, \end{aligned} \tag{2.38}$$

where $\tilde{a}$ is now a trilinear form. Such reformulation will lead to the choice of an adapted space discretization that preserves, for all sufficiently smooth functions v and u, the property

$$\tilde{a}(u, v, v) = 0, \tag{2.39}$$

and in particular for $u = v/r(\Phi)$.

iii) The coupling term $(\partial_s(R\tilde{v}), \psi(\pi R^2)) = (\partial_s(r(\Phi)\tilde{v}), \psi(\pi r(\Phi)^2))$ is not modified.

iv) The dissipation term reads

$$\Big(u, \frac{\tilde{v}}{R}\Big) = \Big(\frac{v}{r(\Phi)}, \frac{\tilde{v}}{r(\Phi)}\Big). \tag{2.40}$$

v) Finally, the boundary term g is given by

$$g\Big(\pi R^2, u; \frac{\tilde{v}}{R}\Big) = \tilde{g}(r(\Phi), \tilde{v}) := -\pi\, \tilde{v}\, r(\Phi)\big(P_{\text{tot}} - P_{\text{ext}}\big)\Big|_0^L, \tag{2.41}$$

where, for simplicity, we assume that P_{tot} is given. Of course, if more general boundary conditions are considered, g must be modified accordingly.

Using all the expressions above, we obtain the following equation (corresponding to the second equation of System (2.32))

$$\pi\rho(\partial_t v, \tilde{v}) + \tilde{a}\Big(\frac{v}{r}, v, \tilde{v}\Big) - \pi\,(\partial_s(r\tilde{v}), \psi(\pi r^2)) + \rho K_r\Big(\frac{v}{r}, \frac{\tilde{v}}{r}\Big) = \tilde{g}(r, \tilde{v}), \tag{2.42}$$

where, for the sake of clarity, we have written r instead of $r(\Phi)$. The first term in (2.42) clearly shows how the introduction of v simplifies the dynamic behavior of the equation and it will help at the discrete level to demonstrate the energy preservation. Now we deal with the first equation of System (2.32) in which we use as a test function $\tilde{\Phi} \leftarrow \xi(R)\tilde{\Phi}$, with

$$\xi(R) := \frac{\psi(\pi R^2)}{\varphi(R)}. \tag{2.43}$$

We show in Section 2.3.3 that this function is smooth and positive. We obtain

$$2\pi\big(\xi(R)\, R\, \partial_t R, \tilde{\Phi}\big) + \pi\big(\xi(R)\, \partial_s(R^2 u), \tilde{\Phi}\big) = 0. \tag{2.44}$$

If we focus on the first term in (2.44), we can observe that

$$2\pi\, \xi(R)\, R\, \partial_t R = \pi \frac{\psi(\pi R^2)}{\varphi(R)} \partial_t R^2 = \frac{\partial_t \Psi(\pi R^2)}{\varphi(R)}.$$

Now observe that, by definition, $\varphi(R) = \pm\sqrt{\Psi(\pi R^2)}$. Thus, the term above can be rewritten as

$$2\pi\, \xi(R)\, R\, \partial_t R = 2\, \partial_t \varphi(R). \tag{2.45}$$

Since by definition we have $\Phi = \varphi(R)$ and $R = r(\Phi)$, we can write

$$2\pi\big(\xi(R)\, R\, \partial_t R, \tilde{\Phi}\big) + \pi\big(\xi(R)\, \partial_s(R^2 u), \tilde{\Phi}\big) = 2(\tilde{\Phi}, \partial_t \Phi) + \pi\,(\partial_s(rv),\, \tilde{\Phi}\, \xi(r)), \tag{2.46}$$

where again we use the convention $r \equiv r(\Phi)$. At this point, the formulation reads

$$\begin{cases} 2(\tilde{\Phi}, \partial_t \Phi) + \pi\,(\partial_s(Rv),\, \tilde{\Phi}\, \xi(R)) = 0, \\ \pi\rho(\partial_t v, \tilde{v}) + \tilde{a}\Big(\tilde{v}, v, \dfrac{v}{R}\Big) - \pi(\partial_s(R\tilde{v}), \psi(\pi R^2)) + \rho K_r\Big(\dfrac{v}{R}, \dfrac{\tilde{v}}{R}\Big) = \tilde{g}(\tilde{v}, R), \\ R = r(\Phi). \end{cases} \tag{2.47}$$

One can see in System (2.47) an apparent lack of symmetry. Indeed, one could expect the second term in the first equation to be equal to the third term in the second equation. This is true however, since we have, using (2.43),

$$(\partial_s(R\tilde{v}), \psi(\pi R^2)) = (\partial_s(R\tilde{v}),\, \varphi(R)\, \xi(R)) = (\partial_s(R\tilde{v}),\, \Phi\, \xi(R)).$$

This observation is fundamental to obtain an energy estimate. To summarize, we have deduced from the dynamics (2.32) the following formulation:
for all $(\tilde{\Phi}, \tilde{v})$ sufficiently smooth find, for all $t > 0$, $(\Phi(t), v(t))$ solution of

$$\begin{cases} 2(\tilde{\Phi}, \partial_t \Phi) + \pi\,(\partial_s(Rv),\, \tilde{\Phi}\,\xi(R)) = 0, \\ \pi\rho(\partial_t v, \tilde{v}) + \tilde{a}\Big(\tilde{v}, v, \dfrac{v}{R}\Big) - \pi(\partial_s(R\tilde{v}),\, \Phi\,\xi(R)) + \rho K_r\Big(\dfrac{v}{R}, \dfrac{\tilde{v}}{R}\Big) = \tilde{g}(\tilde{v}, R), \\ R = r(\Phi), \end{cases} \tag{2.48}$$

with the following initial data

$$\Phi(0) = \varphi(R(0)) = \varphi(\sqrt{A_0}/\sqrt{\pi}) = 0, \quad v = 0. \tag{2.49}$$

This is what we call the energy-compliant variational formulation. At the continuous level, the energy is easily obtained by choosing $\tilde{\Phi} = \Phi$ and $\tilde{v} = v$. This simple choice of test functions to deduce the energy relation at the continuous level will help in achieving the same energy relation property at a discrete level.

Remark 2.3.2 *The formulation of System (2.48) can be obtained for other tube laws $\psi(A)$. However, some properties should be satisfied by the function ψ. In particular, ψ must be at least continuous and*

$$\psi'(A) > 0, \quad \psi(A_0) = 0.$$

2.3.4 Strong formulation

For the sake of completeness, we show the strong formulation of System (2.48). Choosing a smooth test function with compact support in $[0, L]$, one can show, using integration by parts, that the following partial differential equations hold:

$$\begin{cases} 2\partial_t \Phi + \pi\xi(R)\partial_s(Rv) = 0, \\ \pi\rho\partial_t v + \dfrac{\pi\rho}{2}\Big(2\dfrac{v}{R}\partial_s v + v\,\partial_s\dfrac{v}{R}\Big) + \rho K_r \dfrac{v}{R^2} + \pi R\partial_s(\xi(R)\Phi) = 0, \\ R = r(\Phi). \end{cases} \tag{2.50}$$

Then, choosing a smooth test function in $[0, L]$ vanishing at the boundaries in System (2.48) and using integration by parts for System (2.50), one can deduce the following boundary conditions:

$$\frac{\rho}{2}\frac{v^2}{R} + R\,\xi(R)\Phi = -R\big(P_{\text{tot}} - P_{\text{ext}}\big), \quad s \in \{0, L\}.$$

2.3.5 Analysis of the function $\varphi(R)$

In this section we provide further details on the properties of the function $\varphi(R)$. The definition in System (2.36) is motivated by the expression of $\Psi = \Psi(\pi R^2)$ that is rewritten below:

$$\Psi(\pi R^2) = \frac{\beta}{A_0}\Big[\frac{2}{3}\pi^{\frac{3}{2}}R^3 - \sqrt{A_0}\pi R^2 + \frac{1}{3}A_0^{\frac{3}{2}}\Big] = \frac{\sqrt{\pi}\beta}{3R_0^2}(R - R_0)^2\,(2R + R_0), \tag{2.51}$$

where – in this section – $R_0 = \sqrt{A_0}/\sqrt{\pi}$ is the reference radius of the cross-section. The behavior of this function is shown in Figure 2.3. It is straightforward to see that this

function, as well as its square root, is not bijective. However, using System (2.36), the function $\varphi(R)$ is then given by

$$\varphi(R) = \frac{(R - R_0)}{R_0}\sqrt{\frac{\sqrt{\pi}\beta}{3}\Big(2R + R_0\Big)}. \tag{2.52}$$

In Figure 2.3 we can observe the comparison between $\sqrt{\Psi(\pi R^2)}$ and $\varphi(R)$. For every $R \geq R_0$ the two functions coincide, whereas for $R < R_0$ they are opposite. However, we can also see that φ is bijective from $\mathbb{R}$ to some interval I satisfying $\mathbb{R}^+ \subset I \subset \mathbb{R}$. Moreover, it is easy to prove the following Property.

Theorem 2.3.3 *Assume $R_0 > 0$, then*

$$\begin{array}{rccc} \varphi: & [0,+\infty) & \mapsto & [\Phi_{min},+\infty) \\ & R & \mapsto & \varphi(R) \end{array} \qquad \text{with} \qquad \Phi_{min} = -\sqrt{\frac{\beta\sqrt{\pi}R_0}{3}}$$

is monotone increasing (hence bijective) and belongs to $C^\infty([0,+\infty))$.

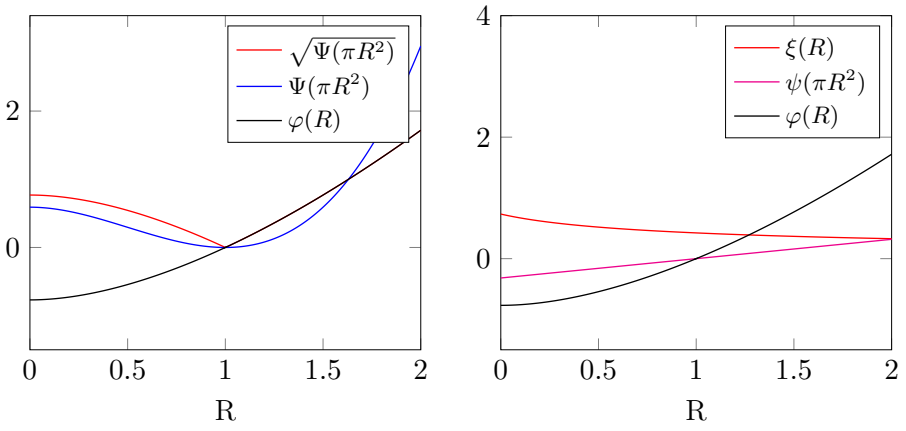

Figure 2.3 – Plot of $\sqrt{\Psi(R)}$, $\Psi(R)$, $\varphi(R)$ and $\xi(R)$ for $R_0 = 1$ and $\beta = 1$.

2.3.6 Analysis of the function $\xi(R)$

We now focus on the property of the function $\xi(R)$ that is defined by $\xi(R) = \psi(\pi R^2)/\varphi(R)$. In particular we want to check whether the function is smooth and bounded. This is not true because $\varphi(R)$ vanishes and, as one can see in Figure 2.3 and in (2.52), this happens at $R = R_0$ where – in this section – $R_0 = \sqrt{A_0}/\sqrt{\pi}$ is the reference radius of the cross-section. Using Eqs. (2.34) and (2.52) one can compute

$$\xi(R) = \frac{\beta\sqrt{\pi}}{\pi R_0^2}\frac{R - R_0}{\varphi(R)} = \frac{\sqrt{3\beta}}{\pi^{\frac{3}{4}}R_0\sqrt{(2R + R_0)}}.$$

We see in Figure 2.3 that $\xi(R)$ has no singularity, it is smooth, strictly positive and monotonically decaying. This result is summarized in the following Property.

Theorem 2.3.4 *Assume $R_0 > 0$, then*

$$\begin{array}{rccc} \xi: & [0,+\infty) & \longrightarrow & \left(0, \sqrt{\dfrac{3\beta}{\pi^{\frac{3}{2}}R_0^3}}\right] \\ & R & \mapsto & \xi(R) \end{array}$$

is monotone decreasing, strictly positive, and belongs to $C^\infty([0,+\infty))$.

2.3.7 Extension of the model in a non-physiological range

There is an equivalence between System (2.27) and System (2.48). More precisely, we can state the following Theorem.

Theorem 2.3.5 *Let* $P_{tot}(t) \in C^0([0,T])$ *be given. We have the following results:*

- *Let* $(A,u) \in C^1([0,T]\times[0,L])^2$ *be solution of System (2.27). If* $A>0$ *and if we define* $R=\sqrt{A}/\sqrt{\pi}$*, then* $(\boldsymbol{\Phi}(R), R\,u) \in C^1([0,T]\times[0,L])^2$ *is solution of System (2.48).*
- *Reciprocally, if* (Φ, v) *is solution of System (2.48) and if*

$$\Phi > \Phi_{min}, \tag{2.53}$$

then $(\pi\, r(\Phi)^2, v/r(\Phi))$ *is solution of System (2.27).*

Although the bound defined in (2.53) is expected physiologically, after space discretization there is no guarantee that such property holds intrinsically at any time and any point. Therefore, we propose to modify System (2.48) for a non-physiological range, *e.g.* close to $R \simeq 0$, or equivalently, $\Phi \simeq \Phi_{min}$. More precisely, $r(\Phi)$ is not defined for Φ taking smaller values than Φ_{min}. To circumvent this problem we introduce, for a given $\epsilon > 0$ – a relaxation parameter – the function r_ϵ, defined by

$$r_\epsilon(\Phi) := \begin{cases} r(\Phi) & \Phi \geq \Phi_\epsilon, \\ \\ a e^{-b\Phi} & \Phi < \Phi_\epsilon, \end{cases} \qquad \text{with} \quad \Phi_\epsilon = \Phi_{min} + \epsilon, \tag{2.54}$$

where $(a,b) \in \mathbb{R}^2$ are only defined by the constraint that $r_\epsilon \in C^1(\mathbb{R})$. In more detail, one needs to check that

$$r(\Phi_\epsilon) = a e^{-b\Phi_\epsilon}, \quad (r)'(\Phi_\epsilon) = -a\,b\,e^{-b\Phi_\epsilon},$$

hence one can compute that

$$b = -\frac{(r)'(\Phi_\epsilon)}{r(\Phi_\epsilon)} \quad \text{and then} \quad a = e^{b\Phi_\epsilon}\, r(\Phi_\epsilon).$$

The main advantage of using r_ϵ instead of r is that r_ϵ is a bijective function from $\mathbb{R}$ to $\mathbb{R}^+ \setminus \{0\}$. Hence, at the discrete level for any value of the unknown Φ we are able to compute a corresponding aortic radius R. In this process we introduce – mathematically speaking – a modeling error with respect to System (2.27). Nevertheless, we have the following straightforward result.

Theorem 2.3.6 *Let* $P_{tot}(t) \in C^0([0,T])$ *be given and* $A_\epsilon = \pi[r_\epsilon(\Phi_\epsilon)]^2$*. We have the following results:*

- *Let* $(A,u) \in C^1([0,T]\times[0,L])^2$ *be solution of System (2.27). If* $A \geq A_\epsilon$ *and if we define* $R=\sqrt{A}/\sqrt{\pi}$*, then* $(\boldsymbol{\Phi}(R), R\,u) \in C^1([0,T]\times[0,L])^2$ *is solution of System (2.48) with* r_ϵ *instead of* r*.*
- *Reciprocally, if* (Φ, v) *is solution of System (2.48) with* r_ϵ *instead of* r *and if*

$$\Phi \geq \varphi_\epsilon, \tag{2.55}$$

then $(\pi\, r_\epsilon(\Phi)^2, v/\varphi_\epsilon(\Phi))$ *is solution of System (2.27).*

Note that we can choose ϵ small enough so that the range of values $A(x,t) \in (0, A_\epsilon)$ for which the mathematical equivalence with System (2.27) is not satisfied can be set as desired. In particular, considering the application to hemodynamics, this interval can be chosen so that a solution of System (2.27) with values $A < A_\epsilon$ is outside the validity of the the tube law described in (2.2).

2.3.8 Viscosity of the wall

In Section 2.2.1 we introduced the third equation of System (2.1) that relates the pressure with the strain and strain rate of the wall. In particular, it takes into account the velocity of radial displacements [Caiazzo et al., 2017] thanks to the term ψ_v that was assumed to vanish in Section 2.3.1 in order to derive the energy-compliant variational formulation. In this section we address the treatment of this term, ψ_v, through the change of variables introduced in Section 2.3. Starting from System (2.21), we have

$$\frac{A}{\rho}\partial_s P(A) = \frac{A}{\rho}\partial_s(\psi_e(A) + \psi_v(A)) = \frac{A}{\rho}\partial_s\Big(\frac{\beta}{A_0}(\sqrt{A} - \sqrt{A_0}) + \frac{\Gamma}{A_0\sqrt{A}}\partial_t A\Big). \tag{2.56}$$

Since we have already dealt in the previous section with the first term, related to ψ_e, we focus now on the last one of the equation above, related to ψ_v. Starting from (2.56) and using the first equation of System (2.21), we obtain

$$\frac{A}{\rho}\partial_s\Big(\frac{\Gamma}{A_0\sqrt{A}}\partial_t A\Big) = -\frac{A}{\rho}\partial_s\Big(\frac{\Gamma}{A_0\sqrt{A}}\partial_s Q\Big). \tag{2.57}$$

This motivates the introduction of the non-linear form $c(\cdot;\cdot,\cdot)$ defined by

$$c(R; v, \tilde{v}) = \frac{\sqrt{\pi}\,\Gamma}{R_0^2}\int_0^L \frac{1}{R}\,\partial_s(R\tilde{v})\,\partial_s(Rv)\,\mathrm{d}s. \tag{2.58}$$

Taking into account the manipulations performed in Section 2.3.2 and Section 2.3.3, one can show that

$$-\Big(\frac{A}{\rho}\partial_s\Big(\frac{\Gamma}{A_0\sqrt{A}}\partial_s Q\Big), \rho\frac{\tilde{v}}{R}\Big) = c(R; v, \tilde{v}) + \pi\, R\,\psi_v(A)\,\tilde{v}\,\Big|_0^L. \tag{2.59}$$

Then, it can be shown that the second equation of System (2.48) can be replaced by

$$\pi\rho(\partial_t v, \tilde{v}) + \tilde{a}\Big(\tilde{v}, v, \frac{v}{R}\Big) - \pi(\partial_s(R\tilde{v}),\, \Phi\,\xi(R)) + c(R; v, \tilde{v}) + \rho K_r\Big(\frac{v}{R}, \frac{\tilde{v}}{R}\Big) = \tilde{g}(\tilde{v}, R).$$

Note that the boundary terms in (2.59) are indeed taken into account, since $\tilde{g}$ – defined in (2.41) – involves the total pressure that is given by (2.6) and now reads

$$P_{\text{tot}} = P_{\text{ext}} + \psi_e\,(A) + \psi_v\,(A) + \frac{\rho}{2}\,u^2.$$

2.3.9 Outflow conditions, inflow conditions and energy relation

In order to complete the weak formulation of the problem given in System (2.48), the outflow and inflow conditions need to be specified. This is done by expanding the term $\tilde{g}$ using the coupling condition described in (2.7) at the outlet, whereas at the inlet we use

$$P_{\text{ar}}(t) = P_{\text{tot}}(0,t) - P_{\text{ext}}, \quad \pi\, R(0,t)\, v(0,t) = Q_{\text{ar}}(t),$$

where $P_{\mathrm{ar}}(t)$ and $Q_{\mathrm{ar}}(t)$ are the arterial pressure and the arterial flow, respectively. We obtain the following system of equations:

$$\begin{cases} 2(\partial_t \Phi, \tilde{\Phi}) + \pi(\partial_s(R\,v), \tilde{\Phi}, \xi(R)) = 0, \\ \pi\rho(\partial_t v, \tilde{v}) + \tilde{a}\Big(\tilde{v}, v, \dfrac{v}{R}\Big) - \pi(\partial_s(R\tilde{v}),\, \Phi\,\xi(R)) + c(R; v, \tilde{v}) + \rho K_r\Big(\dfrac{v}{R}, \dfrac{\tilde{v}}{R}\Big) \\ \qquad\qquad = -\pi\tilde{v}(L)R(L)\big(P_c + R_c\,\pi\,R(L)\,v(L)\big) + \pi\,\tilde{v}(0)\,R(0)\,P_{\mathrm{ar}}, \\ R = r(\Phi), \\ \pi\,R(0)\,v(0) = Q_{\mathrm{ar}}, \\ C_c\dfrac{\mathrm{d}}{\mathrm{d}t}P_c + \dfrac{P_c}{R_{\mathrm{per}}} = \pi\,R(L)\,v(L). \end{cases} \tag{2.60}$$

Note that a similar energy identity to the one given in Theorem 2.2.2 can be derived for this system, as we state below.

Theorem 2.3.7 *Any smooth solution of System (2.60) satisfies the conservation property*

$$\frac{\mathrm{d}}{\mathrm{d}t}\Big(\mathcal{E}_{ar} + \mathcal{E}_w\Big) + \mathcal{D}_{ar} + \mathcal{D}_w = P_{ar}\,Q_{ar}, \tag{2.61}$$

where,

$$\mathcal{E}_{ar} = \int_0^L \Phi^2\,\mathrm{d}s + \frac{\pi\,\rho}{2}\int_0^L v^2\,\mathrm{d}s, \quad \mathcal{E}_w = \frac{C_c}{2}P_c^2,$$

and,

$$\mathcal{D}_{ar} = \rho\,K_r\int_0^L \frac{v^2}{R^2}\,\mathrm{d}s + \frac{\sqrt{\pi}\,\Gamma}{R_0^2}\int_0^L \frac{1}{R}\,(\partial_s(Rv))^2\,\mathrm{d}s, \quad \mathcal{D}_w = \frac{P_c^2}{R_{per}} + R_c(\pi\,R(L)\,v(L))^2.$$

Note that System (2.3.7) can be easily used with or without coupling with the reduced heart model. Hence, we consider two cases:

- Case 1: Imposed inlet flux;
  In this case the arterial pressure P_{ar} is considered as a new unknown, namely a Lagrange multiplier for the constraint $\pi\,R(0)\,v(0) = Q_{\mathrm{ar}}$.
- Case 2: Coupling with the reduced heart model.
  System (2.60) should then be completed with Eqs. (2.10), (2.14) and (2.17), that describe the reduced-order cardiac mechanics, the microscopic actin-myosin binding model and the valve model, respectively. Note that in this model Q_{ar} is an unknown that can be straightforwardly substituted in (2.17) using the relation $Q_{\mathrm{ar}} = \pi\,R(0)\,v(0)$.

2.4 Discretization

2.4.1 Time scheme for the blood flow model

In order to obtain the time discretization of the scheme, we assume a given sequence of time instants $\{t^n\}_{n\in\mathbb{N}}$ such that $t^{n+1} > t^n$ and we define the time step as $\Delta t_n := t^{n+1} - t^n$. Moreover, we define the half time sequence as $t^{n+\frac{1}{2}} := t^n + \Delta t_n/2$. The scheme proposed below is formally an implicit second-order time discretization scheme: we consider

System (2.48), we rewrite it at time $t^{n+1/2}$ and we approximate all the terms using a centered finite difference, i. e. for every n

$$\partial_t v(t^{n+\frac{1}{2}}) \sim \frac{v^{n+1}-v^n}{\Delta t_n}, \quad \partial_t \Phi(t^{n+\frac{1}{2}}) \sim \frac{\Phi^{n+1}-\Phi^n}{\Delta t_n}, \quad \frac{\mathrm{d}}{\mathrm{d}t}P_c \sim \frac{P_c^{n+1}-P_c^n}{\Delta t_n}$$

and

$$v(t^{n+\frac{1}{2}}) \sim \frac{v^{n+1}+v^n}{2} =: v^{n+\frac{1}{2}}, \quad \Phi(t^{n+\frac{1}{2}}) \sim \frac{\Phi^{n+1}+\Phi^n}{2} =: \Phi^{n+\frac{1}{2}},$$

$$P_c(t^{n+\frac{1}{2}}) \sim \frac{P_c^{n+1}+P_c^n}{2} =: P_c^{n+\frac{1}{2}}.$$

Moreover, as in [Chapelle et al., 2012], we introduce some intermediate unknowns, i.e. $R^{n+\frac{1}{2}\sharp}$ and $\xi^{n+\frac{1}{2}\sharp}$, as follows :

$$R(t^{n+\frac{1}{2}}) \sim R^{n+\frac{1}{2}\sharp} := r(\Phi^{n+\frac{1}{2}}), \quad \xi(t^{n+\frac{1}{2}}) \sim \xi^{n+\frac{1}{2}\sharp} := \xi(R^{n+\frac{1}{2}\sharp}).$$

With these considerations, we obtain the following semi-discrete problem

$$\begin{cases} 2\Big(\dfrac{\Phi^{n+1}-\Phi^n}{\Delta t_n}, \tilde{\Phi}\Big) + \pi\left(\partial_s(R^{n+\frac{1}{2}\sharp}v^{n+\frac{1}{2}}), \tilde{\Phi}\,\xi^{n+\frac{1}{2}}\right) = 0, \\ \pi\rho\Big(\dfrac{v^{n+1}-v^n}{\Delta t_n}, \tilde{v}\Big) + \tilde{a}\Big(\tilde{v}, v^{n+\frac{1}{2}}, \dfrac{v^{n+\frac{1}{2}}}{R^{n+\frac{1}{2}\sharp}}\Big) - \pi\Big(\partial_s(R^{n+\frac{1}{2}\sharp}\tilde{v}), \Phi^{n+\frac{1}{2}}\,\xi^{n+\frac{1}{2}}\Big) \\ \qquad +c(R^{n+\frac{1}{2}\sharp}; v^{n+\frac{1}{2}}, \tilde{v}) + \rho K_r\Big(\dfrac{v^{n+\frac{1}{2}}}{R^{n+\frac{1}{2}\sharp}}, \dfrac{\tilde{v}}{R^{n+\frac{1}{2}\sharp}}\Big) = \pi\,\tilde{v}(0)\,R^{n+\frac{1}{2}\sharp}(0)\,P_{\mathrm{ar}}^{n+\frac{1}{2}} \\ \qquad -\pi\,\tilde{v}(L)R^{n+\frac{1}{2}\sharp}(L)\left(P_c^{n+\frac{1}{2}} + R_c\,\pi\,R^{n+\frac{1}{2}\sharp}(L)\,v^{n+\frac{1}{2}}(L)\right), \\ R^{n+\frac{1}{2}\sharp} = r(\Phi^{n+\frac{1}{2}}), \\ \xi^{n+\frac{1}{2}\sharp} = \xi(R^{n+\frac{1}{2}\sharp}), \\ \pi\,R^{n+\frac{1}{2}\sharp}(0)\,v^{n+\frac{1}{2}}(0) = Q_{\mathrm{ar}}^{n+\frac{1}{2}\sharp}, \\ C_c\dfrac{P_c^{n+1}-P_c^n}{\Delta t_n} + \dfrac{P_c^{n+\frac{1}{2}}}{R_{\mathrm{per}}} = \pi\,R^{n+\frac{1}{2}\sharp}(L)\,v^{n+\frac{1}{2}}(L). \end{cases} \tag{2.62}$$

In (2.62) the terms $Q_{\mathrm{ar}}^{n+\frac{1}{2}\sharp}$ and $P_{\mathrm{ar}}^{n+\frac{1}{2}}$ are not completely characterized yet. These quantities appear below when considering the time discretization of the valve model.
Once (2.62) is obtained, we have to check if the semi-discrete scheme preserves the total energy, as given in Section 2.3.9 for the continuous domain. This is the purpose of the following Section. Energy preservation can be proven rather simply by following the strategy performed at the continuous level. We substitute the test functions with the proper variables as explained in Section 2.3.3. More precisely, we set

$$\tilde{v} = v^{n+\frac{1}{2}}, \quad \tilde{\Phi} = \Phi^{n+\frac{1}{2}}.$$

We observe that

$$\Big(\frac{\Phi^{n+1}-\Phi^n}{\Delta t_n}, \Phi^{n+\frac{1}{2}}\Big) = \frac{1}{2}\frac{\|\Phi^{n+1}\|^2 - \|\Phi^n\|^2}{\Delta t_n},$$

where, by definition $\|u\|^2 = (u,u)$ is the $L^2(0,L)$-norm. Identically, we have

$$\Big(\frac{v^{n+1}-v^n}{\Delta t_n}, v^{n+\frac{1}{2}}\Big) = \frac{1}{2}\frac{\|v^{n+1}\|^2 - \|v^n\|^2}{\Delta t_n}.$$

The first two equations of System (2.62) become

$$\begin{cases} \dfrac{\|\Phi^{n+1}\|^2 - \|\Phi^n\|^2}{\Delta t_n} + \pi\,(\partial_s(R^{n+\frac{1}{2}\sharp}v^{n+\frac{1}{2}}),\, \Phi^{n+\frac{1}{2}}\,\xi^{n+\frac{1}{2}}) = 0, \\ \dfrac{\pi\rho}{2}\dfrac{\|v^{n+1}\|^2 - \|v^n\|^2}{\Delta t_n} + \tilde{a}\Big(v^{n+\frac{1}{2}}, v^{n+\frac{1}{2}}, \dfrac{v^{n+\frac{1}{2}}}{R^{n+\frac{1}{2}\sharp}}\Big) \\ \qquad -\pi(\partial_s(R^{n+\frac{1}{2}\sharp}v^{n+\frac{1}{2}}),\, \Phi^{n+\frac{1}{2}}\,\xi^{n+\frac{1}{2}}) + c(R^{n+\frac{1}{2}\sharp}; v^{n+\frac{1}{2}}, v^{n+\frac{1}{2}}) \\ \qquad\qquad +\rho K_r\Big(\dfrac{v^{n+\frac{1}{2}}}{R^{n+\frac{1}{2}\sharp}}, \dfrac{v^{n+\frac{1}{2}}}{R^{n+\frac{1}{2}\sharp}}\Big) = \text{ boundary terms.} \end{cases} \tag{2.63}$$

Now, we can observe that the second term of the continuity equation and the third term of the momentum equation are equal (up to a change of sign). Thus, the latter can be substituted with $(\|\Phi^{n+1}\|^2 - \|\Phi^n\|^2)/\Delta t_n$, which gives

$$\begin{aligned} &\frac{\pi\rho}{2}\frac{\|v^{n+1}\|^2 - \|v^n\|^2}{\Delta t_n} + \frac{\|\Phi^{n+1}\|^2 - \|\Phi^n\|^2}{\Delta t_n} + \tilde{a}\Big(v^{n+\frac{1}{2}}, v^{n+\frac{1}{2}}, \frac{v^{n+\frac{1}{2}}}{R^{n+\frac{1}{2}\sharp}}\Big) \\ &\quad + c(R^{n+\frac{1}{2}\sharp}; v^{n+\frac{1}{2}}, v^{n+\frac{1}{2}}) + \rho K_r\Big(\frac{v^{n+\frac{1}{2}}}{R^{n+\frac{1}{2}\sharp}}, \frac{v^{n+\frac{1}{2}}}{R^{n+\frac{1}{2}\sharp}}\Big) = \text{ boundary terms.} \end{aligned} \tag{2.64}$$

The equation above can be further simplified by noticing that

$$\tilde{a}(v^{n+\frac{1}{2}}, v^{n+\frac{1}{2}}, v^{n+\frac{1}{2}}/R^{n+\frac{1}{2}\sharp}) = 0,$$

thanks to (2.39). Then, we can define,

$$\mathcal{E}^n_{\text{ar}} = \frac{\pi\rho}{2}\|v^n\|^2 + \|\Phi^n\|^2, \quad \mathcal{E}^n_{\text{w}} = \frac{C_c}{2}(P^n_c)^2,$$

and,

$$\mathcal{D}^{n+\frac{1}{2}}_{\text{ar}} = \rho K_r\Big\|\frac{v^{n+\frac{1}{2}}}{R^{n+\frac{1}{2}\sharp}}\Big\|^2 + \frac{\sqrt{\pi}\,\Gamma}{R_0^2}\Big\|\frac{1}{\sqrt{R^{n+\frac{1}{2}\sharp}}}\partial_s(R^{n+\frac{1}{2}\sharp}v^{n+\frac{1}{2}})\Big\|^2,$$

$$\mathcal{D}^{n+\frac{1}{2}}_{\text{w}} = \frac{(P_c^{n+\frac{1}{2}})^2}{R_{\text{per}}} + R_c(\pi\,R^{n+\frac{1}{2}\sharp}(L)\,v^{n+\frac{1}{2}}(L))^2, \tag{2.65}$$

and prove, by using a telescopic sum and by adequately dealing with the boundary terms, a semi-discrete equivalent form of (2.61), showing that Theorem 2.3.7 has a counterpart at the semi-discrete level.

Theorem 2.4.1 *Any solution of System (2.62) satisfies the following conservation property for all $n \in \mathbb{N}$,*

$$\frac{\mathcal{E}^{n+1}_{ar} - \mathcal{E}^n_{ar}}{\Delta t_n} + \frac{\mathcal{E}^{n+1}_{w} - \mathcal{E}^n_{w}}{\Delta t_n} + \mathcal{D}^{n+\frac{1}{2}}_{ar} + \mathcal{D}^{n+\frac{1}{2}}_{w} = P^{n+\frac{1}{2}}_{ar}\,Q^{n+\frac{1}{2}\sharp}_{ar}. \tag{2.66}$$

Note that the energy relation obtained in Theorem 2.4.1 holds with a time step that may vary between each iteration. This property is fundamental since, in practice, cardiac models often adapt the time step to deal with the abrupt changes of phase due the opening and closure of the aortic valve.

2.4.2 Time scheme for the heart model

The discretization of the heart model was performed following a similar approach to the one described in the previous section. This allows to obtain, as for the arterial model, a discrete equivalent of the conservation property described in Section 2.2.2. The time discretization method used in [Chapelle et al., 2012] is adapted to the zero-dimensional formulation of the cavity with the additional introduction of the so-called Hilber-Hughes-Taylor (HHT) Method scheme proposed in [Hauret and Le Tallec, 2006] for the treatment of kinetics variables and inertial terms. The discrete velocity $\dot{y}^n$ and the displacement y^n are related by the use of an auxiliary variable $\ddot{y}^n$ – that stands for an approximation of the acceleration. We proceed discretizing the equations of System (2.10) at time $t^{n+\frac{1}{2}}$ except for the ventricular, atrial and arterial pressures that are interpolated using a θ-scheme ($P_v^{n+\theta} = (1-\theta)P_v^n + \theta P_v^{n+1},\ \theta \in [0,1]$). Deviations from the classical implicit mid-point scheme used in Section 2.4.1 are introduced to generate controlled numerical dissipation terms that damp out purely numerical high frequencies modes that cannot be properly resolved with a finite time step – see also Section 2.5.1.2. The HHT kinematics equations are

$$\begin{cases} \dfrac{\dot{y}^{n+1} - \dot{y}^n}{\Delta t_n} = \ddot{y}^{n+\frac{1}{2}} + \alpha \Delta t_n \dfrac{\ddot{y}^{n+1} - \ddot{y}^n}{\Delta t_n}, \\ \dfrac{y^{n+1} - y^n}{\Delta t_n} = \dot{y}^{n+\frac{1}{2}} + \dfrac{\alpha^2}{4} \Delta t_n^2 \dfrac{\ddot{y}^{n+1} - \ddot{y}^n}{\Delta t_n}. \end{cases} \tag{2.67}$$

and the dynamics equations then read

$$\begin{cases} \rho_0 \left|\Omega_0\right| \left(\dfrac{\dot{y}^{n+1} - \dot{y}^n}{\Delta t_n}\right) + \dfrac{\left|\Omega_0\right|}{R_0} k_s \left(\dfrac{y^{n+\frac{1}{2}}}{R_0} - e_c^{n+\frac{1}{2}}\right) \\ \qquad\qquad + \Lambda_{\text{hyp}}^{n+\frac{1}{2}\sharp} + \mathcal{W}_v\left(y^{n+\frac{1}{2}}, \dfrac{y^{n+1} - y^n}{\Delta t_n}\right) = P_v^{n+\theta} S^{n+\frac{1}{2}\sharp}, \\ \mu \dfrac{e_c^{n+1} - e_c^n}{\Delta t_n} - k_s \left(\dfrac{y^{n+\frac{1}{2}}}{R_0} - e_c^{n+\frac{1}{2}}\right) = -\tau_c^{n+\frac{1}{2}\sharp}, \end{cases} \tag{2.68}$$

where we use the adapted [Gonzalez, 2000] energy-preserving non-linear choice

$$\Lambda_{\text{hyp}}^{n+\frac{1}{2}\sharp} = \begin{cases} \dfrac{\mathcal{W}_p(y^{n+1}) - \mathcal{W}_p(y^n)}{y^{n+1} - y^n} & \text{if } y^{n+1} \neq y^n, \\ \dfrac{\partial \mathcal{W}_p}{\partial y}(y^{n+\frac{1}{2}}) & \text{if } y^{n+1} = y^n = y^{n+\frac{1}{2}}, \end{cases}$$

and additionally

$$S^{n+\frac{1}{2}\sharp} = \begin{cases} \dfrac{V(y^{n+1}) - V(y^n)}{y^{n+1} - y^n} & \text{if } y^{n+1} \neq y^n, \\ \dfrac{\partial V}{\partial y}(y^{n+\frac{1}{2}}) & \text{if } y^{n+1} = y^n = y^{n+\frac{1}{2}}. \end{cases}$$

Note that in practice, the expressions for $y^{n+1} \neq y^n$ are implemented using a series development of $\mathcal{W}_p$ and V, respectively, to avoid numerical rounding errors. Further, $\tau_c^{n+\frac{1}{2}\sharp}$ is computed from the already proposed energy-balanced time discretization of System (2.14)

and (2.16) [Chapelle et al., 2012], namely

$$\tau_c^{n+\frac{1}{2}\sharp} = \sqrt{k_c^{n+1}}\lambda_c^{n+\frac{1}{2}} \text{ with}$$
$$\begin{cases} \dfrac{k_c^{n+1}-k_c^n}{\Delta t_n} = -\Big(|\nu^{n+1}| + \alpha\Big|\dfrac{e_c^{n+1}-e_c^n}{\Delta t_n}\Big|\Big)k_c^{n+1} \\ \qquad\qquad + n_0(e_c^n)k_0|\nu^{n+1}|_+ \\ \dfrac{\lambda_c^{n+1}-\lambda_c^n}{\Delta t_n} = -\dfrac{1}{2}\Big(|\nu^{n+1}| + \alpha\Big|\dfrac{e_c^{n+1}-e_c^n}{\Delta t_n}\Big|\Big)\lambda_c^{n+\frac{1}{2}} \\ \quad + \dfrac{n_0(e_c^n)}{\sqrt{k_c^{n+1}}}\left(\sigma_0 - \dfrac{k_0\,\lambda_c^{n+\frac{1}{2}}}{2\sqrt{k_c^{n+1}}}\right)|\nu^{n+1}|_+ + \sqrt{k_c^{n+1}}\dfrac{e_c^{n+1}-e_c^n}{\Delta t_n}. \end{cases} \tag{2.69}$$

Since the function $n_0(\cdot)$ has maximum value 1, it is straightforward to prove [Chapelle et al., 2012], from backward Euler time discretization, the a priori bound $0 < k_c^n \leq k_0$ for all $n \geq 1$ if it is satisfied at $n = 0$. Moreover, the time discretization of the variable λ^n is consistent with the dynamics of $\lambda_c = \tau_c/\sqrt{k_c}$ given in Remark 2.2.5.
In order to retrieve a discrete equivalent of the discrete energy balance obtained in Section 2.2.2, we multiply the second equation of System (2.68) by $(y^{n+1}-y^n)/\Delta t$ and the third one by $|\Omega_0|\,(e_c^{n+1}-e_c^n)/\Delta t_n$, then we sum, obtaining

$$\frac{\mathcal{E}_{\text{hr}}^{n+1}-\mathcal{E}_{\text{hr}}^n}{\Delta t_n} + \frac{\mathcal{E}_{\text{hr,num}}^{n+1}-\mathcal{E}_{\text{hr,num}}^n}{\Delta t_n} + \mathcal{D}_{\text{hr}}^{n+\frac{1}{2}} + \mathcal{D}_{\text{hr,num}}^{n+\frac{1}{2}\sharp} = -|\Omega_0|\,\frac{e_c^{n+1}-e_c^n}{\Delta t_n}\,\tau_c^{n+\frac{1}{2}\sharp} + P_v^{n+\theta}\frac{V(y^{n+1})-V(y^n)}{\Delta t_n}, \tag{2.70}$$

where we have introduced the discrete energy

$$\mathcal{E}_{\text{hr}}^n := \frac{\rho_0|\Omega_0|}{2}(\dot{y}^n)^2 + \mathcal{W}_p(y^n) + \frac{|\Omega_0|k_s}{2}\left(\frac{y^n}{R_0} - e_c^n\right)^2, \tag{2.71}$$

the discrete dissipation term

$$\mathcal{D}_{\text{hr}}^{n+\frac{1}{2}} := \mathcal{W}_v\left(y^{n+\frac{1}{2}}, \frac{y^{n+1}-y^n}{\Delta t_n}\right)\frac{y^{n+1}-y^n}{\Delta t_n} + \mu\,|\Omega_0|\left(\frac{e_c^{n+1}-e_c^n}{\Delta t_n}\right)^2, \tag{2.72}$$

as well as a numerical stored energy

$$\mathcal{E}_{\text{hr,num}}^n := \alpha^2\Delta t_n^2\frac{\rho_0|\Omega_0|}{8}(\ddot{y}^n)^2 \tag{2.73}$$

and a numerical dissipated energy

$$\mathcal{D}_{\text{hr,num}}^{n+\frac{1}{2}\sharp} := \alpha^3\Delta t_n^3\frac{\rho_0|\Omega_0|}{4}\left(\frac{\ddot{y}^{n+1}-\ddot{y}^n}{\Delta t_n}\right)^2, \tag{2.74}$$

which scale both with powers of Δt_n. Moreover, multiplying the second equation of (2.69) by $|\Omega_0|\,\lambda_c^{n+\frac{1}{2}}$ we obtain

$$\frac{\mathcal{E}_c^{n+1}-\mathcal{E}_c^n}{\Delta t_n} + \mathcal{D}_c^{n+\frac{1}{2}} = \frac{|\Omega_0|\,n_0(e_c^n)}{\sqrt{k_c^{n+1}}}\left(\sigma_0\lambda_c^{n+\frac{1}{2}} - \frac{k_0\,(\lambda_c^{n+\frac{1}{2}})^2}{2\sqrt{k_c^{n+1}}}\right)|\nu^{n+1}|_+ + |\Omega_0|\,\frac{e_c^{n+1}-e_c^n}{\Delta t_n}\,\tau_c^{n+\frac{1}{2}\sharp}, \tag{2.75}$$

with

$$\mathcal{E}_c^n := \frac{|\Omega_0|}{2}(\lambda_c^n)^2, \quad \mathcal{D}_c^{n+\frac{1}{2}} := \left(|\nu^{n+1}| + \alpha\left|\frac{e_c^{n+1}-e_c^n}{\Delta t_n}\right|\right)\frac{|\Omega_0|}{2}\,(\lambda_c^{n+\frac{1}{2}})^2. \tag{2.76}$$

Note that (2.71), (2.72) and (2.76) are the time-discrete equivalent of (2.11), (2.12) and (2.13) respectively. Summing (2.70) and (2.75), we obtain the following result.

Theorem 2.4.2 *Any solution of System* (2.68) *and System* (2.69) *satisfies the following conservation property for all* $n \in \mathbb{N}$:

$$\begin{aligned}\frac{\mathcal{E}_{hr}^{n+1}-\mathcal{E}_{hr}^n}{\Delta t_n} + \frac{\mathcal{E}_c^{n+1}-\mathcal{E}_c^n}{\Delta t_n} + \mathcal{D}_{hr}^{n+\frac{1}{2}} + \mathcal{D}_c^{n+\frac{1}{2}} &= P_v^{n+\theta}\frac{V(y^{n+1})-V(y^n)}{\Delta t_n} \\ &+ \frac{|\Omega_0|\,n_0(e_c^n)}{\sqrt{k_c^{n+1}}}\left(\sigma_0\lambda_c^{n+\frac{1}{2}} - \frac{k_0\,(\lambda_c^{n+\frac{1}{2}})^2}{2\sqrt{k_c^{n+1}}}\right)|\nu^{n+1}|_+. \end{aligned}\tag{2.77}$$

2.4.3 Time scheme for the valves and the energy relation for the complete semi-discrete system

The discretization strategy applied for the valve formulation is the same that we showed for the arterial and ventricular model. In particular, we use an implicit mid-point rule, i.e.

$$-\frac{\mathrm{d}}{\mathrm{d}t}(v(y)) = Q_v \sim -\frac{V(y^{n+1})-V(y^n))}{\Delta t_n},$$

and

$$Q_{\mathrm{ar}} \sim Q_{\mathrm{ar}}^{n+\frac{1}{2}\sharp} = \pi\, R^{n+\frac{1}{2}\sharp}\, v^{n+\frac{1}{2}}, \qquad \frac{|P_v - P_{\mathrm{ar}}|_+}{K_{\mathrm{ar}}} \sim \frac{|P_v^{n+\theta} - P_{\mathrm{ar}}^{n+\frac{1}{2}}|_+}{K_{\mathrm{ar}}}.$$

System (2.17) is then discretized as follows:

$$\begin{cases} C_{\mathrm{mi}}\dfrac{P_v^{n+1}-P_v^n}{\Delta t_n} + \dfrac{|P_v^{n+\theta}-P_{\mathrm{ar}}^{n+\frac{1}{2}}|_+}{K_{\mathrm{ar}}} \\ \qquad + \dfrac{|P_v^{n+\theta}-P_{\mathrm{at}}^{n+\frac{1}{2}}|_+}{K_{\mathrm{iso}}} - \dfrac{|P_{\mathrm{at}}^{n+\frac{1}{2}}-P_v^{n+\theta}|_+}{K_{\mathrm{at}}} = -\dfrac{V(y^{n+1})-V(y^n))}{\Delta t_n}, \\ C_{\mathrm{ar}}\dfrac{P_{\mathrm{ar}}^{n+1}-P_{\mathrm{ar}}^n}{\Delta t_n} - \dfrac{|P_v^{n+\theta}-P_{\mathrm{ar}}^{n+\frac{1}{2}}|_+}{K_{\mathrm{ar}}} = -Q_{\mathrm{ar}}^{n+\frac{1}{2}\sharp}. \end{cases} \tag{2.78}$$

To obtain an energy identity we multiply the first equation of System (2.78) by $P_v^{n+\theta}$ and the second one by $P_{\mathrm{ar}}^{n+\frac{1}{2}}$, then we sum the two equations. The discrete conservation property reads

$$\begin{aligned}\frac{\mathcal{E}_v^{n+1}-\mathcal{E}_v^n}{\Delta t_n} + \mathcal{D}_v^{n+\theta} + \mathcal{D}_{v,\mathrm{num}}^{n+\frac{1}{2}\sharp} &= \frac{|P_{\mathrm{at}}^{n+\frac{1}{2}} - P_v^{n+\theta}|_+\, P_{\mathrm{at}}^{n+\frac{1}{2}}}{K_{\mathrm{at}}} \\ &- \frac{|P_v^{n+\theta}-P_{\mathrm{at}}^{n+\frac{1}{2}}|_+\, P_{\mathrm{at}}^{n+\frac{1}{2}}}{K_{\mathrm{iso}}} - P_v^{n+\theta}\frac{V(y^{n+1})-V(y^n)}{\Delta t_n} - P_{\mathrm{ar}}^{n+\frac{1}{2}}\,Q_{\mathrm{ar}}^{n+\frac{1}{2}\sharp}, \end{aligned}\tag{2.79}$$

where the discrete energy for the valve model reads

$$\frac{\mathcal{E}_v^{n+1}-\mathcal{E}_v^n}{\Delta t_n} = \frac{C_{\mathrm{mi}}}{2}\frac{(P_v^{n+1})^2-(P_v^n)^2}{\Delta t_n} + \frac{C_{\mathrm{ar}}}{2}\frac{(P_{\mathrm{ar}}^{n+1})^2-(P_{\mathrm{ar}}^n)^2}{\Delta t_n},$$

the dissipation is

$$\mathcal{D}_v^{n+\theta} = \frac{|P_v^{n+\theta} - P_{\text{ar}}^{n+\frac{1}{2}}|_+^2}{K_{\text{ar}}} + \frac{|P_v^{n+\theta} - P_{\text{at}}^{n+\frac{1}{2}}|_+^2}{K_{\text{iso}}} + \frac{|P_{\text{at}}^{n+\frac{1}{2}} - P_v^{n+\theta}|_+^2}{K_{\text{at}}},$$

and the numerical dissipation reads

$$\mathcal{D}_{v,\text{num}}^{n+\frac{1}{2}\sharp} = \big(\theta - \frac{1}{2}\big) C_{\text{mi}} \Delta t_n \Big(\frac{P_v^{n+1} - P_v^n}{\Delta t_n} \Big)^2.$$

Finally, summing Eqs. (2.64), (2.77) and (2.79)), we obtain the semi-discrete conservation property for the global system.

Corollary 2.4.2.1 *Any solution of System* (2.62), (2.68),(2.69) *and* (2.78)*) satisfies the following conservation property for all* $n \in \mathbb{N}$,

$$\begin{aligned}
&\frac{\mathcal{E}_{ar}^{n+1} - \mathcal{E}_{ar}^n}{\Delta t_n} + \frac{\mathcal{E}_w^{n+1} - \mathcal{E}_w^n}{\Delta t_n} + \frac{\mathcal{E}_{hr}^{n+1} - \mathcal{E}_{hr}^n}{\Delta t_n} + \frac{\mathcal{E}_{hr,num}^{n+1} - \mathcal{E}_{hr,num}^n}{\Delta t_n} + \frac{\mathcal{E}_v^{n+1} - \mathcal{E}_v^n}{\Delta t_n} \\
&\qquad + \mathcal{D}_w^{n+\frac{1}{2}} + \mathcal{D}_{hr}^{n+\frac{1}{2}} + \mathcal{D}_{hr,num}^{n+\frac{1}{2}\sharp} + \mathcal{D}_{ar}^{n+\frac{1}{2}} + \mathcal{D}_v^{n+\frac{1}{2}} + \mathcal{D}_{v,num}^{n+\frac{1}{2}\sharp} \\
&\qquad = \frac{|\Omega_0|\, n_0(e_c^n)}{\sqrt{k_c^{n+1}}} \left(\sigma_0 \lambda_c^{n+\frac{1}{2}} - \frac{k_0\, (\lambda_c^{n+\frac{1}{2}})^2}{2\sqrt{k_c^{n+1}}} \right) |\nu^{n+1}|_+ \\
&\qquad + \frac{|P_{at}^{n+\frac{1}{2}} - P_v^{n+\theta}|_+\, P_{at}^{n+\frac{1}{2}}}{K_{at}} - \frac{|P_v^{n+\theta} - P_{at}^{n+\frac{1}{2}}|_+\, P_{at}^{n+\frac{1}{2}}}{K_{iso}}.
\end{aligned} \tag{2.80}$$

Corollary 2.4.2.1 shows that without a source term, i.e when ν^{n+1} and $P_{\text{at}}^{n+\frac{1}{2}}$ vanish, the energy – that is a norm for the solution – is decaying. This is the expected stability property of a robust time discretization.

2.4.4 Space discretization of the blood flow model

The space discretization is rather simple and does not represent a main issue for the global formulation. However, there are some terms, in the aortic model formulation, that have to be treated carefully when choosing the space discretization method. This is the reason why, in this section, we will only present the space discretization of the arterial model without dealing with how the total discretization of the aorta model couples with the other elements of the model. Indeed, these couplings are straightforward from what has been already explained.

First, we introduce a finite dimensional subspace of $H^1(0, L)$ of continuous functions that is denoted by V_h and we assume an interpolation operator $\mathcal{I}_h : C^0([0, L]) \to V_h$ as given. For each $n \in \mathbb{N}$, we look for the solutions $(\Phi_h^n, v_h^n) \in V_h \times V_h$, for all $(\tilde{\Phi}_h, \tilde{v}_h) \in V_h \times V_h$,

of

$$
\begin{cases}
2\Big(\dfrac{\Phi_h^{n+1}-\Phi_h^n}{\Delta t_n},\tilde{\Phi}_h\Big)_h+\pi\,(\partial_s(R_h^{n+\frac{1}{2}\sharp}v_h^{n+\frac{1}{2}}),\,\tilde{\Phi}_h\,\xi_h^{n+\frac{1}{2}})_h=0,\\
\pi\rho\Big(\dfrac{v_h^{n+1}-v_h^n}{\Delta t_n},\tilde{v}_h\Big)_h+a_h(v_h^{n+\frac{1}{2}},R_h^{n+\frac{1}{2}\sharp};\tilde{v}_h)\\
\quad-\pi(\partial_s(R_h^{n+\frac{1}{2}\sharp}\tilde{v}_h),\,\Phi_h^{n+\frac{1}{2}}\,\xi_h^{n+\frac{1}{2}})_h+c_h(R_h^{n+\frac{1}{2}\sharp},v_h^{n+\frac{1}{2}},\tilde{v}_h)+\rho K_r(u_h^{n+\frac{1}{2}},\tilde{u}_h)_h\\
\quad=\quad\text{boundary terms},\\
R_h^{n+\frac{1}{2}\sharp}=\mathcal{I}_h\,r(\Phi_h^{n+\frac{1}{2}}),\\
\xi_h^{n+\frac{1}{2}\sharp}=\mathcal{I}_h\,\xi(R_h^{n+\frac{1}{2}\sharp}),\\
u_h^{n+\frac{1}{2}}=\mathcal{I}_h\,\dfrac{v_h^{n+\frac{1}{2}}}{R_h^{n+\frac{1}{2}\sharp}},\\
\tilde{u}_h=\mathcal{I}_h\,\dfrac{\tilde{v}_h}{R_h^{n+\frac{1}{2}\sharp}}.
\end{cases}
\tag{2.81}
$$

In the equations above the missing boundary terms are easily deduced from the second equation of System (2.62) by replacing $R^{n+\frac{1}{2}\sharp}$ by $R_h^{n+\frac{1}{2}\sharp}$, v by v_h and $\tilde{v}$ by $\tilde{v}_h$. Moreover, we have introduced two other notations:

i) We use the notation $(\cdot,\cdot)_h$ to represent an approximation of the scalar product in $L^2(0,L)$ by quadrature formulae. In particular $(\cdot,\cdot)_h$ is a positive definite bilinear form and is equivalent to the $L^2(0,L)$-norm in V_h. In what follows, for any $u_h\in V_h$ we define $\|u_h\|_h^2:=(u_h,u_h)_h$.

ii) The critical point from the energetic point of view in performing the space discretization of our scheme can be found in the definition of the term a_h. As stated in Section 2.4.1 for the energy conservation, this term has to satisfy the property defined in (2.39). One way to guarantee this condition is to consider the exact – i.e. we compute the integrals exactly – trilinear form $\tilde{a}$. That is why the form a_h is defined by

$$
a_h(v_h^{n+\frac{1}{2}},R_h^{n+\frac{1}{2}\sharp};\tilde{v}_h):=\tilde{a}(\tilde{v}_h,v_h^{n+\frac{1}{2}},u_h^{n+\frac{1}{2}}).
\tag{2.82}
$$

With this definition and thanks to (2.39), it is possible to check that, for all $(v_h,R_h)\in V_h\times V_h$,

$$
a_h(v_h,R_h;v_h)=\tilde{a}\Big(v_h,v_h,\mathcal{I}_h\,\frac{v_h}{R_h}\Big)=0.
\tag{2.83}
$$

Even though the introduction of the interpolation operator in the definition of $u_h^{n+\frac{1}{2}}$ involved in a_h given by (2.82) seems unnecessary, one can observe from the structure of the trilinear form $\tilde{a}$ that its last argument would not be polynomial without interpolation. This implies that the application of a standard quadrature method (*e.g.* the Gauss integration) would not give an exact integration property, and therefore the property stated by (2.83) may be lost.

Using (2.83), it is straightforward to prove that the energy relation stated in Theorem 2.4.1 can be extended to the fully-discrete case. We obtain the following result.

Theorem 2.4.3 *Any solution of System (2.62) satisfies the following conservation property for all* $n \in \mathbb{N}$

$$\frac{\mathcal{E}_h^{n+1} - \mathcal{E}_h^n}{\Delta t_n} + \mathcal{D}_h^{n+\frac{1}{2}} = \tilde{g}(v_h^{n+\frac{1}{2}}, R_h^{n+\frac{1}{2}\sharp}),$$

with

$$\mathcal{E}_h^n = \frac{\pi\rho}{2}\|v^n\|_h^2 + \|\Phi^n\|_h^2,$$

$$\mathcal{D}_h^{n+\frac{1}{2}} = \rho K_r \left\| \mathcal{I}_h \frac{v_h^{n+\frac{1}{2}}}{R_h^{n+\frac{1}{2}\sharp}} \right\|_h^2 + \frac{\sqrt{2}\Gamma}{R_0^2} \left\| \frac{1}{\sqrt{R_h^{n+\frac{1}{2}\sharp}}} \partial_s (R_h^{n+\frac{1}{2}\sharp} v_h^{n+\frac{1}{2}}) \right\|_h^2. \quad (2.84)$$

When using the model described for simulations we divide the domain $[0, L]$ into regular subdomains $\ell_j = [s_j, s_{j+1}]$ of fixed length Δs, such that $s_j = j\Delta s$ with $j = \{0, 1, \dots, J\}$. In particular, we define the space V_h as

$$V_h = \{v_h \in C^0([0, L]) \,/\, \forall j \in \{0, 1, \dots, J\} \in v_h|_{\ell_j} \in \mathbb{P}_1(\ell_j)\},$$

and we use $\mathbb{P}_1$-finite elements. The space V_h is spanned by the Lagrange nodal basis functions $\{w_j\}_{j=0}^J$ that satisfy the property $w_j(s_i) = \delta_{ij}$. The interpolation operator then reads

$$(\mathcal{I}_h v)(s) = \sum_{j=0}^{J} v(s_j) w_j(s).$$

We have, for all $(v_h, u_h) \in V_h \times V_h$,

$$(v_h, u_h)_h = \frac{\Delta s}{2} v_h(s_0) u_h(s_0) + \Delta s \sum_{j=1}^{J-1} v_h(s_j) u_h(s_j) + \frac{\Delta s}{2} v_h(s_J) u_h(s_J).$$

The scalar product $(\cdot, \cdot)_h$ is defined using the trapezoidal rule, while the term $\tilde{a}(\tilde{v}_h, v_h, u_h)$ should be computed exactly to ensure energy preservation. To do so, it is sufficient to use the Simpson quadrature method in each element for the underlying integration, since – thanks to the use of the interpolation operator – the integrand is a second-order polynomial in each element.

2.5 Simulations and numerical results

In order to show the results of our work, we consider three different model settings:

- The *uncoupled aortic model* is composed by a single 1D straight vessel with a homogeneous circular cross-section representing the upper thoracic aorta and by a Windkessel RCR model that takes into account the impedance and compliance of all the remaining vessels at the periphery. In this test case the inlet blood flow is imposed, as shown in Figure 2.4. This configuration allows us to study the behavior of the arterial model alone.
- The *uncoupled cardiac model*, depicted in Figure 2.5, is composed by the reduced cardiac model described in the previous sections and by a lumped parameter model as outlet boundary condition that represents the entire circulation. More precisely, we have reduced the 1D model of the aorta into an RC-model, the parameters of the resulting 0D model being the equivalent resistance and compliance of the 1D vessel combined with the RCR boundary model parameters. The equivalent resistance and

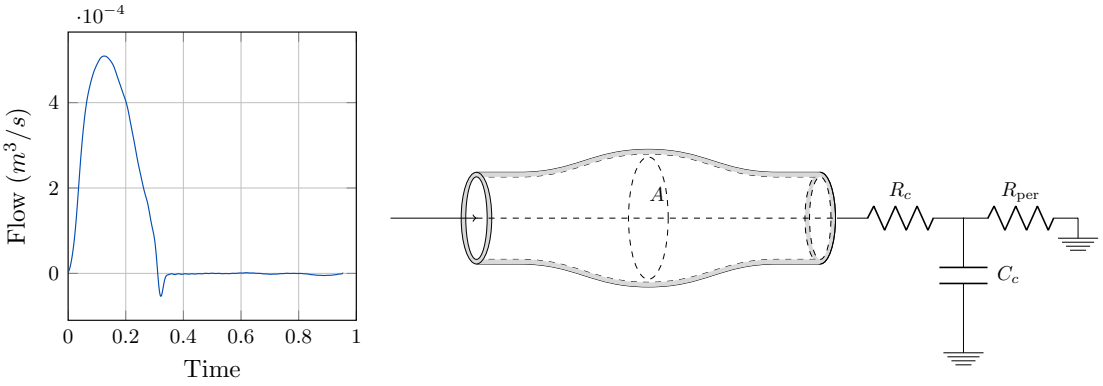

Figure 2.4 – Scheme of the *uncoupled aortic model*: single 1D vessel that represents the upper thoracic aorta and a three-element Windkessel model as boundary conditions to represent the remaining part of the circulation.

compliance of the 1D vessel are obtained by (formulas readapted from [Epstein et al., 2015])

$$R_{1\text{D}} = \frac{22\mu_b L}{\pi R_0^4} \qquad \text{and} \qquad C_{1\text{D}} = \frac{3}{2}\frac{\pi R_0^3 L}{E h_0}, \tag{2.85}$$

where μ_b is the blood viscosity. This setting allows to show the outcome of the cardiovascular model when the circulation is represented by a simple Windkessel model.

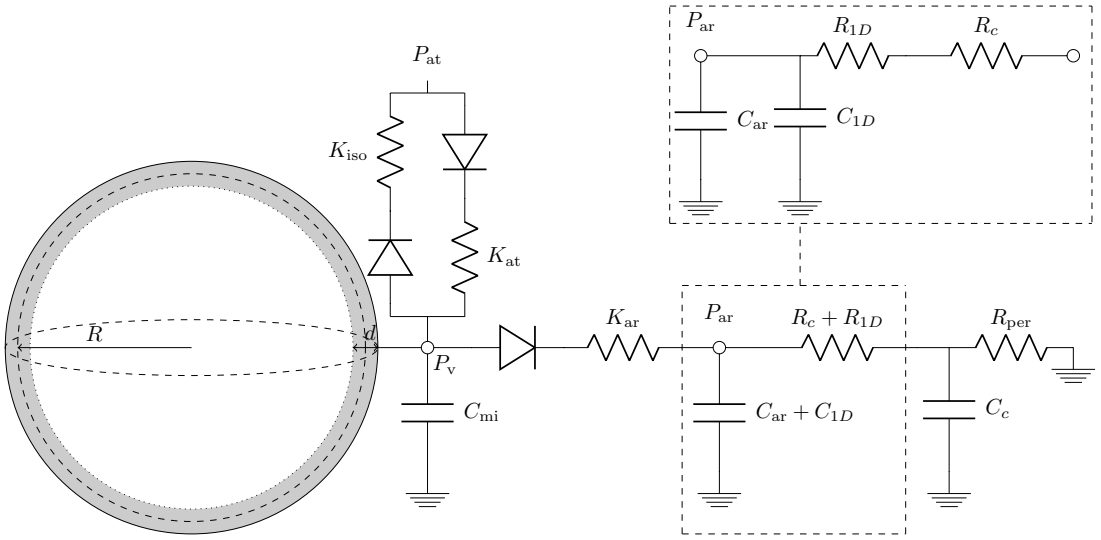

Figure 2.5 – Scheme of the *uncoupled cardiac model*: reduced cardiac model with a lumped-parameter model as boundary conditions to represent the entire circulation. The configuration is obtained from the *fully coupled model* by reducing the 1D vessel to an RC-model.

- The *fully coupled model* studied in the present work, with the reduced-dimensional model of the heart and the aortic model coupled through a transmission condition which includes the valve as represented in Figure 2.2.

The simulation results are divided into two main sections. In Section 2.5.1 we present the numerical validation of the proposed formulation, starting from the comparison between the results obtained using the *uncoupled aortic model* and the results of other numerical schemes. Then, we verify that the energy relation is indeed satisfied at the numerical level

and discuss its beneficial effect on the computations. In Section 2.5.2 we highlight the importance of the coupling involving two case studies: dicrotic notch and physiological ageing. The first case study is considered to demonstrate the need of having a one dimensional model as an outlet boundary for the heart to capture all the important features of pressure waves in the larger elastic arteries (e.g. the aorta), whereas in the second one we show how the simulations of specific conditions of the circulation (e.g. stiffening of the vessels due to ageing) benefit from the presence of a cardiac model whose behavior depends on the arterial conditions. Both cases reflect the natural interplay between the components of the cardiovascular system [Formaggia et al., 1999] .

2.5.1 Numerical validation

2.5.1.1 Benchmark for the uncoupled aortic model

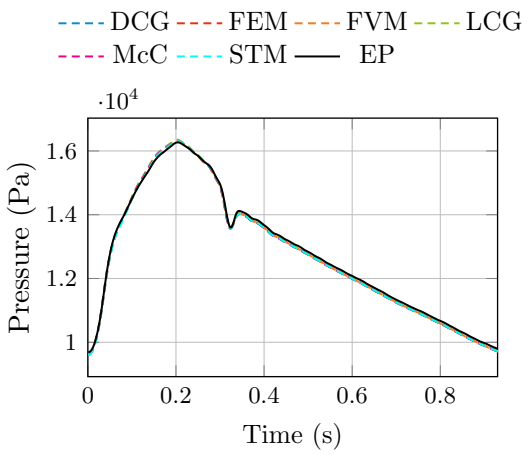

Figure 2.6 – Validation of the proposed energy-preserving formulation through the comparison of the results of our approach and those reported in [Boileau et al., 2015]. DCG: discontinuous Galerkin; FEM: Galerkin least-squares finite element method; FVM: finite volume method; LCG: locally conservative Galerkin; McC: finite difference MacCormack method; STM: simplified trapezium rule method; EP: energy-preserving scheme proposed in this work.

In order to support the validity of the developed method, our scheme is tested in one of the benchmarks presented in [Boileau et al., 2015]. In this work, different numerical schemes are compared for 1D arterial modeling in a set of test cases and they made the results freely available. In the following example we take into account the third benchmark configuration [Boileau et al., 2015], that corresponds to the upper thoracic aorta (setting presented in Figure 2.4). For this particular test case the authors considered a single uniform vessel represented by a one-dimensional model, that relies on the classical blood flow equations described in System 2.1 in the equivalent (A, u) formulation -the state variables are the cross section and the velocity- and an RCR model as outlet boundary condition. More precisely, in this benchmark, equations (2.1), (2.7) and (2.8) are solved with $Q_{ar}(t)$ imposed.

The parameters of the model and the inflow boundary condition used in [Boileau et al., 2015] were taken from [Xiao et al., 2013] and are reported, respectively, in Table 6.1 and Figure 2.4. We considered these same parameters and inlet conditions, as shown in Figure 2.6, and we compared our results with those of other numerical schemes available in the datasets of [Boileau et al., 2015]. In Figure 2.6 it is possible to observe that the pressure curves obtained by the numerical schemes reported are consistent, hence validates

Table 2.1 – Model parameters of the upper thoracic aorta (Readapted from [Xiao et al., 2013]).

Property	Value
Length, L	24.137 cm
Radius at diastolic pressure, R_0	1.2 cm
Initial flow velocity, $u(s,0)$	0 m s^{-1}
Initial pressure, $P(s,0)$	0 Pa
Wall thickness, h_0	1.2 mm
Blood density, ρ	1060 Kg m^{-3}
Friction parameter, K_r	276.46 mPa s
Wall viscosity, ν	0 mPa s
Velocity profile, α_{vp}	1
Young's modulus, E	400.0 kPa
Diastolic pressure, P_D	9.46 kPa
External pressure, P_{ext}	0 Pa
Windkessel resistance, R_c	$1.1752 \cdot 10^7$ Pa s m^{-3}
Windkessel compliance, C_c	$1.0163 \cdot 10^{-8}$ m^3 Pa^{-1}
Windkessel resistance, R_{per}	$1.1167 \cdot 10^8$ Pa s m^{-3}

our implementation. This shows that our formulation is consistent with well-known discretizations. At the price of a higher computational cost – due to the implicit nature – the proposed scheme has, in addition, the advantage to offer a provably stable numerical coupling with a numerical approximation of a non-linear description of the heart.

2.5.1.2 Spurious high frequencies filtering

In the discretization section, we have introduced two parameters α and θ associated with a controlled artificial viscosity of order δt in order to damp possible undesired oscillations (when $\alpha > 0$ and $\theta > 1/2$). We emphasize that these oscillations are not due to numerical instability, but to energy exchanges between model compartments introduced by the time discretization procedure, in particular the conservative part involving mid-points. We denote these oscillations spurious high frequencies. To illustrate this effect, we show in Figure 2.7 the time evolution over a cardiac cycle of the ventricular pressure P_v^n, the aortic valve flux $K_{\text{ar}}^{-1}|P_v^n - P_{\text{ar}}^n|_+$ and the proximal arterial pressure P_{ar}^n that are computed with the parameters chosen as in [Le Gall et al., 2020]. We compare three different configurations, $(\alpha,\theta) = (0, 0.5)$ (no artificial viscosity), $(\alpha,\theta) = (0, 0.75)$ (artificial viscosity only on P_v) and $(\alpha,\theta) = (1, 0.75)$ (artificial viscosity on $\dot{y}$ and P_v). It can be seen that the latter case avoids all kinds of spurious frequencies while preserving, qualitatively, the consistency of the approximation and the cost of the numerical scheme. Of note, the artificial viscosity decreases the formal order of accuracy of the scheme, an acceptable price to pay as our time-step is already rather small to account for the stiff parts of the pressure variation.

2.5.1.3 Numerical validation of the energy balance behind the coupling strategy

As an illustration of the validity of the energy-preserving numerical methods developed in this work, we present the numerical evaluation of the energy conservation residuals of the three main model elements (2.66), (2.77) and (2.79). For that, we define the residuals as

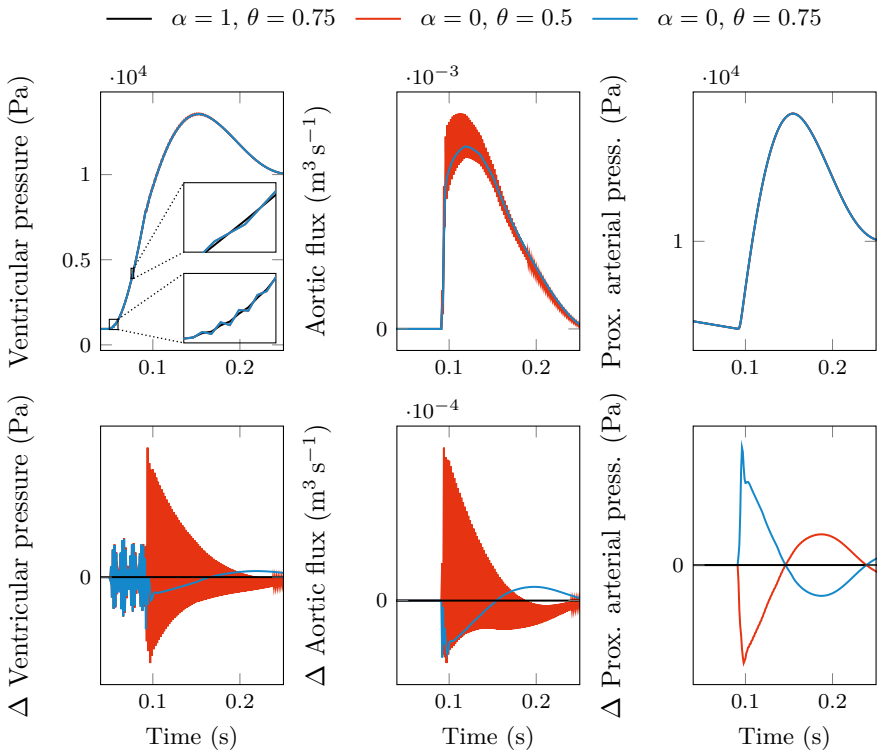

Figure 2.7 – Illustration of the ability of our numerical method to filter out spurious high-frequency modes. The upper plots correspond to the time evolution over a cardiac cycle of $(P_v^n, |P_v^n - P_{\mathrm{ar}}^n|_+ / K_{\mathrm{ar}}, P_{\mathrm{ar}}^n)$ for three different choices of parameters for the numerical viscosity. The lower plots show the time evolution of the difference with respect to a baseline case computed with $(\alpha, \theta) = (1, 0.75)$.

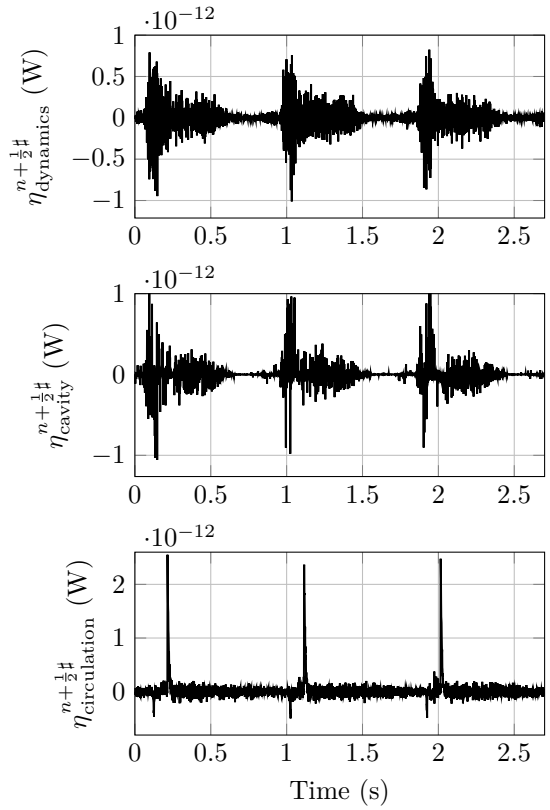

Figure 2.8 – Illustration that the energy balances are satisfied at the discrete level. The energy conservation residuals (2.66), (2.77) and (2.79) are evaluated numerically over time.

$$
\begin{cases}
\eta^{n+\frac{1}{2}\sharp}_{\text{dynamics}} = \dfrac{\mathcal{E}^{n+1}_{\text{hr}} - \mathcal{E}^{n}_{\text{hr}}}{\Delta t_n} + \dfrac{\mathcal{E}^{n+1}_{\text{hr,num}} - \mathcal{E}^{n}_{\text{hr,num}}}{\Delta t_n} + \dfrac{\mathcal{E}^{n+1}_{c} - \mathcal{E}^{n}_{c}}{\Delta t_n} \\
\qquad\qquad + \mathcal{D}^{n+\frac{1}{2}}_{hr} + \mathcal{D}^{n+\frac{1}{2}\sharp}_{\text{hr,num}} + \mathcal{D}^{n+\frac{1}{2}}_{c} - \dot{\mathcal{W}}^{n+\frac{1}{2}\sharp} - \mathcal{P}^{n+\frac{1}{2}\sharp}_{\text{ATP}}, \\
\eta^{n+\frac{1}{2}\sharp}_{\text{cavity}} = \dfrac{\mathcal{E}^{n+1}_{v} - \mathcal{E}^{n}_{v}}{\Delta t_n} + \mathcal{D}^{n+\theta}_{v} + \mathcal{D}^{n+\frac{1}{2}\sharp}_{v,\text{num}} - \mathcal{P}^{n+\frac{1}{2}\sharp}_{\text{ATP}} + \dot{\mathcal{W}}^{n+\frac{1}{2}\sharp} + P^{n+\frac{1}{2}}_{\text{ar}} Q^{n+\frac{1}{2}\sharp}_{\text{ar}}, \\
\eta^{n+\frac{1}{2}\sharp}_{\text{circulation}} = \dfrac{\mathcal{E}^{n+1}_{\text{ar}} - \mathcal{E}^{n}_{\text{ar}}}{\Delta t_n} + \dfrac{\mathcal{E}^{n+1}_{w} - \mathcal{E}^{n}_{w}}{\Delta t_n} + \mathcal{D}^{n+\frac{1}{2}}_{\text{ar}} + \mathcal{D}^{n+\frac{1}{2}}_{w} - P^{n+\frac{1}{2}}_{\text{ar}} Q^{n+\frac{1}{2}\sharp}_{\text{ar}}.
\end{cases}
$$

Their time evolution is presented in Figure 2.8 over several heart cycles for the simulation with the parameters inspired from [Le Gall et al., 2020] and whose results are presented in Figures 2.10 and 2.9. We can notice that the magnitude of the residuals is 12 orders of magnitude lower than that of the individual energy fluxes that compose them. This result thus validates the fact that the energy balances are indeed satisfied at the discrete level. Having an energy-preserving formulation for the discretization of the model equations ensures that we can make sense of the individual terms of the energy balance. On the one hand, it allows to get a better picture on the solution of the model equations by analyzing the fluxes of energy between the different elements of the model. We present in Figure 2.9

some of the energy fluxes that can be computed. We define the following notations

$$\begin{cases} \mathcal{P}_{\text{in,at}}^{n+\frac{1}{2}\sharp} = \dfrac{|P_{\text{at}}^{n+\frac{1}{2}} - P_v^{n+\theta}|_+}{K_{\text{at}}} P_{\text{at}}^{n+\frac{1}{2}} - \dfrac{|P_v^{n+\theta} - P_{\text{at}}^{n+\frac{1}{2}}|_+}{K_{ar}} P_{\text{at}}^{n+\frac{1}{2}}, \\ \dot{\mathcal{W}}^{n+\frac{1}{2}\sharp} = -P_v^{n+\theta} \dfrac{V(y^{n+1}) - V(y^n)}{\Delta t_n}, \\ \mathcal{P}_{\text{ATP}}^{n+\frac{1}{2}\sharp} = \dfrac{|\Omega_0|\, n_0(e_c^n)}{\sqrt{k_c^{n+1}}} \left(\sigma_0 \lambda_c^{n+\frac{1}{2}} - \dfrac{k_0\, (\lambda_c^{n+\frac{1}{2}})^2}{2\sqrt{k_c^{n+1}}} \right) |\nu^{n+1}|_+. \end{cases}$$

In the numerical results, we see how the contraction of the atrium creates an initial flux of energy $\mathcal{P}_{\text{in,at}}$ towards the left ventricle. Then, the chemical energy flux $\mathcal{P}_{\text{ATP}}$ provided at the micro level is transformed into the mechanical power $\dot{\mathcal{W}}$ by the left ventricle. It can be noted that the model predicts an energetic yield $\int_t^{t+T} |\dot{\mathcal{W}}(\tau)|_+ \,\mathrm{d}\tau / \int_t^{t+T} \mathcal{P}_{\text{ATP}}(\tau)\,\mathrm{d}\tau$ of 26.2 %, which lies in the physiological range: 25–35 % [Schipke, 1994; Knaapen et al., 2007]. The average power produced by the ventricle over a heartbeat is 1.02 W, which is in accordance with the values obtained experimentally [Dini et al., 2013; Le Gall et al., 2020]. Moreover, the peak of mechanical power reaches 10.4 W, which is consistent with the evaluation of this quantity from other mechanical models for patients suffering from aortic valve disease [Gsell et al., 2018]. The mechanical power is then transferred with little dissipation through the valves into the aorta that receives the influx of energy $P_{\text{ar}} Q_{\text{ar}}$. On the other hand, being able to compute the individual energy fluxes inside the model is of great interest from an application point of view, since some of the terms of the energy balance are indeed used by medical doctors. For instance, anesthetists are interested in the work developed by the left ventricle for the monitoring of the heart [Le Gall et al., 2020] during surgical intervention, wheres cardiologists see this same parameter as a potential biomarker for the evaluation of left ventricle dysfunctions [Dini et al., 2013] and the myocardial efficiency is considered as a relevant indicator to assess the state of patients having aortic or valve pathologies [Güçlü et al., 2015; Fernandes et al., 2017].

2.5.2 Physiological outcomes of the coupling

In this section, we examine the physiological interest of coupling the arterial and the cardiac model. The three model settings described above are involved to highlight the differences in the results when one of the two components, i.e. the cardiac model or the one-dimensional vessel, is not taken into account – the *fully coupled model* allowing to study the effect of the mutual interplay between the heart and the arterial network.

2.5.2.1 Importance of the downstream circulation for the heart: the dicrotic notch

The physiological arterial pressure curve shows two main parts: the systolic and the diastolic phase. During the first phase, the heart ejects the blood into the aortic root and the arterial pressure increases rapidly and reaches a peak, known as the systolic pressure value. Then, the pressure starts falling but it is interrupted by an incisura, known as the dicrotic notch, that happens at the time of the passage to the diastolic phase and causes a second peak. The pressure then continues its downslope to its minimum, the diastolic pressure [Mackanzie, 1902; Esper and Pinsky, 2014]. Any change in the shape of this curve represents a modification in the vessel condition, that is why it is important to be able to properly reproduce these features. We focus here on the reproduction of the dicrotic

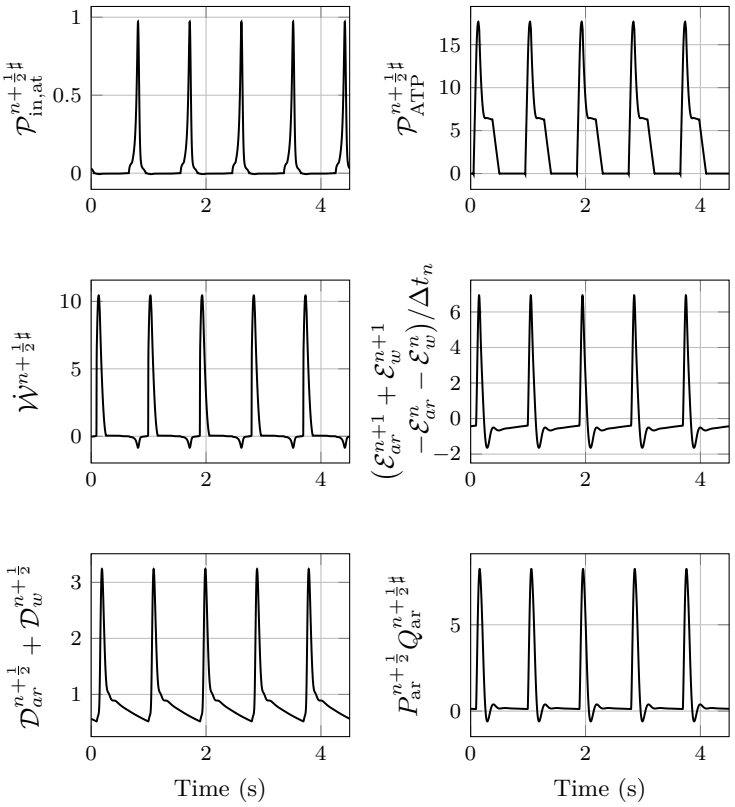

Figure 2.9 – Energy fluxes in the coupled heart and 1D aortic circulation model obtained with the energy-preserving numerical scheme. All quantities are given in Watts.

notch. For that purpose, we perform a simulation using the *uncoupled cardiac model* and the *fully coupled model* and we compare the results.

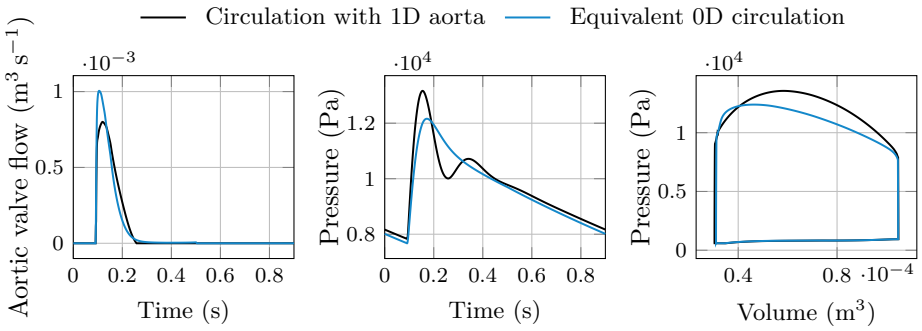

Figure 2.10 – The important role of the one-dimensional aortic model as a boundary condition for the reduced cardiac model is highlighted comparing the output of the *uncoupled cardiac model* (blue line) and the *fully coupled model* (black line) settings, with a focus on the presence of the dicrotic notch in the aortic pressure curve. From left to right we depict the blood flow coming from the aortic valve, the aortic pressure (P_{ar}) and the pressure-volume loops in the left ventricle.

From the results presented in Figure 2.10 we can observe that only the pressure curve obtained with the *fully coupled model* (black curve in the center) shows a dicrotic notch. Moreover, this was obtained with an inflow condition (in black in the left box), coming from the heart, which does not present a backflow. This confirms the latest findings of [Politi et al., 2016] and suggests that the dicrotic notch is not caused by the presence of the backflow but can be observed when wave propagation phenomena are represented. In addition, although both settings are able to reproduce a physiological shape for the curves, there are more differences between the two results beyond the reproducibility of the dicrotic notch. First, we can observe that the peak of the blood flow is slightly increased when the lumped-parameter model is used to represent the full circulation. Moreover, from the pressure-volume loops (in the right box) we can notice a distinction in shape between the two ejections. This suggests that the systolic blood pressure reaches a lower peak value when the circulation is completely represented by a lumped-parameter model. The last consideration is confirmed even more clearly in the pressure curves, since the lumped-parameter model is able to fit the diastolic decay of pressure but it is not sufficient to properly reproduce the systolic peak [Epstein et al., 2015] and, more generally, the systolic phase. In fact, only when a distributed aortic model is considered it is possible to obtain a more physiological wave showing a noticeable dicrotic notch. These results suggest that when a cardiovascular model is used to analyze phenomena strongly associated with the ventriculo-arterial interaction, lumped-parameter models are not sufficient to represent the downstream circulation and it is necessary to employ a higher-dimensional model (*e.g.* a 1D-model) that is able to capture the influence of pulse wave transmission within the circulation.

2.5.2.2 Importance of the heart for the aorta: Ageing

During ageing, the vessel walls undergo a degeneration of elastin fibers, a decrease in smooth muscle and an increase in collagen. These changes cause the stiffening of the arteries and in particular of the aorta. As a result, it is observed that the systolic peak pressure increases and the aortic and left ventricular late systolic pressure augment, whereas the aortic blood flow peak and the diastolic pressure decrease. These features are indeed commonly observed among elderly subjects. Of note, the effects of ageing on the heart are

minimal with respect to those in the main arteries [Vlachopoulos et al., 2011].

As it was done in [Formaggia et al., 2006], we use the simulation of ageing to highlight the importance of accounting for heart-circulation interactions in cardiovascular modeling. In order to simulate the ageing of the vessel, we modify some relevant arterial parameters. We follow here the scheme proposed by [Fossan et al., 2018], carrying out the appropriate manipulations to adapt this strategy to our model (single one-dimensional vessel). The parameter β, which is a surrogate of the arterial wall stiffness, the total arterial resistance and the total compliance are modified to represent "older" vessels. To take into account the contribution of the 1D model to the total resistance, the average pressure observed at the beginning of the aorta ($\overline{P}_{\text{inlet}}$) is used as a marker for the impedance of the vessel. A target value ($\overline{P}_{\text{target}}$) for this inlet pressure is calculated in order to induce the increasing pressure that is observed in normal ageing, and it is chosen as a 10% increase from the baseline inlet pressure. The peripheral resistance – R_{per} in our RCR model – is updated conforming to

$$R_{\text{per},k+1} + R_c = \frac{\overline{P}_{\text{target}}}{\overline{P}_{\text{inlet},k}}(R_{\text{per},k} + R_c),$$

where k is the ageing process iterative index. The parameter β is then modified as $\beta_{\text{new}} = 2.5\beta$. The total arterial compliance is decreased as $C_{\text{tot,new}} = C_{\text{tot}}/2$, with the total compliance C_{tot} being defined as

$$C_{\text{tot}} = C_{\text{1D}} + C_{\text{0D,distal}} + C_{\text{0D,transmission}}$$

where C_{1D}, $C_{\text{0D,distal}}$ and $C_{\text{0D,transmission}}$ are the equivalent compliance of the one-dimensional arterial model, the distal Windkessel model and the transmission model (if present), respectively. Then, $C_{\text{1D,new}}$ is updated according to the changes in β – see (2.85) – and $C_{\text{0D,distal,new}}$ is obtained from

$$C_{\text{0D,distal,new}} = C_{\text{tot,new}} - C_{\text{1D,new}} - C_{\text{0D,transmission}}.$$

The simulation of ageing is performed with the *uncoupled aortic model* and the *fully coupled model* settings. The obtained results are presented in Figure 2.11. In both simulation settings, we can observe numerous changes with respect to the baseline case that are typical of the ageing process: higher systolic peak, lower diastolic pressure and a small increase in wave propagation speed (the dicrotic notch is anticipated). However, the pressure curve obtained with the coupled model is more physiological. In particular, it is possible to see a trend towards the merging of the pressure systolic peak and the dicrotic peak, as it happens when the ageing process is advanced [Vlachopoulos et al., 2011], and the dicrotic notch fades away. Indeed, without a cardiac model the inflow has to be imposed and therefore it does not adapt to the arterial conditions. In the ageing case with the *uncoupled aortic model* it is possible to observe a double reflection that does not reflect the arterial response to ageing. Furthermore, when using a coupled model, the blood flow is impacted itself by the ageing process. Our simulation shows a decreased peak compared to the baseline case. Finally, the use of a coupled heart-circulation model allows to compute the variation of the left ventricular pressure-volume loop as a result of the ageing process. This enables to monitor the quantitative effects of the arterial ageing on the cardiac function.

2.6 Conclusions

In this work, we present an original method to couple reduced-order blood flow circulation models and heart models through the point of view of energy balance both at the continuous

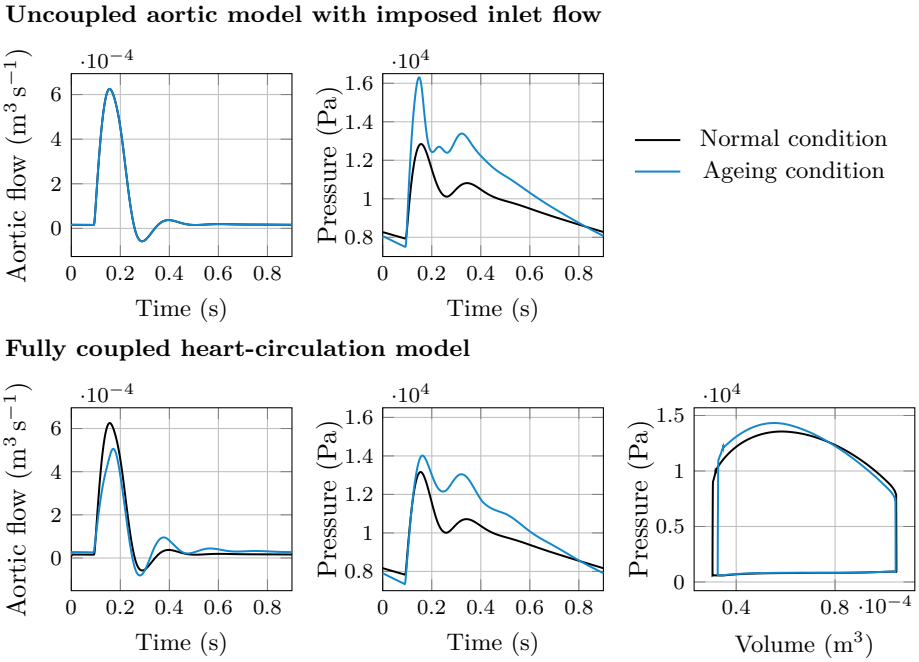

Figure 2.11 – The important role of the cardiac model as an inlet condition for the distributed arterial model is highlighted comparing the output of the *uncoupled aortic model* (top left and right) and the *fully coupled model* (bottom left to right) settings, with a focus on the effects of ageing on the elastic arteries. On the left we depict the blood flow at the first element of the aortic model, in the center we show the aortic pressure (P_{ar}) at the same space element and at the bottom right we depict the pressure-volume loops in the left ventricle, for normal physiological conditions (black line) and for an arterial ageing conditions (blue line).

and the discrete level. This is a difficult path as model reduction is often associated with the loss of energy balances for limit models. In fact, our coupled formulation is here proven to satisfy a full energy balance at the continuous level, with an additional consistent and controlled numerical dissipation on the fully discrete scheme. This allows to control the energy sources avoiding instabilities such as for instance uncontrolled back flows or perpetual motion cardiac engines. Essentially, our controlled coupling improves the modeling from the cardiac side and from the cardiovascular side. On the one hand, from the cardiac point of view we obtain better physiological signals with respect to the completely lumped heart-plus-Windkessel model proposed in [Caruel et al., 2013]. On the other hand, we introduce a more physiological heart engine than a phenomenological time-varying elastance model acting as a flow generator in [Formaggia et al., 2006]. We believe that this paves the way for suitably investigating physiological aspects of heart-circulation coupling, as illustrated here with the dicrotic notch and the ageing process.

2.7 Appendix

Details on the construction of the approximate radius function

In this appendix we describe how the discrete function $r_h(\Phi)$ is constructed. This construction is based on a pre-computation step in which the approximate tube law $r_h(\Phi)$ is sought as a bijective C^1-functions of $\mathbb{R}$ to $\mathbb{R}^+$ that corresponds to a quadratic piecewise approximation of $r(\Phi)$ on an interval $[\Phi_0, \Phi_N]$ and some smooth analytic functions over $(-\infty, \Phi_0]$ and $[\Phi_N, +\infty)$. After this pre-computations step the values of $r_h(\Phi)$ and $r_h'(\Phi)$ can be obtained either by quadratic (or linear) interpolation or evaluation of one (or two) transcendental functions. We first choose a set of points

$$\{\Phi_n\}_{n=0}^{n=N} \quad \text{with} \quad \Phi_n < \Phi_{n+1}$$

that represents a sufficiently fine sampling of the interval $[\Phi_0, \Phi_N]$. Then we compute $r(\Phi_0)$ and $r'(\Phi_n)$ for each $n \in \{0, \dots, N\}$, using equations (2.35) and (2.36) and the relation $r(\Phi) = \varphi^{-1}(\Phi)$. For each $n \in \{0, \dots, N\}$ the value $r'(\Phi_n)$ corresponds to the value of the function $r_h'(\Phi_n)$ and for $\Phi \in [\Phi_{n-1}, \Phi_n]$ the value of $r_h'(\Phi)$ is obtained by affine interpolation. More precisely

$$r_h'(\Phi) = \frac{\Phi - \Phi_{n-1}}{\Phi_n - \Phi_{n-1}} r_h'(\Phi_n) + \frac{\Phi_n - \Phi}{\Phi_n - \Phi_{n-1}} r_h'(\Phi_{n-1}), \quad \Phi \in [\Phi_{n-1}, \Phi_n].$$

The function $r_h(\Phi)$ for $\Phi \in [\Phi_0, \Phi_N]$ is obtained by integrating the function $r_h'(\Phi)$ between Φ_0 and Φ and setting $r_h(\Phi_0) = r(\Phi_0)$. In practice the values $\{r_h(\Phi_n)\}_{n=0}^{n=N}$ are tabulated. They are given by for $n \in \{1, \dots, N\}$

$$r_h(\Phi_0) = r(\Phi_0) \quad \text{and} \quad r_h(\Phi_n) = r_h(\Phi_{n-1}) + (\Phi_n - \Phi_{n-1}) \frac{r'(\Phi_n) + r'(\Phi_{n-1})}{2},$$

and the function $r_h(\Phi)$ for $\Phi \in [\Phi_{n-1}, \Phi_n]$ is given by

$$r_h(\Phi) = r_h(\Phi_{n-1}) + \frac{\frac{1}{2}(\Phi - \Phi_{n-1})^2}{\Phi_n - \Phi_{n-1}} r_h'(\Phi_n) + \frac{\frac{1}{2}(\Phi_n - \Phi_{n-1})^2 - \frac{1}{2}(\Phi_n - \Phi)^2}{\Phi_n - \Phi_{n-1}} r_h'(\Phi_{n-1}).$$

For small values of Φ we prescribe an exponential behavior (following the modification of the model introduced in Section 2.3.7),

$$r_h(\Phi) = r(\Phi_0)\, e^{\frac{r'(\Phi_0)}{r(\Phi_0)}(\Phi - \Phi_0)}, \quad \Phi \in (-\infty, \Phi_0].$$

A large value of Φ corresponds to a large value of R in (2.35). For these values one can expect that $r(\Phi)$ behaves as an affine function of $\Phi^{\frac{2}{3}}$. Thus we set

$$r_h(\Phi) = \frac{3}{2} \Phi_N^{\frac{1}{3}} r'(\Phi_N)\, \Phi^{\frac{2}{3}} + r_h(\Phi_N) - \frac{3}{2} \Phi_N\, r'(\Phi_N), \quad \Phi \in [\Phi_N, +\infty).$$

Bibliography

Alastruey, J., Parker, K. H., and Sherwin, S. J. (2008). Lumped parameter outflow models for 1-d blood flow simulations: Effect on pulse waves and parameter estimation. *Commun. Comput. Phys.*

Arthurs, C. J., Xiao, N., Moireau, P., Schaeffter, T., and Figueroa, C. A. (2020). A flexible framework for sequential estimation of model parameters in computational hemodynamics. *Advanced Modeling and Simulation in Engineering Sciences*, pages 1–37.

Arts, T., Delhaas, T., Bovendeerd, P., Verbeek, X., and Prinzen, F. W. (2005). Adaptation to mechanical load determines shape and properties of heart and circulation: the circadapt model. *American Journal of Physiology-Heart and Circulatory Physiology*, 288(4):H1943–H1954.

Audebert, C., Bucur, P., Bekheit, M., Vibert, E., Vignon-Clementel, I., and Gerbeau, J.-F. (2017). Kinetic scheme for arterial and venous blood flow, and application to partial hepatectomy modeling. *Computer Methods in Applied Mechanics and Engineering*, 314:102–125.

Augustin, C. M., Neic, A., Liebmann, M., Prassl, A. J., Niederer, S. A., Haase, G., and Plank, G. (2016). Anatomically accurate high resolution modeling of human whole heart electromechanics: a strongly scalable algebraic multigrid solver method for nonlinear deformation. *Journal of computational physics*, 305:622–646.

Bestel, J., Clément, F., and Sorine, M. (2001). A Biomechanical Model of Muscle Contraction. *Medical Image Computing and Computer-Assisted Intervention - MICCAI 2001*, 2208(2):1159–1161.

Boileau, E., Nithiarasu, P., Blanco, P. J., Müller, L. O., Fossan, F. E., Hellevik, L. R., Donders, W. P., Huberts, W., Willemet, M., and Alastruey, J. (2015). A benchmark study of numerical schemes for one-dimensional arterial blood flow modelling. *International Journal for Numerical Methods in Biomedical Engineering*, 31(10):e02732.

Bollache, E., Kachenoura, N., Redheuil, A., Frouin, F., Mousseaux, E., Recho, P., and Lucor, D. (2014). Descending aorta subject-specific one-dimensional model validated against in vivo data. *Journal of Biomechanics*, 47(2):424–431.

Brault, A., Dumas, L., and Lucor, D. (2017). Uncertainty quantification of inflow boundary condition and proximal arterial stiffness coupled effect on pulse wave propagation in a vascular network. *International Journal for Numerical Methods in Biomedical Engineering*, 33(10).

Burtschell, B. (2016). *Mechanical modeling and numerical methods for poromechanics : Application to myocardium perfusion.* PhD thesis. 2016SACLX022.

Caiazzo, A., Caforio, F., Montecinos, G., Müller, L. O., Blanco, P. J., and Toro, E. F. (2017). Assessment of reduced-order unscented kalman filter for parameter identification in 1-dimensional blood flow models using experimental data. *International journal for numerical methods in biomedical engineering*, 33(8):e2843.

Caruel, M., Chabiniok, R., Moireau, P., Lecarpentier, Y., and Chapelle, D. (2013). Dimensional reduction of cardiac models for effective validation and calibration. In *Functional Imaging and Modeling of the Heart*, pages 259–267. Springer Berlin Heidelberg.

Chabiniok, R., Moireau, P., Kiesewetter, C., Hussain, T., Razavi, R., and Chapelle, D. (2017). Assessment of atrioventricular valve regurgitation using biomechanical cardiac modeling. In *Functional Imaging and Modelling of the Heart*, pages 401–411. Springer International Publishing.

Chapelle, D., Le Tallec, P., Moireau, P., and Sorine, M. (2012). Energy-preserving muscle tissue model: formulation and compatible discretizations. *Journal for Multiscale Computational Engineering.*

Dini, F. L., Guarini, G., Ballo, P., Carluccio, E., Maiello, M., Capozza, P., Innelli, P., Rosa, G. M., Palmiero, P., and Galderisi, M. (2013). The left ventricle as a mechanical engine: from Leonardo da Vinci to the echocardiographic assessment of peak power output-to-left ventricular mass. *Journal of Cardiovascular Medicine*, 14(3):214–220.

Epstein, S., Willemet, M., Chowienczyk, P. J., and Alastruey, J. (2015). Reducing the number of parameters in 1d arterial blood flow modeling: less is more for patient-specific simulations. *American Journal of Physiology-Heart and Circulatory Physiology*, 309(1):H222–H234.

Esper, S. A. and Pinsky, M. R. (2014). Arterial waveform analysis. *Best Practice & Research Clinical Anaesthesiology*, 28(4):363–380. Hemodynamic Monitoring Devices.

Fernandes, J. F., Goubergrits, L., Brüning, J., Hellmeier, F., Nordmeyer, S., da Silva, T. F., Schubert, S., Berger, F., Kuehne, T., and Kelm, M. (2017). Beyond pressure gradients: the effects of intervention on heart power in aortic coarctation. *PLoS ONE*, 12(1):e0168487.

Formaggia, L., Gerbeau, J.-F., Nobile, F., and Quarteroni, A. (2000). On the Coupling of 3D and 1D Navier-Stokes Equations for Flow Problems in Compliant Vessels. *Computer Methods in Applied Mechanics and Engineering*, 191(561-582):6–7.

Formaggia, L., Lamponi, D., Tuveri, M., and Veneziani, A. (2006). Numerical modeling of 1d arterial networks coupled with a lumped parameters description of the heart. *Computer Methods in Biomechanics and Biomedical Engineering*, 9(5):273–288.

Formaggia, L., Nobile, F., Quarteroni, A., and Veneziani, A. (1999). Multiscale modelling of the circulatory system: a preliminary analysis. *Computing and Visualization in Science*, 2(2-3):75–83.

Fossan, F. E., Mariscal-Harana, J., Alastruey, J., and Hellevik, L. R. (2018). Optimization of topological complexity for one-dimensional arterial blood flow models. *Journal of The Royal Society Interface*, 15(149):20180546.

Gonzalez, O. (2000). Exact energy and momentum conserving algorithms for general models in nonlinear elasticity. *Computer Methods in Applied Mechanics and Engineering*, 190(13-14):1763–1783.

Gsell, M. A., Augustin, C. M., Prassl, A. J., Karabelas, E., Fernandes, J. F., Kelm, M., Goubergrits, L., Kuehne, T., and Plank, G. (2018). Assessment of wall stresses and mechanical heart power in the left ventricle: Finite element modeling versus Laplace analysis. *International Journal for Numerical Methods in Biomedical Engineering*, 34(12):e3147.

Guan, D., Liang, F., and Gremaud, P. A. (2016). Comparison of the windkessel model and structured-tree model applied to prescribe outflow boundary conditions for a one-dimensional arterial tree model. *Journal of Biomechanics*, 49(9):1583–1592.

Güçlü, A., Knaapen, P., Harms, H. J., Vonk, A. B., Stooker, W., Groepenhoff, H., Lammertsma, A. A., van Rossum, A. C., Germans, T., and van der Velden, J. (2015). Myocardial efficiency is an important determinant of functional improvement after aortic valve replacement in aortic valve stenosis patients: a combined PET and CMR study. *European Heart Journal–Cardiovascular Imaging*, 16(8):882–889.

Hauret, P. and Le Tallec, P. (2006). Energy-controlling time integration methods for nonlinear elastodynamics and low-velocity impact. *Computer Methods in Applied Mechanics and Engineering*, 195(37-40):4890–4916.

Hirschvogel, M., Bassilious, M., Jagschies, L., Wildhirt, S. M., and Gee, M. W. (2017). A monolithic 3d-0d coupled closed-loop model of the heart and the vascular system: Experiment-based parameter estimation for patient-specific cardiac mechanics. *International journal for numerical methods in biomedical engineering*, 33(8):e2842.

Holzapfel, G. A. and Ogden, R. W. (2009). Constitutive modelling of passive myocardium: a structurally based framework for material characterization. *Phil. Trans. R. Soc. A*, 367:3445– 3475.

Kerckhoffs, R. C., Neal, M. L., Gu, Q., Bassingthwaighte, J. B., Omens, J. H., and McCulloch, A. D. (2007). Coupling of a 3d finite element model of cardiac ventricular mechanics to lumped systems models of the systemic and pulmonic circulation. *Annals of biomedical engineering*, 35(1):1–18.

Kimmig, F., Chapelle, D., and Moireau, P. (2019). Thermodynamic properties of muscle contraction models and associated discrete-time principles. *Advanced Modeling and Simulation in Engineering Sciences*, 6(1):6.

Knaapen, P., Germans, T., Knuuti, J., Paulus, W. J., Dijkmans, P. A., Allaart, C. P., Lammertsma, A. A., and Visser, F. C. (2007). Myocardial energetics and efficiency: current status of the noninvasive approach. *Circulation ...*, 115(7):918–927.

Le Gall, A., Vallee, F., Pushparajah, K., Hussain, T., Mebazaa, A., Chapelle, D., Gayat, E., and Chabiniok, R. (2020). Monitoring of cardiovascular physiology augmented by a patient-specific biomechanical model during general anesthesia. A proof of concept study. *PLoS ONE*, 15(5):e0232830.

Lombardi, D. (2013). Inverse problems in 1D hemodynamics on systemic networks: A sequential approach. *International Journal for Numerical Methods in Biomedical Engineering*, 30(2):160–179.

Lumens, J., Delhaas, T., Kirn, B., and Arts, T. (2009). Three-Wall Segment (TriSeg) Model Describing Mechanics and Hemodynamics of Ventricular Interaction. *Annals of Biomedical Engineering*, 37(11):2234–2255.

Mackanzie, J. (1902). The study of the pulse, arterial, venous and hepatic and of the movements of the heart. *JAMA: The Journal of the American Medical Association*, XXXIX(11):648.

Manzoni, A., Bonomi, D., and Quarteroni, A. (2018). Reduced order modeling for cardiac electrophysiology and mechanics: New methodologies, challenges and perspectives. In *Mathematical and Numerical Modeling of the Cardiovascular System and Applications*, pages 115–166. Springer.

Matthys, K. S., Alastruey, J., Peiró, J., Khir, A. W., Segers, P., Verdonck, P. R., Parker, K. H., and Sherwin, S. J. (2007). Pulse wave propagation in a model human arterial network: Assessment of 1-d numerical simulations against in vitro measurements. *Journal of Biomechanics*, 40(15):3476–3486.

Müller, L. O. and Toro, E. F. (2014). A global multiscale model for the human circulation with emphasis on the venous system. *International Journal for Numerical Methods in Biomedical Engineering*. Published online in Wiley Online Library (wileyonlinelibrary.com). DOI: 10.1002/cnm.2622. Preprint available at `http://www.newton.ac.uk/preprints/NI13007.pdf`.

Mynard, J. P. and Smolich, J. J. (2015). One-dimensional haemodynamic modeling and wave dynamics in the entire adult circulation. *Annals of Biomedical Engineering*, pages 1–18.

Politi, M. T., Ghigo, A., Fernández, J. M., Khelifa, I., Gaudric, J., Fullana, J. M., and Lagrée, P.-Y. (2016). The dicrotic notch analyzed by a numerical model. *Computers in Biology and Medicine*, 72:54–64.

Pontrelli, G. (2004). A multiscale approach for modelling wave propagation in an arterial segment. *Computer Methods in Biomechanics and Biomedical Engineering*, 7(2):79–89.

Quarteroni, A. and Formaggia, L. (2004). Mathematical modelling and numerical simulation of the cardiovascular system. In *Handbook of Numerical Analysis*, pages 3–127. Elsevier.

Quarteroni, A., Veneziani, A., and Vergara, C. (2016). Geometric multiscale modeling of the cardiovascular system, between theory and practice. *Computer Methods in Applied Mechanics and Engineering*, 302:193–252.

Reymond, P., Merenda, F., Perren, F., Rüfenacht, D., and Stergiopulos, N. (2009). Validation of a one-dimensional model of the systemic arterial tree. *American Journal of Physiology-Heart and Circulatory Physiology*, 297(1):H208–H222.

Sainte-Marie, J., Chapelle, D., Cimrman, R., and Sorine, M. (2006). Modeling and estimation of the cardiac electromechanical activity. *Computers & structures*, 84(28):1743–1759.

Schipke, J. D. (1994). Cardiac efficiency. *Basic research in cardiology*, 89(3):207–240.

Segers, P., Rietzschel, E., De Buyzere, M., Stergiopulos, N., Westerhof, N., Van Bortel, L., Gillebert, T., and Verdonck, P. (2008). Three-and four-element windkessel models: assessment of their fitting performance in a large cohort of healthy middle-aged individuals. *Proc Inst Mech Eng H*, 222(4):417–428.

Segers, P., Stergiopulos, N., Westerhof, N., Wouters, P., Kolh, P., and Verdonck, P. (2003). Systemic and pulmonary hemodynamics assessed with a lumped-parameter heart-arterial interaction model. *J Eng Math*, 47(3-4):185–199.

Shi, Y., Lawford, P., and Hose, R. (2011). Review of zero-d and 1-d models of blood flow in the cardiovascular system. *BioMedical Engineering OnLine*, 10(1):33.

Shishido, T., Hayashi, K., Shigemi, K., Sato, T., Sugimachi, M., and Sunagawa, K. (2000). Single-beat estimation of end-systolic elastance using bilinearly approximated time-varying elastance curve. *Circulation*, 102(16):1983–1989.

Vignon-Clementel, I., Arbia, G., Baretta, A., Corsini, C., Esmaily Moghadam, M., Troianowski, G., Yang, W., Feinstein, J., Hsia, T.-Y., Marsden, A. L., Migliavacca, F., Pennati, G., and The Modeling Of Congenital Hearts Alliance (mocha) Investigators, F. (2012). From Patient-Specific Data to Multiscale Hemodynamics Simulations: the Challenge of Boundary Conditions. In Middleton, J., editor, *10th International*

Symposium on Computer Methods in Biomechanics and Biomedical Engineering, ISBN: 978-0-9562121-5-3, pages 603–608, Berlin, Germany. Arup.

Vlachopoulos, C., ORourke, M., and Nichols, W. W. (2011). *McDonalds Blood Flow in Arteries*. CRC Press.

Westerhof, N., Bosman, F., De Vries, C. J., and Noordergraaf, A. (1969). Analog studies of the human systemic arterial tree. *Journal of Biomechanics*, 2(2):121 – 143.

Westerhof, N., Lankhaar, J.-W., and Westerhof, B. E. (2009). The arterial windkessel. *Medical & biological engineering & computing*, 47(2):131–141.

Willemet, M. and Alastruey, J. (2014). Arterial pressure and flow wave analysis using time-domain 1-d hemodynamics. *Annals of Biomedical Engineering*, 43(1):190–206.

Xiao, N., Alastruey, J., and Figueroa, C. A. (2013). A systematic comparison between 1-d and 3-d hemodynamics in compliant arterial models. *International Journal for Numerical Methods in Biomedical Engineering*, 30(2):204–231.

CHAPTER 3

A cardiovascular model of the upper limb

It's not enough what I did in the past - there is also the future.
— Rita Levi-Montalcini

The aim of this chapter is to present the modeling choices made to derive the cardiovascular model of the upper limb, including the aorta up to the upper thoracic aorta and the arm arteries from the subclavian artery up to the radial artery, bounded by lumped-parameter models and coupled to a reduced model of the heart. The coupling equations are introduced and some preliminary results of the simulations are showed to demonstrate the capability of the model to produce a physiological behavior.
The content of this chapter has been realized in collaboration with François Kimmig.

Contents

3.1 Motivations

In Chapter 1 and 2 we have pointed out how one-dimensional models are widespread in the cardiovascular modeling and, in particular, to represent the blood circulation thanks to their suitability to describe wave propagation phenomena. However, the blood circulates throughout the entire body, traveling along more than 100,000 km [Jones, 1997], and a model that represents each one of the vessels with a 1D segment would be neither computationally affordable nor useful. In the literature, as we have seen in the previous chapters, it is possible to find models that represent the main important arteries [Alastruey et al., 2008; Boileau et al., 2015; Matthys et al., 2007; Willemet and Alastruey, 2014], including the coronary arteries [Reymond et al., 2009] and the venous system [Ho et al., 2012; Müller and Toro, 2014], while other works focus on vessels supplying blood to a specific region of the body [Alastruey et al., 2006; Blanco et al., 2012; Brook and Pedley, 2002; Dumas et al., 2016; He et al., 2004; Lazović et al., 2015; Li and Cheng, 1993; Watanabe et al., 2013] or on a single vessel [Bollache et al., 2014; Pontrelli, 2004], and the list is far from being exhaustive. When modeling, the choice to take into account one or more vessels is driven by many factors: limitations imposed by the computational cost, a priori knowledge for the parametrization and focus of the study. In our work, we need to rely on a model with a suitable representation of the upper limb vessels. The blood circulation of the arm has already been addressed for various purposes, He et al. [2004] developed a 1D thermo-fluid model representing arteries, capillaries and veins of the upper limb to study the influence of stiffness and blood viscosity on blood pressure and temperature. Alastruey et al. [2006] described three different anatomical configurations of the hands and took into account the brachial, radial and ulnar arteries, to simulate the modified Allen's test and prove its efficiency to detect sufficient collateral flow in the hand. Blanco et al. [2012] performed a sensitivity analysis for the outflow parameters of a detailed anatomical model of the arm comprehensive of 67 arterial segments and 16 vascular territories. Lazović et al. [2015] used direct measurements of radial pressure to derive a model of the radial artery to relate the differences in pulse pressure waves to the different ranges of age. Since our final purpose is to use radial pressure measurements to retrieve the informations regarding the heart, the cardiac output (CO) and the central aortic pressure (CAP) we extend and slightly modify the model presented in the previous chapter, that relies on a formulation energetically stable, to take into account the arterial network that link the measurements location with the cardiac model and the proximal site of the aorta.

3.2 Modeling choices

The upper limb is the region of the body that goes from the shoulder to the hand. The main arteries that drives blood throughout this area, as described in the introduction, are the subclavian artery that branches directly from the aorta for the left arm and from the brachiocephalic trunk for the right arm, the axillary artery and the brachial artery. Then, the vessel bifurcates into two smaller ones: the radial and the ulnar artery that give rise to smaller branches and form an anastomosis at the level of the hand. The subclavian, axillary and brachial artery succeed one another without giving rise to relevant branches, while the radial and ulnar artery, that present a similar cross-section, irradiate almost symmetrically towards the deep and superficial palmar arch. Taking into account all these characteristics and relying upon the symmetry of the upper limb we derive a mathematical formulation, following the numerical choices presented in Chapter 2 and relying on the same state variables, that describes the model configuration depicted in Figure 3.1. This model includes the cardiac cavity of Caruel et al. [2013] and the arterial pathways from the

aortic valve to the hand with a representation of the upper thoracic aorta as in [Manganotti et al., 2021].

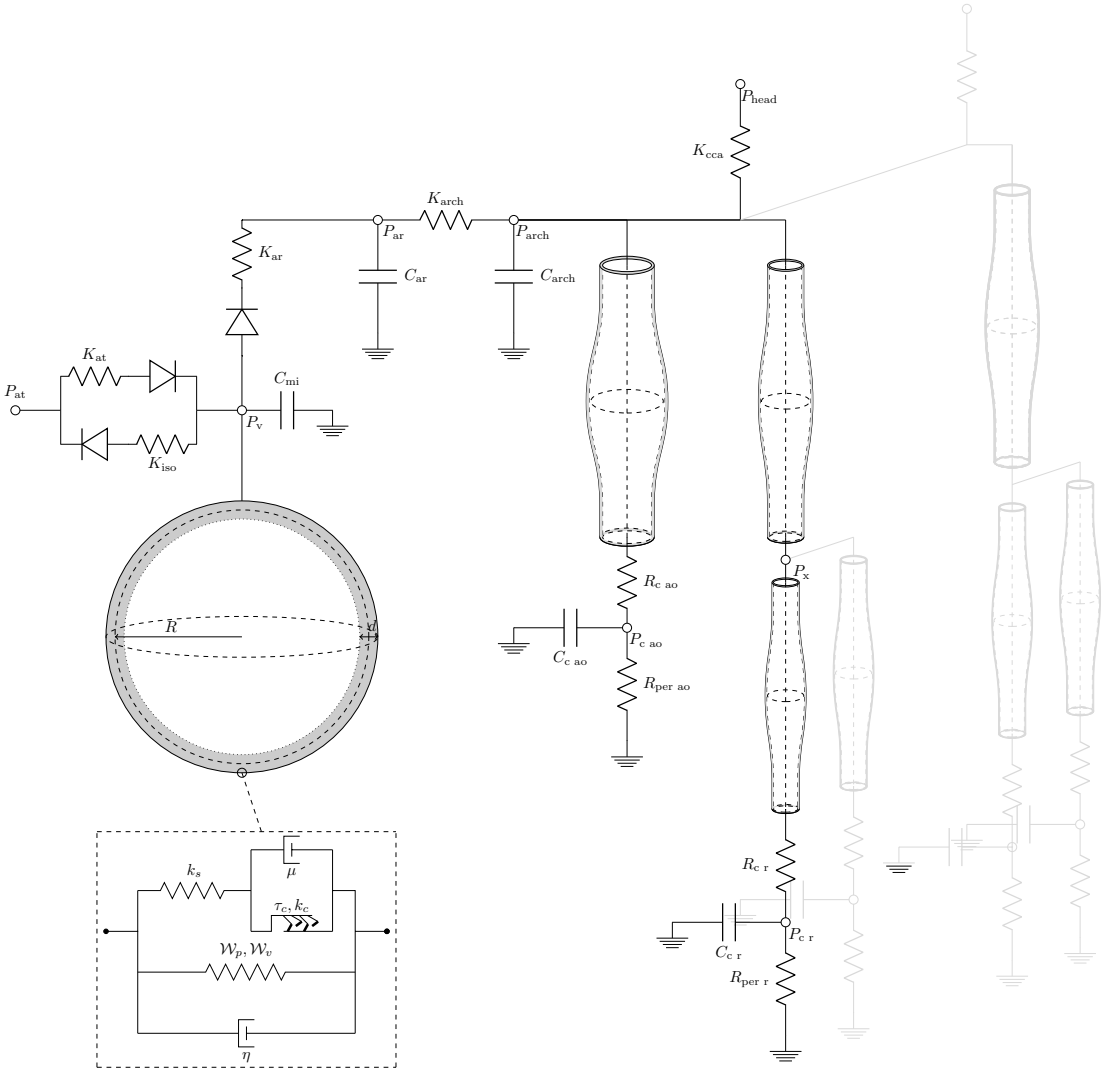

Figure 3.1 – Representation of the model configuration. The cardiac cavity, the rheological model and the valve are the same as in Chapter 2. Then, a Windkessel model couples the heart and the one-dimensional circulation that takes into account the upper thoracic aorta and the main arteries of the arm. The vessels of the right arm as well as the left ulnar artery are depicted in light grey as they are not modeled as a segment but instead their contribution is accounted in the branching conditions. Modified from a figure provided by F. Kimmig.

3.2.1 The aortic valve

The formulation of the aortic valve, modeled by means of a 0D model, that plays the role of a coupling element between the cardiac model and the arterial is described in Chapter 2. To recall the equation, we have

$$C_{ar}\dot{P}_{ar} - \frac{|P_v - P_{ar}|_+}{K_{ar}} + Q_{ar} = 0, \tag{3.1}$$

where C_{ar} is the compliance of the area around the open aortic valve, K_{ar} the resistance of the valve, P_{ar} and P_v respectively the arterial and the ventricular pressure, prescribed

by the heart model, while Q_{ar} is the blood flow ejected from the heart into the arterial circulation.

3.2.2 The aortic arch

The blood flow coming from the left ventricle travels along the aortic arch, that is here represented by two additional terms in the lumped-parameter model that works as a transmission condition between the reduced model of the heart and the one-dimensional arterial models. We represent this part of the vessel as a RC-model described by

$$C_{arch}\dot{P}_{arch} - \frac{P_{ar} - P_{arch}}{K_{arch}} + Q_{ul} + Q_{head} + Q_{ao} = 0, \tag{3.2}$$

with C_{arch} being the compliance of the aortic arch and K_{ar} its resistance, P_{arch} is the pressure at the point of the main bifurcation of the model: where the arteries that travels towards the head and along the arms arise, while Q_{ul}, Q_{head} and Q_{ao} represent the blood that flows in the upper limb, meaning both arms, towards the head through the common carotid arteries and the one that continues along the aorta. Relying on the hypothesis that in normal conditions the flow distribution to the brachiocephalic trunk, that then divide into right common carotid artery and right subclavian artery, and to the sum of the left common carotid artery and the left subclavian artery is almost the same [Huberts et al., 2012], Eq. 3.2 becomes

$$C_{arch}\dot{P}_{arch} - \frac{P_{ar} - P_{arch}}{K_{arch}} + 2(Q_{arm} + Q_{cca}) + Q_{ao} = 0, \tag{3.3}$$

where Q_{arm} is the blood flow that enters the left or the right subclavian artery and Q_{cca} the flow inside one carotid artery. Moreover, the carotid artery is represented by a resistive element with an imposed pressure at one end, which implies $Q_{cca} = \frac{P_{head} - P_{arch}}{K_{cca}}$, where P_{head} represents the pressure at the distal end of the carotid artery and K_{cca} the resistance encountered by the flux entering the carotid. Finally, Q_{arm} and Q_{ao} are given by the one-dimensional models of the arm and the aorta.

3.2.3 The upper thoracic aorta

The model formulation that describe the aorta corresponds to the one-dimensional model derived in [Manganotti et al., 2021]. We refer to v_{ao}, φ_{ao} etc as the state variables for the upper thoracic aorta, the formulation reads,

$$\begin{cases} \partial_t \varphi_{ao} + \pi\xi(R_{ao})\partial_s(R_{ao}v_{ao}) = 0, & \text{in } (0, L_{ao}), \\ \pi\rho\partial_t v_{ao} + \dfrac{\pi\rho}{2}\left(2\dfrac{v_{ao}}{R_{ao}}\partial_s v_{ao} + v_{ao}\partial_s\dfrac{v_{ao}}{R_{ao}}\right) + \rho K_{r\,ao}\dfrac{v_{ao}}{R_{ao}^2} & \\ +\pi R_{ao}\partial_s(\xi(R_{ao})\varphi_{ao}) = 0, & \text{in } (0, L_{ao}), \end{cases} \tag{3.4}$$

while at the boundaries we have

$$\begin{cases} \dfrac{\rho}{2}\dfrac{v_{ao}^2}{R_{ao}} + R_{ao}\xi(R_{ao})\varphi = -R_{ao}(P_{tot} - P_{ext}) & \text{at } s = 0 \text{ and } s = L_{ao}, \\ Q_{ao} = \pi R_{ao}(0)v_{ao}(0), \end{cases} \tag{3.5}$$

where $P_{tot} - P_{ext}$ is now given by

$$\begin{cases} P_{tot} - P_{ext} = P_{arch}, & \text{at } s = 0, \\ P_{tot} - P_{ext} = P_{c\,ao} + R_{c\,ao}\pi R_{ao}v_{ao} & \text{at } s = L_{ao}, \end{cases} \tag{3.6}$$

with $P_{c\,ao}$ the pressure at the outlet Windkessel model described by

$$C_{c\,ao}\dot{P}_{c\,ao} + \frac{P_{c\,ao}}{R_{per\,ao}} = \pi R_{ao} v_{ao} \quad \text{at } s = L_{ao}. \tag{3.7}$$

3.2.4 The axis subclavian-axillary-brachial artery

The subclavian, axillary and brachial artery are modeled as a single one-dimensional segment, that we will refer to as the SAB model, with average anatomical properties in terms of cross-section and with a length that represents the sum of the length of each vessel. The formulation that describes this segment has the same equations as the upper thoracic aorta, with different values for $P_{tot} - P_{ext}$ at its boundaries. We will refer to v_b, φ_b etc. as the state variables regarding this segment. The formulation reads

$$\begin{cases} \partial_t \varphi_b + \pi \xi(R_b) \partial_s (R_b v_b) = 0, & \text{in } (0, L_b), \\ \pi\rho\partial_t v_b + \dfrac{\pi\rho}{2}\left(2\dfrac{v_b}{R_b}\partial_s v_b + v_b \partial_s \dfrac{v_b}{R_b}\right) + \rho K_{r\,b}\dfrac{v_b}{R_b^2} + \pi R_b \partial_s(\xi(R_b)\varphi_b) = 0, & \text{in } (0, L_b), \end{cases} \tag{3.8}$$

with

$$\begin{cases} \dfrac{\rho}{2}\dfrac{v_b^2}{R_b} + R_b \xi(R_b)\varphi = -R_b(P_{tot} - P_{ext}) & \text{at } s = 0 \text{ and } s = L_b, \\ Q_{arm} = \pi R_b(0) v_b(0), \end{cases} \tag{3.9}$$

where

$$\begin{cases} P_{tot} - P_{ext} = P_{arch}, & \text{at } s = 0, \\ P_{tot} - P_{ext} = P_x & \text{at } s = L_b, \end{cases} \tag{3.10}$$

with P_x the pressure at the branching point, where the brachial artery divides into the radial and the ulnar artery. The expression of this pressure depends on the choice for the treatment of the one-dimensional branching conditions and will be presented later in this chapter.

3.2.5 The radial and ulnar artery

For the radial and ulnar artery, we rely again on the symmetric properties of the arterial network of the upper limb. We suppose that the blood flow, from the brachial artery, splits in a half and flows in the two branches (note that another repartition of the flow can be chosen). Relying on this hypothesis, we model the radial artery, that it is of our interest for the sake of this project, using the same formulation presented above for the other one-dimensional segments. The ulnar artery will be considered as a duplicate of the radial artery (see Section 3.3). We obtain

$$\begin{cases} \partial_t \varphi_r + \pi \xi(R_r) \partial_s (R_r v_r) = 0, & \text{in } (0, L_r), \\ \pi\rho\partial_t v_r + \dfrac{\pi\rho}{2}\left(2\dfrac{v_r}{R_r}\partial_s v_r + v_r \partial_s \dfrac{v_r}{R_r}\right) + \rho K_{r\,r}\dfrac{v_r}{R_r^2} + \pi R_r \partial_s(\xi(R_r)\varphi_r) = 0, & \text{in } (0, L_r), \end{cases} \tag{3.11}$$

with the usual boundary conditions, at $s = 0$ and $s = L_r$ described as

$$\frac{\rho}{2}\frac{v_r^2}{R_r} + R_r \xi(R_r)\varphi = -R_r(P_{tot} - P_{ext}), \tag{3.12}$$

completed by

$$\begin{cases} P_{tot} - P_{ext} = P_x, & \text{at } s = 0, \\ P_{tot} - P_{ext} = P_{c\,r} + R_{c\,r}\pi R_r v_r & \text{at } s = L_r, \end{cases} \tag{3.13}$$

where P_{cr} is the pressure of the three-element Windkessel model that describe the vessels downstream the distal extremity of the radial artery. System 3.11 and 3.13 are completed, together with Eq. 3.12, by

$$C_{cr}\dot{P}_{cr} + \frac{P_{cr}}{R_{per\,r}} = \pi R_r v_{ao} \quad \text{at } s = L_r. \tag{3.14}$$

3.3 One-dimensional branching conditions

In the model configuration addressed in this chapter we deal with the presence of branching that characterizes the arterial tree. The behavior of the flow at the ramification point should be described by a 3D model. However, if the focus is not on the flow at the specific location of the branching, then it is possible to rely on reduced-order models, e.g. one-dimensional models [Formaggia et al., 2003]. In the anatomical region described by our model, the first side branches rise from the aortic vessel: the right brachiocephalic trunk followed by the left common carotid artery and the left subclavian artery. However, the region of the aorta where these vessels rise is the aortic arch, that in our configuration is represented by a lumped-parameter model. The branching point of these three vessels, that represents also the inlet point of the upper thoracic aorta model, is represented by a single point at the extremity of the 0D model of the aortic arch – here the nodal pressure – P_{arch}. It ensures the continuity of pressure at the junction while the governing equation of the Windkessel model prescribe the conservation of the mass. If we move forward along the arm vessels we encounter another main bifurcation. At the distal end of the brachial artery. At this point, the vessel divides into the radial and ulnar artery. In our model this region is represented by three one-dimensional segments: one representing the subclavian-axillary-brachial axis, containing the mother vessel, and the two others representing the daughter vessels: the radial and ulnar artery. In order to connect these three models we have to define suitable interface conditions. At the junction of three 1D models we have six unknowns: $(v_b(L_b), \varphi_b(L_b))$, $(v_r(0), \varphi_r(0))$ and $(v_u(0), \varphi_u(0))$, with the latter couple being the state variables for the ulnar artery. However, thanks to the hypothesis on the symmetric split of the blood flow between radial and ulnar artery, we have that $(v_r(0), \varphi_r(0)) = (v_u(0), \varphi_u(0))$ and we finally restrain the unknowns to $(v_b(L_b), \varphi_b(L_b))$ and $(v_r(L_b), \varphi_r(L_b))$. First, we prescribe the conservation of mass at the branching point, that reads

$$Q_b(L_b) - 2Q_r(0) = 0,$$

with the positive sign meaning that the blood is flowing out of the vessel. Using the state variables introduced in Chapter 2 we obtain

$$\pi R_b(L_b)v_b(L_b) - 2\pi R_r(0)v_r(0) = 0. \tag{3.15}$$

The preservation of the energy density for the two one-dimensional models separately is achieved, as the formulations have the same properties to the one described in [Manganotti et al., 2021]. However, an energy density for the coupling of them is preserved if the boundary terms, being $P_b(L_b)Q_b(L_b)$ and $P_r(0)Q_r(0)$ with $P_b(L_b)$ and $P_r(0)$ being respectively the brachial and radial total pressure at the branching point, respect the following condition

$$-P_b(L_b)Q_b(L_b) + 2P_r(0)Q_r(0) \leq 0. \tag{3.16}$$

However, the second condition at a vessel junction being the continuity of the total pressure, that assures the continuity of the momentum at the branching point [Peiro et al., 2003], we impose

$$P_b(L_b) = P_r(0) := P_x,$$

and, after substitution with the variables of Eq. 3.15, Eq. 3.16 becomes

$$-R_b(L_b)v_b(L_b) + 2R_r(0)v_r(0) \leq 0$$

which is true if Eq. 3.15 stands. At this point, we need to define the total pressure P_x in order to be able to solve the two coupled problems. In order to do that, within the various possible choices (e.g. employing additional resistive elements as in [van den Boom et al., 2018]), we test two options. The first one, is to treat P_x as a Lagrange multiplier for the constraint $\pi R_b(L_b)v_b(L_b) - 2\pi R_r(L_b)v_r(L_b) = 0$. The second choice is to introduce a penalization – ε_b – which involves a dynamics for P_x that reads

$$\pi R_b(L_b)v_b(L_b) - 2\pi R_r(0)v_r(0) = \varepsilon_b \frac{d}{dt} P_x. \tag{3.17}$$

We have shown that for values of ε_b small enough (e.g. $\varepsilon_b \sim 10^{-16}$) the results obtained with the two definition of the total pressure are equivalent. However, it could be challenging to deal with the Lagrange multiplier with certain inverse problem techniques that may be applied to the model. For this reason, in the following chapters we rely on the penalized approach.

3.4 Results and discussion

In order to test the behavior of the complete model, we discretize in time and space as in Chapter 2. Then, given an input atrial pressure we perform a simulation and obtain the results shown in Figure 3.2. We comment the shape of the pressure-volume loop, the arterial pressure and the flow waves according to the physiological knowledge. In particular, for the pressure and blood flow we refer to the descriptions of the waves in the arteries of Vlachopoulos et al. [2011]. From Figure 3.2, we can observe how the systolic peak pressure in the aortic pressure wave increases moving away from the aortic valve towards the peripheral end of the vessel, while the blood flow decreases. One can also notice that the positive flow in the brachiocephalic artery is shorter in time and is followed by a wide back flow. Finally, we can comment on the differences in shape of the pressure wave between the aorta and the arteries of the upper limb, an important aspect is the extensive increase in the systolic peak [Hamilton et al., 1936] and the decrease in the dicrotic notch, which should reflect the mean pressure value. These results are qualitatively in agreement with the physiological knowledge about pressure and flow wave. However, in order to validate the model, a more accurate comparison is required. This could for example be performed with the benchmark results given in Boileau et al. [2015], even if our model configuration differs from the arterial network models proposed in their work, in particular for the presence of a cardiac model, and it would require some adjustments in the parametrization to account for the vessels that are not described by a 1D formulation in our configuration. Another option would be to compare our results with *in vivo* or *in vitro* data, that however implies a parametrization 'by hand' if data assimilation problems are not foreseen. The model described in this chapter is conceived to take into account the arterial network that links the central pressure and the heart with the peripheral end of the radial artery. It is the preliminary step for the final purpose of this thesis, being to apply data assimilation techniques to retrieve input pressure and flow by using radial pressure records. The results depicted in Figure 3.2 shows that the model is able to well reproduce wave propagation phenomena and compute pressure and flow wave that reflect the physiological characteristics expected. However, some aspects of the model could be improved: first, the SAB axis could be replaced by the modeling of the three vessels it

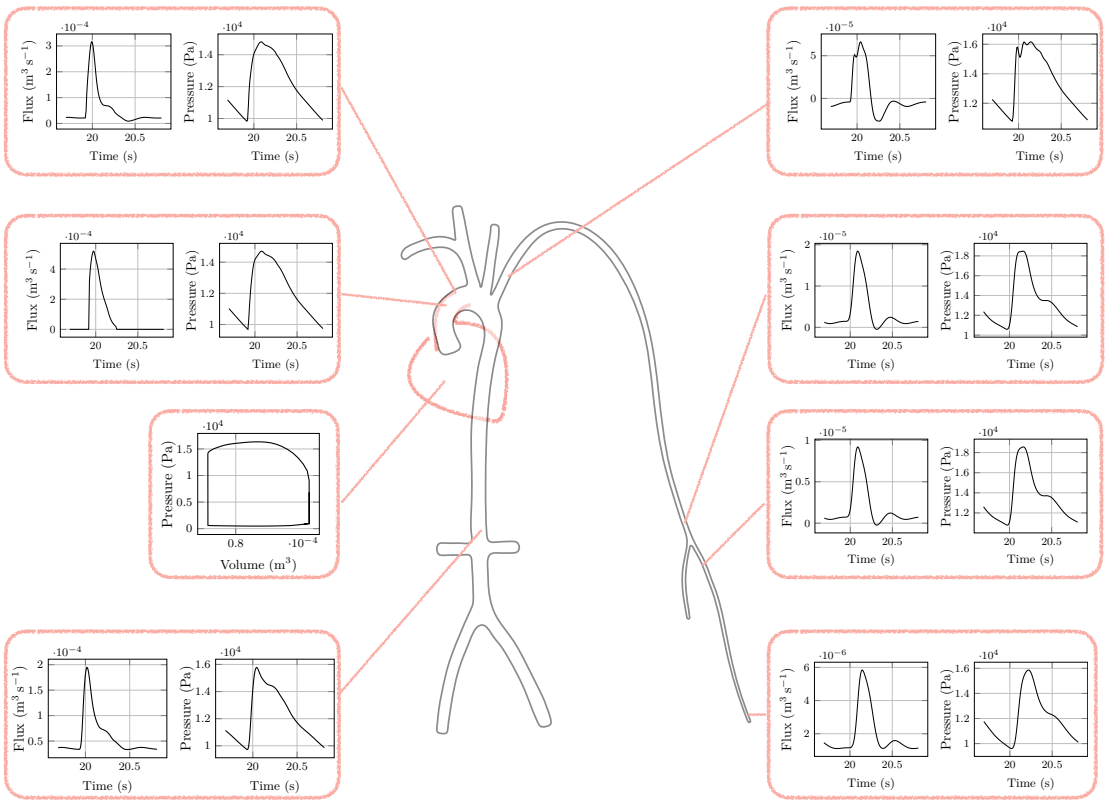

Figure 3.2 – The results obtained with the complete model including the left ventricle model and the aortic and upper limb arterial circulation are presented at different sites of the complete model. In particular the pressure-volume loop is shown to describe the left ventricle behavior, while the pressure and blood flow wave are displayed at some location for each one-dimensional segment to highlight the changes in shape along the arterial tree and how it reflects the physiological knowledge. Modified from a figure provided by F. Kimmig.

includes or it could take into account the tapering of the lumen to reflect the changes in vessel radius between the subclavian, axillary and brachial artery. Moreover, a strategy to model the flux loss due to smaller side vessels in the arm circulation should improve the accuracy of the model. More details about these two improvements are given in the following chapter.

Bibliography

Alastruey, J., Parker, K. H., Peiró, J., and Sherwin, S. J. (2006). Can the modified allens test always detect sufficient collateral flow in the hand? a computational study. *Computer Methods in Biomechanics and Biomedical Engineering*, 9(6):353–361.

Alastruey, J., Parker, K. H., and Sherwin, S. J. (2008). Lumped parameter outflow models for 1-d blood flow simulations: Effect on pulse waves and parameter estimation. *Commun. Comput. Phys.*

Blanco, P., Watanabe, S., and Feijóo, R. (2012). Identification of vascular territory resistances in one-dimensional hemodynamics simulations. *Journal of biomechanics*, 45(12):2066–2073.

Boileau, E., Nithiarasu, P., Blanco, P. J., Müller, L. O., Fossan, F. E., Hellevik, L. R., Donders, W. P., Huberts, W., Willemet, M., and Alastruey, J. (2015). A benchmark study of numerical schemes for one-dimensional arterial blood flow modelling. *International Journal for Numerical Methods in Biomedical Engineering*, 31(10):e02732.

Bollache, E., Kachenoura, N., Redheuil, A., Frouin, F., Mousseaux, E., Recho, P., and Lucor, D. (2014). Descending aorta subject-specific one-dimensional model validated against in vivo data. *Journal of Biomechanics*, 47(2):424–431.

Brook, B. and Pedley, T. (2002). A model for time-dependent flow in (giraffe jugular) veins: uniform tube properties. *Journal of Biomechanics*, 35(1):95–107.

Caruel, M., Chabiniok, R., Moireau, P., Lecarpentier, Y., and Chapelle, D. (2013). Dimensional reduction of cardiac models for effective validation and calibration. In *Functional Imaging and Modeling of the Heart*, pages 259–267. Springer Berlin Heidelberg.

Dumas, L., Bouti, T. E., and Lucor, D. (2016). A robust and subject-specific hemodynamic model of the lower limb based on noninvasive arterial measurements. *Journal of Biomechanical Engineering*, 139(1).

Formaggia, L., Lamponi, D., and Quarteroni, A. (2003). One-dimensional models for blood flow in arteries. *Journal of Engineering Mathematics*, 47(3):251–276.

Hamilton, W. F., Woodbury, R. A., and Harper, H. T., J. (1936). Physiologic relationship between intrathoracic, intraspinal and arterial pressures. *Journal of the American Medical Association*, 107(11):853–856.

He, Y., Liu, H., and Himeno, R. (2004). A one-dimensional thermo-fluid model of blood circulation in the human upper limb. *International Journal of Heat and Mass Transfer*, 47(12):2735–2745.

Ho, H., Mithraratne, K., and Hunter, P. (2012). Numerical simulation of blood flow in an anatomically-accurate cerebral venous tree. *IEEE transactions on medical imaging*, 32(1):85–91.

Huberts, W., Bode, A. S., Kroon, W., Planken, R. N., Tordoir, J. H. M., van de Vosse, F. N., and Bosboom, E. M. H. (2012). A pulse wave propagation model to support decision-making in vascular access planning in the clinic. *Med. Eng. Phys.*, 34(2):233–248.

Jones, A. (1997). The blood. *The Lancet*, 349(9056):963.

Lazović, B., Mazić, S., Zikich, D., and Åœikić, D. (2015). The mathematical model of the radial artery blood pressure waveform through monitoring of the age-related changes. *Wave Motion*, 56:14–21.

Li, C. and Cheng, H. (1993). A nonlinear fluid model for pulmonary blood circulation. *Journal of biomechanics*, 26(6):653–664.

Manganotti, J., Caforio, F., Kimmig, F., Moireau, P., and Imperiale, S. (2021). Coupling reduced-order blood flow and cardiac models through energy-consistent strategies: modeling and discretization. *Advanced Modeling and Simulation in Engineering Sciences*, 8(1):1–37.

Matthys, K. S., Alastruey, J., Peiró, J., Khir, A. W., Segers, P., Verdonck, P. R., Parker, K. H., and Sherwin, S. J. (2007). Pulse wave propagation in a model human arterial network: Assessment of 1-d numerical simulations against in vitro measurements. *Journal of Biomechanics*, 40(15):3476–3486.

Müller, L. O. and Toro, E. F. (2014). A global multiscale model for the human circulation with emphasis on the venous system. *International Journal for Numerical Methods in Biomedical Engineering*. Published online in Wiley Online Library (wileyonlinelibrary.com). DOI: 10.1002/cnm.2622. Preprint available at `http://www.newton.ac.uk/preprints/NI13007.pdf`.

Peiro, J., Sherwin, S., Parker, K., Franke, V., Formaggia, L., Lamponi, D., and Quarteroni, A. (2003). Numerical simulation of arterial pulse propagation using one-dimensional models. *Wall-fluid interactions in physiological flows*, pages 1–36.

Pontrelli, G. (2004). A multiscale approach for modelling wave propagation in an arterial segment. *Computer Methods in Biomechanics and Biomedical Engineering*, 7(2):79–89.

Reymond, P., Merenda, F., Perren, F., Rüfenacht, D., and Stergiopulos, N. (2009). Validation of a one-dimensional model of the systemic arterial tree. *American Journal of Physiology-Heart and Circulatory Physiology*, 297(1):H208–H222.

van den Boom, T., Stevens, R., Delhaas, T., van de Vosse, F., and Huberts, W. (2018). Zero-dimensional lumped approach to incorporate the dynamic part of the pressure at vessel junctions in a 1d wave propagation model. *International Journal for Numerical Methods in Biomedical Engineering*, 34(9):e3116.

Vlachopoulos, C., ORourke, M., and Nichols, W. W. (2011). *McDonalds Blood Flow in Arteries*. CRC Press.

Watanabe, S. M., Blanco, P. J., and Feijóo, R. A. (2013). Mathematical model of blood flow in an anatomically detailed arterial network of the arm. *ESAIM: Mathematical Modelling and Numerical Analysis*, 47(4):961–985.

Willemet, M. and Alastruey, J. (2014). Arterial pressure and flow wave analysis using time-domain 1-d hemodynamics. *Annals of Biomedical Engineering*, 43(1):190–206.

CHAPTER 4

Cardiovascular modeling perspectives

Going only part of the way is not the same as going the wrong way.
— Jostein Gaarder, *Sophie's World*

Contents

In the previous chapters we have presented an arterial model, coupled with a reduced cardiac model [Caruel et al., 2013], that represents the main arterial vessels of the thorax and upper limb with one-dimensional models and accounts for the contribution of other vessels with boundary Windkessel models. This model shows good results in terms of pressure wave propagation and reproduction of physiological blood pressure and flow waves, plus it relies on a stable discrete formulation [Manganotti et al., 2021]. Even if the results presented in this part are satisfactory and promising, some improvement in the modeling choices should be taken into account for future perspectives, that we address in the following sections.
In the previous chapters we have pointed out that wave reflection is a key phenomena to understand arterial circulation. These reflections are influenced by the narrowing (tapering) of the aorta and the large arteries, especially in older humans. However, the effect caused by the increased impedance induced by tapering seems to be balanced by the presence of small side branches that generates a loss of flow. The combination of these two phenomena can lead to a system that can be described as a flow in a cylinder [Vlachopoulos et al., 2011]. However, the amount of tapering and number of side vessels that balance exactly it is not, to our knowledge, defined for each vessel, thus these two effects could be taken into account in a one-dimensional model to enhance a more precise representation of wave propagation phenomena in the arterial circulation.

4.1 Short term perspective: the tapering of the vessels

In the circulation model presented in Chapter 3 we have modeled the upper thoracic aorta as a uniform circular cylinder, moreover, the subclavian, axillary and brachial artery are represented by a single one-dimensional segment. However, the cross-section at the beginning of the subclavian artery differs from the cross section at the distal end of the brachial artery, and the lumen narrowing in the aortic vessel is quite pronounced as well. In order to enhance the representation of these vessels one way could be to include the tapering in the model. This can be done by considering linear tapering as in [Blanco et al., 2014], even if other strategies have been investigated [Abdullateef et al., 2021]. Including the narrowing of vessels in the model involves that the reference radius R_0 is no longer constant along the vessel, which would introduce the term of type $\frac{\partial R_0}{\partial x}$ in the momentum equation of the one-dimensional blood flow formulation.

4.2 Medium term perspective

4.2.1 Modeling side vessels flow loss

Side branches arises from arteries every $3-4\,\text{cm}$, and microscopic branches are even more concentrated [Vlachopoulos et al., 2011]. The contribution of flow loss of each vessel might be negligible but the global effect should be considered for larger arteries, especially if tapering is also introduced. In order to take into account the effects caused by these branches without modeling each one of them we would like to model the vessel wall as a porous media, which allows for leakage of flow through it.
A similar idea was already introduced to model microvascular networks [Cattaneo and Zunino, 2014; D'angelo and Quarteroni, 2008; Possenti et al., 2019; Vidotto et al., 2019] where the fluid described by a one-dimensional model is embedded in a porous media and a fluid exchange takes place between the two of them, or to give a tool that is able to reproduce filtration into vessel walls (e.g. drugs absorption) [Badia et al., 2009].
In order to model the vessel wall as a porous media we would start from a linearized version

[Barré et al., 2021; Burtschell et al., 2019] of the 3D porous formulation of Chapelle and Moireau [2014], that reads

$$\begin{cases} \rho_s(1-\phi)\dfrac{\partial^2}{\partial t^2}u_s - \mathrm{div}(\sigma_s(u_s)) - \mathrm{div}(\sigma_s(\dfrac{\partial}{\partial t}u_s)) = \phi^2 k_f^{-1}(v_f - \dfrac{\partial}{\partial t}u_s) + (\alpha-\phi)\nabla p \\ \quad = \rho_s(1-\phi)f, \\ \rho_f\phi\dfrac{\partial}{\partial t}v_f - \mathrm{div}(\phi\sigma_f(v_f)) + \phi^2 k_f^{-1}(v_f - \dfrac{\partial}{\partial t}u_s) - \theta v_f + \phi\nabla p = \rho_f\phi f, \\ \dfrac{\alpha-\phi}{\kappa}\dfrac{\partial}{\partial t}p + \mathrm{div}(\alpha\dfrac{\partial}{\partial t}u_s + \phi(v_f - \dfrac{\partial}{\partial t}u_s)) = \dfrac{\theta}{\rho_f}. \end{cases}$$

where the state variables are the structure displacement u_s, the velocity of fluid v_f and the fluid pressure p, while σ_s represents the stress tensor, ρ_s and ρ_f are respectively the solid and fluid density, ϕ represents the porosity, k_f is the hydraulic conductivity tensor, f the external body force, α the Biot-Willis coefficient, κ the bulk modulus and θ the source term. Which in our case would be taken as a simple sink term – $\theta = -\rho_f k_{cv}(p - P_{sv})$ [Chapelle et al., 2010] – where k_{cv} is a small conductance and P_{sv} the pressure in the small side vessel. We perform an asymptotic investigation in the spirit of [Chabiniok et al., 2022], we drop the equation of v_f assuming that $v_f = v_s = \frac{\partial}{\partial t}u_s$, and retrieve a system of the form

$$\begin{cases} -\tilde{\gamma}\dfrac{\partial\zeta}{\partial t} + \tilde{b}\zeta - \tilde{d}\dfrac{\partial}{\partial x}p = P - P_{ext}, \\ \tilde{e}\dfrac{\partial}{\partial t}p + \tilde{f}\dfrac{\partial}{\partial t}\zeta + \tilde{h}\zeta + \rho_f k_{cv}(p - P) = 0. \end{cases}$$

with ζ representing the displacement and defined as $\zeta = R - R_0$, where R is the radius of the vessel and R_0 the reference radius, and with $\tilde{d}$, $\tilde{e}$, $\tilde{f}$ and $\tilde{h}$ some parameters to define and $\tilde{\gamma}$ and $\tilde{b}$ chosen as in Chapter 1. These equations should be coupled with the blood flow formulation described in the previous chapters, through a term that model leakage through the wall. This is added to both the conservation and momentum equation of the one-dimensional formulation, as done in [Schaaf and Abbrecht, 1972]. We expect the blood flow formulation introduced in Chapter 1 to read

$$\begin{cases} \dfrac{\partial A}{\partial t} + \dfrac{\partial Q}{\partial x} + L_p = 0, \\ \dfrac{\partial Q}{\partial t} + \dfrac{\partial}{\partial x}\Big(\alpha\dfrac{Q^2}{A}\Big) + \dfrac{A}{\rho}\dfrac{\partial P}{\partial x} + \omega(Q)L_p = -k\dfrac{Q}{A}, \\ P = P_{ext} + \tilde{\gamma}\dfrac{\partial\zeta}{\partial t} + \tilde{b}\zeta - \tilde{d}\dfrac{\partial}{\partial x}p, \\ \tilde{e}\dfrac{\partial}{\partial t}p + \tilde{f}\dfrac{\partial}{\partial t}\zeta + \tilde{h}\zeta + \rho_f k_{cv}(p - P_{sv}) = 0, \end{cases}$$

where L_p is a term that accounts for the leakage of blood through the walls and $\omega(Q)$ is a parameters that depends on the axial flux. In more details, the side out flow term could be defined as a function linearly dependent on pressure P.
This strategy would lead to a coupled Biot-reduced Navier-Stokes problem that allows to model the presence of small side branches for the large arteries.

4.2.2 Coupling with a 3D model of the hart

The coupling between 3D and 1D models has already been adressed in the literature for diffent reasons [Blanco et al., 2007; Blanco and Feijóo, 2010; Caforio et al., 2021;

Dobroserdova and Olshanskii, 2013; Formaggia et al., 2000]. For example, Blanco and Feijóo [2010] couple some 3D specific arteries to 1D arteries within a detailed closed-loop model, the coupling equations are represented by a restriction of the flow rate and pressure at the interface. Dobroserdova and Olshanskii [2013] analyze different possible coupling conditions for consecutive 3D-1D fluid models in order to obtain an energy consistent coupling. Caforio et al. [2021] provide a model with a 3D electromechanics heart and a 1D circulation model. The coupling is performed by imposing a zero balance between the volume change in the cardiac cavity and in the blood stream. However, the above mentioned works do not pursue the analysis of the energy stability at the discrete level. For this reason, our objective would be to couple a fluid-structure interaction model of the heart with the one-dimensional circulation model described in this work, with a focus on the analysis of the energy properties at the discrete level. Moreover, considering the physics of the problem, the coupling would be strongly dependent on the choice of the valve model. In particular, if we introduce a 3D valve, the coupling would reduce to a coupling between a 3D and a 1D vessel, as in [Blanco and Feijóo, 2010] and [Dobroserdova and Olshanskii, 2013]. However, if we choose a 0D valve, the coupling conditions and energy properties would not change with respect to those described in Chapter 2.

4.3 Long term perspective: a closed-loop model

In order to obtain a proper description of the cardiovascular phenomena and be able to provide a predictive model we should 'complete' our model by including the venous return and build a closed-loop model. The flow wave returning back to the heart affects the heart contractility, this feedback is what motivated the works of Kerckhoffs et al. [2007] and Veress et al. [2013], that coupled a lumped-parameter model of the circulation with a 3D representation of the heart. Blanco and Feijóo [2010] developed a closed-loop cardiovascular model with a lumped-parameter representation of the heart and a mixed 3D-1D-0D model of the circulation. However, the above mentioned works do not include a model with a coupling between a one-dimensional circulation model and a physiological reduced cardiac model engine. Considering the focus of our work on the circulation in the upper limb, this could lead to the choice of a lumped-parameter model to include the venous return, leading to a 0D-1D-0D closed-loop model of the coupling between the heart and the circulation.

Bibliography

Abdullateef, S., Mariscal-Harana, J., and Khir, A. W. (2021). Impact of tapering of arterial vessels on blood pressure, pulse wave velocity, and wave intensity analysis using one-dimensional computational model. *International Journal for Numerical Methods in Biomedical Engineering*, 37(11):e3312.

Badia, S., Quaini, A., and Quarteroni, A. (2009). Coupling biot and navier–stokes equations for modelling fluid–poroelastic media interaction. *Journal of Computational Physics*, 228(21):7986–8014.

Barré, M., Grandmont, C., and Moireau, P. (2021). Analysis of a linearized poromechanics model for incompressible and nearly incompressible materials. working paper or preprint.

Blanco, P., Feijóo, R., and Urquiza, S. (2007). A unified variational approach for coupling 3d–1d models and its blood flow applications. *Computer Methods in Applied Mechanics and Engineering*, 196(41-44):4391–4410.

Blanco, P. J. and Feijóo, R. A. (2010). A 3d-1d-0d computational model for the entire cardiovascular system. *Mecánica Computacional*, 29(59):5887–5911.

Blanco, P. J., Watanabe, S. M., Passos, M. A. R., Lemos, P. A., and Feijóo, R. A. (2014). An anatomically detailed arterial network model for one-dimensional computational hemodynamics. *IEEE Transactions on biomedical engineering*, 62(2):736–753.

Burtschell, B., Moireau, P., and Chapelle, D. (2019). Numerical analysis for an energy-stable total discretization of a poromechanics model with inf-sup stability. *Acta Mathematicae Applicatae Sinica, English Series*, 35(1):28–53.

Caforio, F., Augustin, C. M., Alastruey, J., Gsell, M. A., and Plank, G. (2021). A coupling strategy for a 3d-1d model of the cardiovascular system to study the effects of pulse wave propagation on cardiac function. *arXiv preprint arXiv:2111.05683*.

Caruel, M., Chabiniok, R., Moireau, P., Lecarpentier, Y., and Chapelle, D. (2013). Dimensional reduction of cardiac models for effective validation and calibration. In *Functional Imaging and Modeling of the Heart*, pages 259–267. Springer Berlin Heidelberg.

Cattaneo, L. and Zunino, P. (2014). Computational models for fluid exchange between microcirculation and tissue interstitium. *Networks and Heterogeneous Media*, 9(1):135–159.

Chabiniok, R., Burtschell, B., Chapelle, D., and Moireau, P. (2022). Dimensional reduction of a poromechanical cardiac model for myocardial perfusion studies. *Applications in Engineering Science*, page 100121.

Chapelle, D., Gerbeau, J.-F., Sainte-Marie, J., and Vignon-Clementel, I. (2010). A poroelastic model valid in large strains with applications to perfusion in cardiac modeling. *Computational Mechanics*, 46(1):91–101.

Chapelle, D. and Moireau, P. (2014). General coupling of porous flows and hyperelastic formulations – From thermodynamics principles to energy balance and compatible time schemes. *European Journal of Mechanics - B/Fluids*, 46:82–96. Updated version of previously published research report.

D'angelo, C. and Quarteroni, A. (2008). On the coupling of 1d and 3d diffusion-reaction equations: application to tissue perfusion problems. *Mathematical Models and Methods in Applied Sciences*, 18(08):1481–1504.

Dobroserdova, T. K. and Olshanskii, M. A. (2013). A finite element solver and energy stable coupling for 3d and 1d fluid models. *Computer Methods in Applied Mechanics and Engineering*, 259:166–176.

Formaggia, L., Gerbeau, J.-F., Nobile, F., and Quarteroni, A. (2000). On the Coupling of 3D and 1D Navier-Stokes Equations for Flow Problems in Compliant Vessels. *Computer Methods in Applied Mechanics and Engineering*, 191(561-582):6–7.

Kerckhoffs, R. C., Neal, M. L., Gu, Q., Bassingthwaighte, J. B., Omens, J. H., and McCulloch, A. D. (2007). Coupling of a 3d finite element model of cardiac ventricular mechanics to lumped systems models of the systemic and pulmonic circulation. *Annals of biomedical engineering*, 35(1):1–18.

Manganotti, J., Caforio, F., Kimmig, F., Moireau, P., and Imperiale, S. (2021). Coupling reduced-order blood flow and cardiac models through energy-consistent strategies: modeling and discretization. *Advanced Modeling and Simulation in Engineering Sciences*, 8(1):1–37.

Possenti, L., Casagrande, G., Di Gregorio, S., Zunino, P., and Costantino, M. L. (2019). Numerical simulations of the microvascular fluid balance with a non-linear model of the lymphatic system. *Microvascular Research*, 122:101–110.

Schaaf, B. W. and Abbrecht, P. H. (1972). Digital computer simulation of human systemic arterial pulse wave transmission: a nonlinear model. *Journal of Biomechanics*, 5(4):345–364.

Veress, A., Raymond, G., Gullberg, G., and Bassingthwaighte, J. (2013). Left ventricular finite element model bounded by a systemic circulation model. *Journal of biomechanical engineering*, 135(5).

Vidotto, E., Koch, T., Köppl, T., Helmig, R., and Wohlmuth, B. (2019). Hybrid models for simulating blood flow in microvascular networks. *Multiscale Modeling & Simulation*, 17(3):1076–1102.

Vlachopoulos, C., ORourke, M., and Nichols, W. W. (2011). *McDonalds Blood Flow in Arteries*. CRC Press.

Part II

Inverse problems

CHAPTER 5

Introduction to data assimilation for unsteady problems

If we want to achieve our goal, then let us empower ourselves with the weapon of knowledge [...]
— Malala Yousafzai

Contents

5.1 Methods

A natural system, in any kind of field, can be studied through some measurements taken on it. However, the data collected are sampled and are usually noisy. Moreover, as we have seen previously, it is not always possible to easily perform those measurements, especially when the system under study is within the human body. So, how can we observe the behavior of such a system without having a full access on the data concerning it?
In Part I we have seen how models can help the understanding of a physiological phenomena like the blood flow in arteries. Nevertheless, the use of mathematical models is subjected to many '*a priori*' choices concerning the modeling hypothesis, the geometry, the physical parameters, the input etc.
In order to overcome the limitations of both the measurements and the model it is possible to rely on data assimilation. With *data assimilation* we refer to all those methods and strategies that combine the data directly obtained on the system and the mathematical model that represents it. "Assimilation is the process of finding the model representation which is most consistent with the observations" [Lorenc, 1995]. Moreover, it can be seen as a tool to get rid of the measurements noise relying on the physical background of the mathematical models [Bertoglio, 2012]. The main idea is to find an optimal balance between minimizing the discrepancy between model outcomes and data and increasing the precision of the model [Chapelle et al., 2013]. Formally, we can describe the model as a dynamical system

$$\begin{cases} \dot{z} = f(z, \theta, t) + B\nu(t) & \text{in } (0, T), \\ z(0) = z_0, \end{cases}$$

where $z \in \mathcal{Z}$ is the state variable, $f(z, \theta, t)$ the dynamical operator with the physical parameters $\theta \in \mathcal{P}$ and B and $\nu(t) \in \mathcal{U}$ respectively the control operator and an input source. In this system one may want to find θ and z_0, usually hard to obtain from measurements and crucial for the results obtained with a mathematical model. When the two estimations are associated we deal with the so-called augmented state. Finally, the observations are defined as

$$y_\delta = h(z, t) + \chi(t) \quad \text{in } (0, T),$$

where y are the real measurements, h is the observation operator that links the data with the corresponding variable in the model and χ the noise. We now present some of the available methods for data assimilation. This can be done by means of a deterministic or probabilistic interpretation, for example with a Bayesan framework [Lassila et al., 2013]. However, in this presentation we focus on the deterministic analysis. The objective of most of the data assimilation approaches is to to minimize a cost function that reads,

$$\mathcal{J}(z) = \frac{1}{2} \left|\left| y_\delta - \Psi_T \begin{pmatrix} z \\ \nu \\ \theta \end{pmatrix} \right|\right|^2_{\mathcal{Y}_T} + \frac{1}{2} ||z_0 - \hat{z}_0||^2_{N_0} \quad \text{in } (0, T)$$

where we can define

$$\Psi_T : (z_0, \nu, \theta) \mapsto h(z_{|z_0,\nu,\theta}, t),$$

$\mathcal{Y}_T = L^2((0, T), \mathcal{Y})$, N_0 the operator defining the norm $||z_0 - \hat{z}_0||^2_{N_0} = (z_0 - \hat{z}_0, N_0(z_0 - \hat{z}_0))_{\mathcal{Z}}$ and $\hat{z}_0$ is the given initial condition, chosen 'a priori' for the simulation. The results of the minimization gives $\hat{z}$, being the estimator of the state z. From a probabilistic point of view the inverse of $\mathcal{Y}_T$ can be seen as a prior mean and $N_0 = P_0^{-1}$ is a covariance error when $\hat{z} = \mathbb{E}(z)$ [Simon, 2006]. For the various application the minimization is performed on the

fully discretized functional. The available methods to solve this problem can be divided in mainly two families: the variational and sequential approach [Bouttier and Courtier, 2002].

5.1.1 Variational methods

Also known as batch model, as it corrects the state taking into account both present and past data [Lal, 2017]. The variational method's aim is to minimize a functional of type

$$\mathcal{J}_T(z_0,\nu,\theta)=\int_0^T\Big[||y_\delta-h(z_{|z_0,\nu,\theta},t)||^2_{\mathcal{Y}}+\kappa||\nu||^2_{\mathcal{U}}\Big]dt+||\xi_z||^2_{(P_0)^{-1}}+||\xi_\theta||^2_{(P_\theta)^{-1}},$$

where $P_\theta^{-1}=N_\theta$ is an appropriate norm. In the functional, z is constrained to satisfy the dynamics of the system, with $z(0)=z_0+\xi_z$ and the parameters defined as $\theta=\theta_0+\xi_\theta$. The solution is usually obtained by minimizing $\mathcal{J}$, this involves computing its gradient and deriving its adjoint-model [Banks and Kunisch, 2012; Chavent, 2010; Ismail et al., 2013; Martin et al., 2005; Sixou et al., 2017]. In order to do that, the tangent of the operator to minimize has to be computed, and reads

$$\begin{cases}\Big(\dfrac{\partial\mathcal{J}_T}{\partial\xi_z},\delta\xi_z\Big)=(N_0\xi_z,\delta\xi_z)-(p_z(0),\delta\xi_z),\\ \Big(\dfrac{\partial\mathcal{J}_T}{\partial\xi_\theta},\delta\xi_\theta\Big)=(N_\theta\xi_\theta,\delta\xi_\theta)-(p_\theta(0),\delta\xi_\theta),\\ \Big(\dfrac{\partial\mathcal{J}_T}{\partial\nu},\delta\nu\Big)=\displaystyle\int_0^T[(\nu,\delta\nu)-(p_z,B\delta\nu)]dt,\end{cases}$$

which can be rewritten as

$$\begin{cases}\Big(\dfrac{\partial\mathcal{J}_T}{\partial\xi_z},\delta\xi_z\Big)=(N_0(\xi_z-P_0p_z(0)),\delta\xi_z),\\ \Big(\dfrac{\partial\mathcal{J}_T}{\partial\xi_\theta},\delta\xi_\theta\Big)=(N_\theta(\xi_\theta-P_\theta p_\theta(0)),\delta\xi_\theta),\\ \Big(\dfrac{\partial\mathcal{J}_T}{\partial\nu},\delta\nu\Big)=\displaystyle\int_0^T[(\nu,\delta\nu)-(B^*p_z,\delta\nu)]dt,\end{cases}$$

where p_z and p_θ are the adjoint variables, that are described by the following system

$$\begin{cases}\dot{p}_z+\dfrac{\partial f^*}{\partial z}p_z=-\dfrac{\partial h^*}{\partial z}(y_\delta-h(z,t)),\\ p_z(T)=0,\\ \dot{p}_\theta+\dfrac{\partial f^*}{\partial\theta}p_\theta=0,\\ p_\theta(T)=0.\end{cases}$$

Then, the minimizer $(\bar{\xi}_z,\bar{\xi}_\theta,\bar{\nu})$ of $\mathcal{J}_T$ formally writes

$$\begin{cases}\bar{\xi}_z=P_0\bar{p}_z,\\ \bar{\xi}_\theta=P_\theta\bar{p}_\theta,\\ \bar{\nu}=B^*\bar{p}_z,\end{cases}$$

with $(\bar{p}_z, \bar{p}_\theta)$ solution of the two-ends problem [Lions, 1973]

$$\begin{cases} \dot{\bar{z}} = f(\bar{z}, \theta) + BB^* \bar{p}_z, \\ \bar{z}_0 = \hat{z}_0 + P_0 \bar{p_z}, \\ \dot{\bar{p}}_z + \dfrac{\partial f^*}{\partial \bar{z}} \bar{p}_z = -\dfrac{\partial h^*}{\partial \bar{z}} (y_\delta - h(\bar{z}, t)), \\ \bar{p}_z(T) = 0, \\ \dot{\bar{p}}_\theta + \dfrac{\partial f^*}{\partial \bar{\theta}} \bar{p}_\theta = 0, \\ \bar{p}_\theta(T) = 0, \end{cases}$$

and $\bar{z} = z_{|\bar{\xi}_z, \bar{\xi}_\theta, \bar{\nu}}$ is the trajectory associated with the minimization. The solution for such system can be obtained by solving a space-time boundary problem. An alternative is to solve it through a gradient-descent approach which, with some relaxation sequences (ρ_z^k) and (ρ_θ^k), at each iteration $k \in \mathbb{N}$ reads

$$\begin{cases} \xi_z^{k+1} = \xi_z^k - \rho_z^k P_0 \dfrac{\partial \mathcal{J}}{\partial \xi_z}, \\ \xi_\theta^{k+1} = \xi_\theta^k - \rho_\theta^k P_\theta \dfrac{\partial \mathcal{J}}{\partial \xi_\theta}, \\ \nu^{k+1} = B^* p_z^k. \end{cases}$$

and leads equivalently to solve a two-ends problem: a forward one

$$\begin{cases} \dot{z}^k = f(z^k, \theta^k) z^k + BB^* p_z^{k-1}, \\ z^k(0) = \hat{z}_0 + (1 - \rho^k)(z^{k-1}(0) - \hat{z}_0) + \rho^k P_0 p_z^{k-1}(0), \end{cases}$$

and a backward one

$$\begin{cases} p^k + \dfrac{\partial f(z^k, \theta^k)^*}{\partial z} p_z^k = -\dfrac{\partial h^*}{\partial z} (y_\delta - h(z^k, t)), \\ p_z(T) = 0, \\ \dot{p}_\theta^k + \dfrac{\partial f(z^k, \theta^k)^*}{\partial \theta} p_\theta^k = 0, \\ p_\theta(T) = 0. \end{cases}$$

Note that the adjoint is usually derived from the time discrete optimal minimization criterion, that is in turn defined from the discrete physical system, so the two systems presented above are usually employed in their time discrete version.
Though, these are not the only possibilities, the iterative process can be avoided by computing the Hessian of the optimization criterion. However, this option is convenient when the system does not imply many DOFs, because it requires the computation of the inverse of the Hessian matrix. Finally, other methods exist, said 'gradient-free', that are employed in order to avoid the computation of the cost functional's derivative. In this category we can find the evolutionary algorithms, such as the genetic algorithms [Dumas and El Alaoui, 2007] or the covariance matrix adaptation evolution strategy (CMA-ES), the particle swarm optimization (PSO) [Hansen et al., 2011] ot the Nelder-mead method [Fowler et al., 2008].
The method we have presented in this section is known as 4D-Var and aims at finding the optimal trajectory that minimize the discrepancies with respect to observations [Le Dimet and Talagrand, 1986; Robert et al., 2005], when time is not taken into account (e.g. static forward formulation) it is called 3D-Var [Courtier et al., 1998]. This theory was originally

derived for weather predictions [Rabier et al., 2000] and oceanic studies [Devenon et al., 2001]. However, 4D-Var methods applied on non-linear model equations and solved with the above mentioned method require a high computational cost, that increases with the size of the system. Most of the system mentioned above are described by non-linear systems [Robert et al., 2005] and in order to reduce the computational cost, many works have been developed that imply successive minimizations with an increasing T [Blum et al., 1998] or an incremental approach that converges towards the solution [Courtier et al., 1994] using for example non tangent models [Gratton et al., 2007; Lawless et al., 2005].

5.1.2 Sequential methods

Also known as filtering, it retrieves the optimal estimation involving data from past time. It implies the simulation of equations that are similar to those of the forward system and which present a feedback term to correct the discrepancy between data and computed quantities. In the case where only initial conditions have to be estimated the sequential estimator dynamics is of the form

$$\begin{cases} \dot{\hat{z}} = f(\hat{z}, t) + K(y_\delta - h(\hat{z}, t)) \quad \text{in } (0, T), \\ \hat{z}(0) = \hat{z}_0, \end{cases}$$

where K is the filter and the therm $y_\delta - h(\hat{z})$ is called the innovation. The objective is to correct z to converge towards the expected trajectory, that means getting as close as possible to the data. One of the most famous filter is the Kalman filter (KF) [Kalman and Bucy, 1961], that implies the dynamic and observation operators to be linear. Hence, $f(z, t) = Az$ with A a linear dynamic operator and $h(z) = Cz$ a linear observation operator, this leads to the following system

$$\begin{cases} \dot{\hat{z}} = A\hat{z} + PC^*(y - C\hat{z}) \quad \text{in } (0, T), \\ \dot{P} - PA^* - AP + PC^*CP = 0 \quad \text{in } (0, T), \\ P(0) = P_0, \\ \hat{z}(0) = \hat{z}_0, \end{cases}$$

with $P_0 = N_0^{-1}$ the covariance uncertainty. It is possible to observe that here the Kalman filter and the variational methods are equivalent (see for instance [Aussal and Moireau, 2022]). Indeed, the solution of the direct and backward simulation, z_∞ and p_∞ respectively, are linked to the system of the KF by

$$\bar{z}(t) = \hat{z}(t) + P(t)\bar{p}(t), \quad \forall t \in [0, T], \quad \text{hence} \quad \bar{z}(T) = \hat{z}(T).$$

In order to get rid of the limitation of using linear operators, many variations of the classical KF has been developed. In what follows we summarize the most popular Kalman filter methods. First of all, the Extendend Kalman Filter (EKF) [Gelb et al., 1974; Jazwinski, 2007], the idea is to derive a linearized version of the operators to substitute the original ones in the filter equations. The EKF presents the same limitation of the KF concerning the size of the systems it deals with. This point could be solved considering less DOFs in the discretization. It is alike that the discrete optimal filter is directly obtained from the discretized dynamical system. Hence, once derived from the discretized physical system, the two steps involved in the methods: the prediction first and correction then, read

$$\begin{cases} \hat{\vec{Z}}^-_{n+1} = \Phi_{n+1|n}(\vec{Z}^+_n), \\ \mathbf{P}^-_{n+1} = \dfrac{\partial \Phi_{n+1|n}(\vec{Z}^+_n)}{\partial \vec{Z}} \mathbf{P}^+_n \dfrac{\partial \Phi^T_{n+1|n}(\vec{Z}^+_n)}{\partial \vec{Z}}, \end{cases}$$

for the prediction, with $\hat{\vec{Z}}^-_{n+1}$ being the a priori estimation and $\mathbf{P}^-_{n+1}$ the a priori covariance, and

$$\begin{cases} \mathbf{P}^+_{n+1} = \Big(\dfrac{\partial h(\hat{\vec{Z}}^-_{n+1})^T}{\partial \vec{Z}}\mathbf{W}^{-1}_{n+1}\dfrac{\partial h(\hat{\vec{Z}}^-_{n+1})}{\partial \vec{Z}} + (P^-_{n+1})^{-1}\Big)^{-1}, \\ \mathbf{K}_{n+1} = \mathbf{P}^+_{n+1}\dfrac{\partial h(\hat{\vec{Z}}^-_{n+1})}{\partial \vec{Z}}\mathbf{W}^{-1}_{n+1}, \\ \hat{\vec{Z}}^+_{n+1} = \hat{\vec{Z}}^-_{n+1} + \mathbf{K}_{n+1}(\vec{Z}_{n+1} - h(\hat{\vec{Z}}^-_{n+1})), \end{cases}$$

for the correction, with $\mathbf{P}^+_{n+1}$ the a posteriori covariance,$\mathbf{W}^{-1} = \mathbf{M}$ the covariance of the noise, $\mathbf{K}_{n+1}$ the gain of the filter and $\hat{\vec{Z}}^+_{n+1}$ the a posteriori estimation. However, the EKF involves the computation of the tangent operator and it leads to an approximation of the original optimal result. In order to achieve a better estimation, the Unscented Kalman Filter (UKF) [Julier et al., 1995, 2000; Julier and Uhlmann, 2004; Wan and Van Der Merwe, 2000] has been developed. This approach introduces the use of empirical quantities at some specific points instead of the means and covariances involved in the previous method. These particles are placed around $\hat{\vec{Z}}^+_n$ with $\mathbf{P}^+_n$ covariance and spread following the non-linear system. The gain becomes

$$\begin{cases} \mathbf{K}_{n+1} = (\mathbf{P}^{\vec{Z},\vec{Y}}_{n+1})(\mathbf{P}^{\vec{Y},\vec{Y}}_{n+1})^{-1}, \\ \mathbf{P}^{\vec{Z},\vec{Y}}_{n+1} = \sum_{i=1}^d \alpha_i(\vec{Z}^{[i]-}_{n+1} - \hat{\vec{Z}}^-_{n+1})(\vec{Y}^{[i]-}_{n+1} - \vec{Y}^-_{n+1})^T, \\ \mathbf{P}^{\vec{Y},\vec{Y}}_{n+1} = \sum_{i=1}^d \alpha_i(\vec{Y}^{[i]-}_{n+1} - \vec{Y}^-_{n+1})(\vec{Y}^{[i]-}_{n+1} - \vec{Y}^-_{n+1})^T + W_{n+1}, \end{cases}$$

with $\sum_{i=1}^d \alpha_i = 1$ the weights, while the predictions satisfies $\vec{Z}^{[i]-}_{n+1} = \mathbf{A}(\vec{Z}^{[i]+}_n)$ and the observations are defined as

$$\vec{Y}^{[i]-}_{n+1} = h(\vec{Z}^{[i]-}_{n+1}), \;\; \vec{Y}^-_{n+1} = \sum_{i=1}^d \alpha_i \vec{Y}^{[i]}_{n+1}.$$

Finally, the prediction step becomes

$$\begin{cases} \hat{\vec{Z}}^+_{n-1} = \hat{\vec{Z}}_{n+1} + \mathbf{K}_{n+1}(\vec{Y}_{n+1} - \vec{Y}^-_{n+1}), \\ \mathbf{P}^+_{n+1} = \mathbf{P}^-_{n+1} - \mathbf{P}^{\vec{Z},\vec{Y}}_{n+1}(\mathbf{P}^{\vec{Y},\vec{Y}}_{n+1})^{-1}(\mathbf{P}^{\vec{Z},\vec{Y}}_{n+1})^T, \end{cases}$$

for any $\vec{Z}^{[i]+}_{n+1}$. Another approach based on the so-called 'sigma-point' – the chosen particles – is the Ensemble Kalman Filter (EnKF) [Evensen, 1994] that differs from the UKF because it usually relies on more particles and considers many strategies to choose their position. The last two methods have the advantage to avoid both the computation of tangent operators and the solution of two problems – forward and backward – as in the variational approach. Despite the improvements implemented thanks to the introduction of the Sigma-Point KFs the limitation regarding the system size remains one of the main disadvantages of the KFs. The Reduced-Order Extended Kalman Filter (ROEKF), or Singular Evolutive Extended Kalman Filter [Pham et al., 1998], has been introduced with the purpose of getting rid of this limit by using a reduced covariance operator. In this case the prediction-correction steps respectively read

$$\begin{cases} \hat{\vec{Z}}^-_{n+1} = \Phi_{n+1|n}(\vec{Z}^+), \\ \mathbf{L}_{n+1} = \dfrac{\partial \Phi_{n+1|n}}{\partial \vec{Z}}\mathbf{L}_n, \end{cases}$$

and

$$\begin{cases} \mathbf{U}_{n+1} = \mathbf{U}_n + \mathbf{L}_{n+1}^T \dfrac{\partial h(\hat{\vec{Z}}_{n+1}^-)^T}{\partial \vec{Z}} \mathbf{W}_{n+1}^{-1} \dfrac{\partial h(\hat{\vec{Z}}_{n+1}^-)}{\partial \vec{Z}} \mathbf{L}_{n+1}, \\ \mathbf{K}_{n+1} = \mathbf{P}_{n+1}^+ \dfrac{\partial h(\hat{\vec{Z}}_{n+1}^-)^T}{\partial \vec{Z}} \mathbf{W}_{n+1}^{-1}, \\ \hat{\vec{Z}}_{n+1} = \hat{\vec{Z}}_{n+1}^- + \mathbf{K}_{n+1}(\vec{Y}_{n+1} - h(\hat{\vec{Z}}_{n+1}^-), \end{cases}$$

where L is an extension operator such that $\mathbf{P}_n^{n+1} = L_n U_n^{-1} L_n^T$, with U a matrix of small size. The reduced approach can also be applied to the UKF leading to the Reduced-Order Unscented Kalman Filter (ROUKF) [Moireau and Chapelle, 2011], in this approach the sigma-points are placed in the small dimension space. Leading to the following two steps procedure

$$\begin{cases} \hat{\vec{Z}}_{n+1}^{[i]-} = \Phi_{n+1|n}(\hat{\vec{Z}}_n^{[i]+}), \quad \text{with } 1 \leq i \leq r+1, \\ \hat{\vec{Z}}_{n+1}^- = \sum_{i=1}^{r+1} \alpha_i \hat{\vec{Z}}_{n+1}^{[i]-}, \end{cases}$$

for the prediction, while the correction step becomes

$$\begin{cases} \mathbf{L}_{n+1} = [\hat{\vec{Z}}_{n+1}^{[*]-}] \mathbf{D}_\alpha [\vec{I}^{[*]}]^T, \\ \vec{Y}_{n+1}^{[i]-} = \mathbf{C}_{n+1}(\hat{\vec{Z}}_{n+1}^{[i]-}), \\ \vec{Y}_{n+1}^- = \sum_{i=1}^{r+1} \alpha_i \vec{Y}_{n+1}^{[i]-}, \\ \Gamma_{n+1} = [\vec{Y}_{n+1}^{[*]-}] \mathbf{D}_\alpha [\vec{I}^{[*]}]^T, \\ \mathbf{U}^{n+1} = \mathbf{1} + \Gamma_{n+1}^T \mathbf{W}_{n+1}^{-1} \Gamma_{n+1}, \\ \hat{\vec{Z}}_{n+1}^+ = \hat{\vec{Z}}_{n+1}^- - \mathbf{L}_{n+1} \mathbf{U}^{n+1} \Gamma_{n+1}^T \mathbf{W}_{n+1}^{-1} (\vec{Y}_{n+1} - \vec{Y}_n), \end{cases}$$

where $\mathbf{D}_\alpha$ is a diagonal matrix containing the weights, $[\vec{I}^{[*]}]$ the concatenation of the vectors $(\vec{I}^{[i]})_{1 \leq i \leq r+1}$ that represent the unitary sigma-point.
Nowadays, DA methods are used for any kind of application and lead to the estimation of either the state initial conditions, the parameters, or both of them with various techniques. However, in the following section we will focus on the cardiovascular application, as it is the background of this thesis.

5.2 Data assimilations applied to hemodynamics

In this section we inspire from the historical approach of Arthurs et al. [2020].
The application of data assimilation to the cardiovascular field is an evolving topic. The outcome is twofold: first it makes clinical data exploitable, being able to deal with the noise and to extrapolate direct information from indirect measurements, second it improves the models and make them more 'subject-specific'. The estimations investigated concern mainly 'hidden' models parameters (e.g. outlet boundary parameters, cardiac contractility, vessel wall elasticity etc), model state initial conditions or physiological markers hardly accessible by measurements (e.g. blood velocity at central sites). The intent of tuning resistance of outflow boundary conditions to circulation model was first addressed by Schaaf and Abbrecht [1972] by imposing a given blood flow distribution through the different vessels, or in Murray [1926] using bifurcations equations. Olufsen [1999] proposed a semi-analytical approach based on the linearization of Navier-Stokes equations to retrieve the impedance of the structured tree outflow boundary conditions such that the dynamic boundary conditions reproduced physiological values. Later on, Olufsen et al.

[2002] proposed a strategy to calibrate the impedance of the Windkessel model representing the middle cerebral artery by fitting the impedance obtained from Fourier analysis of the flow and pressure measurements. Similarly, Grinberg and Karniadakis [2008] developed a strategy to tune the RC time-dependent parameters without involving either variational nor sequential strategy. Their approach relies on imposing the outlet flow rate in a 3D arterial network. Likewise, Troianowski et al. [2011] used PC-MRI flow rates to obtain, via fixed-point iterations, the total resistance of the 3-element Windkessel model imposed as outlet boundary condition to the 3D model of the pulmonary vessels based on 3D MRA images. A similar approach was used by Blanco et al. [2012] for the outlet resistance of a 1D model of the arterial network, relying on a quasi-Newton method (Broyden's algorithm). Lagrée [2000] focused on the estimation of the vessel elasticity for an artery flow model by using synthetic data of the artery displacements as observations for an optimization problem solved through an adjoint-based method. Martin et al. [2005] relied on a variational approach solved via an adjoint-based optimization to determine the compliance of a one-dimensional arterial model. DeVault et al. [2008] adjusted the boundary conditions of a 1D model representing the Circle of Willis, by means of an EnKF using measurements of pressure and velocity. Spilker and Taylor [2010] developed a method that involves input systolic/diastolic pressure as observations for 3D models of an idealized common carotid artery, an idealized iliac arterial bifurcation and a patient-specific abdominal aorta. The parameters of the outlet Windkessel model are tuned to match the desired pressure and flow waves by solving non-linear equations through a quasi-Newton method. Ismail et al. [2013] tried to overcome the limitation of the initial condition found in [Spilker and Taylor, 2010], in order to do so the researchers involved an adjoint based calibration, avoiding the dependence on previous steps in the optimization. The work of Spilker and Taylor [2010] inspired also the one of Itu et al. [2015], they improved the performance of the algorithm by introducing better guess for the initial solution and by reducing the number of iteration required. D'Elia et al. [2011] proposed a linear inverse problem based on a *Discretize-then-Optimize* variational approach [D'Elia and Veneziani, 2010] and solved it iteratively, it was applied on both a 2D and 3D model geometry for the blood flow to retrieve the optimal boundary condition that match MRI velocity data. Moireau and Chapelle [2011] derived the ROUKF and presented the results obtained for a joint state-parameter estimation to retrieve the contractility of a cardiac model using velocity measurements obtained via tagged-MRI. Perego et al. [2011] relied on a 4D optimization problem to retrieve the Young modulus of a vessel by using synthetic data of vessel displacement, used as observations for a FSI model. Lassila et al. [2013] addressed two inverse problems application, the first one from a deterministic point of view, by minimizing a least-square problems by means of quasi-Newton approximations, and the second one from a statistical point of view through Bayesian uncertainty quantification. The test case chosen are, in order, a material parameter estimation for an FSI model of a stenosed artery by using pressure gradient data and a residual flow uncertainty problem in an occluded femoral artery with a shape optimization of the bypass. Lombardi [2013] proposes a ROUKF to estimate the arterial stiffness of a 1D model of the arterial network using simulated 4D MRI measures and pressure and flow rates at defined locations. In the work of Pant et al. [2014] the parameters for the boundary conditions of a 3D model of the aorta are calibrated upon the estimated parameters of a 0D model through an UKF by using measured flow and pressure. Pant et al. [2017] applied a UKF to a ventricular model [Pant et al., 2016] to estimate lumped parameters model of the heart (e.g. volume, valve cross-section etc.) by using *in vivo* flow measurements at different heart rates. Caiazzo et al. [2017] used the ROUKF for the first time with in vitro data [Alastruey et al., 2011] for the estimation of the terminal resistances of the boundary conditions of a one-dimensional blood flow model

in one numerical simulation and the arterial thickness together with the Young modulus of the arterial wall in another test case. Lal et al. [2017] involved synthetic and experimental data [Saito et al., 2011] and applied the EnKF to estimate the Young modulus and viscoelastic and reflection coefficient at the outlet boundary for a 1D model of the cardiovascular system. Sixou et al. [2017] proposed a sequence of optimal control problems on small time intervals, solved via an adjoint method, where the optimization variable was the fluid velocity in a synthetic fluid flow and the observations the 2D CT projections. Müller et al. [2018] explored the behavior of the ROUKF in the frequency domain to estimate the compliance of a 1D blood flow model and the parameters that affect the cardiac output by using *in vivo* measurements [Reymond et al., 2011]. Arthurs et al. [2020] proposed, for the first time, a ROUKF applied on a 3D model of the aorta with lumped-parameter boundary conditions without involving any intermediate reduced parameters model for the calibration of the higher-order one. In particular they estimated the Windkessel parameters and the stiffness of the vessel wall using synthetic data of pressure, velocity and wall-motion for the validation and patient-specific non invasive data of pressure and velocity for the estimation.

5.3 Discussion

We have seen that the works involving data assimilation for cardiovascular application rely on various strategies. The variational or the sequential approach are involved depending on the data available, the model implied and so the numerical properties of the inverse problem itself. In particular, many aspects have a key role in the choice of the IP method: wether the cardiovascular model is based on a linear or non-linear formulation, the number of DOFs expected after discretization, the flexibility required by the user, the type of noise that affects the data and the time interval in which they are available. In our work we apply the IP on the one-dimensional model presented in Part I, it is a reduced-order model – so it does not involve many DOFs – based on a non-linear formulation. Moreover, the data we want to exploit as observations are some *in vivo* pressure measurements registered via an intra-aortic or intra-radial catheter. The wave record is available at one specific location and for the duration of a cardiac cycle at least. The aim of this work is to be able to estimate the inlet of the cardiovascular model, meaning the central pressure or the blood flow at the beginning of the aorta, by using distal measurements usually accessible during surgeries. This objective represents a step towards an augmented cardiovascular monitoring during general anesthesia. In particular, it could help in preventing dangereous situations, such as hypotension, that often occur during surgeries. Moreover, such a strategy could be integrated within connected devices such as smart whatches or other technologies that give users informations about their cardiovascular activity. In this work, we rely on a 4D-Var approach, which is suitable to control the periodicity of the pressure and flow waves. Moreover, this method is less constraining for what concern the size of the system. In the following we will present the optimal control strategy applied to a linearized aortic model, an extensive analysis of the mathematical and numerical aspects of the method is presented and some preliminary result on a simple test case are shown to display the behavior of the IP in presence of noise and dealing with a sampling mismatch, which can occur quite often when real clinical data are involved. Moreover, we present an iterative algorithm based on a quasi-Newton method [Gratton et al., 2007; Lawless et al., 2005] that allows us to perform the IP with a certain control of the non-linearity impact. Finally, we present the estimations of the central pressure obtained with two test case: first a simple one where the model represents the upper thoracic aorta and the observation is an intra-aortic distal pressure, as in the linear case, second the real application scenario, where the

model includes the main arteries of the upper limb and the central pressure is retrieved by using radial pressure records.

Bibliography

Alastruey, J., Khir, A. W., Matthys, K. S., Segers, P., Sherwin, S. J., Verdonck, P. R., Parker, K. H., and Peiró, J. (2011). Pulse wave propagation in a model human arterial network: assessment of 1-d visco-elastic simulations against in vitro measurements. *Journal of biomechanics*, 44(12):2250–2258.

Arthurs, C. J., Xiao, N., Moireau, P., Schaeffter, T., and Figueroa, C. A. (2020). A flexible framework for sequential estimation of model parameters in computational hemodynamics. *Advanced Modeling and Simulation in Engineering Sciences*, pages 1–37.

Aussal, M. and Moireau, P. (2022). Kernel representation of Kalman observer and associated H-matrix based discretization. working paper or preprint.

Banks, H. T. and Kunisch, K. (2012). *Estimation techniques for distributed parameter systems*. Springer Science & Business Media.

Bertoglio, C. (2012). *Forward and Inverse Problems in Fluid-Structure Interaction. Application to Hemodynamics*. Theses, Université Pierre et Marie Curie - Paris VI.

Blanco, P., Watanabe, S., and Feijóo, R. (2012). Identification of vascular territory resistances in one-dimensional hemodynamics simulations. *Journal of biomechanics*, 45(12):2066–2073.

Blum, J., Luong, B., and Verron, J. (1998). Variational assimilation of altimeter data into a non-linear ocean model: temporal strategies. In *ESAIM: Proceedings*, volume 4, pages 21–57. EDP Sciences.

Bouttier, F. and Courtier, P. (2002). Data assimilation concepts and methods march 1999. *Meteorological training course lecture series. ECMWF*, 718:59.

Caiazzo, A., Caforio, F., Montecinos, G., Müller, L. O., Blanco, P. J., and Toro, E. F. (2017). Assessment of reduced-order unscented kalman filter for parameter identification in 1-dimensional blood flow models using experimental data. *International journal for numerical methods in biomedical engineering*, 33(8):e2843.

Chapelle, D., Fragu, M., Mallet, V., and Moireau, P. (2013). Fundamental principles of data assimilation underlying the verdandi library: applications to biophysical model personalization within euheart. *Med. Biol. Eng. Comput.*, 51(11):1221–1233.

Chavent, G. (2010). *Nonlinear least squares for inverse problems: theoretical foundations and step-by-step guide for applications*. Springer Science & Business Media.

Courtier, P., Andersson, E., Heckley, W., Vasiljevic, D., Hamrud, M., Hollingsworth, A., Rabier, F., Fisher, M., and Pailleux, J. (1998). The ecmwf implementation of three-dimensional variational assimilation (3d-var). i: Formulation. *Quarterly Journal of the Royal Meteorological Society*, 124(550):1783–1807.

Courtier, P., Thépaut, J.-N., and Hollingsworth, A. (1994). A strategy for operational implementation of 4d-var, using an incremental approach. *Quarterly Journal of the Royal Meteorological Society*, 120(519):1367–1387.

D'Elia, M., Perego, M., and Veneziani, A. (2011). A variational data assimilation procedure for the incompressible navier-stokes equations in hemodynamics. *Journal of Scientific Computing*, 52(2):340–359.

D'Elia, M. and Veneziani, A. (2010). Methods for assimilating blood velocity measures in hemodynamics simulations: Preliminary results. *Procedia Computer Science*, 1(1):1231–1239.

DeVault, K., Gremaud, P. A., Novak, V., Olufsen, M. S., Vernières, G., and Zhao, P. (2008). Blood flow in the circle of willis: Modeling and calibration. *Multiscale Modeling and Simulation*, 7(2):888–909.

Devenon, J.-L., Dekeyser, I., Leredde, Y., and Lellouche, J.-M. (2001). Data assimilation method by a variational methodology using the adjoint of a 3-d coastal circulation primitive equation model. *Oceanologica Acta*, 24(5):395–407.

Dumas, L. and El Alaoui, L. (2007). How genetic algorithms can improve a pacemaker efficiency. In *Proceedings of the 9th annual conference companion on Genetic and evolutionary computation*, pages 2681–2686.

Evensen, G. (1994). Sequential data assimilation with a nonlinear quasi-geostrophic model using monte carlo methods to forecast error statistics. *Journal of Geophysical Research: Oceans*, 99(C5):10143–10162.

Fowler, K., Gray, G., and Olufsen, M. (2008). Modeling heart rate regulation—part ii: Parameter identification and analysis. *Cardiovascular engineering*, 8(2):109–119.

Gelb, A. et al. (1974). *Applied optimal estimation*. MIT press.

Gratton, S., Lawless, A. S., and Nichols, N. K. (2007). Approximate gauss–newton methods for nonlinear least squares problems. *SIAM Journal on Optimization*, 18(1):106–132.

Grinberg, L. and Karniadakis, G. E. (2008). Outflow boundary conditions for arterial networks with multiple outlets. *Annals of biomedical engineering*, 36(9):1496–1514.

Hansen, N., Ros, R., Mauny, N., Schoenauer, M., and Auger, A. (2011). Impacts of invariance in search: When cma-es and pso face ill-conditioned and non-separable problems. *Applied Soft Computing*, 11(8):5755–5769.

Ismail, M., Wall, W. A., and Gee, M. W. (2013). Adjoint-based inverse analysis of windkessel parameters for patient-specific vascular models. *Journal of Computational Physics*, 244:113–130.

Itu, L., Sharma, P., Passerini, T., Kamen, A., Suciu, C., and Comaniciu, D. (2015). A parameter estimation framework for patient-specific hemodynamic computations. *Journal of Computational Physics*, 281:316–333.

Jazwinski, A. H. (2007). *Stochastic processes and filtering theory*. Courier Corporation.

Julier, S., Uhlmann, J., and Durrant-Whyte, H. (2000). A new method for the nonlinear transformation of means and covariances in filters and estimators. *IEEE Transactions on Automatic Control*, 45(3):477–482.

Julier, S. J. and Uhlmann, J. K. (2004). Unscented filtering and nonlinear estimation. *Proceedings of the IEEE*, 92(3):401–422.

Julier, S. J., Uhlmann, J. K., and Durrant-Whyte, H. F. (1995). A new approach for filtering nonlinear systems. In *Proceedings of 1995 American Control Conference-ACC'95*, volume 3, pages 1628–1632. IEEE.

Kalman, R. E. and Bucy, R. S. (1961). New results in linear filtering and prediction theory.

Lagrée, P.-Y. (2000). An inverse technique to deduce the elasticity of a large artery. *The European Physical Journal Applied Physics*, 9(2):153–163.

Lal, R. (2017). *Data assimilation and uncertainty quantification in cardiovascular biomechanics*. Theses, Université Montpellier.

Lal, R., Mohammadi, B., and Nicoud, F. (2017). Data assimilation for identification of cardiovascular network characteristics. *International journal for numerical methods in biomedical engineering*, 33(5):e2824.

Lassila, T., Manzoni, A., Quarteroni, A., and Rozza, G. (2013). A reduced computational and geometrical framework for inverse problems in hemodynamics. *International journal for numerical methods in biomedical engineering*, 29(7):741–776.

Lawless, A., Gratton, S., and Nichols, N. (2005). An investigation of incremental 4d-var using non-tangent linear models. *Quarterly Journal of the Royal Meteorological Society*, 131(606):459–476.

Le Dimet, F.-X. and Talagrand, O. (1986). Variational algorithms for analysis and assimilation of meteorological observations: theoretical aspects. *Tellus A: Dynamic Meteorology and Oceanography*, 38(2):97–110.

Lions, J. L. (1973). The optimal control of distributed systems. *Russian Mathematical Surveys*, 28(4):13–46.

Lombardi, D. (2013). Inverse problems in 1D hemodynamics on systemic networks: A sequential approach. *International Journal for Numerical Methods in Biomedical Engineering*, 30(2):160–179.

Lorenc, A. C. (1995). *Atmospheric data assimilation*. Meteorological Office Berkshire, UK.

Martin, V., Clément, F., Decoene, A., and Gerbeau, J.-F. (2005). Parameter identification for a one-dimensional blood flow model. In *ESAIM: Proceedings*, volume 14, pages 174–200. EDP Sciences.

Moireau, P. and Chapelle, D. (2011). Reduced-order unscented kalman filtering with application to parameter identification in large-dimensional systems. *ESAIM: Control, Optimisation and Calculus of Variations*, 17(2):380–405.

Müller, L. O., Caiazzo, A., and Blanco, P. J. (2018). Reduced-order unscented kalman filter with observations in the frequency domain: application to computational hemodynamics. *IEEE Transactions on Biomedical Engineering*, 66(5):1269–1276.

Murray, C. D. (1926). The physiological principle of minimum work. *Proceedings of the National Academy of Sciences*, 12(3):207–214.

Olufsen, M. S. (1999). Structured tree outflow condition for blood flow in larger systemic arteries. *American Journal of Physiology-Heart and Circulatory Physiology*, 276(1):H257–H268.

Olufsen, M. S., Nadim, A., and Lipsitz, L. A. (2002). Dynamics of cerebral blood flow regulation explained using a lumped parameter model. *American Journal of Physiology-Regulatory, Integrative and Comparative Physiology*, 282(2):R611–R622.

Pant, S., Corsini, C., Baker, C., Hsia, T.-Y., Pennati, G., and Vignon-Clementel, I. E. (2017). Inverse problems in reduced order models of cardiovascular haemodynamics: aspects of data assimilation and heart rate variability. *Journal of The Royal Society Interface*, 14(126):20160513.

Pant, S., Corsini, C., Baker, C., Hsia, T.-Y., Pennati, G., Vignon-Clementel, I. E., of Congenital Hearts Alliance (MOCHA) Investigators, M., et al. (2016). Data assimilation and modelling of patient-specific single-ventricle physiology with and without valve regurgitation. *Journal of biomechanics*, 49(11):2162–2173.

Pant, S., Fabrèges, B., Gerbeau, J.-F., and Vignon-Clementel, I. E. (2014). A multiscale filtering-based parameter estimation method for patient-specific coarctation simulations in rest and exercise. In *Statistical Atlases and Computational Models of the Heart. Imaging and Modelling Challenges*, pages 102–109. Springer Berlin Heidelberg.

Perego, M., Veneziani, A., and Vergara, C. (2011). A variational approach for estimating the compliance of the cardiovascular tissue: An inverse fluid-structure interaction problem. *SIAM journal on scientific computing*, 33(3):1181–1211.

Pham, D. T., Verron, J., and Roubaud, M. C. (1998). A singular evolutive extended kalman filter for data assimilation in oceanography. *Journal of Marine systems*, 16(3-4):323–340.

Rabier, F., Järvinen, H., Klinker, E., Mahfouf, J.-F., and Simmons, A. (2000). The ecmwf operational implementation of four-dimensional variational assimilation. i: Experimental results with simplified physics. *Quarterly Journal of the Royal Meteorological Society*, 126(564):1143–1170.

Reymond, P., Bohraus, Y., Perren, F., Lazeyras, F., and Stergiopulos, N. (2011). Validation of a patient-specific one-dimensional model of the systemic arterial tree. *American Journal of Physiology-Heart and Circulatory Physiology*, 301(3):H1173–H1182.

Robert, C., Durbiano, S., Blayo, E., Verron, J., Blum, J., and Le Dimet, F.-X. (2005). A reduced-order strategy for 4d-var data assimilation. *Journal of Marine Systems*, 57(1-2):70–82.

Saito, M., Ikenaga, Y., Matsukawa, M., Watanabe, Y., Asada, T., and Lagrée, P.-Y. (2011). One-dimensional model for propagation of a pressure wave in a model of the human arterial network: Comparison of theoretical and experimental results. *Journal of Biomechanical Engineering*, 133(12).

Schaaf, B. W. and Abbrecht, P. H. (1972). Digital computer simulation of human systemic arterial pulse wave transmission: a nonlinear model. *Journal of Biomechanics*, 5(4):345–364.

Simon, D. (2006). *Optimal state estimation: Kalman, H infinity, and nonlinear approaches*. John Wiley & Sons.

Sixou, B., Boissel, L., and Sigovan, M. (2017). Vascular blood flow reconstruction from tomographic projections with the adjoint method and receding optimal control strategy. *Journal of Physics: Conference Series*, 904:012001.

Spilker, R. L. and Taylor, C. A. (2010). Tuning multidomain hemodynamic simulations to match physiological measurements. *Annals of Biomedical Engineering*, 38(8):2635–2648.

Troianowski, G., Taylor, C. A., Feinstein, J. A., and Vignon-Clementel, I. E. (2011). Three-dimensional simulations in glenn patients: clinically based boundary conditions, hemodynamic results and sensitivity to input data. *Journal of biomechanical engineering*, 133(11).

Wan, E. A. and Van Der Merwe, R. (2000). The unscented kalman filter for nonlinear estimation. In *Proceedings of the IEEE 2000 Adaptive Systems for Signal Processing, Communications, and Control Symposium (Cat. No. 00EX373)*, pages 153–158. Ieee.

CHAPTER 6

Inlet flow recovery from distal pressure in linearized hemodynamics: An optimal control approach

As you see, it is not that I don't know my own mind, I know it very well but only up to a certain point in the matter. I know perfectly well what the question is. It's the answer I want.

— Alessandro Baricco, *Ocean Sea*

The goal of this work is to derive a reliable – stable and accurate – inverse problem strategy for reconstructing cardiac output – blood flow that enters the ascending aorta – from measurements of pressure at a distal site of the arterial tree, assumed here to be the descending aorta. We assume that a reduced one- dimensional model of the aorta can be linearized around its steady state, leading to a wave system with an outlet boundary condition representing the global resisitive and compliant behavior of the distal vessels. Using this model, we aim to reconstruct the inlet flow from a pressure measurement at the distal outlet. First, we study the observability of the problem and prove that the inversion of the flow to pressure input-output operator is mildly ill-posed of degree one, in the space of time-periodic solutions. We then develop a variational approach where we minimize the discrepancy between the measurements and a simulated state and penalize the error with respect to a periodic state. The penalty strategy is shown to be convergent and provides an efficient solution to the minimization. Numerical results illustrate the robustness of our approach to noise and the potential of our method to reconstruct inlet flow from real pressure recordings during anesthesia.

This chapter contains an article submitted to *Inverse problems* and realized in collaboration with Sébastien Imperiale and Philippe Moireau. My contributions include the linearization, the observability results, the discretization of the inverse problems and its implementation as well as the numerical results.

Contents

6.1 Introduction

During general anesthesia, close monitoring of the patient's hemodynamic state is required to avoid episodes of hypotension, which can be very dangerous for the outcome of surgery [Joachim et al., 2017]. Cardiac output (CO) and central aortic pressure (CAP) – located at the heart's outlet – are two markers known to provide important information about the cardiovascular system [Chen et al., 1997]. Indeed, pressure in the ascending aorta is influenced by left ventricular ejection fraction and can be used to derive information about cardiac activity and the arterial system [Fetics et al., 1999; Vlachopoulos et al., 2011]. Direct measurements of CO and CAP are invasive and the data obtained can be very noisy. However, pressure can be recorded at peripheral sites with less invasive techniques and a lower noise level. Although CAP correspond to left ventricular pressures during diastole, they are not equivalent to distal pressures [Pauca et al., 2001]. For this reason, studies have been performed using available peripheral pressure data to access the hemodynamic state at central sites. The most common strategy is to use a transfer function (TF) that relates CAP to pressure at peripheral sites. The TF is usually based on an autoregressive exogenous (ARX) model [Chen et al., 1997; Joachim et al., 2017; Ljung, 1999; Pauca et al., 2001; Stok et al., 2011]. This type of TF has been shown to be more efficient than the one derived by standard Fourier techniques [Fetics et al., 1999]. The TF method is based on the assumption that the influence of upper limb condition on radial pressure varies only slightly between subjects [Millasseau et al., 2003], so it is usually a general function that does not take into account patient characteristics – such as age – that influence important aspects of the circulation. Moreover, this strategy is not able to provide a good prediction for the dicrotic notch (DN) [Fetics et al., 1999], which provides important information about the propagation of the pressure wave in the arterial tree [Politi et al., 2016]. To overcome these limitations, we develop an inverse problem (IP) strategy based on a reduced-order (RO) model of the circulation and, in particular, on a one-dimensional (1D) model, since it is able to capture wave propagation effects [Peiro et al., 2003; Reymond et al., 2009]. This RO model is suitable for representing the larger arteries of the circulation [Matthys et al., 2007; Willemet and Alastruey, 2014], a single vessel [Bollache et al., 2014; Manganotti et al., 2021], or multiple interbranched vessels forming a network [Epstein et al., 2015; Fossan et al., 2018]. Moreover, they can be coupled with data assimilation techniques [D'Elia et al., 2011] to build personalized models and move towards patient-specific simulations [Arthurs et al., 2020; Caiazzo et al., 2017; Lombardi, 2013; Müller et al., 2018]. The IP solution leads to the estimation of the physical parameters of the problems reflecting the hemodynamic characteristics of the patient [Lal et al., 2017; Martin et al., 2005; Moireau et al., 2012] or to the reconstruction of physiological markers, such as fluid velocity in [Sixou et al., 2017]. In this work, we derive a variational IP strategy and apply it to a stable RO model. For the latter, we rely on a stable formulation of a 1D model representing the upper thoracic aorta [Manganotti et al., 2021]. Our data assimilation technique is able to estimate the CO as well as the pressure and blood flow at every location of the thoracic aorta, using the distal pressure in the vessel. The introduction of a model provides the opportunity to adapt the parameters to different clinical conditions and to take advantage of the ability of 1D models to describe wave propagation and to represent important markers such as the DN. In this work, we rely on a linearized formulation for blood flow propagation because we focus on the mathematical analysis of the inverse problem and, in particular, prove an observability result. We believe that such an analysis is a fundamental prerequisite for developing an inversion strategy for the nonlinear blood flow model. However, despite linearizing the original nonlinear model [Manganotti et al., 2021] around a steady state, we are able to obtain good estimates using synthetic noisy data and real clinical data

registered *in vivo* during operations as observations for the inverse problem. In Section 6.2 we present the choice of configuration for the aortic model and its mathematical and numerical non-linear formulation, as well as the linearization around a reference vessel radius. Section 6.3 introduces the analysis of the forward problem that leads to important properties such as the existence and uniqueness of a solution. In Section 6.4 we focus on the inverse problem and we study the observability and we introduce the optimal control approach. Finally, in Section 6.5 we provide a description of the discretized optimization and we show the results obtained with both synthetic and real *in vivo* observations.

6.2 Problem Settings

6.2.1 A non-linear hemodynamics model

The model used in this work derives from the non-linear 1D equations that describe the blood flow in a generic arterial segment. Typically, for all $t > 0$ and $s \in (0, L)$ the blood flow $Q(t, s)$ and the cross section $A(t, s)$ are given by

$$\begin{cases} \partial_t A + \partial_s Q = 0, \\ \partial_t Q + \alpha_{vp} \partial_s \dfrac{Q^2}{A} + \dfrac{A}{\varrho} \partial_s P(A) + k_\nu \dfrac{Q}{A} = 0, \\ P(A) = P_{ext} + \Psi_e(A) + \Psi_v(A), \end{cases} \tag{6.1}$$

where α_{vp} is a coefficient for the velocity profile, ϱ the density of blood and k_ν a dissipative parameter, while $P(A)$ is the pressure inside the vessel, linked to cross-section variations through Ψ_e and Ψ_v that are respectively the elastic and viscoelastic terms of the tube law, and p_{ext} is the external pressure. The model employed in this paper is described in [Manganotti et al., 2021], the formulation is based on an appropriate change of variables so that the energy density of the system becomes quadratic with respect to the new unknowns – φ and v – defined as

$$v := Ru;$$

$$\varphi := \begin{cases} \sqrt{\Psi(\pi R^2)} & R \geq R_0, \\ -\sqrt{\Psi(\pi R^2)} & 0 \leq R < R_0, \end{cases}$$

$$\text{with} \quad \Psi(\pi R^2) = \frac{\beta}{A_0} \left[\frac{2}{3} \pi^{\frac{3}{2}} R^3 - \sqrt{A_0} \pi R^2 + \frac{1}{3} A_0^{\frac{3}{2}} \right],$$

where $R = \sqrt{\frac{A}{\pi}}$ is the radius of the vessel, $u = \frac{Q}{A}$ the blood velocity, β is a parameters that is linked to the Young modulus of the vessel and A_0 the initial cross-section of the arterial segment.
The formulation reads, for all $t \geq 0$ and $s \in (0, L)$

$$\begin{cases} 2\partial_t \varphi + \pi \xi(R) \partial_s (Rv) = 0, \\ \pi \varrho \partial_t v + \dfrac{\pi \varrho}{2} \left(2 \dfrac{v}{R} \partial_s v + v \partial_s \dfrac{v}{R} \right) + \varrho k_\nu \dfrac{v}{R^2} + \pi R \partial_s (\xi(R) \varphi) = 0, \end{cases} \tag{6.2}$$

where $\xi(R)$ is a smooth function of R. At the inlet and outlet of the segment we use the following boundary conditions,

$$\begin{cases} \pi R\,\xi(R)\,\varphi = \dfrac{\pi\varrho}{2}\dfrac{v^2}{R} - \pi R\,P_{tot}, & \text{at } s=0, \\ \pi R\,\xi(R)\,\varphi = -\dfrac{\pi\varrho}{2}\dfrac{v^2}{R} + \pi R\,P_{tot}, & \text{at } s=L, \end{cases} \tag{6.3}$$

with P_{tot} being the total pressure. Moreover, we have

$$\begin{cases} \pi R v = \nu_{in}, & \text{at } s=0, \\ P_{tot} = R_c\big(\pi R v\big) + P_c, & \text{at } s=L, \\ C_c\dot{P}_c = \pi R v - R_{per}^{-1}P_c, & \text{at } s=L, \end{cases} \tag{6.4}$$

where ν_{in} is the input blood flow, P_c the pressure at the outlet of the vessel and R_c, R_{per} and C_c the outlet Windkessel parameters.
In (6.2, 6.3, 6.4) the main unknowns are (v, φ, P_c) whereas P_{tot} at $s=0$ acts as a Lagrange multiplier for the constraint $\pi R v = \nu_{in}$. The problem is completed by periodic conditions in time, i.e., $v(\cdot,0) = v(\cdot,T)$, $\varphi(\cdot,0) = \varphi(\cdot,T)$ and $P_c(0) = P_c(T)$ where T is a heart-beat period.

6.2.2 A linearized hemodynamics model

Our mathematical analysis is carried out on the linearized version of System 6.2 around a reference area and zero blood flow, which corresponds to a linearization around $\varphi = 0$ and $v = 0$ – and this is a benefit of the formulation (6.2) proposed in [Manganotti et al., 2021]. The linearized problem associated with the small perturbations $(\hat{\varphi}, \hat{v})$ is a system of standard 1D dissipative wave equations. For all $t > 0$ and $s \in (0, L)$

$$\begin{cases} 2\partial_t\hat{\varphi} + \pi\,R_0\,\xi\big(R_0\big)\partial_s\hat{v} = 0, \\ \pi\varrho\partial_t\hat{v} + \varrho k_\nu\dfrac{\hat{v}}{R_0^2} + \pi\,R_0\,\xi\big(R_0\big)\partial_s\hat{\varphi} = 0, \end{cases} \tag{6.5}$$

where $R_0 = \Phi^{-1}(0)$. The boundary conditions for (6.5) are deduced from (6.3) and (6.4) and read,

$$\begin{cases} \pi R_0\hat{v} = \nu_{in} & at\ s=0, \\ \xi(R_0)\hat{\varphi} = \pi R_c R_0\hat{v} + \hat{P}_c & \text{at } s=L, \\ C_c\dot{\hat{P}}_c = \pi R_0\hat{v} - R_{per}^{-1}\,\hat{P}_c & \text{at } s=L. \end{cases} \tag{6.6}$$

To ease the presentation, we introduce a set of variables (a, v, P) such that (6.5, 6.6) have a simpler form. More precisely we set,

$$a(s,t) = \sqrt{2}\,\hat{\varphi}(\alpha s, \beta t), \quad v(s,t) = \sqrt{\pi\varrho}\,\hat{v}(\alpha s, \beta t), \quad P(t) = \gamma\hat{P}_c(\beta t),$$

and rewrite (6.5) in the domain $(0,1) = (0, L/\alpha)$. Then, choosing $\alpha = L$ gives, for all $t > 0$ and $s \in (0,1)$

$$\begin{cases} \partial_t a + \dfrac{\beta}{L}\dfrac{\sqrt{\pi}\,R_0\,\xi\big(R_0\big)}{\sqrt{2\varrho}}\partial_s v = 0, \\ \partial_t v + \dfrac{\beta\,k_\nu}{\pi R_0^2}v + \dfrac{\beta}{L}\dfrac{\sqrt{\pi}\,R_0\,\xi\big(R_0\big)}{\sqrt{2\varrho}}\partial_s a = 0. \end{cases} \tag{6.7}$$

and, for all $t > 0$

$$\begin{cases} v(0,t) = \dfrac{\sqrt{\varrho}}{R_0\sqrt{\pi}}\nu_{in}(\beta\, t) = \nu(t) \\ a(1,t) = \dfrac{\sqrt{2\pi}\, R_c\, R_0}{\xi(R_0)\sqrt{\varrho}}v(1,t) + \dfrac{\sqrt{2}}{\gamma\xi(R_0)}P(t), \\ \dot{P}(t) = \beta\gamma\dfrac{\sqrt{\pi}R_0}{C_c\sqrt{\varrho}}v(1,t) - \dfrac{\beta R_{per}^{-1}}{C_c}\, P(t). \end{cases} \tag{6.8}$$

We finally set

$$\frac{\beta}{L}\frac{\sqrt{\pi}\, R_0\, \xi\big(R_0\big)}{\sqrt{2\varrho}} = 1 \Rightarrow \beta = \frac{L\sqrt{2\varrho}}{\sqrt{\pi}R_0\xi(R_0)},$$

and

$$\frac{\sqrt{2}}{\gamma\xi(R_0)} = \beta\gamma\frac{\sqrt{\pi}R_0}{C_c\sqrt{\varrho}} \Rightarrow \gamma^2 = \frac{C_c}{L},$$

for symmetry reasons.

6.2.3 Statement of the problem

Following the developments of the previous section we consider the following 1D wave propagation problem: find $a(s,t)$ and $v(s,t)$ in $(0,1)\times[0,T]$ solution of

$$\begin{cases} \partial_t a(s,t) + \partial_s v(s,t) = 0, \\ \partial_t v(s,t) + \partial_s a(s,t) + k\, v(s,t) = 0, \end{cases} \tag{6.9}$$

where $k > 0$ accounts for dissipative effects. This system is completed with boundary conditions that involves an input $\nu(t)$ at $s = 0$ as well as a new unknown $P(t) \in \mathbb{R}$ at $s = 1$. More precisely, we have

$$v(0,t) = \nu(t), \quad \begin{cases} a(1,t) = k_r\, v(1,t) + c_r\, P(t), \\ \dot{P}(t) + RP(t) - c_r\, v(1,t) = 0. \end{cases} \tag{6.10}$$

Above, k_r and R account for dissipation while c_r is a coupling coefficient. To close the set of equations we consider periodic initial conditions

$$(a(0), v(0), P(0)) = (a(T), v(T), P(T)), \tag{6.11}$$

for some given time period T.

We can now define the inverse problem that is the main focus of this paper. Given a noisy measurement of the output pressure $P(t), t \in [0,T]$, can we propose a stable – with respect to the measurement noise – reconstruction of the input flow $\nu(t)$?

6.3 The forward problem

6.3.1 Semigroup formalism

Let us first assume that the problem (6.9, 6.10) is completed with the initial conditions

$$(a(0), v(0), P(0)) = (a_0, v_0, P_0). \tag{6.12}$$

Now, to write (6.9, 6.10, 6.12) in an abstract form, we first introduce the state space

$$\mathcal{Z} = \mathrm{L}^2(0,1) \times \mathrm{L}^2(0,1) \times \mathbb{R},$$

that is an Hilbert space equipped with the scalar product: for all $z = (a, v, P) \in \mathcal{Z}$ and $q = (b, w, Q) \in \mathcal{Z}$,

$$(z, q)_{\mathcal{Z}} = (v, w)_{\mathrm{L}^2(0,1)} + (v, w)_{\mathrm{L}^2(0,1)} + PQ.$$

We then define the operator $(A, \mathcal{D}(A))$ by

$$A = \begin{pmatrix} 0 & -\partial_s & 0 \\ -\partial_s & -k & 0 \\ 0 & c_r\gamma_r & -R \end{pmatrix} \tag{6.13}$$

with γ_r the trace operator in $s = 1$ and

$$\mathcal{D}(A) := \Big\{(a, v, P) \in \mathrm{H}^1(0,1) \times \mathrm{H}^1_\ell(0,1) \times \mathbb{R} \,|\, a(1) = k_r v(1) + c_r P\Big\}, \tag{6.14}$$

where $\mathrm{H}^1_\ell(0,1) = \{w \in \mathrm{H}^1(0,1) \,|\, w(0) = 0\}$.

Proposition 6.3.1 *The operator $(A, \mathcal{D}(A))$ is maximal dissipative.*

Proof: Proofs of such result are rather classical, however the maximal property is subject to technicalities to invert a right hand side in $\mathcal{Z}$. To this end, we propose a proof based on T-coercivity [Ciarlet, 2012] in 6.7.1 ■

We here recall that as A is maximal dissipative, it is the generator of C^0-semigroup of contraction $\Phi : \mathbb{R}^+ \ni t \mapsto e^{tA} \in \mathcal{L}(\mathcal{Z})$, allowing to define solutions of

$$\begin{cases} \dot{z} = Az, & \text{in } (0,T), \\ z(0) = z_0, \end{cases} \tag{6.15}$$

that corresponds to solutions of (6.9, 6.10, 6.12). If $z_0 \in \mathcal{D}(A)$, then $z \in \mathrm{C}^1([0,T]; \mathcal{Z}) \cap \mathrm{C}^0([0,T]; \mathcal{D}(A))$ defined by

$$z(t) = e^{tA} z_0 \tag{6.16}$$

will be called a *strict* solution of the homogeneous problem. If $z_0 \in \mathcal{Z}$, then $z \in \mathrm{C}^0([0,T]; \mathcal{Z})$ defined by (6.16) will be called a *mild* solution of the homogeneous problem.

In a second step, we need to characterize the adjoint operator of A that is well defined since $\mathcal{D}(A)$ is dense in $\mathcal{Z}$. Given the space

$$\mathcal{D}(A^*) = \left\{ q \in \mathcal{Z} \;\middle|\; \sup_{z \in \mathcal{D}(A),\, z \neq 0} \frac{|(Az, q)_{\mathcal{Z}}|}{\|z\|_{\mathcal{Z}}} < +\infty \right\}, \tag{6.17}$$

the adjoint operator A^* is the unique operator such that $(Az, q)_{\mathcal{Z}} = (z, A^* q)_{\mathcal{Z}}$, for all $z \in \mathcal{D}(A)$ and all $q \in \mathcal{D}(A^*)$.

Lemma 6.3.2 *We have*

$$A^* = \begin{pmatrix} 0 & \partial_s & 0 \\ \partial_s & -k & 0 \\ 0 & -c_r\gamma_r & -R \end{pmatrix} \tag{6.18}$$

with

$$\mathcal{D}(A^*) = \{(b, w, Q) \in \mathrm{H}^1(0,1) \times \mathrm{H}^1_\ell(0,1) \times \mathbb{R} \,|\, b(1) = -k_r w(1) + c_r Q\}$$

Proof: Choosing $z = (a, v, P) \in \mathcal{D}(A)$ and $q = (b, w, Q) \in \big[\mathrm{H}^1(0,1) \times \mathrm{H}^1(0,1) \times \mathbb{R}\big]$, we obtain, using (6.7.1), that $(Az, q)_{\mathcal{Z}} = (\!(z, q)\!) + \langle z, q\rangle$ with

$$(\!(z, q)\!) = (b', v)_{\mathrm{L}^2(0,1)} + (w', a)_{\mathrm{L}^2(0,1)} - k(w, v)_{\mathrm{L}^2(0,1)} - RPQ,$$

and, since $z \in \mathcal{D}(A)$,

$$\begin{aligned} \langle z, q\rangle &= -b(1)v(1) - w(1)a(1) + w(0)a(0) + c_r v(1)Q \\ &= -v(1)\big(b(1) + k_r w(1) - c_r Q\big) - c_r w(1)P + w(0)a(0). \end{aligned}$$

Since $(\!(\cdot, q)\!)$ is obviously a continuous linear form on $\mathcal{Z}$ for all $q \in \big[\mathrm{H}^1(0,1) \times \mathrm{H}^1(0,1) \times \mathbb{R}\big]$, the space $\mathcal{D}(A^*)$ should be chosen as an appropriate subspace such that $\langle \cdot, q\rangle$ is also a continuous linear form on $\mathcal{Z}$. It can then be proven that this implies

$$w(0) = 0, \quad b(1) = -k_r w(1) + c_r Q,$$

hence fixing $\mathcal{D}(A^*)$. Then we get that $\langle z, q\rangle = -c_r w(1)P$ which implies that for all $(z, q) \in \mathcal{Z} \times \mathcal{D}(A^*)$,

$$(z, A^*q)_{\mathcal{Z}} = (\!(z, q)\!) - c_r w(1)P, \tag{6.19}$$

which defines A^* as expected. ■

Note that using the adjoint definition, we have that any mild solution $z \in \mathrm{C}^0([0,T]; \mathcal{Z})$ of the homogeneous problem (6.15) also belongs to $\mathrm{C}^1([0,T]; \mathcal{D}(A^*)')$, see [Tucsnak and Weiss, 2009, Thm. 4.1.6].

6.3.2 Non-homogeneous problem

To deal with the non-homogeneous problem, that is the problem when considering ν non-zero, we first need to introduce a lifting of ν. To do so, let us consider the solution $(a_\nu, v_\nu, P_\nu) \in \mathrm{H}^1(0,1) \times \mathrm{H}^1(0,1) \times \mathbb{R}$ of

$$\begin{cases} v_\nu'(s) = 0, & s \in (0,1) \\ a_\nu'(s) + k v_\nu(s) = 0, & s \in (0,1) \\ a_\nu(1) = k_r v_\nu(1) + c_r P_\nu, & \\ RP_\nu = c_r v_\nu(1), & \\ v_\nu(0) = \nu. & \end{cases} \tag{6.20}$$

namely

$$\begin{cases} a_\nu(s) = \Big(k(1-s) + k_r + C\dfrac{c_r}{R}\Big)\,\nu, & s \in (0,1) \\ v_\nu(s) = \nu, & s \in (0,1) \\ P_\nu = \dfrac{c_r}{R}\nu. & \end{cases} \tag{6.21}$$

This allows to introduce the Dirichlet mapping

$$D_\ell : \left| \begin{array}{ccc} \mathbb{R} & \to & \mathcal{Z} \\ \nu & \mapsto & z = (a_\nu, v_\nu, P_\nu) \text{ solution of (6.20).} \end{array} \right. \tag{6.22}$$

In the spirit of [Bensoussan et al., 2007], giving $\nu \in \mathrm{H}^1(0,T)$, a solution $z = (a, v, P)$ of (6.9,6.10,6.12) can then be defined from

$$\tilde{z} = z - D_\ell \nu, \tag{6.23}$$

such that $\tilde{z} = (\tilde{a}, \tilde{v}, \tilde{P})$ is solution of

$$\left\{ \begin{array}{ll} \partial_t \tilde{a}(s,t) + \partial_x \tilde{v}(s,t) = -\partial_t a_\nu(s,t), & (s,t) \in (0,1) \times (0,T) \\ \partial_t \tilde{v}(s,t) + \partial_x \tilde{a}(s,t) + k\, \tilde{v}(s,t) = -\partial_t v_\nu(s,t), & (s,t) \in (0,1) \times (0,T) \\ \dot{\tilde{P}}(t) + R\tilde{P}(t) - c_r\, \tilde{v}(1,t) = -\dot{P}_\nu(t), & t \in (0,T) \end{array} \right.$$

with the boundary conditions and the initial conditions

$$\left\{ \begin{array}{ll} \tilde{v}(0,t) = 0, & t \in (0,T) \\ \tilde{a}(1,t) = k_r \tilde{v}(1,t) + c_r \tilde{P}(t), & t \in (0,T) \end{array} \right. \qquad \left\{ \begin{array}{ll} \tilde{a}(s,0) = a_0 - a_{\nu(0)}, & s \in (0,1) \\ \tilde{v}(s,0) = v_0 - v_{\nu(0)}, & s \in (0,1) \\ \tilde{P}(0) = P_0 - P_{\nu(0)}. & \end{array} \right.$$

Namely, $\tilde{z}$ is solution of

$$\left\{ \begin{array}{l} \dot{\tilde{z}} = A\tilde{z} + D_\ell \dot{\nu}(t), \quad t \in (0,T), \\ \tilde{z}(0) = z_0 - D_\ell \nu(0), \end{array} \right. \tag{6.24}$$

Following [Bensoussan et al., 2007], we have used in (6.24) the following abuse of notation: the operator A is in fact an extension of $(A, \mathcal{D}(A))$ as an operator in $\mathcal{D}(A^*)'$ with a dense domain that is identified with $\mathcal{Z}$, hence the two equations of (6.24) should be understood in $\mathcal{D}(A^*)'$.

The standard semi-group theory can be used to show existence and uniqueness result for (6.24). Namely, when $z_0 - D_\ell \nu(0) \in \mathcal{Z}$ (note that it suffices that $z_0 \in \mathcal{Z}$) and $\nu \in \mathrm{H}^2(0,T)$, there exists one and only one solution $\tilde{z} \in \mathrm{C}^0([0,T]; \mathcal{Z}) \cap \mathrm{C}^1([0,T]; \mathcal{D}(A^*)')$ obtained from the Duhamel formulae, namely for all $t \in [0,T]$,

$$\begin{aligned} \tilde{z}(t) &= e^{tA}\tilde{z}_0 + \textstyle\int_0^t e^{(t-s)A} D_\ell \dot{\nu}(s)\, \mathrm{d}s \\ &= e^{tA} z_0 - e^{tA} D_\ell \nu(0) + \left[e^{(t-s)A} D_\ell \nu(s) \right]_0^t - \textstyle\int_0^t e^{(t-s)A} A D_\ell \nu(s)\, \mathrm{d}s \\ &= e^{tA} z_0 - D_\ell \nu(t) - \textstyle\int_0^t e^{(t-s)A} A D_\ell \nu(s)\, \mathrm{d}s. \end{aligned}$$

Therefore, when $z_0 \in \mathcal{Z}$ and $\nu \in \mathrm{H}^2(0,T)$, there exists a unique solution of (6.9, 6.10, 6.12), it satisfies,

$$z = (a, v, P) \in \mathrm{C}^0([0,T]; \mathcal{Z}) \cap \mathrm{C}^1([0,T]; \mathcal{D}(A^*)')$$

and is expressed by the Duhamel formulae

$$\forall t \in [0,T], \quad z(t) = e^{tA} z_0 - \int_0^t e^{(t-s)A} A D_\ell \nu(s)\, \mathrm{d}s, \tag{6.25}$$

hence is solution of the dynamics

$$\begin{cases} \dot{z} = Az + B\nu, & \text{in } (0,T) \\ z(0) = z_0, \end{cases} \tag{6.26}$$

where $B = -AD_\ell \in \mathcal{L}(\mathbb{R}, \mathcal{D}(A^*)')$ should be understood in the following sense: for all $\nu \in \mathbb{R}$ and $q = (b, w, Q) \in \mathcal{D}(A^*)$

$$\begin{aligned} -\langle B\nu, q\rangle_{\mathcal{D}(A^*)',\mathcal{D}(A^*)} &= \langle AD_\ell\nu, q\rangle_{\mathcal{D}(A^*)',\mathcal{D}(A^*)} \\ &= (D_\ell\nu, A^*q)_{\mathcal{Z}} \\ &= (b', v_\nu)_{\mathrm{L}^2(0,1)} + (w', a_\nu)_{\mathrm{L}^2(0,1)} - k(w,v)_{\mathrm{L}^2(0,1)} \\ &\quad -c_r w(1)P - RPQ \\ &= b(1)v_\nu(1) - b(0)v_\nu(0) + w(1)a_\nu(1) - w(0)a_\nu(0) \\ &\quad -c_r w(1)P - RPQ \\ &= -b(0)\nu, \end{aligned}$$

giving additionally $B^* = (\delta_0, 0, 0) \in \mathcal{L}(\mathcal{D}(A^*), \mathbb{R})$ where δ_0 is the trace operator in $s = 0$. As $B \in \mathcal{L}(\mathbb{R}, \mathcal{D}(A^*)')$, we can introduce the operator

$$\Lambda \in \mathcal{L}\big(L^2(0,T)), C^0([0,T]; \mathcal{D}(A^*)')\big)$$

defined by

$$(\Lambda\nu)(t) = -\int_0^t e^{(t-s)A} B\nu(s)\,\mathrm{d}s. \tag{6.27}$$

Proposition 6.3.3 *The operator B is an admissible control operator for the semi-group associated with A, that is to say,*

$$\Lambda \in \mathcal{L}\big(L^2(0,T)), C^0([0,T]; \mathcal{Z})\big). \tag{6.28}$$

Proof: Following [Tucsnak and Weiss, 2009, Theorem 4.4.3], we are going to prove that B^* is an admissible observation operator for Φ^*, the semigroup associated with A^*. Let us denote by $q_0 \in \mathcal{D}(A^*)$, and $q \in C^1([0,T]; \mathcal{Z}) \cap C^0([0,T]; \mathcal{D}(A^*))$ the solution of $\dot{q} = A^*q$, $q(0) = q_0$. The adjoint operator A^* is also maximal dissipative, hence $q = (b, w, Q) \in \mathrm{C}^1([0,T; \mathcal{Z})] \cap \mathrm{C}^0([0,T; \mathcal{D}(A)^*)]$ is solution to

$$\begin{cases} \partial_t b(s,t) - \partial_s w(s,t) = 0, & (s,t) \in (0,1)\times(0,T) \\ \partial_t w(s,t) - \partial_s b(s,t) + k\, w(s,t) = 0, & (s,t) \in (0,1)\times(0,T) \\ \dot{Q}(t) + RQ(t) + c_r w(r,t) = 0, & t \in (0,T) \end{cases} \tag{6.29}$$

with boundary conditions

$$\begin{cases} w(0,t) = 0, & t \in (0,T) \\ b(1,t) = -k_r w(1,t) + c_r Q(t). & t \in (0,T) \end{cases} \tag{6.30}$$

Let us introduce a multiplier $m \in C^1([0,1])$ to be specified later. We multiply the first equation of (6.29) by $m(s)w(s,t)$ and the second one by $m(s)b(s,t)$. We integrate with respect to time and space, after summation, we get

$$\begin{aligned} -\frac{1}{2}\int_0^T \int_0^1 m\,\partial_s(b^2 + w^2)\,\mathrm{d}s\,\mathrm{d}t = & -\textstyle\int_0^T\int_0^1 m\,\partial_t(b\,w)\,\mathrm{d}s\,\mathrm{d}t \\ & + \textstyle\int_0^T\int_0^1 m\,b\,w\,\mathrm{d}s\,\mathrm{d}t. \end{aligned}$$

Using by parts integration and Young's inequality we arrive at

$$-\frac{1}{2}\int_0^T [m(b^2+w^2)]_0^1 \,\mathrm{d}t \leq \mathcal{F}_m(T) + \mathcal{F}_m(0) + \int_0^T \mathcal{F}_m(t) + \mathcal{F}_{|m'|}(t)\,\mathrm{d}t$$

where, for any smooth function $n \in C^0([0,1])$ (here $n = m$ or $n = |m'|$),

$$\mathcal{F}_n(t) = \frac{1}{2}\int_0^1 n(s)\left(b^2(s,t) + w^2(s,t)\right)\mathrm{d}s.$$

Now choosing $m(s) = 1 - s$ and denoting $\mathcal{F}(t)$ the functional $\mathcal{F}_m(t)$ with $m \equiv 1$ we obtain that

$$\frac{1}{2}\int_0^T b^2(0,t)\,\mathrm{d}t \leq \mathcal{F}(T) + \mathcal{F}(0) + 2\int_0^T \mathcal{F}(t)\,\mathrm{d}t.$$

Since one can easily shows by standard energy estimates that $\mathcal{F}(t) \leq \frac{1}{2}\|q_0\|_{\mathcal{Z}}^2$ for all $t > 0$, we finally obtain

$$\int_0^T b^2(0,t)\,\mathrm{d}t \leq 2\left(1+T\right)\|q_0\|_{\mathcal{Z}}^2.$$

Moreover, since $b(0,t) = B^*\Phi^*(t)q_0$ we have shown that, for all $T > 0$, there exists a constant $c_{st}(T)$ such that

$$\forall q_0 \in \mathcal{D}(A^*), \quad \int_0^T |B^*\Phi^*(t)q_0|^2\,\mathrm{d}t \leq c_{st}(T)\|q_0\|_{\mathcal{Z}}^2$$

ensuring that B^* is an admissible control operator for Φ^*, hence B is an admissible observation operator for Φ. ■

We finally obtain the existence result for our problem (6.9, 6.10, 6.12) by the mean of the abstract dynamics (6.26). When $\nu \in \mathrm{L}^2(0,T)$, and $z_0 \in \mathcal{Z}$, we have from [Tucsnak and Weiss, 2009, Proposition 4.2.5] the existence of a solution

$$z = (a, v, P) \in \mathrm{C}^0([0,T];\mathcal{Z})$$

given by (6.25), i.e.,

$$\forall t \in [0,T], \quad z(t) = e^{tA}z_0 + (\Lambda\nu)(t). \tag{6.31}$$

When $\nu \in \mathrm{H}^1(0,T)$, and $z_0 \in \mathcal{Z}$ satisfies,

$$Az_0 + B\nu(0) \in \mathcal{Z},$$

then, the solution of (6.26) satisfies

$$z = (a, v, P) \in \mathrm{C}^1([0,T];\mathcal{Z}). \tag{6.32}$$

Corollary 6.3.3.1 *When $\nu \in \mathrm{H}^1(0,T)$, $z_0 = (a_0, v_0, P_0) \in \mathrm{H}^1(0,1) \times \mathrm{H}^1(0,1) \times \mathbb{R}$ and*

$$v_0(0) = \nu(0), \quad a_0(1) = k_r\, v_0(1) + c_r\, P_0, \tag{6.33}$$

then the unique solution of (6.26) satisfies

$$z = (a, v, P) \in \mathrm{C}^1([0,T];\mathcal{Z}) \cap \mathrm{C}^0([0,T];\mathrm{H}^1(0,1) \times \mathrm{H}^1(0,1) \times \mathbb{R}),$$

and the boundary conditions

$$v(0,t) = \nu(t), \quad a(1,t) = k_r\, v(1,t) + c_r\, P(t).$$

This solution is called the strict solution of the non-homogeneous problem (6.26)

Proof: The first step is to apply [Tucsnak and Weiss, 2009, Proposition 4.2.10] to prove that the unique solution of (6.26) belongs to $\mathrm{C}^1([0,T];\mathcal{Z})$. To do so, one should check that $Az_0 + B\nu(0)$ – a priori an element of $\mathcal{D}(A^*)'$ – can be identified with an element of $\mathcal{Z}$. We have, for all $q = (b, w, Q) \in \mathcal{D}(A^*)$, using (6.19) and (6.27),

$$\begin{aligned}\langle Az_0 + B\nu(0), q\rangle_{\mathcal{D}(A^*)',\mathcal{D}(A^*)} &= (z_0, A^*q)_{\mathcal{Z}} + b(0)\nu(0)\\ &= (\!(z,q)\!) - c_r w(1)P_0 + b(0)\nu(0).\end{aligned}$$

Integrating by parts yields

$$\begin{aligned}\langle Az_0 + B\nu(0), q\rangle_{\mathcal{D}(A^*)',\mathcal{D}(A^*)} = \; & -(b, v_0')_{\mathrm{L}^2(0,1)} - (w, a_0')_{\mathrm{L}^2(0,1)} - k(w,v)_{\mathrm{L}^2(0,1)}\\ & + b(1)v_0(1) - b(0)v_0(0) + w(1)a_0(1)\\ & - RPQ - c_r w(1)P_0 + b(0)\nu(0),\end{aligned}$$

using now that $b(1) = -k_r w(1) + c_r Q$ – since $q \in \mathcal{D}(A^*)$ – and (6.33), one can simplify the equation above,

$$\begin{aligned}\langle Az_0 + B\nu(0), q\rangle_{\mathcal{D}(A^*)',\mathcal{D}(A^*)} &= -(b, v_0')_{\mathrm{L}^2(0,1)} - (w, a_0')_{\mathrm{L}^2(0,1)} - k(w,v)_{\mathrm{L}^2(0,1)}\\ &\quad - RPQ + c_r Q v_0(1).\end{aligned}$$

This shows that $Az_0 + B\nu(0)$ can be identified with an element of $\mathcal{Z}$, hence the regularity $\mathrm{C}^1([0,T];\mathcal{Z})$ of the solution. This last regularity property implies in particular that $Az + B\nu$ can be identified with an element of $\mathrm{C}^0([0,T];\mathcal{Z}), \dot{z}$ to be specific, and with the same computations as before, but using a function $q \in \mathcal{D}(A^*)$ with (b, w) with compact support and $Q = 0$,

$$\begin{aligned}\langle Az + B\nu, q\rangle_{\mathcal{D}(A^*)',\mathcal{D}(A^*)} &= (\dot{z}, q)_{\mathcal{Z}} = (b, \dot{v})_{\mathrm{L}^2(0,1)} + (w, \dot{a})_{\mathrm{L}^2(0,1)}\\ &= -(b, v')_{\mathrm{L}^2(0,1)} - (w, a')_{\mathrm{L}^2(0,1)} - k(w,v)_{\mathrm{L}^2(0,1)}.\end{aligned}$$

This equality implies that (6.9) are satisfied in a strong sense, hence (a, v) belong to $\mathrm{C}^0([0,T];\mathrm{H}^1(0,1)\times\mathrm{H}^1(0,1))$. Now, for any, $q \in \mathcal{D}(A^*)$ with $Q = 0$, we have

$$(\dot{z}, q)_{\mathcal{Z}} = (\!(z,q)\!) - c_r w(1)P + b(0)\nu(t).$$

Integration by part yields, after simplifications,

$$0 = -k_r w(1)v(1,t) - b(0)v(0,t) + w(1)a(1,t) - c_r w(1)P(t) + b(0)\nu(t).$$

Choosing $Q = 0$ and $w(1) = 0$ we deduce that $v(0,t) = \nu(t)$. Then, choosing again $Q = 0$ we deduce that $a(1,t) = k_r\, v(1,t) + c_r\, P(t)$. ■

6.3.3 Periodic solutions

We now expect to prove an additional fundamental property for the homogeneous problem (6.15), namely that the associated semigroup satisfies for all $t \in [0,T]$, $\|\Phi(t)\|_{\mathcal{L}(\mathcal{Z})} < \rho < 1$, which will later be used to prove the existence of periodic solutions for our model (6.9, 6.10, 6.12) or equivalently for the abstract dynamic (6.26).

The energy functional. Let $m \in C^1([0,1])$ be a smooth function, We denote by $\mathcal{E}(t)$ the energy of system (6.9), defined by

$$\forall t > 0, \quad \mathcal{E}(t) := \frac{1}{2}\int_0^1 \Big(a^2(s,t) + v^2(s,t)\Big)\,\mathrm{d}s + \frac{1}{2}P^2(t).$$

We have the so-called energy identity.

Lemma 6.3.4 *Any strict solution z in the sense of Corollary 6.3.3.1 satisfies for all $t \in [0,T]$,*

$$\mathcal{E}(t) + k\int_0^t\int_0^1 v^2(s,\tau)\,\mathrm{d}s\,\mathrm{d}\tau + \int_0^t k_r v^2(1,\tau)\,\mathrm{d}\tau + \int_0^t RP^2(\tau)\,\mathrm{d}\tau = \mathcal{E}(0) + \int_0^t \nu(\tau)a(0,\tau)\,\mathrm{d}\tau. \tag{6.34}$$

Proof: We multiply the first equation of (6.9) by $a(s,t)$ and the second one by $v(s,t)$. We integrate with respect to time and space, after summation, and integration by part we get

$$\frac{1}{2}\int_0^1 a^2(s,t) + v^2(s,t)\,\mathrm{d}s + \int_0^t\int_0^1 k\,v^2(s,\tau)\,\mathrm{d}s\,\mathrm{d}\tau + \int_0^t v(1,\tau)a(1,\tau)\,\mathrm{d}\tau = \frac{1}{2}\int_0^1 a^2(s,0) + v^2(s,0)\,\mathrm{d}s + \int_0^t v(0,\tau)a(0,\tau)\,\mathrm{d}\tau. \tag{6.35}$$

Then, we multiply the second equation of (6.10) by $P(t)$ and integrate with respect to time to obtain

$$\frac{1}{2}\big(P^2(t) - P^2(0)\big) + \int_0^t (R\,P^2(\tau) - c_r\,v(1,\tau)\,P(\tau))\,\mathrm{d}\tau = 0. \tag{6.36}$$

Substituting (6.36) in (6.35) gives (6.34). ■

Note that the previous lemma, justifies the classical energy balance of (6.15), namely, we have, in absence of input source ν,

$$\forall t > 0, \quad \mathcal{E}(t) \leq \mathcal{E}(0), \tag{6.37}$$

consistent with the dissipative aspect of $(A, \mathcal{D}(A))$. In fact we have an even stronger property.

Theorem 6.3.5 *Assume that $\nu = 0$, then for every $t_0 > 0$ there exists $\varrho < 1$ such that, any mild solution $z = (a, v, P) \in \mathrm{C}^0([0,T];\mathcal{Z})$ of (6.15) satisfies,*

$$\forall t \geq t_0 > 0, \quad \mathcal{E}(t) \leq \varrho\,\mathcal{E}(0). \tag{6.38}$$

Proof: We first show that (6.38) is true for strict solutions in $\mathrm{C}^1([0,T];\mathcal{Z}) \cap \mathrm{C}^0([0,T];\mathcal{D}(A))$. The result is then extended to mild solution by density arguments. The proof of (6.38) for strict solutions is obtained by contradiction. If (6.38) does not hold there exists a sequence of solutions $\{(a_n, v_n, P_n)\}_{n>0}$ such that the corresponding energy functional $\mathcal{E}_n(t)$ satisfies for some $t_1 > 0$,

$$\mathcal{E}_n(0) = 1 \quad \text{and} \quad \lim_{n\to+\infty} \mathcal{E}_n(t_1) = 1. \tag{6.39}$$

Note that the energy relation (6.34) holds since strict solutions of the homogeneous problem are in particular strict solutions of the non-homogeneous problem with $\nu = 0$. Therefore, since $\mathcal{E}_n$ is a decaying function of time, we deduce that, thanks to the energy relation (6.34), that for all $\tau \leq t_1$,

$$\lim_{n\to+\infty} \left(\int_0^\tau \int_0^1 v_n^2(s,t)\,\mathrm{d}s\,\mathrm{d}t + \int_0^\tau v_n^2(1,t)\,\mathrm{d}t + \int_0^\tau P_n^2(t)\,\mathrm{d}t \right) = 0. \tag{6.40}$$

Moreover, using the boundary conditions (6.10), we also have, for all $\tau \leq t_1$,

$$\lim_{n\to+\infty} \int_0^\tau a_n^2(1,t)\,\mathrm{d}t = 0. \tag{6.41}$$

Let us then rely on a multiplier strategy by multiplying the first equation of (6.9) by $s\,t\,v(s,t)$ and the second one by $s\,t\,a(s,t)$ and integrating with respect to time and space, we get after summation

$$\int_0^\tau \int_0^1 \left(\partial_t(s\,t\,a\,v) + s\,t\,\partial_s \frac{v^2}{2} + s\,t\,\partial_s \frac{a^2}{2} + s\,(k\,t-1)\,a\,v \right) \mathrm{d}s\,\mathrm{d}t = 0.$$

Integrating by parts and rearranging terms shows that, for all strict solutions of (6.9) with $\nu = 0$ and all $\tau > 0$,

$$\begin{aligned} \frac{1}{2}\int_0^\tau \int_0^1 t\,a^2\,\mathrm{d}s\,\mathrm{d}t = \frac{1}{2}\int_0^\tau \left(v^2(1,t) + a^2(1,t)\right)\mathrm{d}t. \\ + \int_0^1 s\,\tau\,a\,v\,(s,\tau)\,\mathrm{d}s + \frac{1}{2}\int_0^\tau \int_0^1 \left(2\,(k\,t-1)\,s\,a\,v\, - t\,v^2\right)\mathrm{d}s\,\mathrm{d}t. \end{aligned} \tag{6.42}$$

Thanks to (6.42) applied to our sequence of solutions $\{(a_n, v_n, P_n)\}_{n>0}$ and thanks to (6.40) and (6.41) we deduce that, for all $\tau \leq t_1$,

$$\liminf_{n\to+\infty} \int_0^\tau \int_0^1 t\,a_n^2\,\mathrm{d}s\,\mathrm{d}t = 0.$$

This implies that

$$\liminf_{n\to+\infty} \int_{t_1/2}^{t_1} \int_0^1 a_n^2\,\mathrm{d}s\,\mathrm{d}t = 0,$$

hence, with (6.40) and (6.41),

$$\liminf_{n\to+\infty} \int_{t_1/2}^{t_1} \mathcal{E}_n(t)\,\mathrm{d}t = 0. \tag{6.43}$$

However, $\lim_{n\to+\infty} \mathcal{E}_n(t_1) = 1$ and the decay property of the energy functional $\mathcal{E}_n(t)$, implies that

$$\liminf_{n\to+\infty} \int_{t_1/2}^{t_1} \mathcal{E}_n(t)\,\mathrm{d}t \geq \liminf_{n\to+\infty} \mathcal{E}_n(t_1) \int_{t_1/2}^{t_1} \mathrm{d}t = \frac{t_1}{2}.$$

which contradicts (6.43) and ends the proof. ■

Remark 6.3.6 *In the proof above the fact that $k > 0$ appears necessary. When dissipation in the domain vanishes but $k_r > 0$ one can still deduce a decay result of the energy due to the dissipation at the boundary. This results is given for the sake of completeness in 6.7.2.*

Existence and uniqueness of a periodic solution. We conclude this section by obtaining that Φ satisfies, thanks to Theorem 6.3.5, for $T > 0$

$$\exists\, \rho < 1, \quad \forall z_0 \in \mathcal{Z}, \quad \|e^{TA} z_0\|_{\mathcal{Z}} \leq \rho \|z_0\|_{\mathcal{Z}}. \tag{6.44}$$

Then, considering the non-homogeneous dynamics (6.26), we recall the Duhamel formulae that

$$z(T) = e^{TA} z(0) + (\Lambda \nu)(T),$$

such that seeking a T-periodic solution imposes

$$(\mathrm{Id} - e^{TA}) z(0) = (\Lambda \nu)(T).$$

Using the strict contraction property (6.44), we have that $(\mathrm{Id} - e^{TA})$ is invertible with a bounded inverse giving by the Neumann series

$$\forall z \in \mathcal{Z}, \quad (\mathrm{Id} - e^{TA})^{-1} z = \sum_{k \geq 0} e^{kTA} z.$$

Therefore, giving $\nu \in \mathrm{L}^2(0,T)$, there exists one and only one T-periodic solution of (6.26)

$$z \in \mathrm{C}^0([0,T]; \mathcal{Z}) \cap \mathrm{C}^1([0,T]; \mathcal{D}(A^*)'), \quad z(0) = z(T),$$

given for $t \in [0,T]$ by

$$z(t) = e^{tA} (\mathrm{Id} - e^{TA})^{-1} (\Lambda \nu)(T) + (\Lambda \nu)(t). \tag{6.45}$$

This solution is called the *mild periodic solution of* (6.26) When ν is smoother one can show that solutions are also smooth. To state this results we introduce the space

$$\mathrm{H}^1_\sharp(0,T) := \Big\{ u \in \mathrm{H}^1(0,T) \mid u(T) = u(0) \Big\}.$$

Theorem 6.3.7 *For $T > 0$ given, assume that $\nu \in \mathrm{H}^1_\sharp(0,T)$, then the unique T-periodic solution of (6.26) satisfies*

$$z = (a, v, P) \in \mathrm{C}^1([0,T]; \mathcal{Z}) \cap \mathrm{C}^0([0,T]; \mathrm{H}^1(0,1) \times \mathrm{H}^1(0,1) \times \mathbb{R}),$$

and the boundary conditions

$$v(0,t) = \nu(t), \quad a(1,t) = k_r\, v(1,t) + c_r\, P(t). \tag{6.46}$$

Such solution is called a strict periodic solution of (6.26).

Proof: It suffices to show that $z(0)$ satisfies $Az(0) + B\nu(0) \in \mathcal{Z}$ where $z(0)$ is given by

$$Az(0) = -A(\mathrm{Id} - e^{TA})^{-1} (\Lambda \nu)(T) = -(\mathrm{Id} - e^{TA})^{-1} A (\Lambda \nu)(T).$$

One can show, using the periodicity of ν, that

$$\begin{aligned} (\Lambda \nu)(T) &= \int_0^T e^{(T-s)A} A D_\ell \nu(s)\, \mathrm{d}s \\ &= -\int_0^T e^{(T-s)A} D_\ell \dot{\nu}(s)\, \mathrm{d}s + \Big[e^{(T-s)A} D_\ell \nu(T) \Big]_0^T, \\ &= -\int_0^T e^{(T-s)A} D_\ell \dot{\nu}(s)\, \mathrm{d}s + (\mathrm{Id} - e^{TA}) D_\ell \nu(0). \end{aligned}$$

The computations above are valid in $\mathcal{D}(A^*)'$. Moreover, in the final inequality, each terms belongs to $\mathcal{Z}$. Therefore, We can apply the operator A – seen as an operator from $\mathcal{Z}$ to $\mathcal{D}(A^*)'$ – to get

$$\begin{aligned} A(\Lambda\nu)(T) &= -\int_0^T e^{(T-s)A} A D_\ell \dot{\nu}(s)\,\mathrm{d}s + (\mathrm{Id} - e^{TA}) A D_\ell \nu(0) \\ &= (\Lambda\dot{\nu})(T) + (\mathrm{Id} - e^{TA}) B\nu(0). \end{aligned}$$

We have shown that

$$Az(0) + B\nu(0) = -(\mathrm{Id} - e^{TA})^{-1}(\Lambda\dot{\nu})(T).$$

Thanks to the admissibility of B, the operator Λ is continuous from $\mathrm{L}^2(0,T)$ to $C^0([0,T];\mathcal{Z})$. Therefore, the last term in the previous identity is in fact an element of $\mathcal{Z}$. ■

6.4 The inverse problem

6.4.1 The input-output operator

The observed quantity is the output pressure P. We therefore introduce the bounded observation operator $C \in \mathcal{L}(\mathcal{Z}, \mathbb{R})$.

$$C : \left| \begin{array}{rcl} \mathcal{Z} & \to & \mathbb{R} \\ (a, v, P) & \mapsto & P \end{array} \right.$$

and the input-output linear operator

$$\Psi_T : \left| \begin{array}{rcl} \mathrm{L}^2(0,T) & \to & \mathrm{L}^2(0,T) \\ \nu & \mapsto & C z_{|\nu}. \end{array} \right.$$

where $z_{|\nu}$ is solution of

$$\left\{ \begin{array}{ll} \dot{z}_{|\nu} = A z_{|\nu} + B\nu, & \text{in } (0,T) \\ z_{|\nu}(0) = z_{|\nu}(T) \end{array} \right. \tag{6.47}$$

Our objective is then to invert Ψ_T which, from (6.45), is explicitly given by

$$(\Psi_T \nu)(t) = C e^{tA} (\mathrm{Id} - e^{TA})^{-1} (\Lambda\nu)(T) + C(\Lambda\nu)(t).$$

As we prove that B is admissible, (6.28) and the fact that $(\mathrm{Id} - e^{AT})^{-1}$ is bounded implies that $\Psi_T \in \mathcal{L}(\mathrm{L}^2(0,T))$.

6.4.2 Observability

We must now quantify what can be reconstructed from the measurements through stability estimates similar to observability inequality in control theory. This will be done with two similar results where the source term is controlled by the output pressure, with two choices of norms.

Theorem 6.4.1 *There exists a constant c_{st} such that the strict periodic solution of (6.26) satisfies*

$$\int_0^T |\nu(t)|^2\,\mathrm{d}t \le c_{st} \int_0^T \left(|P(t)|^2 + |\dot{P}(t)|^2 \right) \mathrm{d}t.$$

Proof: By multiplying the first equation of (6.9) by $e^{\alpha s}v(s,t)$ and the second one by $e^{\alpha s}a(s,t)$ and integrating with respect to time and space, after summation, we get

$$\int_0^T \int_0^1 \Big(\partial_t(e^{\alpha s}\, a\, v) + e^{\alpha s}\, \partial_s \frac{v^2}{2} + e^{\alpha s}\, \partial_s \frac{a^2}{2} + k e^{\alpha s}\, a\, v\Big)\, \mathrm{d}s\, \mathrm{d}t = 0.$$

Integrating by parts, using the periodicity, and rearranging terms gives

$$\begin{aligned} \frac{1}{2}\int_0^T \big(v^2(0,t) + a^2(0,t)\big)\, \mathrm{d}t - \frac{1}{2}\int_0^T \big(v^2(1,t) + a^2(1,t)\big)e^{\alpha}\, \mathrm{d}t \\ = \frac{1}{2}\int_0^T \int_0^1 e^{\alpha s}\big(2k\, a\, v - \alpha v^2 - \alpha a^2\big)\, \mathrm{d}s\, \mathrm{d}\tau. \end{aligned} \tag{6.48}$$

We remark that the right hand side of the equation above is negative if $\alpha = k$, so that, using the boundary condition $v(0,t) = \nu(t)$, we can write

$$\frac{1}{2}\int_0^T \nu^2(t)\, \mathrm{d}t \le \frac{e^k}{2}\int_0^T (v^2(1,t) + a^2(1,t))\, \mathrm{d}t.$$

Moreover, using (6.46) and the equations satisfied by P, we get that there exists a constant c_{st} such that

$$\begin{aligned} &\frac{1}{2}\int_0^T \nu^2(t)\, \mathrm{d}t \\ &\le c_{st}e^k \int_0^T \Big[\Big(\frac{1}{c_r^2} + \frac{k_r^2}{c_r^2}\Big)(\dot P + RP)^2 + c_r^2 P^2 + 2k_r P(\dot P + RP)\Big]\, \mathrm{d}t, \end{aligned}$$

hence, applying the Young inequality, we obtain that there exists another constant c_{st} such that

$$\frac{1}{2}\int_0^T |\nu(t)|^2\, \mathrm{d}t \le c_{st}\int_0^T (|\dot P(t)|^2 + |P(t)|^2)\, \mathrm{d}t.$$

■

In fact, Theorem 6.4.1 can be completed with a similar observability inequality but in a weaker norm. In order to state the second result, we need to introduce the following notation for the time average of functions: for every $f \in L^2(0,T)$, we define

$$\langle f\rangle_T := \frac{1}{T}\int_0^T f(t)\, \mathrm{d}t.$$

We also need the following decomposition Lemma.

Lemma 6.4.2 *For every $f \in L^2(0,T)$ there exists a unique $g = \mathcal{I}_T(f) \in \mathrm{H}^1_\sharp(0,T)$ denoted such that*

$$f = \dot g + \langle f\rangle_T \qquad \text{and} \qquad \langle g\rangle_T = 0. \tag{6.49}$$

Moreover, there exists a constant c_{st} such that, for any $f \in \mathrm{L}^2(0,T)$,

$$\|\mathcal{I}_T(f)\|_{\mathrm{L}^2(0,T)} \le c_{st}\, \|f\|_{\mathrm{L}^2(0,T)}\,. \tag{6.50}$$

Proof: To prove the existence, observe that the function $g(t)$ defined by

$$g(t) = g(0) + \int_0^t f(\tau)\, \mathrm{d}\tau - t\,\langle f\rangle_T\,, \tag{6.51}$$

satisfies (6.49) as soon as

$$g(0) = -\left\langle \int_0^t f(\tau)\,\mathrm{d}\tau \right\rangle_T + \langle t \rangle_T \langle f \rangle_T . \tag{6.52}$$

Since the decomposition is linear, uniqueness is proven by showing that $f = 0$ implies $g = 0$. When $f = 0$ we obtain $\partial_t g = 0$ from (6.51) and since $\langle g \rangle = 0$ we indeed obtain $g = 0$. The estimates (6.50) is a simple consequence of the explicit formulae (6.51) and (6.52). ■

For smoother periodic functions an interpolation result can be obtained.

Theorem 6.4.3 *Every $f \in \mathrm{H}^1_\sharp(0,T)$ satisfies*

$$\|f - \langle f \rangle_T\|^2_{\mathrm{L}^2(0,T)} \leq \left\|\dot{f}\right\|_{\mathrm{L}^2(0,T)} \|\mathcal{I}_T(f)\|_{\mathrm{L}^2(0,T)} .$$

Proof: Let $f \in \mathrm{H}^1_\sharp(0,T)$ and denote $\bar{f} = f - \langle f \rangle_T$. We have

$$\begin{aligned}
\int_0^T |\bar{f}(t)|^2\,\mathrm{d}t &= \left| \int_0^T \bar{f}(t) \left(\tfrac{\mathrm{d}}{\mathrm{d}t}(\mathcal{I}_T(\bar{f}))(t) + \underbrace{\langle \bar{f} \rangle_T}_{0} \right) \mathrm{d}t \right| \\
&= \left| \left[\mathcal{I}_T(\bar{f})(t) \bar{f}(t) \right]_0^T - \int_0^T \dot{\bar{f}}(t) \mathcal{I}_T(\bar{f})(t)\,\mathrm{d}t \right| \\
&\leq \left\| \dot{\bar{f}} \right\|_{\mathrm{L}^2(0,T)} \left\| \mathcal{I}_T(\bar{f}) \right\|_{\mathrm{L}^2(0,T)} \\
&\leq \left\| \dot{f} \right\|_{\mathrm{L}^2(0,T)} \|\mathcal{I}_T(f)\|_{\mathrm{L}^2(0,T)} .
\end{aligned}$$

■

Theorem 6.4.4 *There exists a constant c_{st} such that, for any $\nu \in \mathrm{L}^2(0,T)$, the mild periodic solution of (6.26) satisfies*

$$\langle \nu \rangle_T^2 + \int_0^T |\mathcal{I}_T(\nu)(t)|^2\,\mathrm{d}t \leq c_{st} \int_0^T |P(t)|^2\,\mathrm{d}t. \tag{6.53}$$

Proof: We denote by $\tilde{z} = (\tilde{a}, \tilde{v}, \tilde{P})$ the strict periodic solution associated with the source term $\mathcal{I}_T(\nu) \in \mathrm{H}^1_\sharp(0,T)$ as well as $\bar{z} = (\bar{a}, \bar{v}, \bar{P})$ the strict periodic solution of associated with the constant source term $\langle \nu \rangle_T$. Applying Theorem 6.4.1 for each solution $\tilde{z}$ and $\bar{z}$ we have

$$\langle \nu \rangle_T^2 + \int_0^T |\mathcal{I}_T(\nu)(t)|^2\,\mathrm{d}t \leq c_{st} \int_0^T \left(|\tilde{P}|^2 + |\dot{\tilde{P}}|^2 + \frac{1}{T}|\bar{P}|^2 + \frac{1}{T}|\dot{\bar{P}}|^2 \right) \mathrm{d}t.$$

It remains to estimate the right hand side of the previous equation with the norm of P. This can be done using the linearity of the problem,

$$\nu = \frac{d}{dt}\mathcal{I}_T(\nu) + \langle \nu \rangle_T \quad \Rightarrow \quad z = \dot{\tilde{z}} + \bar{z} \quad \Rightarrow \quad P = \dot{\tilde{P}} + \bar{P}. \tag{6.54}$$

This last equation implies $\bar{P}(t) = \langle P \rangle_T$ hence $\dot{\tilde{P}} = 0$. The function $\mathcal{I}_T(\nu)$ having zero average one can easily show that this is also the case for $\tilde{P}$. And therefore by Poincaré-Wirtinger inequality,

$$\int_0^T |\tilde{P}|^2 \, \mathrm{d}t \leq c_{pw}^2 \int_0^T |\dot{\tilde{P}}|^2 \, \mathrm{d}t$$
$$\Rightarrow \quad \langle \nu \rangle_T^2 + \int_0^T |\mathcal{I}_T(\nu)(t)|^2 \, \mathrm{d}t \leq c_{st} \, (1 + c_{pw}^2) \int_0^T |\dot{\tilde{P}}|^2 \, \mathrm{d}t + c_{st} \, \langle P \rangle_T^2 \, .$$

Estimate (6.53) can then be deduced from (6.54) using standard techniques.

■

As a first direct consequence of Theorem 6.4.4 and the linearity of Ψ_T, we have that $\Psi_T \in \mathcal{L}(\mathrm{L}^2(0,T))$ is injective. Indeed (6.53) is nothing but

$$\langle \nu \rangle_T^2 + \int_0^T |\mathcal{I}_T(\nu)(t)|^2 \, \mathrm{d}t \leq c_{st} \; \|\Psi_T \nu\|_{L^2(0,T)}^2. \tag{6.55}$$

6.4.3 Least-square approach

We now introduce y_δ which takes into account the observation corresponding to an unknown noisy solution of System 6.47. From the previous analysis, we may now decide to invert Ψ_T to find the unknown solution using a least squares minimization including a generalized Tikhonov regularization [Engl et al., 1996; Tikhonov, 1963] of the form

$$\min_{\nu \in \mathrm{H}^1_\sharp(0,T)} \left\{ \mathscr{J}_\kappa(\nu) = \frac{1}{2} \int_0^T \left[|y_\delta(t) - C z_{|\nu}(t)|^2 + \kappa(|\dot{\nu}(t)|^2 + |\nu|^2) \right] \, \mathrm{d}t \right\}, \tag{6.56}$$

with $\kappa > 0$ and where $z_{|\nu}$ is constrained to be solution of (6.47). For further computations it is useful to rewrite the functional $\mathscr{J}_\kappa : \mathrm{H}^1_\sharp(0,T) \mapsto \mathbb{R}$, as follows,

$$\mathscr{J}_\kappa(\nu) = \frac{\kappa}{2} \, \|\nu\|_{\mathrm{H}^1(0,T)}^2 + \frac{1}{2} \, \|y_\delta - \Psi_T \nu\|_{\mathrm{L}^2(0,T)}^2 \, , \tag{6.57}$$

which shows – since $\Psi_T \in \mathcal{L}(\mathrm{L}^2(0,T))$ is continuous – that $\mathscr{J}_\kappa$ is continuous and quadratic.

Theorem 6.4.5 *For all $\kappa > 0$, $\mathscr{J}_\kappa$ is strongly convex, hence admits one unique minimiser $\bar{\nu} \in \mathrm{H}^1_\sharp(0,T)$.*

Proof: The functionnal $\mathscr{J}_\kappa$ is differentiable in the sense of Fréchet with

$$\mathscr{J}_\kappa(\nu_2) - \mathscr{J}_\kappa(\nu_1) = \langle \mathrm{D}\mathscr{J}_\kappa(\nu_1), \nu_2 - \nu_1 \rangle + \sigma(\nu_2 - \nu_1, \nu_2 - \nu_1)$$

where, here, $\langle \cdot, \cdot \rangle$ stands for the duality product in $\mathrm{H}^1_\sharp(0,T)$ and where

$$\mathrm{D}\mathscr{J}_\kappa \in \mathcal{L}(\mathrm{H}^1_\sharp(0,T), \mathrm{H}^1_\sharp(0,T)')$$

is the Fréchet derivative and σ is a continuous bilinear form in $\mathrm{H}^1_\sharp(0,T) \times \mathrm{H}^1_\sharp(0,T)$ given by

$$\sigma(\nu, \mu) = (\Psi_T \nu, \Psi_T \mu)_{\mathrm{L}^2(0,T)} + \kappa(\nu, \mu)_{\mathrm{H}^1(0,T)}.$$

As σ is coercive in $\mathrm{H}^1_\sharp(0,T)$, we deduce that $\mathscr{J}_\kappa$ is a strongly convex function, hence the existence of one unique minimizer. ■

Remark 6.4.6 *The previous results holds even if we replace the* H^1*-norm by the semi norm* $\|\dot{\nu}\|_{\mathrm{L}^2(0,T)}$*. Indeed in this case, from (6.55), we know that there exists a constant* c_{st} *such that*

$$\sigma(\nu,\nu) \geq c_{st}\Big(\langle\nu\rangle_T^2 + \|\dot{\nu}\|^2_{\mathrm{L}^2(0,T)}\Big)$$

From Poincaré-Wirtinger inequality, σ *is coercive in* $\mathrm{H}^1_\sharp(0,T)$*. Therefore, it will be possible to consider the penalty* $\kappa\|\dot{\nu}\|^2_{\mathrm{L}^2(0,T)} + \kappa'\|\nu\|^2_{\mathrm{L}^2(0,T)}$ *with a vanishing second contribution* $\kappa' \to 0$*. This will penalize large variations of* ν *without penalizing too much large values of* ν*.*

We are now able to prove the convergence of our least-square methods when seeking to recover a *regular enough* input flow from *noisy* measurement.

Theorem 6.4.7 *Given a regular target input flow* $\check{\nu} \in \mathrm{H}^1(0,T)$ *such that* $\|\check{\nu}\|_{\mathrm{H}^1(0,T)} \leq M$ *and some observations* $y_\delta \in L^2(0,T)$ *such that* $\|y_\delta - \Psi_T\check{\nu}\|_{\mathrm{L}^2(0,T)} \leq \delta\|\Psi_T\check{\nu}\|_{L^2(0,T)}$*, then by choosing* $\kappa = \delta^2N^2M^{-2}$*, where* $N = \|\Psi_T\check{\nu}\|_{L^2(0,T)}$*, there exists a constant* c_{st} *independent of* M*,* N *and* δ *such that*

$$\|\check{\nu} - \bar{\nu}\|_{L^2(0,T)} \leq c_{st}(\sqrt{M} + \sqrt{\delta})\sqrt{N\delta}, \tag{6.58}$$

where $\bar{\nu} = \mathrm{argmin}_\nu \mathscr{J}_\kappa$ *is the estimated input flow in* $\mathrm{H}^1_\sharp(0,T)$*.*

Proof: On the one hand, the error system $\tilde{z} = z_{|\check{\nu}} - z_{|\bar{\nu}}$ is solution of

$$\begin{cases} \dot{\tilde{z}} = A\tilde{z} + B(\check{\nu} - \bar{\nu}), & t > 0 \\ \tilde{z}(0) = \tilde{z}(T) \end{cases}$$

hence, using Theorem 6.4.4, there exists a constant c_{st} such that

$$|\langle\check{\nu}\rangle_T - \langle\bar{\nu}\rangle_T|^2 + \int_0^T |\mathcal{I}_T(\check{\nu} - \bar{\nu})(t)|^2\,\mathrm{d}t \leq c_{st}\int_0^T |\check{P}(t) - \bar{P}(t)|^2\,\mathrm{d}t.$$

On the other hand, Theorem 6.4.3 gives that

$$\|\check{\nu} - \bar{\nu}\|_{\mathrm{L}^2(0,T)} \leq \|\dot{\check{\nu}} - \dot{\bar{\nu}}\|^{\frac{1}{2}}_{\mathrm{L}^2(0,T)}\|\mathcal{I}_T(\check{\nu} - \bar{\nu})\|^{\frac{1}{2}}_{\mathrm{L}^2(0,T)} + |\langle\check{\nu}\rangle_T - \langle\bar{\nu}\rangle_T|.$$

Combining these two inequality, we obtain that there exists a constant c_{st} such that

$$\|\check{\nu} - \bar{\nu}\|^2_{\mathrm{L}^2(0,T)} \leq c_{st}\Big(\|\dot{\check{\nu}}\|_{L^2(0,T)} + \|\dot{\bar{\nu}}\|_{L^2(0,T)}\Big)\Big(\int_0^T |\check{P}(t) - \bar{P}(t)|^2\,\mathrm{d}t\Big)^{\frac{1}{2}} + c_{st}\int_0^T |\check{P}(t) - \bar{P}(t)|^2\,\mathrm{d}t.$$

Moreover, we have that

$$\|\dot{\bar{\nu}}\|^2_{\mathrm{L}^2(0,T)} \leq \frac{2}{\kappa}\mathscr{J}_\kappa(\bar{\nu}) \leq \frac{2}{\kappa}\mathscr{J}_\kappa(\check{\nu}) \leq M^2 + \frac{\delta^2\|\check{y}\|^2_{L^2(0,T)}}{\kappa} = M^2 + \frac{\delta^2N^2}{\kappa},$$

leading when $\kappa = \delta^2N^2M^{-2}$ to

$$\|\dot{\check{\nu}}\|_{L^2(0,T)} + \|\dot{\bar{\nu}}\|_{L^2(0,T)} \leq (1+\sqrt{2})M.$$

Likewise, since $\check{P}(t) = \Psi_T \check{\nu}$ and $\bar{P}(t) = \Psi_T \bar{\nu}$, we have that

$$\begin{aligned}\int_0^T |\check{P} - \bar{P}|^2 \,\mathrm{d}t &\leq 2\int_0^T |\Psi_T \check{\nu} - y_\delta|^2 \,\mathrm{d}t + 2\int_0^T |\Psi_t \bar{\nu} - y_\delta|^2 \,\mathrm{d}t \\ &\leq 2\delta^2 N^2 + 4\mathscr{J}_\kappa(\bar{\nu}) \leq 2\delta^2 N^2 + 4\mathscr{J}_\kappa(\check{\nu}) \leq 4\delta^2 N^2 + 2\kappa M,\end{aligned}$$

leading when $\kappa = \delta^2 N^2 M^{-2}$ to

$$\left\|\check{P}(t) - \bar{P}(t)\right\|_{\mathrm{L}^2(0,T)} \leq \sqrt{6}\delta N.$$

This ultimately gives a constant c_{st} independent of M, N and δ such that

$$\|\check{\nu} - \bar{\nu}\|^2_{\mathrm{L}^2(0,T)} \leq c_{st}(M+N)N\delta,$$

and concludes the proof. ■

Minimizing (6.57) is made difficult by the dynamics constraint with an additional periodicity constraint since (6.57) could also be understood as the minimization of a functional $\mathscr{J}_\kappa : \mathcal{Z} \times \mathrm{H}^1_\sharp(0,T) \mapsto \mathbb{R}$ given by

$$\mathscr{J}_\kappa(\zeta,\nu) = \frac{1}{2}\int_0^T \left[|y_\delta(t) - Cz_{|\zeta,\nu}(t)|^2 + \kappa(|\dot{\nu}(t)|^2 + |\nu|^2)\right] \mathrm{d}t, \tag{6.59}$$

over the convex set

$$\mathcal{K} = \left\{(\zeta,\nu) \in \mathcal{Z} \times \mathrm{H}^1_\sharp(0,T) \;\middle|\; z_{|\zeta,\nu}(T) = z_{|\zeta,\nu}(0)\right\} \tag{6.60}$$

with $z_{|\zeta,\nu}$ solution of the dynamics

$$\begin{cases} \dot{z}_{|\zeta,\nu} = Az_{|\zeta,\nu} + B\nu, \quad t \in [0,T] \\ z_{|\zeta,\nu}(0) = \zeta \end{cases} \tag{6.61}$$

or equivalently, $z_{|\zeta,\nu} \in \mathrm{C}^0([0,T];\mathcal{Z})$ satisfying

$$z_{|\zeta,\nu}(t) = e^{tA}\zeta + (\Lambda\nu)(t).$$

In order to practically minimize the functional (6.59), we can therefore rely on a penalized approach with the minimization of $\mathscr{J}_{\kappa,\varepsilon} : \mathcal{Z} \times \mathrm{H}^1_\sharp(0,T) \mapsto \mathbb{R}$ given by

$$\begin{aligned}\mathscr{J}_{\kappa,\varepsilon}(\zeta,\nu) &= \varepsilon^{-1}\left\|z_{|\zeta,\nu}(T) - z_{|\zeta,\nu}(0)\right\|^2_{\mathcal{Z}} \\ &\quad + \tfrac{1}{2}\int_0^T \left[|y_\delta(t) - Cz_{|\zeta,\nu}(t)|^2 + \kappa(|\dot{\nu}(t)|^2 + |\nu|^2)\right] \mathrm{d}t,\end{aligned} \tag{6.62}$$

over its domain of definition. To simplify further computations we introduce the bounded operator

$${}^\flat\Psi_T : \left| \begin{array}{rcl} \mathcal{Z} \times \mathrm{L}^2(0,T) & \to & \mathrm{L}^2(0,T) \\ (\zeta,\nu) & \mapsto & Cz_{|\zeta,\nu}. \end{array} \right.$$

and rewrite the functional $\mathscr{J}_{\kappa,\varepsilon}$ as

$$\begin{aligned}\mathscr{J}_{\kappa,\varepsilon}(\zeta,\nu) &= \varepsilon^{-1}\left\|(\mathrm{Id} - e^{TA})\zeta + (\Lambda\nu)(T)\right\|^2_{\mathcal{Z}} \\ &\quad + \tfrac{\kappa}{2}\|\nu\|^2_{\mathrm{H}^1(0,T)} + \frac{1}{2}\left\|y_\delta - {}^\flat\Psi_T \begin{pmatrix} \zeta \\ \nu \end{pmatrix}\right\|^2_{\mathrm{L}^2(0,T)}.\end{aligned} \tag{6.63}$$

Theorem 6.4.8 *For all $\kappa > 0$, there exists a unique minimiser $\bar{\xi} = (\bar{\zeta}, \bar{\nu}) \in \mathcal{Z} \times \mathrm{H}^1_\sharp(0,T)$ of the strongly-convex functional $\mathscr{J}_{\kappa,\varepsilon}$.*

Proof: We introduce this time the bounded operator

$$ {}^\flat\Psi_T : \left| \begin{array}{rcl} \mathcal{Z} \times \mathrm{L}^2(0,T) & \to & \mathrm{L}^2(0,T) \\ (\zeta, \nu) & \mapsto & C z_{|\zeta,\nu}. \end{array} \right. $$

which is also bounded as an operator from $\mathcal{Z} \times \mathrm{H}^1_\sharp(0,T)$ to $\mathrm{L}^2(0,T)$. Again, the functional $\mathscr{J}_{\kappa,\varepsilon}$ is continuous and quadratic. Further, $\mathscr{J}_{\kappa,\varepsilon}$ is differentiable in the sense of Fréchet with

$$ \begin{aligned} \mathscr{J}_{\kappa,\varepsilon}(\zeta_2,\nu_2) - \mathscr{J}_\kappa(\zeta_1,\nu_1) \qquad &= \left\langle \mathrm{D}\mathscr{J}_\kappa(\zeta_1,\nu_1), \begin{pmatrix} \zeta_2 - \zeta_1 \\ \nu_2 - \nu_1 \end{pmatrix} \right\rangle \\ &\quad + {}^\flat\sigma((\zeta_2 - \zeta_1, \nu_2 - \nu_1), (\zeta_2 - \zeta_1, \nu_2 - \nu_1)) \end{aligned} $$

where $\mathrm{D}\mathscr{J}_{\kappa,\varepsilon} \in \mathcal{L}(\mathcal{Z} \times \mathrm{H}^1_\sharp(0,T), (\mathcal{Z} \times \mathrm{H}^1_\sharp(0,T))')$ is the Fréchet derivative and ${}^\flat\sigma$ is a bilinear form continuous in $(\mathcal{Z} \times \mathrm{H}^1_\sharp(0,T)) \times (\mathcal{Z} \times \mathrm{H}^1_\sharp(0,T))$ given by

$$ \begin{aligned} {}^\flat\sigma \quad ((\zeta,\nu),(\eta,\mu)) &= \kappa(\nu,\mu)_{\mathrm{H}^1(0,T)} + \left({}^\flat\Psi_T \begin{pmatrix} \zeta \\ \nu \end{pmatrix}, {}^\flat\Psi_T \begin{pmatrix} \eta \\ \mu \end{pmatrix} \right)_{\mathrm{L}^2(0,T)} \\ &\quad \big((\mathrm{Id} - e^{TA})\zeta + (\Lambda\nu)(T), (\mathrm{Id} - e^{TA})\eta + (\Lambda\mu)(T) \big)_{\mathrm{L}^2(0,T)} \end{aligned} $$

Therefore, ${}^\flat\sigma$ is positive. Further, let us consider (ζ,ν) such that ${}^\flat\sigma((\zeta,\nu),(\zeta,\nu)) = 0$. We then have $\nu = 0$, and $(\mathrm{Id} - e^{TA})\zeta = 0$. As $(\mathrm{Id} - e^{TA})$ is invertible, $\zeta = 0$. Therefore, ${}^\flat\sigma$ is definite and $\mathscr{J}_{\kappa,\varepsilon}$ is convex. Finally we show that ${}^\flat\sigma$ is coercive by contradiction. Then, let assume there exists a sequence $(\zeta_n,\nu_n)_{n\in\mathbb{N}}$ such that

$$ \lim_{n\to\infty} {}^\flat\sigma((\zeta_n,\nu_n),(\zeta_n,\nu_n)) = 0 \text{ whereas } \|\zeta_n\|^2_{\mathcal{Z}} + \|\nu_n\|^2_{\mathrm{H}^1(0,T)} = 1. $$

From the definition of ${}^\flat\sigma$, we have

$$ \lim_{n\to\infty} \|\nu_n\|^2_{\mathrm{H}^1(0,T)} = 0. $$

Then, we find that

$$ \lim_{n\to\infty} \left\| (\mathrm{Id} - e^{TA})\zeta_n \right\|_{\mathcal{Z}} = \lim_{n\to\infty} \|\Lambda(T)\nu_n\|_{\mathcal{Z}}. $$

As we have already noticed that there exists a constant c_{st} such that

$$ \|\Lambda(T)\nu_n\|_{\mathcal{Z}} \le c_{st} \|\nu_n\|_{\mathrm{L}^2(0,T)}, $$

and $(\mathrm{Id} - e^{TA})$ has a bounded inverse, we conclude that

$$ \lim_{n\to\infty} \|\zeta_n\|_{\mathcal{Z}} = 0 \text{ and } \lim_{n\to\infty} \|\zeta_n\|_{\mathcal{Z}} = 1, $$

which is absurd. Therefore, ${}^\flat\sigma$ is coercive and $\mathscr{J}_{\kappa,\varepsilon}$ is a strongly-convex functional. ■

We now consider a sequence $(\varepsilon_n)_{n\in\mathbb{N}}$ strictly decreasing and converging to 0, and want to analyze the convergence of the penalty strategy.

$$ \mathcal{Z} \times \mathrm{H}^1_\sharp(0,T) \ni \bar{\xi}_n = (\bar{\zeta}_n, \bar{\nu}_n) = \arg\min_{(\zeta,\nu)} \mathscr{J}_{\kappa,\varepsilon_n}(\zeta,\nu). $$

In what follows, we denote

$$\mathscr{P}(\zeta,\nu) = \left\| z_{|\zeta,\nu}(T) - z_{|\zeta,\nu}(0) \right\|_{\mathcal{Z}}^2,$$

hence

$$\mathscr{J}_{\kappa,\varepsilon}(\zeta,\nu) = \varepsilon^{-1}\mathscr{P}(\zeta,\nu) + \mathscr{J}_\kappa(\zeta,\nu).$$

By a direct application of classical results in convex optimization, one can show the following propositions.

Proposition 6.4.9 *We have the following bounds*

$$\mathscr{J}_{\kappa,\varepsilon_n}(\bar\zeta_n,\bar\nu_n) \le \mathscr{J}_{\kappa,\varepsilon_{n+1}}(\bar\zeta_{n+1},\bar\nu_{n+1}), \tag{6.64}$$

and

$$\mathscr{P}(\bar\zeta_n,\bar\nu_n) \ge \mathscr{P}(\bar\zeta_{n+1},\bar\nu_{n+1}). \tag{6.65}$$

Proof: First, we have

$$\begin{aligned}\mathscr{J}_{\kappa,\varepsilon_n}(\bar\zeta_n,\bar\nu_n) \quad &\le \mathscr{J}_{\kappa,\varepsilon_n}(\bar\zeta_{n+1},\bar\nu_{n+1}) = \varepsilon_n^{-1}\mathscr{P}(\bar\zeta_{n+1},\bar\nu_{n+1}) + \mathscr{J}_\kappa(\bar\zeta_{n+1},\bar\nu_{n+1})\\ &\le \varepsilon_{n+1}^{-1}\mathscr{P}(\bar\zeta_{n+1},\bar\nu_{n+1}) + \mathscr{J}_\kappa(\bar\zeta_{n+1},\bar\nu_{n+1}) = \mathscr{J}_{\kappa,\varepsilon_{n+1}}(\bar\zeta_{n+1},\bar\nu_{n+1}).\end{aligned}$$

Second, we remark that

$$\varepsilon_n^{-1}\mathscr{P}(\bar\zeta_n,\bar\nu_n) + \mathscr{J}_\kappa(\bar\zeta_n,\bar\nu_n) \le \varepsilon_n^{-1}\mathscr{P}(\bar\zeta_{n+1},\bar\nu_{n+1}) + \mathscr{J}_\kappa(\bar\zeta_{n+1},\bar\nu_{n+1})$$

while

$$\varepsilon_{n+1}^{-1}\mathscr{P}(\bar\zeta_{n+1},\bar\nu_{n+1}) + \mathscr{J}_\kappa(\bar\zeta_{n+1},\bar\nu_{n+1}), \le \varepsilon_{n+1}^{-1}\mathscr{P}(\bar\zeta_n,\bar\nu_n) + \mathscr{J}_\kappa(\bar\zeta_n,\bar\nu_n),$$

Adding the last two inequalities leads to

$$(\varepsilon_{n+1}^{-1} - \varepsilon_n^{-1})\mathscr{P}(\bar\zeta_{n+1},\bar\nu_{n+1}) \le (\varepsilon_{n+1}^{-1} - \varepsilon_n^{-1})\mathscr{P}(\bar\zeta_n,\bar\nu_n),$$

and gives (6.65). ■

Proposition 6.4.10 *We have*

$$\mathscr{J}_\kappa(\bar\zeta_n,\bar\nu_n) \le \mathscr{J}_\kappa(\bar\zeta_{n+1},\bar\nu_{n+1}), \tag{6.66}$$

and

$$\mathscr{J}_\kappa(\bar\zeta,\bar\nu) \ge \mathscr{J}_{\kappa,\varepsilon_n}(\bar\zeta_n,\bar\nu_n) \ge \mathscr{J}_\kappa(\bar\zeta_n,\bar\nu_n), \tag{6.67}$$

where $(\bar\zeta,\bar\nu) = \arg\min_{(\zeta,\nu)\in\mathcal{K}} \mathscr{J}_\kappa$ *whith* $\mathcal{K}$ *defined by* (6.60).

Proof: From (6.64) and (6.65) we deduce that

$$\begin{aligned}\mathscr{J}_\kappa(\bar\zeta_n,\bar\nu_n) \qquad &= \mathscr{J}_{\kappa,\varepsilon_n}(\bar\zeta_n,\bar\nu_n) - \varepsilon_n^{-1}\mathscr{P}(\bar\zeta_n,\bar\nu_n)\\ &\le \mathscr{J}_{\kappa,\varepsilon_n}(\bar\zeta_{n+1},\bar\nu_{n+1}) - \varepsilon_n^{-1}\mathscr{P}(\bar\zeta_{n+1},\bar\nu_{n+1})\\ &\le \mathscr{J}_{\kappa,\varepsilon_n}(\bar\zeta_{n+1},\bar\nu_{n+1}) - \varepsilon_{n+1}^{-1}\mathscr{P}(\bar\zeta_{n+1},\bar\nu_{n+1}) = \mathscr{J}_\kappa(\bar\zeta_{n+1},\bar\nu_{n+1}).\end{aligned}$$

Then, we write

$$\mathscr{J}_\kappa(\bar\zeta,\bar\nu) = \varepsilon_n^{-1}\mathscr{P}(\bar\zeta,\bar\nu) + \mathscr{J}_\kappa(\bar\zeta,\bar\nu) \ge \mathscr{J}_{\kappa,\varepsilon_n}(\bar\zeta_n,\bar\nu_n) \ge \mathscr{J}_\kappa(\bar\zeta_n,\bar\nu_n).$$

■

Theorem 6.4.11 *The sequence $(\bar{\zeta}_n, \bar{\nu}_n)_{n\in\mathbb{N}}$ minimizer of $\mathscr{J}_{\kappa,\varepsilon_n}$ converges to the minimizer $(\bar{\zeta}, \bar{\nu})$ of $\mathscr{J}_\kappa$ over $\mathcal{K}$ for the norm in $\mathcal{Z} \times \mathrm{H}^1_\sharp(0,T)$, and we have*

$$\lim_{n\in\mathbb{N}} \mathscr{J}_{\kappa,\varepsilon_n}(\bar{\zeta}_n, \bar{\nu}_n) = \mathscr{J}_\kappa(\bar{\zeta}, \bar{\nu}).$$

Proof: From (6.67), the sequence $(\mathscr{J}_{\kappa,\varepsilon_n}(\bar{\zeta}_n, \bar{\nu}_n))$ is bounded. Therefore, $(\bar{\nu}_n)_{n\in\mathbb{N}}$ is bounded in $\mathrm{H}^1(0,T)$ hence we can extract a subsequence weakly converging in $\mathrm{H}^1_\sharp(0,T)$ and strongly converging in $\mathrm{L}^2(0,T)$. Further, From (6.65) the sequence $\mathscr{P}_{\varepsilon_{n+1}}(\bar{\zeta}_{n+1}, \bar{\nu}_{n+1})$ is decreasing, hence bounded. As ε_n^{-1} tends to infinity, this implies that

$$\lim_{n\to\infty} \left\| (\mathrm{Id} - e^{TA})\bar{\zeta}_n + (\Lambda\bar{\nu}_n)(T) \right\|^2_{\mathcal{Z}} = 0. \tag{6.68}$$

Therefore, we find that

$$\lim_{n\to\infty} \left\| (\mathrm{Id} - e^{TA})\bar{\zeta}_n \right\|_{\mathcal{Z}} = \lim_{n\to\infty} \left\| \Lambda(T)\bar{\nu}_n \right\|_{\mathcal{Z}}. \tag{6.69}$$

By admissibility

$$\left\| \Lambda(T)\bar{\nu}_n \right\|_{\mathcal{Z}} \leq c_{st} \left\| \bar{\nu}_n \right\|_{\mathrm{L}^2(0,T)},$$

we have that $((\mathrm{Id} - \Phi(T))\bar{\zeta}_n)_{n\in\mathbb{N}}$ converges weakly and in a norm in $\mathcal{Z}$, hence is a strongly convergent sequence in $\mathcal{Z}$. By consequence, $\bar{\zeta}_n$ strongly converges in $\mathcal{Z}$.To summarize, we have proven that $(\bar{\zeta}_n, \bar{\nu}_n)_{n\in\mathbb{N}}$ is strongly convergent in $\mathcal{Z} \times \mathrm{L}^2(0,T)$ and we denote the limit $(\bar{\zeta}_\infty, \bar{\nu}_\infty)$.

The sequence $(\bar{\zeta}_n, \bar{\nu}_n)_{n\in\mathbb{N}}$ being in particular weakly convergent in $\mathcal{Z} \times \mathrm{H}^1_\sharp(0,T)$, $\mathscr{J}_\kappa$ being convex and lower-semicontinuous (hence weakly lower-semicontinuous), we deduce that

$$\liminf_{n\to\infty} \mathscr{J}_\kappa(\bar{\zeta}_n, \bar{\nu}_n) \geq \mathscr{J}_\kappa(\bar{\zeta}_\infty, \bar{\nu}_\infty). \tag{6.70}$$

The associated trajectory $z_{|\bar{\zeta}_\infty, \bar{\nu}_\infty}$ is periodic due to (6.68), hence $(\bar{\zeta}_\infty, \bar{\nu}_\infty) \in \mathcal{K}$. As a consequence of (6.70) and (6.67), we obtain that

$$\mathscr{J}_\kappa(\bar{\zeta}_\infty, \bar{\nu}_\infty) \leq \mathscr{J}_\kappa(\bar{\zeta}, \bar{\nu}) \Rightarrow (\bar{\zeta}_\infty, \bar{\nu}_\infty) = (\bar{\zeta}, \bar{\nu}).$$

To conclude we need to show that the sequence $\bar{\nu}_n$ strongly converges in $\mathrm{H}^1(0,T)$. From (6.67) we deduce that

$$\liminf_{n\to\infty} \mathscr{J}_{\kappa,\varepsilon_n}(\bar{\zeta}_n, \bar{\nu}_n) = \limsup_{n\to\infty} \mathscr{J}_{\kappa,\varepsilon_n}(\bar{\zeta}_n, \bar{\nu}_n) = \mathscr{J}_\kappa(\bar{\zeta}, \bar{\nu}),$$

which shows that the limit of $\mathscr{J}_{\kappa,\varepsilon_n}(\bar{\zeta}_n, \bar{\nu}_n)$ is unique and given by $\mathscr{J}_\kappa(\bar{\zeta}, \bar{\nu})$. Moreover

$$\begin{aligned}
\mathscr{J}_\kappa(\bar{\zeta}, \bar{\nu}) = \lim_{n\to\infty} \mathscr{J}_{\kappa,\varepsilon_n}(\bar{\zeta}_n, \bar{\nu}_n) &= \liminf_{n\to\infty} \left(\varepsilon_n^{-1}\mathscr{P}(\bar{\zeta}_n, \bar{\nu}_n) + \mathscr{J}_\kappa(\bar{\zeta}_n, \bar{\nu}_n) \right) \\
&\geq \liminf_{n\to\infty} \varepsilon_n^{-1}\mathscr{P}(\bar{\zeta}_n, \bar{\nu}_n) + \liminf_{n\to\infty} \mathscr{J}_\kappa(\bar{\zeta}_n, \bar{\nu}_n) \\
&\geq \liminf_{n\to\infty} \varepsilon_n^{-1}\mathscr{P}(\bar{\zeta}_n, \bar{\nu}_n) + \mathscr{J}_\kappa(\bar{\zeta}, \bar{\nu})
\end{aligned}$$

hence $\liminf \mathscr{P}(\bar{\zeta}_n, \bar{\nu}_n) = 0$ and since $(\mathscr{P}(\bar{\zeta}_n, \bar{\nu}_n))_{n\geq 0}$ is a decaying sequence, it converges and

$$\lim_{n\to\infty} \mathscr{P}(\bar{\zeta}_n, \bar{\nu}_n) = 0. \tag{6.71}$$

We conclude by observing that the convergence of $(\bar{\zeta}_n, \bar{\nu}_n)_{n\in\mathbb{N}}$ in $\mathcal{Z} \times \mathrm{L}^2(0,T)$ implies

$$\lim_{n\in\mathbb{N}} \left\| y_\delta - {}^\flat\Psi_T\bar{\nu}_n \right\|^2_{\mathrm{L}^2(0,T)} = \left\| y_\delta - {}^\flat\Psi_T\bar{\nu} \right\|^2_{\mathrm{L}^2(0,T)},$$

hence, with this equation, (6.71), and the property that $\mathscr{J}_{\kappa,\varepsilon_n}(\bar{\zeta}_n, \bar{\nu}_n)$ converges towards $\mathscr{J}_\kappa(\bar{\zeta}, \bar{\nu})$ we obtain that

$$\lim_{n\to\infty} \|\bar{\nu}_n\|_{H^1(0,T)} = \|\bar{\nu}\|_{H^1(0,T)}.$$

The convergence of the norm implies here that $\bar{\nu}_n$ strongly converge in $H^1(0,T)$. ■

6.4.4 An optimal control approach

We are now in position to write the optimality system associated to each penalized criterion $\mathscr{J}_{\kappa,\varepsilon}$ and the limit system associated with $\mathscr{J}_\kappa$. Let us now introduce for all $z \in \mathrm{L}^2((0,T);\mathcal{Z})$ and $y_\delta \in \mathrm{L}^2(0,T)$ the adjoint dynamics [Bensoussan, 1971]

$$\begin{cases} \dot{q}_\varepsilon + A^* q_\varepsilon = -\gamma C^*(y_\delta - Cz), & \text{in } (0,T) \\ q_\varepsilon(T) = -\varepsilon^{-1}(z(T) - z(0)) \end{cases} \tag{6.72}$$

which is also well posed as it is considered backward in time with the semi-group generator $-A^*$. Namely, we have $q \in \mathrm{C}^0[0,T], \mathcal{Z}$ given by the Duhamel formula

$$q_\varepsilon(t) = \varepsilon^{-1} e^{(T-t)A^*}(z(0) - z(T)) + \gamma \int_t^T e^{(s-t)A^*} C^*(y_\delta(s) - Cz(s))\,\mathrm{d}s.$$

The adjoint variable allows to easily compute the Fréchet derivatives with respect to ζ and ν. We find for a given $(\zeta, \nu) \in \mathcal{Z} \times \mathrm{H}^1_\sharp(0,T)$

$$\forall \eta \in \mathcal{Z}, \quad \left\langle \mathrm{D}_\zeta \mathscr{J}_{\kappa,\varepsilon}(\zeta,\nu), \eta \right\rangle = \varepsilon^{-1}\big(\zeta - z_{|\zeta,\nu}(T), \eta\big) + (q_{\varepsilon|\zeta,\nu}(0), \eta)_{\mathcal{Z}}, \tag{6.73}$$

and

$$\begin{gathered} \forall \mu \in \mathrm{H}^1_\sharp(0,T), \\ \left\langle \mathrm{D}_\nu \mathscr{J}_{\kappa,\varepsilon}(\zeta,\nu), \mu \right\rangle = \kappa(\nu,\mu)_{\mathrm{H}^1(0,T)} - \textstyle\int_0^T (q_{\varepsilon|\zeta,\nu}(t), B\mu(t))_{\mathcal{Z}}\,\mathrm{d}t, \end{gathered} \tag{6.74}$$

where $q_{\varepsilon|\zeta,\nu}$ is the adjoint variable associated with $z_{|\zeta,\nu}$. We obtain the Euler equation associated with the minimization

$$\begin{gathered} \forall (\eta,\mu) \in \mathcal{Z} \times \mathrm{H}^1_\sharp(0,T), \quad \varepsilon^{-1}(\bar{\zeta}_\varepsilon - \bar{z}_\varepsilon(T), \eta)_{\mathcal{Z}} \\ -(\bar{q}_\varepsilon(0), \eta)_{\mathcal{Z}} + \kappa(\bar{\nu}_\varepsilon, \mu)_{\mathrm{H}^1(0,T)} - \textstyle\int_0^T (\bar{q}_\varepsilon(t), B\mu(t))_{\mathcal{Z}}\,\mathrm{d}t = 0, \end{gathered} \tag{6.75}$$

where $\bar{q}_\varepsilon$ is the adjoint variable associated with the optimal trajectory $\bar{z}_\varepsilon = z_{|\bar{\zeta}_\varepsilon,\bar{\nu}_\varepsilon}$ and the available measurements y_δ. We then introduce $\Delta_\sharp$ the laplacian in time with periodic boundary condition. From Lax-Millgram theorem $\mathrm{Id} - \Delta_\sharp$ is invertible from $\mathrm{L}^2(0,T)$ to $\mathrm{H}^1_\sharp(0,T)$. This leads to the so-called two-ends problem defining the optimal dynamics of the estimator

$$\begin{cases} \dot{\bar{z}}_\varepsilon = A\bar{z}_\varepsilon + \kappa^{-1} B(\mathrm{Id} - \Delta_\sharp)^{-1} B^* \bar{q}_\varepsilon, & \text{in } (0,T) \\ \dot{\bar{q}}_\varepsilon + A^*\bar{q}_\varepsilon = -C^*(y_\delta - C\bar{z}_\varepsilon), & \text{in } (0,T) \\ \bar{z}_\varepsilon(0) = \varepsilon\bar{q}_\varepsilon(0) + \bar{z}_\varepsilon(T) \\ \bar{q}_\varepsilon(T) = \bar{q}_\varepsilon(0) \end{cases} \tag{6.76}$$

We point out that as $(\mathrm{Id} + \Delta_\sharp)^{-1}$ is a non-local term with respect to time. Finally from (6.75) and from $\bar{\zeta}_\varepsilon$ converging to $\bar{\zeta}$ when ε goes to 0 that the optimality system naturally

becomes at the limit

$$\begin{cases} \dot{\bar{z}} = A\bar{z} + \kappa^{-1}B(\mathrm{Id} - \Delta_\sharp)^{-1}B^*\bar{q}, & \text{in } (0,T) \\ \dot{\bar{q}} + A^*\bar{q} = -C^*(y_\delta - C\bar{z}), & \text{in } (0,T) \\ \bar{z}(0) = \bar{z}(T) \\ \bar{q}(T) = \bar{q}(0) \end{cases} \tag{6.77}$$

6.5 Numerical methods

Based on the preceding analysis, we propose an adapted numerical reconstruction strategy based on the following principle: Discretization of the forward problem and control-based formulation of the inverse problem redeveloped at the discrete level. As it is well known that the interaction between control and discretization can be complicated [Zuazua, 2005], the proposed strategy will ensure that our method is numerically well suited.

6.5.1 Model discretization

Concerning the spatial discretization, we rely on a finite element discretization based on the variational formulation associated with problem (6.9, 6.10, 6.12). For any test function in $q = (b, w, Q) \in \mathcal{D}(A)$ we obtain from (6.9, 6.10) that the strict solution $z = (a, v, P)$ satisfies at each time t,

$$\begin{aligned} (\dot{a}, b)_{\mathrm{L}^2(0,1)} + (v', b)_{\mathrm{L}^2(0,1)} \qquad & +(\dot{v}, w)_{\mathrm{L}^2(0,1)} + (a', w)_{\mathrm{L}^2(0,1)} \\ & +k\,(v, w)_{\mathrm{L}^2(0,1)} + \left(\dot{P} + RP - c_r\, v(1,\cdot)\right) Q = 0. \end{aligned}$$

The second term is integrated by parts and boundary terms are substituted either using the property that $q \in \mathcal{D}(A)$ or the boundary condition $v(0,\cdot) = \nu$.

$$\begin{aligned} (\dot{a}, b)_{\mathrm{L}^2(0,1)} \qquad & +(\dot{v}, w)_{\mathrm{L}^2(0,1)} + \dot{P}Q \\ & +(a', w)_{\mathrm{L}^2(0,1)} - (v, b')_{\mathrm{L}^2(0,1)} + k\,(v, w)_{\mathrm{L}^2(0,1)} \\ & +RPQ + k_r v(1,\cdot)w(1) = b(0)\nu. \end{aligned}$$

Then the formulation above is discretized using a conforming approach. A finite-dimensional space $\mathcal{V}_h \subset \mathcal{D}(A)$ is constructed using a space-grid $0 \le x_i = ih \le 1$ with $h = N_x^{-1}$, $0 \le i \le N_x$ and Lagrangian finite element of order $k = 1$,

$$\begin{aligned} \mathcal{V}_h = \Big\{ (a_h \qquad & , v_h, P_h) \in \mathrm{H}^1(0,1) \times \mathrm{H}^1_\ell(0,1) \times \mathbb{R}, \\ & \Big| \, a_h(1) = k_r v_h(1) + c_r P_h,\ a_{h|[x_i,x_{i+1}]} \in \mathbb{P}_k, v_{h|[x_i,x_{i+1}]} \in \mathbb{P}_k \Big\}. \end{aligned} \tag{6.78}$$

The space $\mathcal{V}_h$ is equipped with the scalar product $(\cdot,\cdot)_h$ that is an approximation of the scalar product in $\mathcal{Z}$ using the trapezoidal quadrature formula. We introduce the operator $A_h \in \mathcal{L}(\mathcal{V}_h)$ such that for all functions $z_h = (a_h, v_h, P_h) \in \mathcal{V}_h$ and $q_h = (b_h, w_h, Q_h) \in \mathcal{V}_h$

$$\begin{aligned} (A_h z_h, q_h)_h = (v_h, b_h')_{\mathrm{L}^2(0,1)} - (a_h', w_h)_{\mathrm{L}^2(0,1)} \\ -k(v_h, w_h)_{\mathrm{L}^2(0,1)} - k_r v_h(1) w_h(1) - RPQ, \end{aligned} \tag{6.79}$$

as well as the operator $B_h \in \mathcal{L}(\mathbb{R}, \mathcal{V}_h)$ defined by

$$(B_h\nu, q_h)_h = b_h(0)\nu.$$

The semi-discrete problem is then equivalent to

$$\dot{z}_h = A_h z + B_h \nu. \tag{6.80}$$

For the time-discretization, we use a regular time-grid $0 \leq t_n = n\tau \leq T$ with $\tau = N_T^{-1} T$, $0 \leq n \leq N_T$. We choose a backward-Euler approach for three reasons. First, the scheme is unconditionally stable. Second, the additional numerical dissipation has a strong effects on spurious high frequency components of the solutions that otherwise could have compromised the reconstruction (see for instance the review [Zuazua, 2005]).

After time discretization, (6.80) is replaced by

$$\frac{z_h^{n+1} - z_h^n}{\tau} = A_h z^{n+1} + B_h \nu^{n+1}. \tag{6.81}$$

that can be rewritten

$$z_h^{n+1} = \Phi_{h,\tau} z^n + B_{h,\tau} \nu^{n+1}$$

with $\Phi_{h,\tau} = (\mathrm{Id} - \tau A_h)^{-1}$ and $B_{h,\tau} = \tau(\mathrm{Id} - \tau A_h)^{-1} B_h$. Since $\{\nu^n\}$ is an approximation of a periodic function we impose

$$\nu^{N_T} = \nu^0.$$

6.5.2 Optimization based on generalized inverse computation

We first emphasize that we assume that the measurements are compatible with the chosen time discretization, i.e., we have $(y_\delta^n)_{0 \leq n \leq N}$. Note that if the time step of the model is smaller than the time samples of the measurements, it is always possible to re-sample by interpolation up to additional measurement errors with controlled effect [Cîndea et al., 2015]. Our goal is to minimize the discrete counterpart of the penalized criterion $\mathscr{J}_{\kappa,\varepsilon}$ introduced in (6.62). We define the functional $\mathscr{J}_{\kappa,\varepsilon}^{N_T}$ in the finite dimensional space $\mathcal{V}_h \times \mathbb{R}^{N_T}$ as.

$$\begin{aligned} \mathscr{J}_{\kappa,\varepsilon}^{N_T}(\zeta_h, \nu_h) \qquad & = \varepsilon^{-1} \left\| z_{h|\zeta,\nu}^{N_T} - z_{h|\zeta,\nu}^0 \right\|_{\mathcal{Z}}^2 \\ & + \tfrac{\tau}{2} \textstyle\sum_{n=0}^{N_T-1} \left[|y_\delta^n - C z_{h|\zeta,\nu}^n|^2 + \kappa \left(|\nu^n|^2 + \left| \tfrac{\nu^{n+1} - \nu^n}{\tau} \right|^2 \right) \right], \end{aligned} \tag{6.82}$$

subject to

$$\begin{cases} z_{h|\zeta,\nu}^{n+1} = \Phi_{h,\tau} z_{h|\zeta,\nu}^n + B_{h,\tau} \nu^{n+1}, \quad 0 \leq n \leq N_T - 1 \\ z_{h|\zeta,\nu}^0 = \zeta_h. \end{cases} \tag{6.83}$$

The minimization of such function leads to a discretization of the optimality system (6.76), see 6.7.3 for detail computation.

Minimization of $\mathscr{J}_{\kappa,\varepsilon}^{N_T}(\zeta_h, \nu_h)$ can be performed by inverting the underlying linear system associated with the Euler equation of this quadratic problem. This task is made possible here because our initial problem is one-dimensional in space and therefore has a limited number of degrees of freedom after space and time discretization. Developing the solution of (6.80) using a discrete Duhamel formula

$$z_{h|\zeta,\nu}^n = \Phi_{h,\tau}^n \zeta_h + \sum_{k=1}^{n} \Phi_{h,\tau}^{n-k} B_{h,\tau} \nu^k,$$

the minimization is unconstrained by making the initial condition dependency explicit, namely

$$\begin{aligned}\mathscr{J}^{N_T}_{\kappa,\varepsilon}(\zeta_h,(\nu_n)_{n\in[1,N_T]}) \quad &= \varepsilon^{-1}\left\|(\Phi^{N_T}_{h,\tau}-\mathrm{Id})\zeta_h+\textstyle\sum_{n=1}^{N_T}\Phi^{N_T-n}_{h,\tau}B_{h,\tau}\nu^n\right\|^2_{\mathcal{Z}}\\ &+\tfrac{\tau}{2}\textstyle\sum_{n=0}^{N_T-1}\left[\left|y^n_\delta-C\Phi^n_{h,\tau}\zeta_h+\sum_{k=1}^{n}C\Phi^{n-k}_{h,\tau}B_{h,\tau}\nu^k\right|^2\right.\\ &\left.+\tfrac{\kappa}{2}\left(|\nu^n|^2+\left|\tfrac{\nu^{n+1}-\nu^n}{\tau}\right|^2\right)\right]. \end{aligned} \tag{6.84}$$

In (6.82) and (6.84), we have that $\nu^0=\nu^{N_T}$, such that ν^{N_T} becomes a non independent variable. Introducing

$$X=\begin{pmatrix}\zeta_h\\ \nu^0\\ \vdots\\ \nu^{N_T-1}\end{pmatrix}\in\mathcal{V}_h\times\mathbb{R}^{N_T}\text{ and }Y=\begin{pmatrix}y^0_\delta\\ \vdots\\ y^{N_T-1}_\delta\end{pmatrix}$$

we rewrite

$$\begin{aligned}\mathscr{J}^{N_T}_{\kappa,\varepsilon}(X)=\frac{\varepsilon^{-1}}{2}\left\|\Psi_\sharp X\right\|^2_{\mathcal{Z}}+\frac{1}{2}\left\|Y-\Psi_C X-\Psi_B X\right\|^2_{\mathbb{R}^{N_T}}\\ +\frac{\kappa}{2}\left(X,\begin{pmatrix}0&0\\0&K_\sharp\end{pmatrix}X\right)_{\mathbb{R}^{N_T}},\end{aligned}$$

where

$$\Psi_\sharp=\begin{pmatrix}(\Phi^{N_T}_{h,\tau}-\mathrm{Id}) & \Phi^{N_T-1}_{h,\tau}B_{h,\tau} & \cdots & B_{h,\tau}\end{pmatrix}\in\mathcal{L}(\mathcal{V}_h\times\mathbb{R}^{N_T}),$$

while

$$\Psi_C=\begin{pmatrix}C_h\\ \vdots\\ C_h\Phi^{N_T-1}_{h,\tau}\end{pmatrix}\in\mathcal{L}(\mathcal{V}_h),$$

and

$$\Psi_B=\begin{pmatrix}C_hB_{h,\tau}&&0\\ \vdots&\ddots&0\\ C_h\Phi^{N_T-1}_{h,\tau}B_{h,\tau}&\cdots&C_hB_{h,\tau}\end{pmatrix}\in\mathcal{L}(\mathbb{R}^{N_T}).$$

Therefore, minimizing $\mathscr{J}^{N_T}_{\kappa,\varepsilon}$ can be performed by solving

$$\left[\varepsilon^{-1}\Psi^*_\sharp\Psi_\sharp+\tau\begin{pmatrix}\Psi^*_C\Psi_C&\Psi^*_C\Psi_B\\ \Psi^*_B\Psi_C&\Psi^*_B\Psi_B+\kappa K_\sharp\end{pmatrix}\right]X=\tau\begin{pmatrix}\Psi_C&\Psi_B\end{pmatrix}^*Y, \tag{6.85}$$

to the prize of being able to store the necessary dense matrices.

Of note, this system can be solved only when considering a limited number of degrees of freedom in the time and space discretization. When this is not the case, we indicate in 6.7.3 how a gradient descent approach overcomes such curse of dimensionality.

6.5.3 Numerical results

To illustrate our method, we propose to apply the resulting algorithm to the test case shown in Figure 6.1, which corresponds to the third benchmark case presented in [Boileau et al., 2015]. It consists of a one-dimensional cylindrical vessel with a homogeneous circular cross-section representing the upper thoracic aorta, with a given blood flow as inlet and a three-element Windkessel model as outlet boundary condition. The model parameters were taken from [Xiao et al., 2013] and are reproduced in Table 6.1. Our objective is to estimate the inlet blood flow using some distal pressure measurements (P_{obs}). We present in Section 5.4 the results obtained with synthetic observations for different amounts of artificial noise added to the measurements. Finally in Section 5.5, we exploit this configuration to invert real *in vivo* recording of aortic pressure.

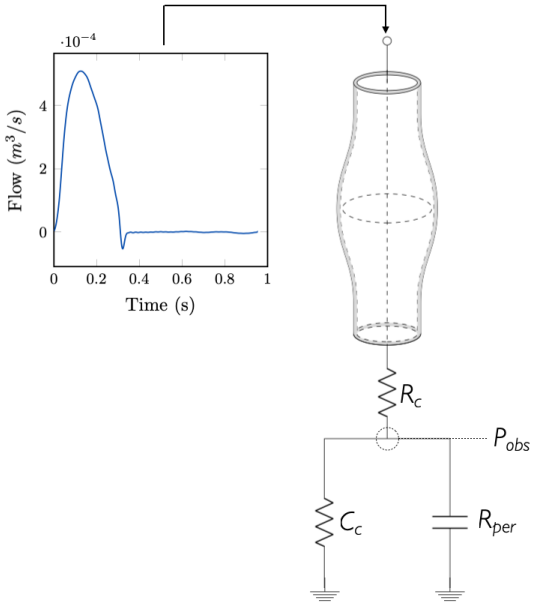

Figure 6.1 – Configuration of the model including a cylindrical homogeneous vessel representing the upper thoracic aorta and a three-elements Windkessel that takes into account the resistive and compliant behavior of the distal vessels. The inlet blood flow is the input for the forward model.

6.5.4 Synthetic results

We perform the forward problem giving an inlet blood flow as input and obtain the state along the vessel. Then, we use the output distal pressure as observation for the inverse problem in order to estimate the inlet flow. The "physical" parameters of the model are the same as in the direct simulation.

Noise and regularization In order to observe the behavior of our reconstruction strategy in presence of noise, very likely when real clinical data are involved, we propose to corrupt the synthetic pressure data $(y_n)_{1\leq n\leq N_T}$ of sampling rate T/N_T with some random artificial noise. We define the discretized noise data as

$$y_n^\delta = y_n + \frac{\delta}{\sqrt{T}}||(y_n)_{1\leq n\leq N_T}||_{\mathrm{L}^2(0,T)}\chi_n, \quad 1 \leq n \leq N_T$$

Table 6.1 – Model parameters of the upper thoracic aorta (Readapted from [Xiao et al., 2013]).

Property	Value
Length, L	24.137 cm
Radius at diastolic pressure, R_0	1.2 cm
Initial flow velocity, $u(s,0)$	0 m s^{-1}
Initial pressure, $P(s,0)$	0 Pa
Wall thickness, h_0	1.2 mm
Blood density, ρ	1060 Kg m^{-3}
Friction parameter, K_r	276.46 mPa s
Velocity profile, α_{vp}	1
Young's modulus, E	400.0 kPa
Diastolic pressure, P_D	9.46 kPa
External pressure, P_{ext}	0 Pa
Windkessel resistance, R_c	$1.1752 \cdot 10^7$ Pa s m^{-3}
Windkessel compliance, C_c	$1.0163 \cdot 10^{-8}$ m^3 Pa^{-1}
Windkessel resistance, R_{per}	$1.1167 \cdot 10^8$ Pa s m^{-3}

where χ_n are independent and identically distributed gaussian variables in $\mathcal{N}(0,1)$ and with the slight abuse of notation the $\mathrm{L}^2(0,T)$ norm for such discrete signal is defined by

$$||(y_n)_{1\leq n\leq N_T}||^2_{\mathrm{L}^2(0,T)} = \frac{T}{N_T}\sum_{n=1}^{N_T} y_n^2$$

One can note that with such choice, we have

$$\frac{||(y_n^\delta - y_n)_{1\leq n\leq N_T}||^2_{\mathrm{L}^2(0,T)}}{||(y_n)_{1\leq n\leq N_T}||^2_{L^2}} = \frac{\delta^2}{N_T}\sum_{i=1}^{N_T}\chi_n^2,$$

which, by property of the empirical variance, gives

$$\lim_{N_T\to\infty}\frac{||(y_n^\delta - y_n)_{1\leq n\leq N_T}||^2_{\mathrm{L}^2(0,T)}}{||(y_n)_{1\leq n\leq N_T}||^2_{\mathrm{L}^2(0,T)}} = \delta^2.$$

As a consequence, our choice of noise corruption is a good numerical approximation of the deterministic measurement error required in Theorem 6.4.7. We test the technique with different levels of noise, in particular we choose $\delta = \{0, 0.005, 0.01, 0.02, 0.03\}$ corresponding to realistic cases. For each different δ, we need to adapt the values of κ to adjust the weight of the Tikhonov regularization. Using Theorem 6.4.7, we obtain the optimal theoretical values for κ, as reported in Table 6.2. However, another way to find the right balance between regularization and agreement with the measurements is through the *L-curve criterion* [Hansen, 2001].where we plot the norm of the solution – $||\nu||^2_{L^2(0,T)}$ – versus the norm of the discrepancy between observations and computed state – $||y_\delta - Cz_{|\zeta,\nu}||^2_{L^2(0,T)}$ – for different values of κ on a log-log plot. The resulting 'L-shape' curve gives the optimal value for the regularization parameter, located in the corner of the 'L' [Hansen, 2001]. In practice, we sample κ regularly in log-scale between 10^{-8} and 1 and we find the ideal regularization parameters, as reported in Table 6.2, to produce the L-curve. Note that both method were meaningless when dealing with $\delta = 0$, in this particular case the optimal value of κ was manually optimized. In Figure 6.2 we show the results obtained for the different levels of noise, comparing the input estimations obtained choosing the optimal value of κ by using Theorem 6.4.7 with the ones obtained relying on the *L-criterion* [Hansen, 2001].

In the fourth column, we picture the L-curves obtained for each value of δ. One can observe that there are almost no difference in the reconstructed output pressure between the two choices of κ. Note that he estimated input flow obtained with the theoretical value of κ shows, as expected, a lower dampening of the oscillations caused by noise while the L-curve based κ, being slightly higher for every value of δ, leads to a smoother curve. Nonetheless both choices seems adapted and work quite well to obtain a coherent input flow.

Table 6.2 – Optimal values for the regularization parameter κ obtained applying Theorem 6.4.7, in the second column, and using the approach involving the analysis of the L-curve, in the third column.

δ	Theorem based κ	L-curve based κ
0.005	$9.55\,10^{-5}$	10^{-3}
0.01	$3.82\,10^{-4}$	$5\,10^{-3}$
0.02	$1.5\,10^{-3}$	10^{-2}
0.03	$3.4\,10^{-3}$	10^{-2}

Sampling mismatch When it comes to real-world applications, measurements have their own sampling time and this may be far from the τ used for numerical simulations imposing to either exploit the data only when they are available or interpolating the data to be compatible with the simulation time-step. In this work, as we are dealing with periodic signals, we choose to rely on a Fourier interpolation. We test two sampled version of the original synthetic observations – $\tau = 8ms$ and $\tau = 5ms$ – being the sampling time often found in catheter-measured arterial pressure. On these sample data, we apply two levels of noise following the approach explained in the previous paragraph, $\delta = \{0.005, 0.02\}$, considered representative of the pressure data usually registered. Finally, we interpolate these data to be discretisation time-step $\tau = 0.001ms$. The results shown in Figure 6.3 are obtained by setting the L-curve based κ values reported in Table 6.2 for the corresponding δ. The results demonstrate the validity of our model-based inversion approach for realistic catheter measurements.

6.5.5 Real data results

Finally, we decided to evaluate our strategy with real clinical data, even if the proposed method is only a first step where we have linearized the initial blood flow model. The data, one *in vivo* measurement of the aortic pressure, were recorded and anonymized by F. Vallée (M.D. and D.r), anaesthetist at Lariboisière Hospital in Paris (APHP). These data are measured using an intra-aortic catheter, equipped with a pressure transducer that can record blood pressure and velocity over time. The pressure measured right above the renal artery is used as observations and the blood flow coming from the left ventricle is reconstructed, the configuration of the IP procedure is depicted in Figure 6.4 and the data injected in the model as well as the source estimated are shown in the boxes at the right and left side of the vessel, respectively. Unfortunately, when the catheter is close to the aortic valve the data are very noisy and, in particular for velocity measurements, hard to analyze from a physiological point of view. For this reason the results depicted in Figure 6.5 show the comparison between the blood velocity computed and the one registered by the catheter close to the pressure observations location and not at the inlet. From Figure 6.5 we can also observe that the computed pressure is in agreement with the data and that the computed blood velocity is in good agreement with the trend of the *in vivo* curve. The latter one presents a high level of noise so it is hard to perform a deeper analysis on the

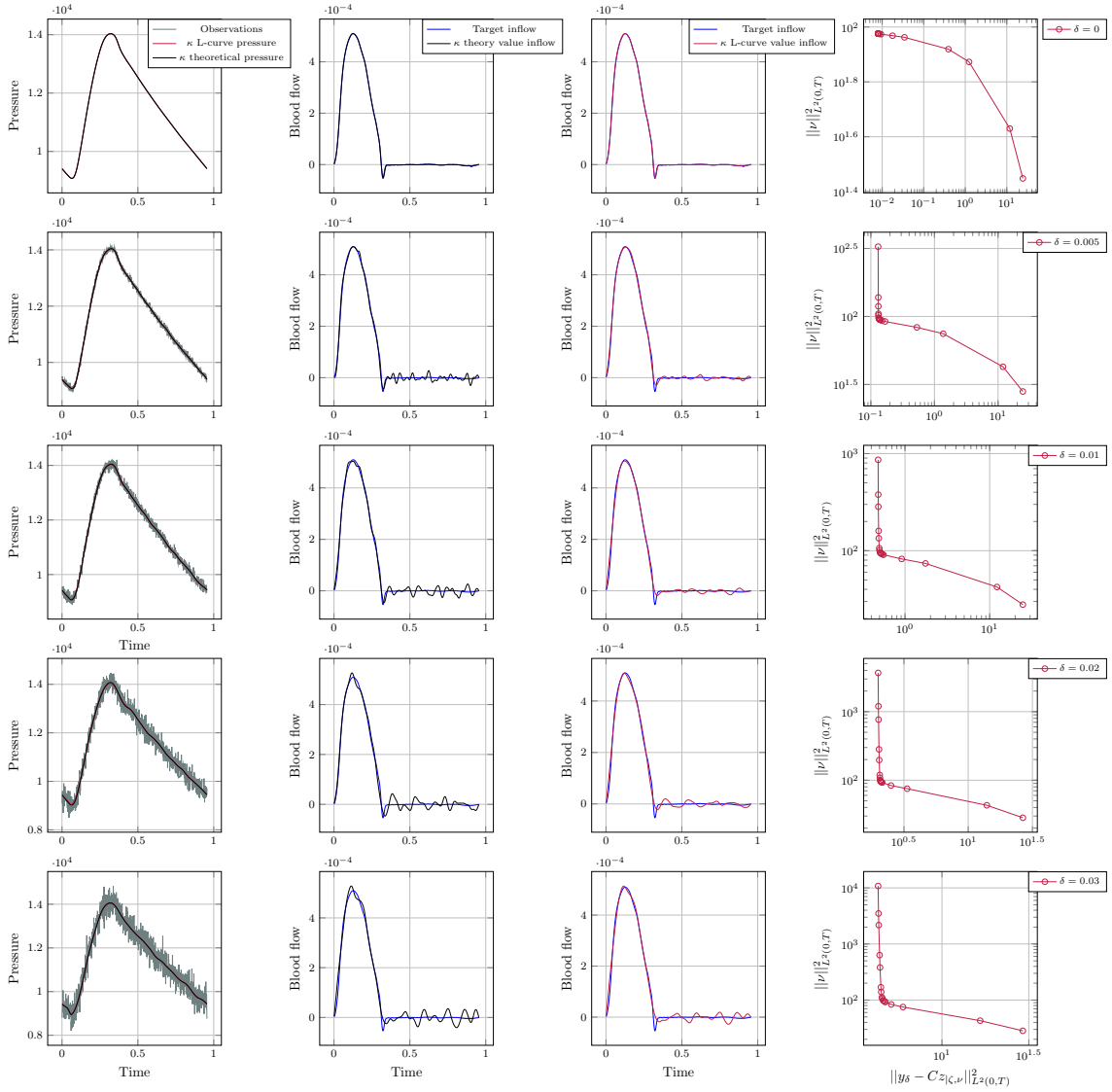

Figure 6.2 – The estimated input flow obtained with the theorem-based choice (black curve in the second column) and with the L-curve-based choice (red curve in the third column) of the regularization parameter κ are compared with the expected flow (blue curve in the second and third column), being the input used for the forward problem. This comparison is done for an increasing level of noise, from the top to the button, and the pressure observation (grey line in the first column) is plotted together with the computed pressure with both choices of κ (black and red curve for the theorem-based and L-curve based κ, respectively). The L-curves obtained for each value of δ are shown in the right column.

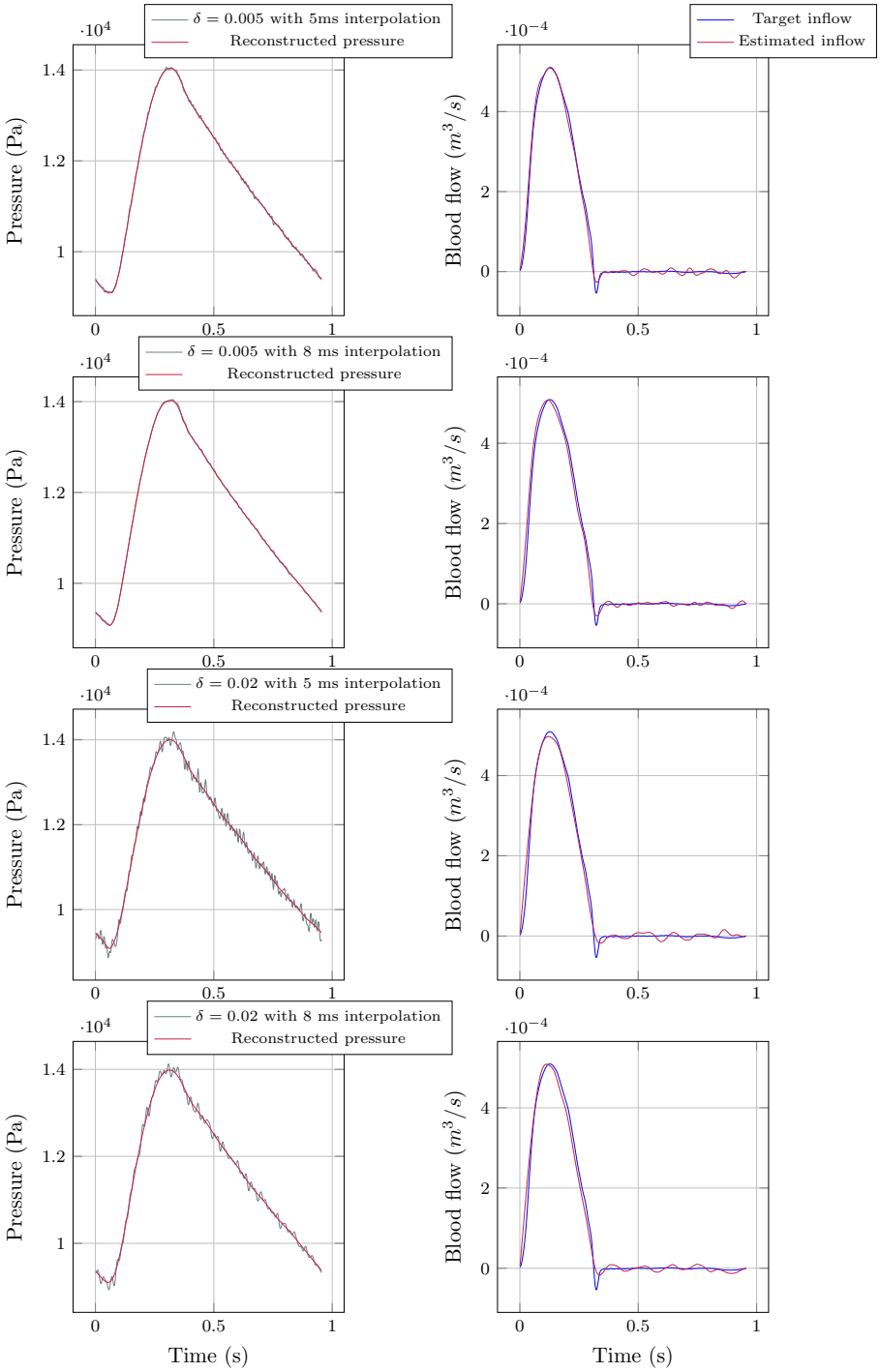

Figure 6.3 – Synthetic pressure data (grey line in the left column) sampled with $\tau = 5ms$ (first and third rows) and $\tau = 8ms$ (second and fourth rows) and with an additional noise of magnitude $\delta = 0.005$ (first and second rows) and $\delta = 0.2$ (third and fourth rows) are interpolated using a MATLAB function based on Fourier interpolation. These data used as observations are compared with the computed output pressure (red line in the left column) and the estimated input flow (red line in the right column) is plotted against the expected estimates (blue line in the right column).

discrepancy between the computed state and the measurements. At a first study we can see that the positive peak of the velocity is well reproduced as well as the trend of the curve, some differences are observable in the baseline value and in the computed negative peak, not present in the data.

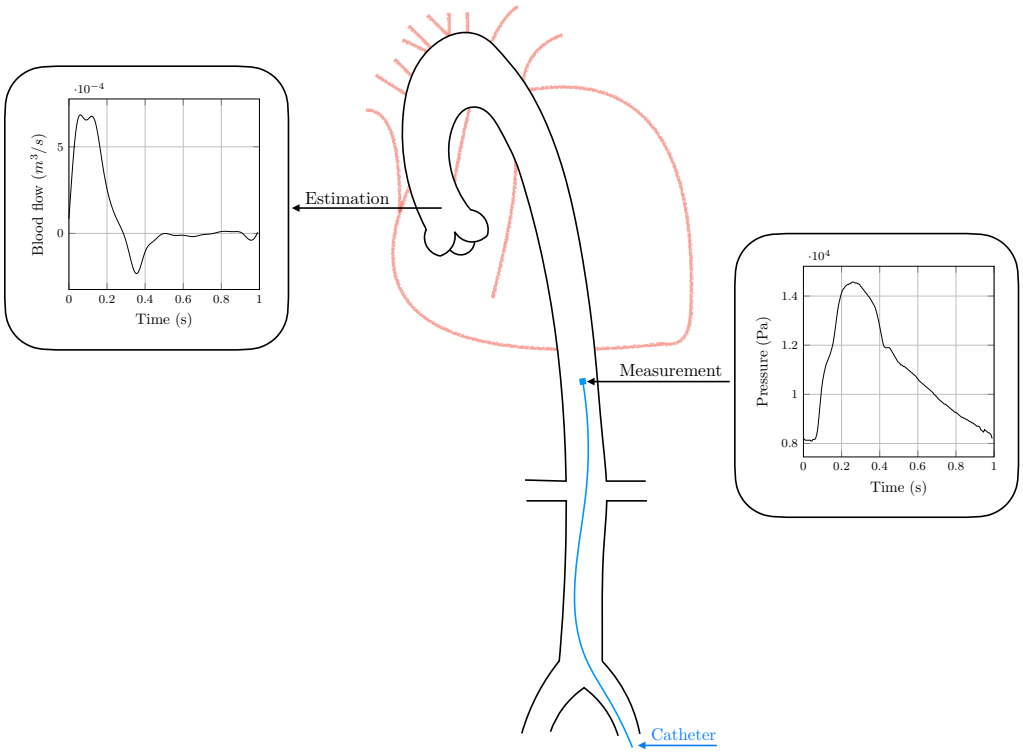

Figure 6.4 – Qualitative representation of an aortic vessel with its main branching vessel, from the heart up to the femoral arteries bifurcation. The location of the measurement site is pointed out by a flesh, on the right, and the distal pressure data used as observation are shown in the box. The estimation spot is also indicated by a flesh, on the left side of the vessel, and the source estimated by using our method is reported in the box.

6.6 Conclusions and Perspectives

In this paper, we present a strategy for an inverse problem based on optimal control theory to recover the inlet flow and initial conditions for a reduced-order model of blood circulation based on a linearized formulation. The forward and inverse problems are analyzed from the mathematical point of view, with a special emphasis on obtaining a fundamental observability condition. This work sets the stage for a new approach to the clinical problem of deriving inaccessible information about cardiac output from accessible peripheral pressure measurements. In practice, we describe an inversion strategy based on a variational approach in which we penalize the periodicity required by the observability condition. Our test in the presence of noise, accounting for sampling mismatches, and using real *in vivo* data are promising but should be extended to evaluate the potential of the estimate for clinical applications. In addition, preliminary parameter estimation is essential to enable patient-specific application. In the clinical context, we could envision such parameter calibration being performed initially using a parameter identification technique such as [Caiazzo et al., 2017] before the catheter is pull-down during the cardiac procedure. A

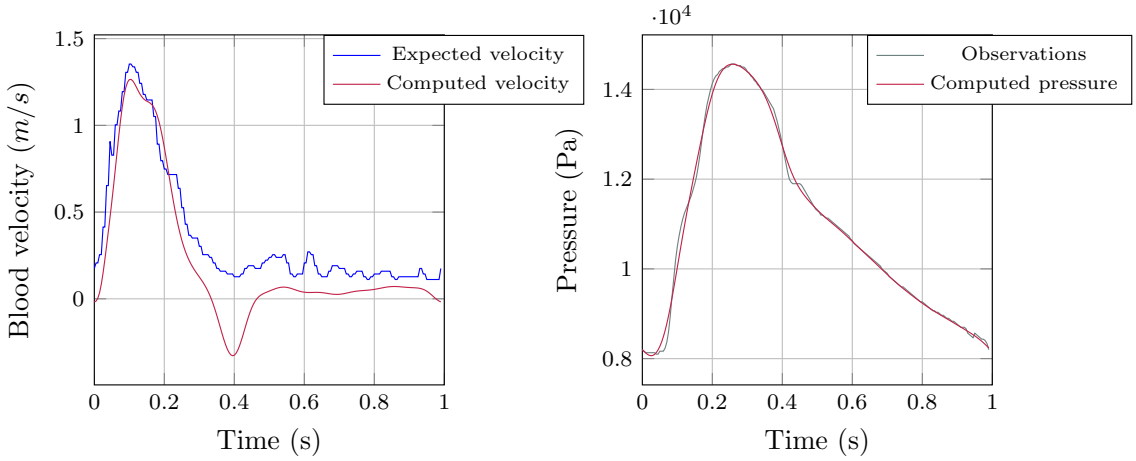

Figure 6.5 – Comparison between the blood velocity computed (in red) and expected (in blue) at a distal location close to the observation site, on the left, and between the pressure computed (in red) and used as input observation (in grey), on the right.

natural evolution of this work is to propose a strategy adapted to the nonlinear model, possibly by iterating over a linearized configuration like the one studied in this work. A second perspective would be to consider a more complex configuration that includes upper limb vessels. This would open the possibility of using radial pressure measurements as observations that can be noninvasive to reconstruct cardiac output.

Acknowledgment

We are very grateful to Fabrice Vallée for providing us with the data that support the findings.

Data availability statement

The data that support the findings of this study are available upon reasonable request from the authors.

6.7 Appendix

6.7.1 The operator $(A, \mathcal{D}(A))$ is maximal dissipative

Let us recall that

$$A = \begin{pmatrix} 0 & -\partial_s & 0 \\ -\partial_s & -k & 0 \\ 0 & c_r\gamma_r & -R \end{pmatrix}$$

with γ_r the trace operator in $s = 1$ and

$$\mathcal{D}(A) := \Big\{(a, v, P) \in \mathrm{H}^1(0,1) \times \mathrm{H}^1_\ell(0,1) \times \mathbb{R} \,|\, a(1) = k_r v(1) + c_r P\Big\},$$

where $\mathrm{H}^1_\ell(0,1) = \{w \in \mathrm{H}^1(0,1) \,|\, w(0) = 0\}$.

We first prove that A is dissipative. Indeed, for all $z = (a, v, P) \in \mathcal{D}(A)$, we have

$$\begin{aligned}(z, Az)_{\mathcal{Z}} &= \int_0^1 \Big[-a'(s)v(s) - v'(s)a(s) - kv(s)^2\Big]\,\mathrm{d}s + c_r v(1)P - RP^2 \\ &= -a(1)v(1) - \int_0^1 kv(s)^2\,\mathrm{d}s + c_r v(1)P - RP^2 \\ &= -k_r v(1)^2 - k\|v\|^2_{\mathrm{L}^2(0,1)} - RP^2 \leq 0.\end{aligned}$$

Then, we need to prove that A is maximal. To do so we consider $\lambda = 0$ and we first show that the bilinear form $\mathcal{D}(A) \times \mathcal{D}(A) \ni (z, q) \mapsto -(Az, q)$ is $\mathtt{T}$-coercive on $\mathcal{D}(A)$ equipped with the norm $\|z\|^2_{\mathcal{D}(A)} = \|a'\|_{\mathrm{L}^2(0,1)} + \|v'\|_{\mathrm{L}^2(0,1)} + P^2$ for $z = (a, v, P) \in \mathcal{D}(A)$ equivalent to the domain graph norm. Note in particular that if $\|a'\|_{\mathrm{L}^2(0,1)} + \|v'\|_{\mathrm{L}^2(0,1)} + P^2 = 0$ for $(a, v, P) \in \mathcal{D}(A)$, then $P = 0$, $v = 0$, hence $a' = 0$ and $a(1) = k_r v(1) + c_r P = 0$ implies that $a = 0$. For a given (α, β) two strictly positive scalar parameters, we define the transformation

$$\mathtt{T}^{\alpha}_{\beta} : \mathcal{D}(A) \ni \begin{pmatrix} a \\ v \\ P \end{pmatrix} \mapsto \begin{pmatrix} a + v' \\ \alpha v + \beta a' \\ P \end{pmatrix}$$

which is clearly bounded in $\mathcal{D}(A)$. This transformation is bijective from $\mathcal{D}(A)$ to $\mathcal{D}(A)$. Indeed, let us consider $(g, h, I) \in \mathcal{D}(A)$ such that

$$\begin{cases} a + v' = g, & \text{in } (0,1), \\ \alpha v + \beta a' = h, & \text{in } (0,1), \\ P = I. \end{cases}$$

where we seek a solution $(a, v, P) \in \mathcal{D}(A)$. We must find a solution in $\mathrm{H}^1(0,1)$ of

$$\begin{cases} \alpha v - \beta v'' = \beta g' - h, & \text{in } (0,1), \\ v(0) = 0 \\ v'(1) + k_r v(1) = g(1) - c_R I \end{cases}$$

which is given by a direct application of Lax-Milgram Theorem. Then, we reconstruct $a(x) = \int_0^x \beta^{-1}(h(s) - \alpha v(s))\,\mathrm{d}s$. The solution $(a, v, P) \in \mathcal{D}(A)$ is unique by unicity in Lax-Milgram Theorem, hence $\mathtt{T}^{\alpha}_{\beta}$ is bijective from $\mathcal{D}(A)$ to $\mathcal{D}(A)$.

Then, we compute for all $z = (a, v, P) \in \mathcal{D}(A)$

$$\begin{aligned}-(Az, \mathtt{T}^{\alpha}_{\beta} z)_{\mathcal{Z}} &= \int_0^1 \Big[(a(s) + v'(s))v'(s) + (\alpha v(s) + \beta a'(s))a'(s)\Big]\,\mathrm{d}s \\ &\quad + \int_0^1 k(\alpha v(s) + \beta a'(s))v(s)\,\mathrm{d}s - c_r v(1)P + RP^2,\end{aligned}$$

By integrating by part the first term and using $a(1) = k_r v(1) + c_r P = 0$, we get

$$\begin{aligned}-(Az, \mathtt{T}^{\alpha}_{\beta} z)_{\mathcal{Z}} &= \int_0^1 \Big[-a'(s)v(s) + v'(s)v'(s) + (\alpha v(s) + \beta a'(s))a'(s)\Big]\,\mathrm{d}s \\ &\quad + \int_0^1 k(\alpha v(s) + \beta a'(s))v(s)\,\mathrm{d}s + k_r v(1)^2 + RP^2,\end{aligned}$$

Choosing $\alpha > 0$, $\beta > 0$ auch that $\alpha + k\beta = 1$, we obtain

$$\begin{aligned}-(Az, \mathtt{T}^{\alpha}_{\beta} z)_{\mathcal{Z}} &= \int_0^1 \Big[v'(s)v'(s) + \beta a'(s)a'(s) + k\alpha v(s)v(s)\Big]\,\mathrm{d}s \\ &\qquad + k_r v(1)^2 + RP^2 \\ &\geq \inf(\alpha, \beta)\,\|z\|^2_{\mathcal{D}(A)}\,.\end{aligned}$$

Therefore from [Ciarlet, 2012, Theorem 1], for all $f \in \mathcal{Z} \subset \mathcal{D}(A)'$, there exists $z \in \mathcal{Z}$ such that $-Az = f$ which implies that $\lambda \mathrm{Id} - A$ is bijective from $\mathcal{D}(A)$ to $\mathcal{Z}$ for $\lambda = 0$, namely A is maximal.

6.7.2 Contraction property using only boundary dissipation

When $k = 0$ the decay of the energy is guaranteed by dissipation effects at the boundary assuming the time window is large enough. In what follows we assume that $k = 0$ and shows a contraction result (in the spirit of Theorem 6.3.5) that hold for all time $t > 2$.

We follow [Diagne et al., 2012] and introduce a Lyapunov functional. Let α be a positive scalar and $m \in \mathrm{C}^1([0,1)]$ be a smooth function, we denote

$$\forall t > 0, \quad \mathcal{L}_m(t) := \mathcal{E}(t) - \mathcal{M}_m(t). \tag{6.86}$$

where

$$\forall t > 0, \quad \mathcal{M}_m(t) := \int_0^1 m(s)\, a(s,t)\, v(s,t)\, \mathrm{d}s.$$

Lemma 6.7.1 *Choose $m = -\alpha\, s$ with $0 \leq \alpha < 1$ then any function $z = (a, v, P) \in \mathrm{C}^0([0,T]; \mathcal{Z})$ satisfies*

$$\forall t > 0, \quad \big(1 - \alpha\big)\mathcal{E}(t) \leq \mathcal{L}_m(t) \leq \big(1 + \alpha\big)\mathcal{E}(t). \tag{6.87}$$

Proof: Substituting the expression of $\mathcal{E}$ and $\mathcal{M}_m$ in (6.86), we have

$$\mathcal{L}_m(t) = \int_0^1 \Big(\frac{1}{2}\left(a^2 + v^2\right) + \alpha\, s\, a\, v\Big)\, \mathrm{d}s + \frac{1}{2}P^2. \tag{6.88}$$

The proof is concluded using the Young inequality. ■

The Lyapunov functional allows us to justify the exponential stability of the system without input source.

Theorem 6.7.2 *The mild solution $z = (a, v, P) \in \mathrm{C}^0([0,T]; \mathcal{Z})$ of (6.15) satisfies*

$$\mathcal{E}(t) \leq \varrho(t_0)\, \mathcal{E}(0) \quad \textit{with} \quad \varrho(t_0) < 1 \quad \textit{and for all} \quad t \geq t_0 > 2.$$

Proof: We start by considering a strict solution in $\mathrm{C}^1([0,T]; \mathcal{Z}) \cap \mathrm{C}^0([0,T]; \mathcal{D}(A))$. By multiplying the first equation of (6.9) by $m(s)v(s,t)$ and the second one by $m(s)a(s,t)$and integrating with respect to time and space, after summation, we get

$$\int_0^t \int_0^1 \Big(\partial_t(m\, a\, v) + m\, \partial_s \frac{v^2}{2} + m\, \partial_s \frac{a^2}{2}\Big)\, \mathrm{d}s\, \mathrm{d}\tau = 0.$$

Integrating by parts and rearranging terms gives

$$\begin{aligned} \frac{1}{2}\int_0^t \big(v^2(0,x) + a^2(0,\tau)\big)m(0)\, \mathrm{d}\tau - \frac{1}{2}\int_0^t \big(v^2(1,\tau) + a^2(1,\tau)\big)m(1)\, \mathrm{d}\tau \\ = \mathcal{M}_m(t) - \mathcal{M}_m(0) - \frac{1}{2}\int_0^t \int_0^1 m'\big(v^2 + a^2\big)\, \mathrm{d}s\, \mathrm{d}\tau. \end{aligned} \tag{6.89}$$

Now, let us differentiate $\mathcal{L}_m$, with respect to time. We obtain

$$\dot{\mathcal{L}}_m = \dot{\mathcal{E}} + \dot{\mathcal{M}}_m$$

Using (6.89) and (6.34) as well as (6.9) one can show that

$$\dot{\mathcal{L}}_m = -\Omega - \Gamma,$$

with

$$\Omega = -\frac{1}{2}\int_0^1 m'(a^2 + v^2)\,\mathrm{d}s,$$

and

$$\Gamma = k_r v^2(1) + RP^2 - \frac{m(0)}{2}a^2(0) + \frac{m(1)}{2}v^2(1) + \frac{m(1)}{2}a^2(1).$$

Our objective is now to bound by below these two quantities by energy terms. The function m is chosen as

$$m(s) = -\alpha\, s.$$

Then, we have

$$\Omega = \frac{\alpha}{2}\int_0^1 v^2 + a^2\,\mathrm{d}s. \tag{6.90}$$

Now, using the first equation of (6.10) in Γ and the definition of m (in particular we use the property that $m(0) = 0$) we can write

$$\Gamma = k_r v^2(1) + RP^2 - \frac{\alpha}{2}\Big[v^2(1) + (k_r v(1) + c_r P)^2\Big],$$

hence since $k_r > 0$ and $R > 0$, we have, for α sufficiently small,

$$\Gamma \geq (R - \alpha c_r^2)\, P^2. \tag{6.91}$$

Combining (6.90) and (6.91), we obtain, for α small,

$$\dot{\mathcal{L}}_m(t) \leq -\alpha\, \mathcal{E}(t).$$

Moreover, for α small, estimate (6.87) holds, hence

$$\dot{\mathcal{L}}_m(t) \leq -c_\alpha\, \mathcal{L}_m(t), \quad c_\alpha = \alpha(1+\alpha)^{-1}.$$

This implies that

$$\mathcal{L}_m(t) \leq e^{-c_\alpha t}\mathcal{L}_m(0) \quad \Rightarrow \quad \mathcal{E}(t) \leq \frac{1+\alpha}{1-\alpha}e^{-c_\alpha t}\mathcal{E}(0).$$

Now, for α small we have

$$\frac{1+\alpha}{1-\alpha} = 1 + 2\,\alpha + O(\alpha^2), \quad c_\alpha = \alpha + O(\alpha^2)$$

hence

$$\frac{1+\alpha}{1-\alpha}e^{-c_\alpha t} = (1+2\,\alpha)(1-\alpha t) + O(\alpha^2) = 1 + \alpha(2-t) + O(\alpha^2). \tag{6.92}$$

This shows that, for $t_0 > 2$, there exists, choosing α small enough, $\rho(t_0) < 1$ such that, for all $t \geq t_0$

$$\mathcal{E}(t) \leq \rho(t_0)\, \mathcal{E}(0). \tag{6.93}$$

We finally conclude the proof by extending the inequality (6.93) to mild solutions by density of $\mathcal{D}(A)$ in $\mathcal{Z}$. ■

6.7.3 A discrete-time optimal control approach

Optimality system at the discrete level – The minimization of the discretized $\mathscr{J}^N_{\kappa,\varepsilon}$ under the finite dimensional constraint (6.83) can be derived using the associated Lagrangian

$$\begin{aligned}\mathscr{L}((z_h^n)_{0\le n\le N_T},(q_h^n)_{0\le n\le N},(\nu^n)_{1\le n\le N_T}) &= \varepsilon^{-1}\left\|z_h^{N_T}-z_h^0\right\|^2_{\mathcal{Z}}\\ &+\tfrac{\tau}{2}\textstyle\sum_{n=0}^{N_T-1}\Big[|y_\delta^n-Cz_h^n|^2+\kappa\Big(|\nu^n|^2+\Big|\frac{\nu^{n+1}-\nu^n}{\tau}\Big|^2\Big)\Big]\\ &+\textstyle\sum_{n=0}^{N_T-1}(q_h^{n+1},z_h^{n+1}-\Phi_{h,\tau}z_h^n-B_{h,\tau}\nu^{n+1})_{\mathcal{Z}}. \end{aligned}\tag{6.94}$$

From Kuhn-Tucker Theorem in finite dimension, we now seek for the saddle-point of the Lagrangian. Writing the optimality condition leads to, for $0<n<N_T$,

$$\begin{aligned}\forall\eta_h\in\mathcal{V}_h,\quad 0 &= \big\langle \mathrm{D}_{z^n}\mathscr{L}((\bar z_h^n)_{0\le n\le N},(\bar q_h^n)_{0\le n\le N},(\bar\nu^n)_{1\le n\le N}),\eta_h\big\rangle\\ &= -\tau(y_\delta^n-C\bar z_h^n,C\eta)+(\bar q_h^n,\eta_h)-(\bar q_h^{n+1},\Phi_{h,\tau}\eta_h),\end{aligned}\tag{6.95}$$

namely

$$\bar q_h^n=\Phi_{h,\tau}^*\bar q_h^{n+1}+\tau C^*(y_\delta^n-C\bar z_h^n),\quad 0<n<N_T.\tag{6.96}$$

Then, from

$$\begin{aligned}\forall\eta\in\mathcal{V}_h,\quad 0 &= \big\langle \mathrm{D}_{z^N}\mathscr{L}((\bar z_h^n)_{0\le n\le N},(\bar q_h^n)_{0\le n\le N},(\bar\nu^n)_{1\le n\le N}),\eta_h\big\rangle\\ &= \varepsilon^{-1}(\bar z_h^{N_T}-\bar z_h^0,\eta_h)_{\mathcal{Z}}+(\bar q_h^{N_T},\eta_h)_{\mathcal{Z}},\end{aligned}\tag{6.97}$$

we deduce

$$\bar q_h^{N_T}=-\varepsilon^{-1}(\bar z_h^{N_T}-\bar z_h^0).$$

Further, we have also

$$\begin{aligned}\forall\eta\in\mathcal{V}_h,\quad 0 &= \big\langle \mathrm{D}_{z^0}\mathscr{L}((\bar z_h^n)_{0\le n\le N}(\bar q_h^n)_{0\le n\le N},(\bar\nu^n)_{1\le n\le N}),\eta\big\rangle\\ &= -\varepsilon^{-1}(\bar z^{N_T}-\bar z^0,\eta_h)_{\mathcal{Z}}-\tau(y_\delta^0-C\bar z^0,C\eta_h)_{\mathcal{Z}}-(\bar q^1,\Phi\eta_h)_{\mathcal{Z}}.\end{aligned}\tag{6.98}$$

Therefore, by defining $\bar q^0=\Phi_{h,\tau}^*\bar q_h^1+\tau C^*(y_\delta^0-C\bar z_h^0)$, namely considering (6.96) also for $n=0$, we find that

$$\bar q_h^0=\varepsilon^{-1}(\bar z_h^{N_T}-\bar z_h^0).\tag{6.99}$$

Finally, by using an Abel transform with $\nu^0=\nu^{N_T}$, we have the classical identity

$$\begin{aligned}\sum_{n=0}^{N_T-1}\Big(\frac{\nu^{n+1}-\nu^n}{\tau}\Big)\Big(\frac{\mu^{n+1}-\mu^n}{\tau}\Big) &= \textstyle\sum_{n=1}^{N_T}\Big(\frac{\nu^{n+1}-2\nu^n+\nu^{n-1}}{\tau^2}\Big)\mu^n\\ &= \textstyle\sum_{n=1}^{N_T}\nu^n\Big(\frac{\mu^{n+1}-2\mu^n+\mu^{n-1}}{\tau^2}\Big),\end{aligned}$$

which leads to the partial derivative

$$\begin{aligned}0 &= \partial_{\nu^n}\mathscr{L}((\bar z_h^n)_{0\le n\le N_T}(\bar q_h^n)_{0\le n\le N_T},(\bar\nu^n)_{1\le n\le N}),\\ &= \kappa\Big(\nu^n+\tfrac{\nu^{n+1}-2\nu^n+\nu^n}{\tau^2}\Big)-B_{h,\tau}^*\bar q^n.\end{aligned}\tag{6.100}$$

We consequently introduce the linear operator $K_\sharp\in\mathcal{M}_{N_T}(\mathbb{R})$ such that for any vector $(\mu_n)_{n\in[1,N_T]}$ and $(\nu_n)_{n\in[1,N_T]})$ such that $\mu_0=\mu_{N_T}$ and $\nu_0=\nu_{N_T}$.

$$((\mu_n)_{n\in[1,N_T]},K_\sharp(\nu_n)_{n\in[1,N_T]}))_{\ell^2([1,N_T])}=-\sum_{n=1}^{N_T}\Big(\frac{-\nu^{n+1}+2\nu^n-\nu^n}{\tau^2}\Big)\mu^n.$$

We ultimately obtain the optimality system

$$\begin{cases} \bar{z}_h^{n+1} = \Phi_{h,\tau}\bar{z}_h^n + B_{h,\tau}((\mathrm{Id}+K_\sharp)^{-1}(B_{h,\tau}\bar{q}_h^n)_{n\in[1,N]})^{n+1}, & 0 \le n \le N_T-1 \\ \bar{q}_h^n = \Phi_{h,\tau}^*\bar{q}_h^{n+1} + \tau C^*(y_\delta^n - C\bar{z}_h^n), & 0 \le n \le N_T-1 \\ \bar{z}_h^0 = \bar{z}_h^{N_T} + \varepsilon\bar{q}_h^0, \\ \bar{q}_h^{N_T} = -\varepsilon^{-1}(\bar{z}_h^{N_T} - \bar{z}_h^0), \end{cases} \tag{6.101}$$

A gradient descent approach – Solving the optimality system (6.101) implies to solve a fully coupled space-time problem which can be overcome, for large-dimensional discretization, using an iterative procedure based on a descent-gradient minimization of the associated functional $\mathscr{J}_{\kappa,\varepsilon}^{N_T}$. We easily obtain from the previous computation on the Lagrangian that the gradient of $\mathscr{J}_{\kappa,\varepsilon}^{N_T}$ is given by

$$\nabla_\zeta \mathscr{J}_{\kappa,\varepsilon}^{N_T} = \varepsilon^{-1}(\bar{z}_h^0 - \bar{z}_h^{N_T}) - q_{h|\zeta,\nu}^0$$

and

$$\nabla_{\nu^n} \mathscr{J}_{\kappa,\varepsilon}^{N_T} = \kappa\Big(\nu^n + \frac{\nu^{n+1} - 2\nu^n + \nu^n}{\tau^2}\Big) - B_{h,\tau}^* q_{h|\zeta,\nu}^n$$

with $(q_{h|\zeta,\nu}^n)_{1\le n\le N_T}$ computed from a given trajectory $(z_{h|\zeta,\nu}^n)$ by following adjoint equation

$$\begin{cases} q_{h|\zeta,\nu}^n = \Phi_{h,\tau}^*\bar{q}_h^{n+1} + \tau C^*\big(y_\delta^n - C\bar{z}_{h|\zeta,\nu}^n\big) \\ q_{h|\zeta,\nu}^{N_T} = -\varepsilon^{-1}(z_{h|\zeta,\nu}^{N_T} - z_{h|\zeta,\nu}^0) \end{cases} \tag{6.102}$$

Therefore, the solution of two-end problem (6.101) is obtained as the limit of the iterative back and forward scheme: given a small enough relaxation sequence (ρ^j), we compute at each iteration $j \in \mathbb{N}$

$$\begin{cases} z_h^{n+1,j+1} = \Phi_{h,\tau} z_h^{N_T} + B_{h,\tau}(1-\rho^j)\nu^{n+1} \\ \qquad\qquad + \rho^j((\mathrm{Id}+K_\sharp)^{-1}(B_{h,\tau}q_h^{n,j})_{n\in[1,N]})^{n+1}, \quad n \ge 0 \\ z_h^{0,j+1} = (1-\rho^j)z_h^{0,j} + \rho^j(\bar{z}_h^{N_T} + \varepsilon q_{h|\zeta,\nu}^{N_T}) \end{cases} \tag{6.103}$$

followed by

$$\begin{cases} \bar{q}_h^{n,j+1} = \Phi_{h,\tau}^*\bar{q}_h^{n+1,j+1} + \tau C^*(y_\delta^n - C\bar{z}_h^{n,j+1}) \\ q_h^{N_T,j+1} = -\varepsilon^{-1}(z_{h|\zeta,\nu}^{N_T,j+1} - z_h^{0,j+1}) \end{cases} \tag{6.104}$$

This can be implemented using the following algorithm:

Algorithm 1: Gradient descent algorithm

```
Choose the initial guesses z_h^{0,0} and (ν^{n,0})_{1≤n≤N_T} ;
while z_h^{0,j} and (ν^{n,j})_{1≤n≤N_T} are not converged do
    Fix ρ^j from the selected descent strategy ;
    Compute (6.103) ;
    Compute (6.104) ;
end
```

However, it is well-known that solving a penalized optimisation problem using a gradient descent approach is unfavorable as, by nature, the underlying linear system to be solved faces ill-conditionning [Luenberger and Ye, 2011].

Bibliography

Arthurs, C. J., Xiao, N., Moireau, P., Schaeffter, T., and Figueroa, C. A. (2020). A flexible framework for sequential estimation of model parameters in computational hemodynamics. *Advanced Modeling and Simulation in Engineering Sciences*, pages 1–37.

Bensoussan, A. (1971). *Filtrage optimal des systèmes linéaires*. Dunod.

Bensoussan, A., Delfour, M. C., Da Prato, G., and Mitter, S. K. (2007). *Representation and Control of Infinite Dimensional Systems*. Birkhauser Verlag, Boston, second edition edition.

Boileau, E., Nithiarasu, P., Blanco, P. J., Müller, L. O., Fossan, F. E., Hellevik, L. R., Donders, W. P., Huberts, W., Willemet, M., and Alastruey, J. (2015). A benchmark study of numerical schemes for one-dimensional arterial blood flow modelling. *International Journal for Numerical Methods in Biomedical Engineering*, 31(10):e02732.

Bollache, E., Kachenoura, N., Redheuil, A., Frouin, F., Mousseaux, E., Recho, P., and Lucor, D. (2014). Descending aorta subject-specific one-dimensional model validated against in vivo data. *Journal of Biomechanics*, 47(2):424–431.

Caiazzo, A., Caforio, F., Montecinos, G., Müller, L. O., Blanco, P. J., and Toro, E. F. (2017). Assessment of reduced-order unscented kalman filter for parameter identification in 1-dimensional blood flow models using experimental data. *International journal for numerical methods in biomedical engineering*, 33(8):e2843.

Chen, C.-H., Nevo, E., Fetics, B., Pak, P. H., Yin, F. C., Maughan, W. L., and Kass, D. A. (1997). Estimation of central aortic pressure waveform by mathematical transformation of radial tonometry pressure. *Circulation*, 95(7):1827–1836.

Ciarlet, P. (2012). T-coercivity: Application to the discretization of helmholtz-like problems. *Computers & Mathematics with Applications*, 64(1):22–34.

Cîndea, N., Imperiale, A., and Moireau, P. (2015). Data assimilation of time undersampled measurements using observers, the wave-like equation example. *ESAIM. Control, Optimisation and Calculus of Variations. European Series in Applied and Industrial Mathematics*, 21(3):635–669.

D'Elia, M., Perego, M., and Veneziani, A. (2011). A variational data assimilation procedure for the incompressible navier-stokes equations in hemodynamics. *Journal of Scientific Computing*, 52(2):340–359.

Diagne, A., Bastin, G., and Coron, J. M. (2012). Lyapunov exponential stability of 1-d linear hyperbolic systems of balance laws. *Automatica*, 48(1):109–114.

Engl, H. W., Hanke, M., and Neubauer, A. (1996). *Regularization of inverse problems*, volume 375 of *Mathematics and its Applications*. Kluwer Academic Publishers Group, Dordrecht.

Epstein, S., Willemet, M., Chowienczyk, P. J., and Alastruey, J. (2015). Reducing the number of parameters in 1d arterial blood flow modeling: less is more for patient-specific simulations. *American Journal of Physiology-Heart and Circulatory Physiology*, 309(1):H222–H234.

Fetics, B., Nevo, E., Chen, C.-H., and Kass, D. (1999). Parametric model derivation of transfer function for noninvasive estimation of aortic pressure by radial tonometry. *IEEE Transactions on Biomedical Engineering*, 46(6):698–706.

Fossan, F. E., Mariscal-Harana, J., Alastruey, J., and Hellevik, L. R. (2018). Optimization of topological complexity for one-dimensional arterial blood flow models. *Journal of The Royal Society Interface*, 15(149):20180546.

Hansen, P. C. (2001). *The L-Curve and Its Use in the Numerical Treatment of Inverse Problems*, volume 4, pages 119–142.

Joachim, J., Vallée, F., Gall, A. L., Matéo, J., Lenck, S., Millasseau, S., Houdart, E., Mebazaa, A., and Gayat, E. (2017). Velocity–pressure loops for continuous assessment of ventricular afterload: influence of pressure measurement site. *Journal of Clinical Monitoring and Computing*, 32(5):833–840.

Lal, R., Mohammadi, B., and Nicoud, F. (2017). Data assimilation for identification of cardiovascular network characteristics. *International journal for numerical methods in biomedical engineering*, 33(5):e2824.

Ljung, L. (1999). *System Identification: Theory for the User*. Prentice Hall information and system sciences series. Prentice Hall PTR.

Lombardi, D. (2013). Inverse problems in 1D hemodynamics on systemic networks: A sequential approach. *International Journal for Numerical Methods in Biomedical Engineering*, 30(2):160–179.

Luenberger, D. and Ye, Y. (2011). *Linear and nonlinear programming*. Springer.

Manganotti, J., Caforio, F., Kimmig, F., Moireau, P., and Imperiale, S. (2021). Coupling reduced-order blood flow and cardiac models through energy-consistent strategies: modeling and discretization. *Advanced Modeling and Simulation in Engineering Sciences*, 8(1):1–37.

Martin, V., Clément, F., Decoene, A., and Gerbeau, J.-F. (2005). Parameter identification for a one-dimensional blood flow model. In *ESAIM: Proceedings*, volume 14, pages 174–200. EDP Sciences.

Matthys, K. S., Alastruey, J., Peiró, J., Khir, A. W., Segers, P., Verdonck, P. R., Parker, K. H., and Sherwin, S. J. (2007). Pulse wave propagation in a model human arterial network: Assessment of 1-d numerical simulations against in vitro measurements. *Journal of Biomechanics*, 40(15):3476–3486.

Millasseau, S. C., Patel, S. J., Redwood, S. R., Ritter, J. M., and Chowienczyk, P. J. (2003). Pressure wave reflection assessed from the peripheral pulse. *Hypertension*, 41(5):1016–1020.

Moireau, P., Bertoglio, C., Xiao, N., Figueroa, C. A., Taylor, C. A., Chapelle, D., and Gerbeau, J.-F. (2012). Sequential identification of boundary support parameters in a fluid-structure vascular model using patient image data. *Biomechanics and Modeling in Mechanobiology*, 12(3):475–496.

Müller, L. O., Caiazzo, A., and Blanco, P. J. (2018). Reduced-order unscented kalman filter with observations in the frequency domain: application to computational hemodynamics. *IEEE Transactions on Biomedical Engineering*, 66(5):1269–1276.

Pauca, A. L., O'Rourke, M. F., and Kon, N. D. (2001). Prospective evaluation of a method for estimating ascending aortic pressure from the radial artery pressure waveform. *Hypertension*, 38(4):932–937.

Peiro, J., Sherwin, S., Parker, K., Franke, V., Formaggia, L., Lamponi, D., and Quarteroni, A. (2003). Numerical simulation of arterial pulse propagation using one-dimensional models. *Wall-fluid interactions in physiological flows*, pages 1–36.

Politi, M. T., Ghigo, A., Fernández, J. M., Khelifa, I., Gaudric, J., Fullana, J. M., and Lagrée, P.-Y. (2016). The dicrotic notch analyzed by a numerical model. *Computers in Biology and Medicine*, 72:54–64.

Reymond, P., Merenda, F., Perren, F., Rüfenacht, D., and Stergiopulos, N. (2009). Validation of a one-dimensional model of the systemic arterial tree. *American Journal of Physiology-Heart and Circulatory Physiology*, 297(1):H208–H222.

Sixou, B., Boissel, L., and Sigovan, M. (2017). Vascular blood flow reconstruction from tomographic projections with the adjoint method and receding optimal control strategy. *Journal of Physics: Conference Series*, 904:012001.

Stok, W. J., Westerhof, B. E., Guelen, I., and Karemaker, J. M. (2011). Aortic pressure wave reconstruction during exercise is improved by adaptive filtering: a pilot study. *Medical and Biological Engineering and Computing*, 49(8):909–916.

Tikhonov, A. N. (1963). Solution of incorrectly formulated problems and the regularization method. *Soviet Math.*, 4:1035–1038.

Tucsnak, M. and Weiss, G. (2009). *Observation and control for operator semigroups*. Birkhäuser Advanced Texts: Basler Lehrbücher. Birkhäuser Verlag, Basel.

Vlachopoulos, C., ORourke, M., and Nichols, W. W. (2011). *McDonalds Blood Flow in Arteries*. CRC Press.

Willemet, M. and Alastruey, J. (2014). Arterial pressure and flow wave analysis using time-domain 1-d hemodynamics. *Annals of Biomedical Engineering*, 43(1):190–206.

Xiao, N., Alastruey, J., and Figueroa, C. A. (2013). A systematic comparison between 1-d and 3-d hemodynamics in compliant arterial models. *International Journal for Numerical Methods in Biomedical Engineering*, 30(2):204–231.

Zuazua, E. (2005). Propagation, Observation, and Control of Waves Approximated by Finite Difference Methods. *SIAM Review*, 47(2):197–243.

CHAPTER 7

Inlet pressure recovery from distal pressure using iterative least squares estimation approach

It is also fundamentally unscientific, letting the conclusion direct the available data, when the opposite should be true. Unless you truly believe you know the answer to every question in life before you have reviewed the evidence, then box thinking is going to limit your ability to make good decisions. It can feel good to have clearly delineated choices, but that is probably a false comfort.

— Camilla Pang, *Explaining Humans*

We present a method to apply an iterative variational inverse problem on a non-linear formulation describing the circulation between the heart and the hand, in order to use radial pressure measurements as observations. First, we describe the well-known iterative methods to solve optimal control problem that involves non-linear dynamics and we derive our simplified iterative procedure. Then, we apply the iterative approach on a test-case representing the upper thoracic aorta model configuration, and on a more realistic set-up including the upper limb arteries. Finally, we show some preliminary results obtained with *in vivo* peripheral pressure data.

Contents

7.1 Introduction

7.1.1 Motivations

The final purpose of this project is to derive a strategy to improve the cardiovascular monitoring during surgeries. We have seen that the access to the informations of interest, typically pressure and blood flow at central sites, is not common and that peripheral measurements are usually available. Current solutions involve the use of a transfer function (TF) to retrieve central from distal pressure waves based on an auto-regressive model [Chen et al., 1997; Joachim et al., 2017; Pauca et al., 2001], and this method has also been implemented into a medical device. However, as we have mentioned in the previous chapters, general transfer functions do not take into account patient variability, and in the attempt to provide a parametrization a previously calibrated model was involved [Karamanoglu and Feneley, 1996, 1997], thus requiring multiple steps and the computation of both a model and a TF. In Chapter 6 we have proposed a different strategy to estimate a central cardiovascular marker such as the blood flow close to the aortic valve by using peripheral measurements of pressure. The strategy is based on a data assimilation technique and in particular a 4D-Variational approach [Laroche and Gauthier, 1998; Robert et al., 2005]. The inverse problem derived is applied on a simple model of the upper thoracic aorta inspired by the formulation presented in [Manganotti et al., 2021]. However, in the previous chapter the blood flow formulation involved is linearized around a steady state and in the perspective of a clinical application this could be an excessive simplification of the circulatory phenomena and thus represent a limitation. Moreover, the model configuration involves a single vessel representing the upper thoracic aorta, hence restraining the possible locations for suitable measurements to the aorta. In this chapter we present an iterative procedure for the optimal control problem that enables the use of a non-linear blood flow formulation. In particular, an approximated Gauss-Newton (GN) method is applied to solve the inverse problem and estimate the central pressure by using peripheral measurements. An important aspect of the method is that the first iteration corresponds to the linear problem analyzed in the previous chapter, thus having the same mathematical properties.

7.1.2 Problem setting

Let us present the physical system in its formal abstract form. The quantity of interest corresponds to a function $z(t) \in Z$, where Z is an Hilbert space, and it is subjected to the dynamics

$$\dot{z}(t) = A(z(t))z(t) + B(z(t))\nu(t) \quad \text{with}\, t \in [0, T]. \tag{7.1}$$

For each $w \in Z$, the operators $A(w)$ and $B(w)$ are respectively the dynamic and the control operator that depend non linearly on w, while $\nu \in U$ is the source term and U another Hilbert space (typically $H^1(0, T)$). Eq. (7.1) is completed with either initial data – $z(0) = z_0$ – or periodic conditions – $z(0) = z(T)$.
A fundamental assumption is first, that for each w, $A(w)$ is a dissipative operator, namely $(A(w)z, z)_Z \leq 0$ for all z sufficiently regular and second, that $\dot{z} = A(w)z$ with zero initial conditions or periodic conditions, has a unique solution. The hypothesis of $A(z)$ being dissipative motivates an iterative algorithm that allows us to compute the solution z for the non linear problem. We solve, at each iteration k

$$\dot{z}_{k+1} = A(z_k)z_{k+1} + B(z_k)\nu \tag{7.2}$$

with, for all k, some given initial conditions – $z_k(0) = z_0$ – or some periodic conditions, which would imply $z_k(T) = z_k(0)$. One can notice that Eq. (7.2) implies the solution for

a linear PDE problem that has a controlled energy behavior. Namely, in absence of source term the energy is decaying. Later in this chapter we will see that after three iterations the method applied on the model formulation of Section 7.4 fits the results obtained with the non-linear formulation with sufficient accuracy. Eq. (7.2) can be seen as a problem resulting from the pseudo-linearization – as it does not involve the variation of $A(z)$ with respect to z – of Eq. (7.1). The main idea is to use this pseudo-linearization to derive an inverse problem strategy for the non-linear formulations of the aorta and the upper limb.

7.1.3 Chapter organization

This chapter is organized as follows: in Section 7.2 we present six continuous algorithms describing iterative non-tangent methods to solve optimal control problems. We start from well-known strategies and gradually approximate the non-linearities of the model dynamics by using 'pseudo-linear' models to obtain an original iterative linear inverse problem. In Section 7.3 we derive the discrete version of the algorithm. In Section 7.4 and Section 7.5 we details the approach to approximate the non-linearities of the model, respectively for a simple test case representing the upper thoracic aorta and for a more realistic set-up including the arteries of the arms. Finally, in Section 7.6 we present some numerical results of input pressure estimation obtained by using synthetic and real clinical data as observations.

7.2 Iterative non-tangent method

The objective of our 4D-Var data assimilation problem is to find ν – the input source – such that the difference between the solution for the model z and the observations y_δ is minimized [Lawless et al., 2005b]. This finds its mathematical expression with the inversion of the operator Ψ_T, which is achieved through a non-linear least square minimization problem provided with a Tikhonov regularization, that reads

$$\min_{\nu \in U} \left\{ \mathcal{J}(\nu) = \frac{1}{2} ||y_\delta - \Psi_T(\nu)||^2_{L^2(0,T;Y)} + \frac{\kappa}{2} ||\nu||^2_U \right\}, \tag{7.3}$$

where Y is a given Hilbert space (in what follows $Y = \mathbb{R}$) and $\Psi_T : U \mapsto L^2(0,T;Y)$ a non-linear operator defined by $\Psi_T(\nu) = C z_{|\nu}$, with $z_{|\nu}$ solution to Eq. (7.2) and C a linear operator denoted as observation operator. The solution for Eq. (7.3) involves the inversion of Ψ_T, due to its non-linearity this process becomes highly expensive. In order to solve (7.3) efficiently we use an incremental method, that we detail in the following paragraphs. Note that each time a dynamic problem is involved we consider it as completed by initial or periodic conditions, unless specified otherwise.

7.2.1 Gauss-Newton Method

The Gauss-Newton (GN) method is an iterative algorithm that involves the minimization of a series of linear least-square approximations of the original non-linear problem [Gratton et al., 2007]. Assuming Ψ_T differentiable and introducing ν^k – as an approximation of the minimizer of (7.3) [Ortega and Rheinboldt, 2000] – at each iteration k, denoted as the *outer iteration* in [Lawless et al., 2005b], we have

$$\nu_{k+1} = \nu_k + \tilde{\nu}_k, \tag{7.4}$$

with

$$\tilde{\nu}_k = \Big(\kappa Id + D\Psi_T^* D\Psi_T \Big)^{-1} \Big(D\Psi_T^* (y_\delta - \Psi_T(\nu_k)) - \kappa \nu_k \Big),$$

and $D\Psi_T \equiv D\Psi_T(\nu_k) : U \mapsto L^2(0,T;Y)$ is a linear operator defined formally as

$$D\Psi_T(\nu_k)\nu = \lim_{\delta \mapsto 0} \frac{\Psi_T(\nu_k + \delta\nu) - \Psi_T(\nu_k)}{\delta},$$

that corresponds to the derivative of the non-linear operator $\Psi_T(\nu_k)$ along the direction ν. Finally $D\Psi_T^*$ is the adjoint of the operator $D\Psi_T$. The second term at the right hand side of Eq. (7.4) belongs to U and is solution for the following minimization

$$\min_{\tilde{\nu}} \left\{ \mathcal{J}_k = \frac{1}{2}||y_\delta - (\Psi_T(\nu_k) + D\Psi_T(\nu_k)\tilde{\nu})||^2_{L^2(0,T;Y)} + \frac{\kappa}{2}||\nu_k + \tilde{\nu}||^2_U \right\}. \tag{7.5}$$

In [Lawless et al., 2005b], the solution to Eq. (7.5) is achieved by using a gradient descent approach, which implies some iterations, defined as *inner iterations*. However, a direct approach is possible through the construction and inversion of the Hessian of the functional $\mathcal{J}$. One of the difficulty is to compute $D\Psi_T(\nu_k)\tilde{\nu} = C\tilde{z}_{|\tilde{\nu}}$, which requires the computation of $\tilde{z}$ by solving the following dynamics

$$\dot{\tilde{z}} = A(z_k)\tilde{z} + B(z_k)\tilde{\nu} + \Big(DA(z_k;\tilde{z})z_k + DB(z_k;\tilde{z})\nu_k \Big), \tag{7.6}$$

with z_k solution for Eq. (7.2) when $\nu = \nu_k$. Eq (7.6) is completed with initial conditions, with $\tilde{z}(0) = 0$ or periodic conditions. The operators $DA(z_k;\cdot)z_k$ and $DB(z_k;\cdot)\nu_k$ are linear in Z and are related to the derivative of A and B, given by

$$DA(z_k;\tilde{z})z_k = \lim_{\delta \mapsto 0} \frac{(A(z_k + \delta\tilde{z}) - A(z_k))z_k}{\delta},$$
$$DB(z_k;\tilde{z})\nu_k = \lim_{\delta \mapsto 0} \frac{(B(z_k + \delta\tilde{z}) - B(z_k))\nu_k}{\delta}.$$

Summing up, the computation of the ν_k is performed using the following algorithm.

Algorithm 2: Gauss-Newton

```
Choose ν_1 and set k = 1;
while the sequence {ν_k} has not converged do
    Compute the state ż_k = A(z_k)z_k + B(z_k)ν_k;
    Compute the operator DΨ_T(ν_k);
    Compute the new source estimation
    ν_{k+1} = (κId + DΨ*_T(ν_k)DΨ_T(ν_k))^{-1}(DΨ*_T(ν_k)(y_δ − Ψ_T(ν_k) + DΨ_T(ν_k)ν_k));
    Update k = k + 1;
end
```

However, for our application case, the computation of Eq. (7.6) is still expensive and the existence of a solution is not demonstrated. For this reason we decide to employ a strategy that introduces some approximation to the GN method.

7.2.2 Approximated Gauss-Newton Method

The cost of a single iteration of the GN method is decreased by a simplification of the dynamics of the model [Laroche and Gauthier, 1998] described in the following sections. In the approximated GN method, the minimization problem described by Eq. (7.5) is replaced by substituting $D\Psi_T(\nu_k)\tilde{\nu}$ with $\Psi_T^\sharp(\nu_k)\tilde{\nu}$, it reads

$$\min_{\tilde{\nu}} \left\{ \mathcal{J}_k = \frac{1}{2}||y_\delta - (\Psi_T(\nu_k) + \Psi_T^\sharp(\nu_k)\tilde{\nu})||^2_{L^2(0,T;Y)} + \frac{\kappa}{2}||\nu_k + \tilde{\nu}||^2_U \right\}, \tag{7.7}$$

where $\Psi_T^\sharp(\nu_k) : U \mapsto L^2(0,T;Y)$ is given by

$$\Psi_T^\sharp(\nu_k)\tilde{\nu} = Cz, \quad \text{where} \quad \dot{z} = A(z_k)z + B(z_k)\tilde{\nu}. \tag{7.8}$$

Moreover, z_k is solution of the non-linear dynamics of Eq. (7.2) with a source term ν_k. One can note that Eq. (7.8) is obtained from Eq. (7.6) by dropping DA and DB. Moreover, Eq. (7.8) describes the dynamics of Eq. (7.2), thus it has the same stability properties. For every k we can compute $\tilde{\nu}_k$, solution of the minimization problem (7.7), it is given by

$$\tilde{\nu}_k = \left[\left(\kappa Id + \Psi_T^{\sharp *}(\nu_k)\Psi_T^\sharp(\nu_k)\right)^{-1}\left(\Psi_T^{\sharp *}(\nu_k)(y_\delta - \Psi_T(\nu_k)) - \kappa\nu_k\right)\right].$$

Then, we define ν_{k+1} as $\nu_{k+1} = \nu_k + \tilde{\nu}_k$, which gives

$$\nu_{k+1} = (\kappa Id + \Psi_T^{\sharp *}(\nu_k)\Psi_T^\sharp(\nu_k))^{-1}\Psi_T^{\sharp *}(\nu_k)(y - \Psi_T(\nu_k) + \Psi_T^\sharp(\nu_k)\nu_k). \tag{7.9}$$

One can show that $(\Psi_T(\nu_k) - \Psi_T^\sharp(\nu_k)) = Cd_k$, where d_k is solution of the homogeneous dynamics

$$\dot{d}_k = A(z_k)d_k,$$

with $d_k(0) = 0$ or periodic conditions. By assumption, the problem is well posed for all z_k and has a unique solution, thus we have $d_k = 0$. Hence, Eq. (7.9) becomes

$$\nu_{k+1} = (\kappa Id + \Psi_T^{\sharp *}(\nu_k)\Psi_T^\sharp(\nu_k))^{-1}\Psi^{\sharp *}(\nu_k)y_\delta. \tag{7.10}$$

One can see that ν_{k+1}, given by Eq. (7.10), is the minimizer of

$$\mathcal{J} = \frac{1}{2}||y_\delta - \Psi_T^\sharp(\nu_k)\nu||^2_{L^2(0,T,Y)} + \frac{\kappa}{2}||\nu||^2_U. \tag{7.11}$$

The algorithm is now given by

Algorithm 3: Approximated Gauss-Newton

```
Choose ν_1 and set k = 1;
while the sequence {ν_k} has not converged do
    Compute the state ż_k = A(z_k)z_k + B(z_k)ν_k;
    Compute the operator Ψ_T^♯(ν_k) using Eq. (7.8);
    Compute the new source estimation
        ν_{k+1} = (κId + Ψ_T^{♯*}(ν_k)Ψ_T^♯(ν_k))^{-1} Ψ^{♯*}(ν_k) y_δ;
    Update k = k + 1;
end
```

One can notice that this method does not require the computation of the tangent operator $D\Psi_T$, but it involves the computation of z_k, solution of a non-linear dynamics with ν_k as a source term. This could induce a high computational cost, not affordable when real clinical application are foreseen. In what follows we propose an alternative that does not require to solve a non-linear dynamics with small deviation from the accuracy provided by non-linear formulations.

7.2.3 Simplified Approximated Gauss-Newton Method

7.2.3.1 Inner iteration strategy

As mentioned in Section 7.1.2, the computation of each z_k can be replaced by an iterative procedure involving the solution of a linear dynamics. More precisely, for a given integer $J > 0$, one can use the approximation

$$z_k \sim z_k^J,$$

where each z_k^j, for $j \in \{1, ..., J\}$, is given by

$$\dot{z}_k^{j+1} = A(z_k^j)z_k^{j+1} + B(z_k^j)\nu_k \quad \text{with} \quad j \in \{0, ..., J-1\} \quad \text{and} \quad z_k^0 = 0.$$

Finally Eq. (7.10) is solved replacing $\Psi_T^\sharp$ with $\Psi_T^{\sharp,J}$, which is solution of the minimization (7.11), after substitution of $\Psi_T^\sharp$, and is defined as

$$\Psi_T^{\sharp\,J}(\nu_k)\tilde{\nu} = Cz \quad \text{where} \quad \dot{z} = A(z_k^J)z + B(z_k^J)\tilde{\nu}. \tag{7.12}$$

The algorithm reads

Algorithm 4: Simplified approximated Gauss-Newton with inner iterations

```
Choose ν_1 and set k = 1;
while the sequence {ν_k} has not converged do
    Choose z_k^0 = 0 and set j = 0;
    while j < J do
        Compute the state ż_k^{j+1} = A(z_k^j) z_k^{j+1} + B(z_k^j) ν_k;
        Update j = j + 1;
    end
    Compute the operator Ψ_T^{♯ J}(ν_k) using Eq. (7.12);
    Compute the new source estimation
        ν_{k+1} = (κId + Ψ_T^{♯ J *}(ν_k) Ψ_T^{♯ J}(ν_k))^{-1} Ψ^{♯ J *}(ν_k) y_δ;
    Update k = k + 1;
end
```

7.2.3.2 Single inner iteration strategy

The strategy above yet introduces inner iterations, although in our application J can be chosen small. We here propose a variant that corresponds to avoid these inner iterations. Nevertheless, we rely on the approximation

$$z_k \sim z_k^0,$$

with

$$\dot{z}_{k+1}^0 = A(z_k^0)z_{k+1}^0 + B(z_k^0)\nu_k.$$

Eq. (7.10) now reads

$$\nu_{k+1} = (\kappa Id + \Psi_T^{\flat *}(z_k^0)\Psi_T^\flat(z_k^0))^{-1}\Psi_T^{\flat *}(z_k^0)y_\delta, \tag{7.13}$$

minimizer of (7.11) where $\Psi_T^\sharp$ is substituted with $\Psi_T^\flat$, that reads

$$\Psi_T^\flat(z_k^0)\tilde{\nu} = Cz \quad \text{where} \quad \dot{z} = A(z_k^0)z + B(z_k^0)\tilde{\nu}. \tag{7.14}$$

Finally, this procedure is described by the following algorithm

Algorithm 5: Simplified approximated Gauss-Newton with a single iteration

```
Choose z_0^0 = 0 and k = 0;
while the sequence {ν_k} has not converged do
    Compute the operator Ψ_T^♭(z_k) using Eq. (7.14);
    Compute the new source estimation
        ν_{k+1} = (κId + Ψ_T^{♭ *}(z_k^0) Ψ_T^♭(z_k^0))^{-1} Ψ^{♭ *}(z_k^0) y_δ;
    Compute the state ż_{k+1}^0 = A(z_k^0) z_{k+1}^0 + B(z_k^0) ν_{k+1};
    Update k = k + 1;
end
```

Penalized periodicity approach We now analyze the case where Algorithm 5 deals with a dynamics that has periodic initial conditions. This involves that the operator $\Psi_T^\flat$ is non local in time. In this work, following the strategy described in Chapter 6, we rely on a penalized strategy, that allows us to avoid the computation of the operator $\Psi_T^\flat$, and instead periodic condition will be imposed by a penalization strategy, and the computation of $\Psi_T^\flat$ will be replaced by the computation of a similar operator that includes the solution of an initial data problem. Following this approach, Eq. (7.14) is now modified to take into account prescribed initial conditions. We define, knowing ν_k and ζ_k

$$\begin{cases} \dot{z}_k^0(0) = A(z_{k-1}^0)z_k^0 + B(z_{k-1}^0)\nu_k, \\ z_k^0(0) = \zeta_k. \end{cases} \tag{7.15}$$

Moreover, we set

$$\phi_T^\flat(z_k^0)\begin{pmatrix}\tilde{\zeta}\\ \tilde{\nu}\end{pmatrix} = z \quad \text{with} \quad \begin{cases} \dot{z} = A(z_k^0)z + B(z_k^0)\tilde{\nu}, \\ z(0) = \tilde{\zeta}, \end{cases} \tag{7.16}$$

and

$$\Psi_T^\flat(z_k^0)\begin{pmatrix}\tilde{\zeta}\\ \tilde{\nu}\end{pmatrix} = C\phi_T^\flat(z_k^0)\begin{pmatrix}\tilde{\zeta}\\ \tilde{\nu}\end{pmatrix}. \tag{7.17}$$

Once the operator $\Psi_T^\flat$ is computed, the new estimates ν_{k+1} and ζ_{k+1} are computed by

$$\begin{aligned}&(\nu_{k+1}, \zeta_{k+1}) \\ &= \underset{(\tilde{\nu},\tilde{\zeta})\in U\times Z}{\arg\min} \left\{ \mathcal{J} = \frac{1}{2}\left|\left| y_\delta - \Psi_T^\flat(z_k^0)\begin{pmatrix}\tilde{\zeta}\\ \tilde{\nu}\end{pmatrix}\right|\right|^2 + \frac{\kappa}{2}||\nu||_U^2 + \frac{1}{2\epsilon}\left|\left|\phi_T^\flat(z_k^0)\begin{pmatrix}\tilde{\zeta}\\ \tilde{\nu}\end{pmatrix}(T) - \tilde{\zeta}\right|\right|_Z^2 \right\}.\end{aligned} \tag{7.18}$$

Finally, to summarize, the strategy is described by the following algorithm

Algorithm 6: Penalized simplified approximated Gauss-Newton with a single iteration

1 Choose $z_0^0 = 0$ and set $k = 1$;
2 **while** *the sequence* $\{\nu_k\}$ *has not converged* **do**
3 Compute the state $\dot{z}_k^0 = A(z_{k-1}^0)z_k^0 + B(z_{k-1}^0)\nu_k$ with $z_k^0(0) = \zeta_k$;
4 Compute the operator $\Psi_T^\flat(z_k^0)$ using Eq. (7.16) and (7.17);
5 Compute the new source estimation ν_{k+1} as well as ζ_{k+1} with Eq. (7.18);
6 Update $k = k + 1$;
7 **end**

7.3 Time discrete optimization strategy

In this section we derive the time-discretized form of Algorithm 6, where for simplicity we assume $U = H^1(0,T)$ with periodic conditions. Hence, given a time step $\tau = T/N_T$ we look for ν^n with $n \in \{0, ..., N_T\}$, where $\nu^n \sim \nu(n\tau)$ and the periodic conditions implies $\nu^0 = \nu^T$. As mentioned in the previous sections, the discrete optimal control problem is obtained from the discrete dynamics of the system. Hence, we discretize in space and time Eq. (7.16) using a midpoint time-scheme, following the choice made in Chapter 2, we

obtain

$$\phi_T^\flat(\{z_k^n\})\begin{pmatrix}\tilde{\zeta}\\ \{\tilde{\nu}^n\}\end{pmatrix}=\{z^n\}\quad\text{with}\quad\begin{cases}\dfrac{z^{n+1}-z^n}{\tau}=A(z_k^{n+\frac{1}{2}})z^{n+\frac{1}{2}}+B(z_k^{n+\frac{1}{2}})\nu^{n+\frac{1}{2}},\\ z(0)=\zeta,\end{cases}\tag{7.19}$$

where for simplicity we take $z_k := z_k^0$. This leads to a minimization criteria of the form

$$\mathcal{J}(\{\nu^{n+\frac{1}{2}}\},\{\zeta\})=\frac{1}{2\epsilon}||\phi_T^\flat(z_k^{N_T})-\zeta||_Z^2+\frac{\tau}{2}\sum_{n=0}^{N_T-1}\left(\left|y_\delta^{n+\frac{1}{2}}-\Psi_T^\flat(\nu_k^{n+\frac{1}{2}})\begin{pmatrix}\tilde{\nu}^{n+\frac{1}{2}}\\ \tilde{\zeta}^{n+\frac{1}{2}}\end{pmatrix}\right|^2+\kappa(|\nu^{n+\frac{1}{2}}|^2)\right).\tag{7.20}$$

In order to ease the presentation of the discrete algorithm we introduce the following notation

$$\Phi_{m|n}^k=\prod_{i=n}^{m-1}A_+^k|_{i+\frac{1}{2}}^{-1}A_-^k|_{i+\frac{1}{2}},\qquad\text{for } m>n\qquad\text{and}\qquad L_{n+\frac{1}{2}}^k=A_+^k|_{n+\frac{1}{2}}^{-1}B_{n+\frac{1}{2}}^k,$$

where

$$A_+^k|_{n+\frac{1}{2}}=\left(\frac{Id}{\tau}-\frac{A(z_k^{n+\frac{1}{2}})}{2}\right),\qquad A_-^k|_{n+\frac{1}{2}}=\left(\frac{Id}{\tau}+\frac{A(z_k^{n+\frac{1}{2}})}{2}\right),$$

and $B_{n+\frac{1}{2}}^k := B(z_k^{n+\frac{1}{2}})$. Finally, we obtain the discrete Duhamel formula

$$z^n=\Phi_{n|0}^k\zeta+\sum_{m=0}^{n-1}\Psi_{n|n-m}^k\nu^{n-m-\frac{1}{2}},\tag{7.21}$$

solution for System 7.19, where $\Psi_{n|n-m}^k=\Phi_{n|n-m}^k L_{n-m-\frac{1}{2}}^k$. As mentioned in the previous chapter, the size of the problem allows us to solve the minimization of Eq. (7.20) by inverting a linear system, at each k. This procedure requires the computation of the Hessian of the minimization functional, which reads

$$H^k=\epsilon^{-1}\Psi_Z^{k*}\Psi_Z^k+\tau\begin{pmatrix}\Psi_C^{kT}\Psi_C^k & \Psi_C^{k*}\Psi_B^k\\ \Psi_B^{kT}\Psi_C^k & \Psi_B^{k*}\Psi_B^k+\kappa K_\sharp^k\end{pmatrix}\qquad H\in\mathcal{L}(\mathbb{R}^{N_T}),\tag{7.22}$$

where $K_\sharp^k$ includes the contributions of the Tikhonov regularization [Tikhonov, 1963], while Ψ_Z^k, Ψ_C^k and Ψ_B^k are defined as

$$\Psi_Z^{k*}=\begin{pmatrix}\Phi_{N_T|0}^{k*}-Id\\ \frac{\partial z^{N_T}}{\partial\nu^0}\\ \cdots\\ \frac{\partial z^{N_T}}{\partial\nu^{N_T-1}}\end{pmatrix}\in\mathcal{L}(Z,Z\times\mathbb{R}^{N_T}),\quad\Psi_C^k=\begin{pmatrix}\frac{C}{2}(I+\Phi_{1|0}^k)\\ \frac{C}{2}(\Phi_{1|0}^k+\Phi_{2|0}^k)\\ \cdots\\ \frac{C}{2}(\Phi_{N_T-1|0}^k+\Phi_{N_T|0}^k)\end{pmatrix}\in\mathcal{L}(Z,Y^{N_T})$$

$$\Psi_B=\begin{pmatrix}C\frac{\partial z^{n+\frac{1}{2}}}{\partial\nu^0} & 0 & 0 & 0\\ \cdots & \cdots & \cdots & 0\\ C\frac{\partial z^{N_T-n+\frac{1}{2}}}{\partial\nu^0} & C\frac{\partial z^{N_T-n+\frac{1}{2}}}{\partial\nu^1} & \cdots & C\frac{\partial z^{N_T-n+\frac{1}{2}}}{\partial\nu^{N_T-1}}\end{pmatrix}\in\mathcal{L}(\mathbb{R}^{N_T}),$$

with

$$\frac{\partial z^n}{\partial \nu^j} = \begin{cases} 0 \quad \text{if} \quad n = 0, \\ \frac{1}{2}(\Psi_{n|j} + \Psi_{n|j+1}) \quad \text{if} \quad 0 < j \leq n-1, \\ \frac{1}{2}\Psi_{n|n} \quad \text{if} \quad j = n, \\ \text{if} \quad j = 0 \begin{cases} \frac{1}{2}\Psi_{n|1} \quad \text{if} \quad n < N_T, \\ \frac{1}{2}\Psi_{N_T|N_T} + \frac{1}{2}\Psi_{N|1} \quad n = N_T, \end{cases} \\ 0 \quad \text{if} \quad j > n. \end{cases} \qquad \text{with} \quad n \in \{0, ..., N_T - 1\}.$$

Finally, we introduce the vector that includes the optimization variables

$$X = \begin{pmatrix} \zeta \\ \nu^0 \\ \vdots \\ \nu^{N_T-1} \end{pmatrix} \in Z \times \mathbb{R}^{N_T},$$

and another one which comprises the noisy measurements employed as observations

$$Y = \begin{pmatrix} y_\delta^{n+\frac{1}{2}} \\ \vdots \\ y_\delta^{N_T-\frac{1}{2}} \end{pmatrix}.$$

Finally, we derive the discrete algorithm corresponding to the penalized simplified approximated Gauss-Newton method with a single inner iteration

Algorithm 7: Discrete penalized simplified approximated Gauss-Newton with a single iteration

Choose $z_0 = 0$ and $k = 1$;
while *the sequence* $\{\nu_k^n\}$ *has not converged* **do**
  Compute the state $z_k^n = \Phi_{n|0}^{k-1}\zeta_k + \sum_{m=0}^{n-1} \Psi_{n|n-m}^{k-1} \nu_k^{n-m-\frac{1}{2}}$;
  Compute the operator $\Psi_T^\flat(z_k^{n+\frac{1}{2}})$ using Eq. (7.21);
  Compute $X^{k+1} = (H^k)^{-1}\tau(\Psi_C^k\, \Psi_B^k)Y$;
  Set $z_{k+1}^0 = \zeta_{k+1}$;
  Update $k = k + 1$;
end

One can notice that the optimization method, as for its structure, is not affected by changes in the underlying physical system. In fact, any change in the model dynamics would only require changes in the dynamic operator A, leading to a flexible inverse problem strategy.

7.4 Test-case: the upper thoracic aorta

The iterative strategy presented above is applied on a simple model configuration representing the upper thoracic aorta, the same one employed in Chapter 6. However, in this section we rely on the non-linear formulation derived in Chapter 2.

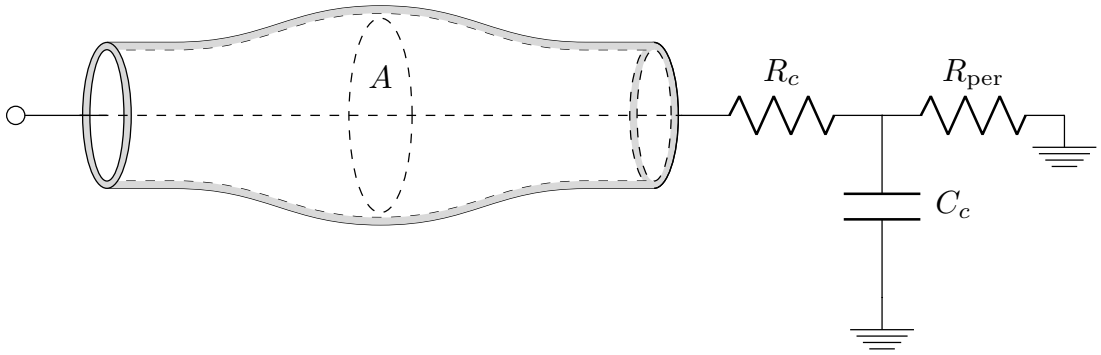

Figure 7.1 – Model configuration of the test-case. A one-dimensional model represents the upper thoracic aorta as a uniform straight deformable tube and a three-element Windkessel model is used as outlet boundary condition to take into account the contribution of the downstream vessels. The input of this model is the inlet total pressure.

7.4.1 Model configuration

The test-case, as depicted in Figure 7.1, involves a one-dimensional model that represents the proximal region of the aorta, namely the upper thoracic aorta, and a lumped-parameter model as outlet boundary condition that substitutes the contribution of the remaining part of the aorta and the distal vessels. The formulation that describes the model reads, for all $t > 0$,

$$\begin{cases} 2\partial_t \varphi + \pi\xi\partial_s(Rv) = 0 \quad \text{for } s \in (0, L), \\ \pi\varrho\partial_t v + \dfrac{\pi\varrho}{2}\Big(2u\partial_s v + v\partial_s u\Big) + \varrho k_\nu \dfrac{v}{R^2} + \pi R\partial_s(\xi\varphi) = 0 \quad \text{for } s \in (0, L). \end{cases} \tag{7.23}$$

The system is completed with some boundary conditions that are defined as

$$\begin{cases} \pi R\xi\varphi = \dfrac{\pi\varrho}{2}uv - \pi R P_{in} \quad \text{at } s = 0, \\ \pi R\xi\varphi = -\dfrac{\pi\varrho}{2}uv + \pi R P_{out} \quad \text{at } s = L, \end{cases} \tag{7.24}$$

while the total pressures P_{in} and P_{out} read

$$\begin{cases} P_{in} = \nu_{in} \quad \text{at } s = 0, \\ P_{out} = R_c \pi R v + P_c \quad \text{at } s = L, \\ C_c \dot{P}_c = \pi R v - \dfrac{P_c}{R_{per}} \quad \text{at } s = L. \end{cases} \tag{7.25}$$

Finally Systems 7.23, 7.24 and 7.25 are closed by some initial conditions, namely

$$(v(s,0), \varphi(s,0), P_c(0)) = (v_0, \varphi_0, P_{c\,0}).$$

7.4.2 Adimensionalization

To ease the manipulation of the formulation and to prepare for the application of the inverse problem we perform an adimensionalization. First, we introduce the adimensionalized

variables defined as

$$\hat{\varphi}(L_0 s, t_0 t) := \frac{\varphi(s,t)}{\varphi_0}, \quad \hat{v}(L_0 s, t_0 t) := \frac{v(s,t)}{v_0}, \quad \hat{P}_c(t_0 t) := \frac{P_c(t)}{P_0}, \quad \hat{\nu}_{in} := \frac{\nu_{in}}{P_0}$$
$$\hat{R}(L_0 s, t_0 t) := \frac{R(s,t)}{R_0}, \quad \hat{\xi}(L_0 s, t_0 t) := \frac{\xi(R)(s,t)}{\xi_0}, \quad \hat{u}(L_0 s, t_0 t) := \frac{u(s,t)}{u_0},$$

with φ_0, v_0, P_0, R_0, ξ_0, u_0, L_0 and t_0 some parameters to be defined. We substitute these new variables in the original non-linear system presented in Chapter 2 obtaining, for all $t > 0$ and $s \in (0, L/L_0)$

$$\begin{cases} 2\dfrac{\varphi_0}{t_0}\partial_t\hat{\varphi} + \pi\dfrac{\xi_0 R_0 v_0}{L_0}\hat{\xi}\partial_s(\hat{R}\hat{v}) = 0, \\ \dfrac{\pi\varrho v_0}{t_0}\partial_t\hat{v} + \dfrac{\pi\varrho}{2}\dfrac{u_0 v_0}{L_0}\Big(2\hat{u}\partial_s\hat{v} + \hat{v}\partial_s\hat{u}\Big) + \varrho k_\nu \dfrac{v_0}{R_0^2}\dfrac{\hat{v}}{\hat{R}^2} + \pi\dfrac{R_0\xi_0\varphi_0}{L_0}\hat{R}\partial_s(\hat{\xi}\hat{\varphi}) = 0. \end{cases} \tag{7.26}$$

Moreover, at the boundary we have

$$\begin{cases} \pi R_0\xi_0\varphi_0\hat{R}\hat{\xi}\hat{\varphi} = \dfrac{\pi\varrho}{2}u_0 v_0\hat{u}\hat{v} - \pi R_0\hat{R}P_{in} \quad \text{at } s = 0, \\ \pi R_0\xi_0\varphi_0\hat{R}\hat{\xi}\hat{\varphi} = -\dfrac{\pi\varrho}{2}u_0 v_0\hat{u}\hat{v} + \pi R_0\hat{R}P_{out} \quad \text{at } s = L/L_0, \end{cases} \tag{7.27}$$

and System 7.25 becomes

$$\begin{cases} P_{in} = P_0\hat{\nu}_{in} \quad \text{at } s = 0, \\ P_{out} = R_c\pi R_0 v_0\hat{R}\hat{v} + P_0\hat{P}_c \quad \text{at } s = L/L_0, \\ \dfrac{C_c P_0}{t_0}\dot{\hat{P}}_c = \pi R_0 v_0\hat{R}\hat{v} - \dfrac{P_0\hat{P}_c}{R_{per}} \quad \text{at } s = L/L_0. \end{cases} \tag{7.28}$$

Then, we define

$$\varphi_0 := \sqrt{\frac{\pi\varrho}{2}}v_0, \quad v_0 := \sqrt{\frac{C_c}{\pi\varrho L_0}}P_0,$$
$$R_0 := R(s,0), \quad \xi_0 := \xi(R_0), \quad u_0 := \frac{v_0}{R_0}$$
$$L_0 := L, \quad t_0 := \sqrt{\frac{2\varrho}{\pi}}\frac{L_0}{\xi_0 R_0},$$

and we assign to P_0 a defined value that has the same order of magnitude as the pressure, e.g. 10^4. After substitution in System 7.26, 7.27 and 7.28 we obtain

$$\begin{cases} \partial_t\hat{\varphi} + \hat{\xi}\partial_s(\hat{R}\hat{v}) = 0, \\ \partial_t v + \dfrac{a_0}{2}\Big(2\hat{u}\partial_s\hat{v} + \hat{v}\partial_s\hat{u}\Big) + k_{adim}\dfrac{\hat{v}}{\hat{R}^2} + \hat{R}\partial_s(\hat{\xi}\hat{\varphi}) = 0, \end{cases} \tag{7.29}$$

for all $t > 0$ and $s \in (0,1)$. At the boundary we have

$$\begin{cases} \hat{R}\hat{\xi}\hat{\varphi} = \dfrac{a_0}{2}\hat{u}\hat{v} - c_{vp}\hat{R}\hat{\nu}_{in} \quad \text{at } s = 0, \\ \hat{R}\hat{\xi}\hat{\varphi} = -\dfrac{a_0}{2}\hat{u}\hat{v} + c_{bo}\hat{R}^2\hat{v} + c_{vp}\hat{R}\hat{P}_c \quad \text{at } s = 1, \end{cases} \tag{7.30}$$

$$\begin{cases} P_{in} = P_0 \hat{\nu}_{in} \quad \text{at } s = 0, \\ P_{out} = R_c \pi R_0 v_0 \hat{R}\hat{v} + P_0 \hat{P}_c \quad \text{at } s = 1, \\ \dot{\hat{P}}_c = c_{vp} \hat{R}\hat{v} - c_{pp} \hat{P}_c \quad \text{at } s = 1, \end{cases} \tag{7.31}$$

where a_0, k_{adim}, c_{bo}, c_{vp} and c_{pp} are defined as follows

$$a_0 = \frac{t_0}{L_0} u_0, \quad k_{adim} = \frac{k_\nu t_0}{\pi} \frac{1}{R_0^2}$$
$$c_{bo} = \frac{\pi R_c}{\varrho} \frac{t_0}{L_0} R_0^2, \quad c_{vp} = \frac{\pi t_0}{C_c} \frac{R_0 v_0}{P_0} \quad \text{and} \quad c_{pp} = \frac{t_0}{C_c R_{per}}.$$

7.4.3 Iterative pseudo-linearization

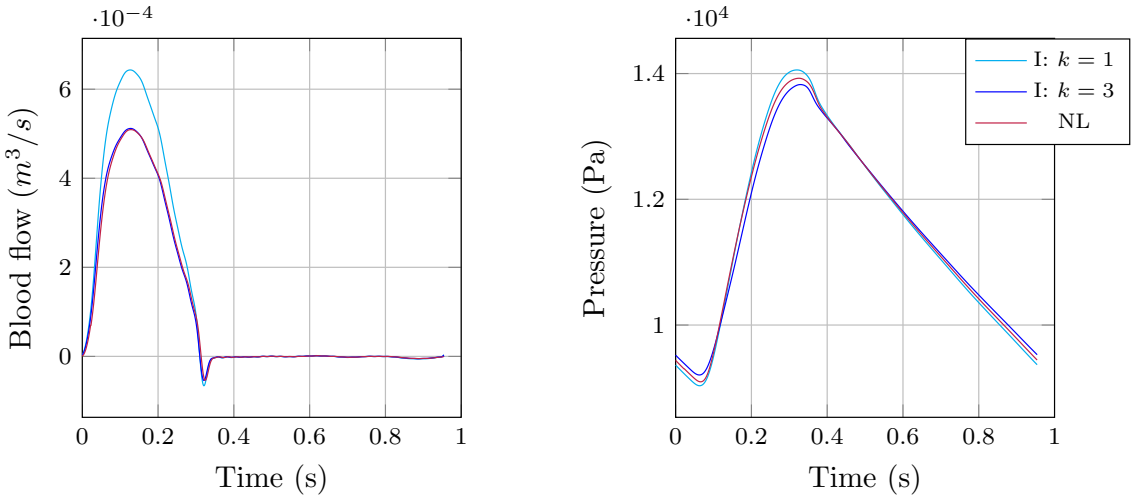

Figure 7.2 – Comparison between the computed blood flow inside the vessel, on the left, and the outlet pressure, on the right, obtained with the fully non-linear model described in [Manganotti et al., 2021] (red curve) and with the pseudo-linearized method presented in this section, iterated in a direct simulation of the model (light blue curve for the first iteration and dark blue for the results at convergence).

The model presented in System 7.29 is highly non-linear, by consequence the application of a data assimilation method can be challenging. In order to overcome this limitation without loosing the precision of the non-linear model we derive an iterative strategy that implies, at each iteration $k \geq 1$, the computation of a 'pseudo-linearized' model. The procedure involves a simplification of the forward formulation of the system and modify the dynamical operator A. More in details, the intermediate variables – $\hat{R}$, $\hat{\xi}$, $\hat{u}$ – are treated as given space-time dependent parameters and are updated according to the new values of $\hat{\varphi}$ and $\hat{v}$ at the end of an iteration, that correspond to a heartbeat of time length T/t_0. We obtain, for all $t \geq 0$, $s \in (0, 1)$ and $k \geq 1$

$$\begin{cases} \partial_t \hat{\varphi}_k + \hat{\xi}_{k-1} \partial_s (\hat{R}_{k-1} \hat{v}_k) = 0, \\ \partial_t \hat{v}_k + \dfrac{a_0}{2} \left(2\hat{u}_{k-1} \partial_s \hat{v}_k + \hat{v}_k \partial_s \hat{u}_{k-1} \right) + k_{adim} \dfrac{\hat{v}_k}{\hat{R}_{k-1}^2} + \hat{R}_{k-1} \partial_s (\hat{\xi}_{k-1} \hat{\varphi}_k) = 0, \end{cases} \tag{7.32}$$

while at the boundary we have

$$\begin{cases} \hat{R}_{k-1}\hat{\xi}_{k-1}\hat{\varphi}_k = \dfrac{a_0}{2}\hat{u}_{k-1}\hat{v}_k - c_{vp}\hat{R}_{k-1}\hat{\nu}_{in\,k} \quad \text{at } s=0, \\ \hat{R}_{k-1}\hat{\xi}_{k-1}\hat{\varphi}_k = -\dfrac{a_0}{2}\hat{u}_{k-1}\hat{v}_k + c_{bo}\hat{R}_{k-1}^2\hat{v}_k - c_{vp}\hat{R}_{k-1}\hat{P}_{c\,k} \quad \text{at } s=1, \end{cases} \tag{7.33}$$

$$\begin{cases} P_{in\,k} = P_0\hat{\nu}_{in\,k} \quad \text{at } s=0, \\ P_{out\,k} = R_c\pi R_0 v_0 \hat{R}_{k-1}\hat{v}_k + P_0\hat{P}_{c\,k} \quad \text{at } s=1, \\ \dot{\hat{P}}_{c\,k} = c_{vp}\hat{R}_{k-1}\hat{v}_k - c_{pp}\hat{P}_{c\,k} \quad \text{at } s=1, \end{cases} \tag{7.34}$$

with $\hat{R}_0$, $\hat{\xi}_0$ and $\hat{u}_0$ based on the initial values of $\hat{\varphi}_0$ and $\hat{v}_0$. In Figure 7.2 it is possible to observe how the choice of this specific 'pseudo-linearization' is a good approximation to the dynamics of the system. In fact, the results of the simplified system converges towards the ones obtained with the original non-linear model described in Chapter 2 in three iterations. Note that these iterations will correspond to the 'outer iterations' of the inverse problem.

Equivalence with the abstract form and energy stability

In order to express System 7.32, 7.33 and 7.34 in the abstract form presented in Section 7.1.2 we define $z = (\hat{\varphi}, \hat{v}, \hat{P}_c)$ and $\nu = \hat{\nu}_{in}$. Moreover, the dynamic and control operators $A^\sharp$ and $B^\sharp$ read

$$A_k^\sharp = \begin{pmatrix} 0 & -\hat{\xi}_k\partial_s(\hat{R}_k\cdot) & 0 \\ -\hat{R}_k\partial_s(\hat{\xi}_k\cdot) & -\dfrac{a_0}{2}\Big(2\hat{u}_k\partial_s(\cdot) - \partial_s\hat{u}_k\Big) - \dfrac{k_{adim}}{\hat{R}_k^2} + c_{bo}\hat{R}_k^2\gamma_{out} & -c_{vp}\hat{R}_k\gamma_{out}^* \\ 0 & c_{vp}\hat{R}_k\gamma_{out} & -c_{pp} \end{pmatrix},$$

$$B_k^\sharp = \begin{pmatrix} 0 \\ c_{vp}\hat{R}_k\gamma_{in} \\ 0 \end{pmatrix},$$

with γ_{in} and γ_{out} the trace operators respectively in $s=0$ and $s=L$.

In order to analyze the energy properties we present the semi-discrete variational formulation of System 7.32. We discretize in time using a midpoint scheme, obtaining

$$\begin{cases} \Big(\dfrac{\hat{\varphi}_k^{n+1} - \hat{\varphi}_k^n}{\tau_a}, \tilde{\hat{\varphi}}\Big) + \Big(\partial_s(\hat{R}_{k-1}^{n+\frac{1}{2}}\hat{v}_k^{n+\frac{1}{2}}), \tilde{\hat{\varphi}}\hat{\xi}_{k-1}^{n+\frac{1}{2}}\Big) = 0, \\ \Big(\dfrac{\hat{v}_k^{n+1} - \hat{v}_k^n}{\tau_a}, \tilde{\hat{v}}\Big) + a\Big(\tilde{\hat{v}}, \hat{v}_k^{n+\frac{1}{2}}, \hat{u}_{k-1}^{n+\frac{1}{2}}\Big) + k_{adim}\left(\dfrac{\hat{v}_k^{n+\frac{1}{2}}}{\hat{R}_{k-1}^{n+\frac{1}{2}}}, \dfrac{\tilde{\hat{v}}}{R_{k-1}^{n+\frac{1}{2}}}\right) \\ \qquad +(\partial_s(\hat{R}_{k-1}^{n+\frac{1}{2}}\tilde{\hat{v}}), \hat{\varphi}_k^{n+\frac{1}{2}}\hat{\xi}_{k-1}^{n+\frac{1}{2}})\hat{R}_{k-1}^{n+\frac{1}{2}} = \text{boundary terms}, \end{cases} \tag{7.35}$$

with $\tau_a := \tau/t_0$ and $a\Big(\tilde{\hat{v}}, \hat{v}_k^{n+\frac{1}{2}}, \hat{u}_{k-1}^{n+\frac{1}{2}}\Big)$ defined as

$$a\Big(\tilde{\hat{v}}, \hat{v}_k^{n+\frac{1}{2}}, \hat{u}_{k-1}^{n+\frac{1}{2}}\Big) := \frac{a_0}{2}\int_0^1 \Big(2\tilde{\hat{v}}\hat{u}_{k-1}^{n+\frac{1}{2}}\partial_s\hat{v}_k + \hat{v}_k^{n+\frac{1}{2}}\tilde{\hat{v}}\hat{u}_{k-1}^{n+\frac{1}{2}}\Big)ds - \frac{a_0}{2}\tilde{\hat{v}}\hat{v}_k^{n+\frac{1}{2}}\hat{u}_{k-1}^{n+\frac{1}{2}}\Big|_0^1.$$

For a suitable choice of $\tilde{\hat{v}}$ and $\tilde{\hat{\varphi}}$ we can retrieve, within each iteration, the energy stability as described in Chapter 2. Indeed, we choose $\tilde{\hat{v}} = \hat{v}_k^{n+\frac{1}{2}}$ and $\tilde{\hat{\varphi}} = \hat{\varphi}_k^{n+\frac{1}{2}}$ and obtain

$$\begin{cases} \dfrac{||\hat{\varphi}_k^{n+1}||^2 - ||\hat{\varphi}_k^n||^2}{\tau_a} + \left(\partial_s(\hat{R}_{k-1}^{n+\frac{1}{2}}\hat{v}_k^{n+\frac{1}{2}}), \hat{\varphi}_k^{n+\frac{1}{2}}\hat{\xi}_{k-1}^{n+\frac{1}{2}}\right) = 0, \\ \dfrac{||\hat{v}_k^{n+1}||^2 - ||\hat{v}_k^n||^2}{\tau_a} + a\left(\hat{v}_k^{n+\frac{1}{2}}, \hat{v}_k^{n+\frac{1}{2}}, \hat{u}_{k-1}^{n+\frac{1}{2}}\right) + k_{adim}\left(\dfrac{\hat{v}_k^{n+\frac{1}{2}}}{\hat{R}_{k-1}^{n+\frac{1}{2}}}, \dfrac{\hat{v}_k^{n+\frac{1}{2}}}{R_{k-1}^{n+\frac{1}{2}}}\right) \\ \qquad +(\partial_s(\hat{R}_{k-1}^{n+\frac{1}{2}}\hat{v}_k^{n+\frac{1}{2}}), \hat{\varphi}_k^{n+\frac{1}{2}}\hat{\xi}_{k-1}^{n+\frac{1}{2}})\hat{R}_{k-1}^{n+\frac{1}{2}} = \text{boundary terms}, \end{cases} \tag{7.36}$$

after coupling of the two equations and using System 7.31 we obtain

$$\frac{||\hat{\varphi}_k^{n+1}||^2 - ||\hat{\varphi}_k^n||^2}{\tau_a} + \frac{||\hat{v}_k^{n+1}||^2 - ||\hat{v}_k^n||^2}{\tau_a} + k_{adim}\left(\frac{\hat{v}_k^{n+\frac{1}{2}}}{\hat{R}_{k-1}^{n+\frac{1}{2}}}, \frac{\hat{v}_k^{n+\frac{1}{2}}}{R_{k-1}^{n+\frac{1}{2}}}\right) = \text{boundary terms},$$

and we can define the energy densities as

$$\mathcal{E}_{vessel}^n = ||\hat{\varphi}_k^n||^2 + ||\hat{v}_k^n||^2, \quad \mathcal{E}_{bc}^n = (\hat{P}_{ck}^{\,n})^2,$$

where $\mathcal{E}_{vessel}^n$ is the current energy density of the one-dimensional vessel, while $\mathcal{E}_{bc}^n$ is the current energy density of the three-elements Windkessel model at the outlet boundary. The dissipation terms read

$$\mathcal{D}_{vessel}^{n+\frac{1}{2}} = k_{adim}\left|\left|\frac{\hat{v}_k^{n+\frac{1}{2}}}{\hat{R}_{k-1}^{n+\frac{1}{2}}}\right|\right|^2, \quad \mathcal{D}_{bc}^{n+\frac{1}{2}} = c_{bo}(\hat{R}_{k-1}^{n+\frac{1}{2}}(1)\hat{v}_k^{n+\frac{1}{2}})^2(1) + c_{pp}\hat{R}_{k-1}^{n+\frac{1}{2}}(1)(\hat{P}_{ck}^{\,n+\frac{1}{2}})^2,$$

where $\mathcal{D}_{vessel}^{n+\frac{1}{2}}$ groups the dissipation terms of the 1D formulation and $\mathcal{D}_{bc}^{n+\frac{1}{2}}$ the dissipative contribution of the outlet boundary. Finally, we retrieve, for all $n \in \mathbb{N}$ the following energy conservation property

$$\frac{\mathcal{E}_{vessel}^{n+1} - \mathcal{E}_{vessel}^n}{\tau_a} + \frac{\mathcal{E}_{bc}^{n+1} - \mathcal{E}_{bc}^n}{\tau_a} + \mathcal{D}_{vessel}^{n+\frac{1}{2}} + \mathcal{D}_{bc}^{n+\frac{1}{2}} = \pi\hat{R}_{k-1}^{n+\frac{1}{2}}(0)\hat{v}_k^{n+\frac{1}{2}}(0)\hat{\nu}_{in\,k},$$

where at the right hand side we have the input source term $\hat{\nu}_{in\,k}^{n+\frac{1}{2}}$.

7.5 Towards the clinical application: the upper limb

In this section we apply the inverse problem based on the iterative strategy described in Section 7.2. The idea is to propose a model configuration that is suitable for the clinical purpose of this work and to test, with a classical simulation, the reliability of the approach for its real application once coupled with a parameter estimation strategy.

7.5.1 Model configuration

The model is made up of four one-dimensional segments, as shown in Figure 7.3, the first one representing the small portion of the aorta between the aortic valve and the branches of the upper limb. Then, a penalized approach (see Chapter 3) is used to model a one-dimensional branching point where the subclavian-axillary-brachial (SAB) artery model is coupled, together with the upper thoracic aorta model. Moreover, the symmetry of the two arms is exploited and taken into account in the branching conditions, allowing us to

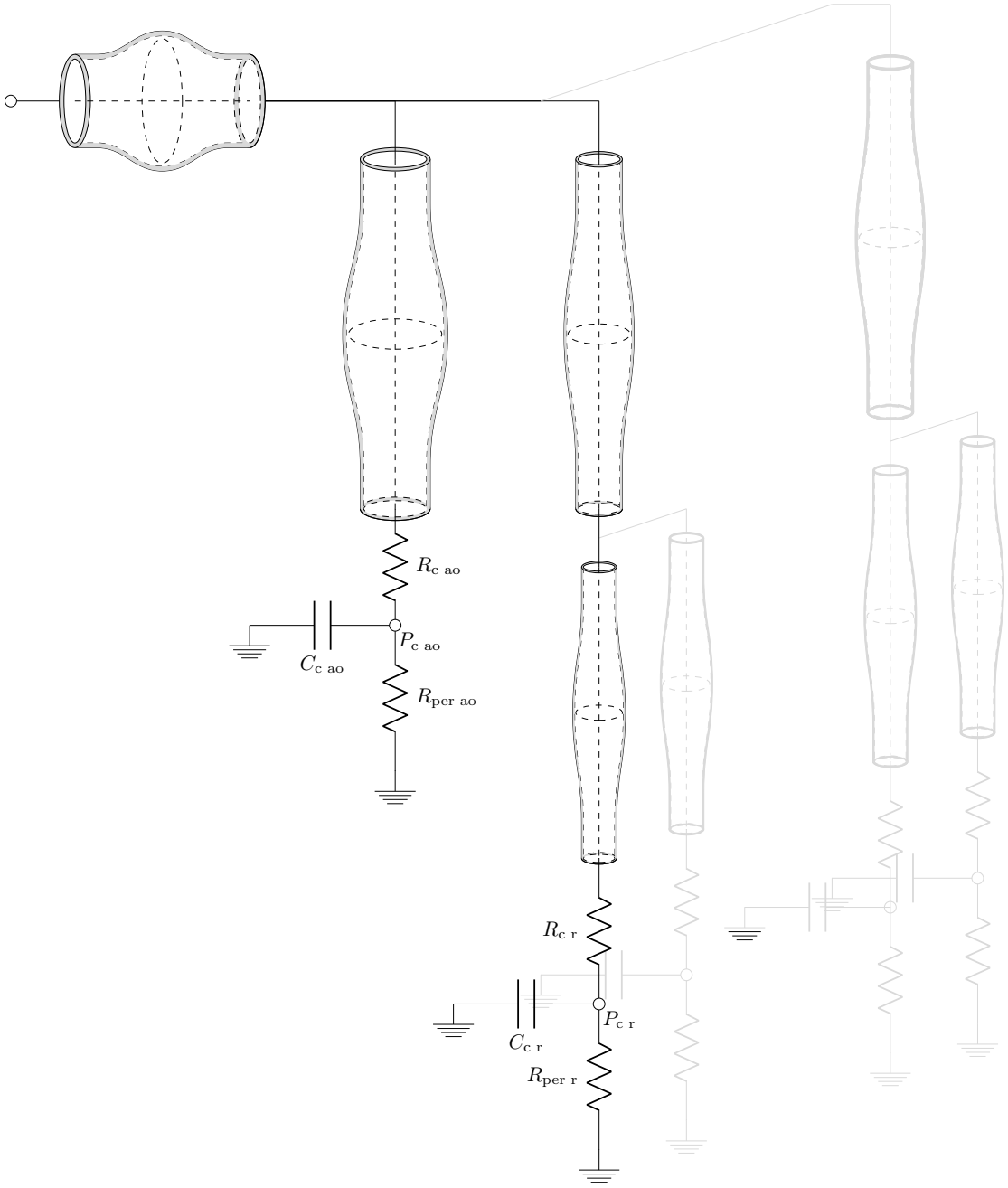

Figure 7.3 – Model configuration representing the aortic arch, the upper thoracic aorta and the main arteries of the left upper limb: the subclavian, axillary and brachial artery represented by a single segment and the radial artery. The arteries of the right upper limb and the left ulnar artery are represented in light grey to symbol the fact that their contribution is taken into account in the branching condition and so they are modeled in relation to the left arm and the radial artery. In our work we choose to consider the flow perfectly symmetric which implies the vessels to show the same physiological behavior. Modified from a figure provided by F. Kimmig.

model a single segment for one of the two arms. Finally, as presented in Chapter 3, at the brachial end of the SAB model there is a bifurcation, where a single one-dimensional segment representing the radial artery arises. The equations that describe this model read

$$\begin{cases} 2\partial_t \varphi_i + \pi \xi_i \partial_s (R_i v_i) = 0, \\ \pi \varrho \partial_t v_i + \dfrac{\pi \varrho}{2}\Big(2u_i \partial_s v_i + v_i \partial_s u_i\Big) + \varrho k_\nu \dfrac{\hat{v}_i}{R_i^2} + \pi R \partial_s(\xi_i \varphi_i) = 0, \end{cases} \tag{7.37}$$

where i corresponds to 'in'– the aortic arch – when $s \in (0, L_{in})$, to 'ao' – the upper thoracic aorta – when $s \in (0, L_{ao})$, to 'b' – the SAB arteries – when $(0, L_b)$ and to 'r' – the radial artery – when $s \in (0, L_r)$. Indeed, at the boundary the formulation becomes

$$\begin{cases} \pi R_i \xi_i \varphi_i = \dfrac{\pi \varrho}{2} u_i v_i - \pi R_i P_{i\,in} \quad \text{at at the inlet}, \\ \pi R_i \xi_i \varphi_i = -\dfrac{\pi \varrho}{2} u_i v_i + \pi R_i P_{i\,out} \quad \text{at at the outlet}. \end{cases} \tag{7.38}$$

With $P_{i\,in}$ and $P_{i\,out}$ being, respectively, the total pressure at the inlet and at the outlet. In what follows, to ease the presentation of the equations describing the boundary conditions, only space dependency is specified, while time dependency is implicit. The total pressure at the extremities, that has the role of coupling term, is slightly different for each segment. For the aortic arch model $P_{in\,in}$ and $P_{in\,out}$ are described by

$$\begin{cases} P_{in\,in} = \nu_{in}, \\ P_{in\,out} = P_{x\,in}, \\ \varepsilon_{in} \dot{P}_{x\,in} = \pi R_{in}(L_{in}) v_{in}(L_{in}) - \pi R_{ao}(0) v_{ao}(0) - 2\pi R_b(0) v_b(0). \end{cases} \tag{7.39}$$

Then, for the upper thoracic aorta we have

$$\begin{cases} P_{ao\,in} = P_{x\,in}, \\ P_{ao\,out} = P_{c\,ao} + \pi R_{c\,ao} R_{ao} v_{ao}, \\ C_{c\,ao} \dot{P}_{c\,ao} = \pi R_{ao}(L_{ao}) v_{ao}(L_{ao}) - \dfrac{\hat{P}_{c\,ao}}{R_{per\,ao}}. \end{cases} \tag{7.40}$$

while for the SAB segment the System reads

$$\begin{cases} P_{b\,in} = P_{x\,in}, \\ P_{b\,out} = P_{x\,ar}, \\ \varepsilon_b \dot{P}_{x\,ar} = \pi R_b(L_b) \hat{v}_b(L_b) - 2\pi R_r(0) v_r(0), \end{cases} \tag{7.41}$$

and finally for the radial artery the total pressures are defined as

$$\begin{cases} P_{r\,in} = P_{x\,ar}, \\ P_{r\,out} = P_{c\,r} + \pi R_{c\,r} R_r(L_r) v_r(L_r), \\ C_{c\,r} \dot{P}_{c\,r} = \pi R_r(L_r) v_r(L_r) - \dfrac{P_{c\,r}}{R_{per\,r}}. \end{cases} \tag{7.42}$$

7.5.2 Adimensionalization

Following the steps performed in Section 7.4.2 for the aortic model, we proceed with an adimensionalization of the non-linear formulation. Considering the differences in the boundary and coupling conditions as well as the presence of more state variables – v and φ for each 1D segment plus the 0D pressures – the adimensionalized variables introduced as well as the choices for the parameters shows some variations with respect to the one of the previous test-case. First, we introduce the adimensionalized variables,

$$\hat{\varphi}(L_{i\,0}s, t_0 t) := \frac{\varphi_i(s,t)}{\varphi_{i\,0}}, \quad \hat{v}(L_{i\,0}s, t_0 t) := \frac{v_i(s,t)}{v_{i\,0}}, \quad \hat{P}_{c\,i}(t_0 t) := \frac{P_{c\,i}(t)}{P_{i\,0}}, \quad \hat{P}_{x\,i} := \frac{P_{x\,i}}{P_{i\,0}}$$
$$\hat{R}(L_{i\,0}s, t_0 t) := \frac{R_i(s,t)}{R_{i\,0}}, \quad \hat{\xi}(L_{i\,0}s, t_0 t) := \frac{\xi(R_i)(s,t)}{\xi_{i\,0}}, \quad \hat{u}(L_{i\,0}s, t_0 t) := \frac{u_i(s,t)}{u_{i\,0}},$$

plus the input $\hat{\nu}_{in} := \nu_{in}/P_{source\,0}$. These variables replace the original ones in System 7.37, that becomes, for all $t > 0$

$$\begin{cases} 2\dfrac{\varphi_{i\,0}}{t_0}\partial_t\hat{\varphi}_i + \pi\dfrac{\xi_{i\,0}R_{i\,0}v_{i\,0}}{L_{i\,0}}\hat{\xi}_i\partial_s(\hat{R}_i\hat{v}_i) = 0, \\ \dfrac{\pi\varrho v_{i\,0}}{t_0}\partial_t v_i + \dfrac{\pi\varrho}{2}\dfrac{u_{i\,0}v_{i\,0}}{L_{i\,0}}\Big(2\hat{u}_i\partial_s\hat{v}_i + \hat{v}_i\partial_s\hat{u}_i\Big) + \varrho k_\nu\dfrac{v_{i\,0}}{R_{i\,0}^2}\dfrac{\hat{v}_i}{\hat{R}_i^2} + \pi\dfrac{R_{i\,0}\xi_{i\,0}\varphi_{i\,0}}{L_{i\,0}}\hat{R}\partial_s(\hat{\xi}_i\hat{\varphi}_i) = 0. \end{cases} \tag{7.43}$$

For what follows, we define $\hat{L}_{in} := L_{in}/L_{in\,0}$, $\hat{L}_{ao} := L_{ao}/L_{ao\,0}$, $\hat{L}_b := L_b/L_{b\,0}$ and $\hat{L}_r := L_r/L_{r\,0}$, being the lengths for each of the 1D vessels after adimensionalization. The boundaries read

$$\begin{cases} \pi R_{i\,0}\xi_{i\,0}\varphi_{i\,0}\hat{R}_i\hat{\xi}_i\hat{\varphi}_i = \dfrac{\pi\varrho}{2}u_{i\,0}v_{i\,0}\hat{u}_i\hat{v}_i - \pi R_{i\,0}\hat{R}_i P_{i\,in} \quad \text{at at the inlet}, \\ \pi R_{i\,0}\xi_{i\,0}\varphi_{i\,0}\hat{R}_i\hat{\xi}_i\hat{\varphi}_i = -\dfrac{\pi\varrho}{2}u_{i\,0}v_{i\,0}\hat{u}_i\hat{v}_i + \pi R_{i\,0}\hat{R}_i P_{i\,out} \quad \text{at at the outlet}. \end{cases} \tag{7.44}$$

Then, for the definition of the total pressures, at the inlet segment we have

$$\begin{cases} P_{in\,in} = P_{source\,0}\hat{\nu}_{in}, \\ P_{in\,out} = P_{in\,0}\hat{P}_{x\,in}, \\ \dfrac{\varepsilon_{in}P_{in\,0}}{t_0}\dot{\hat{P}}_{x\,in} = \pi R_{in\,0}v_{in\,0}\hat{R}_{in}(\hat{L}_{in})\hat{v}_{in}(\hat{L}_{in}) - \pi R_{ao\,0}v_{ao\,0}\hat{R}_{ao}(0)\hat{v}_{ao}(0) - 2\pi R_{b\,0}v_{b\,0}\hat{R}_b(0)\hat{v}_b(0), \end{cases} \tag{7.45}$$

while for the aortic segment the total pressure at the extremities read

$$\begin{cases} P_{ao\,in} = P_{in\,0}\hat{P}_{x\,in}, \\ P_{ao\,out} = P_{ao\,0}\hat{P}_{c\,ao} + \pi R_{c\,ao}R_{ao\,0}v_{ao\,0}\hat{R}_{ao}(\hat{L}_{ao})\hat{v}_{ao}(\hat{L}_{ao}), \\ \dfrac{C_{c\,ao}P_{ao\,0}}{t_0}\dot{\hat{P}}_{c\,ao} = \pi R_{ao\,0}v_{ao\,0}\hat{R}_{ao}(\hat{L}_{ao})\hat{v}_{ao}(\hat{L}_{ao}) - \dfrac{P_{ao\,0}\hat{P}_{c\,ao}}{R_{per\,ao}}. \end{cases} \tag{7.46}$$

For the first segment of the upper limb the System becomes

$$\begin{cases} P_{b\,in} = P_{in\,0}\hat{P}_{x\,in}, \\ P_{b\,out} = P_{b\,0}\hat{P}_{x\,ar}, \\ \dfrac{\varepsilon_b P_{b\,0}}{t_0}\dot{\hat{P}}_{x\,ar} = \pi R_{b\,0}v_{b\,0}\hat{R}_b(\hat{L}_b)\hat{v}_b(\hat{L}_b) - 2\pi R_{r\,0}v_{r\,0}\hat{R}_r(0)\hat{v}_r(0), \end{cases} \tag{7.47}$$

and for the radial segment we obtain

$$\begin{cases} P_{r\,in} = P_{b\,0}\hat{P}_{x\,ar}, \\ P_{r\,out} = P_{r\,0}\hat{P}_{c\,r} + \pi R_{c\,r} R_{r\,0} v_{r\,0} \hat{R}_r(\hat{L}_r)\hat{v}_r(\hat{L}_r), \\ \dfrac{C_{c\,r} P_{r\,0}}{t_0}\dot{\hat{P}}_{c\,r} = \pi R_{r\,0} v_{r\,0} \hat{R}_r(\hat{L}_r)\hat{v}_r(\hat{L}_r) - \dfrac{P_{r\,0}\hat{P}_{c\,r}}{R_{per\,r}}. \end{cases} \tag{7.48}$$

Finally, we define some parameters equally for each segment, namely

$$\varphi_{i\,0} := \sqrt{\frac{\pi\varrho}{2}} v_i, \quad R_{i\,0} := R_i(s,0),$$
$$\xi_{i\,0} := \xi(R_{i\,0}), \quad u_{i\,0} := \frac{v_{i\,0}}{R_{i\,0}},$$

and others differently for each model

parameter	inlet	aorta	SAB axis	radial
$v_{i\,0}$	$\sqrt{\dfrac{\epsilon_{in}}{\pi\varrho L_{in\,0}}} P_{in\,0}$	$\sqrt{\dfrac{\epsilon_{in}}{\pi\varrho L_{ao\,0}}} P_{in\,0}$	$\sqrt{\dfrac{\epsilon_b}{\pi\varrho L_{b\,0}}} P_{b\,0}$	$\sqrt{\dfrac{C_{c\,r}}{\pi\varrho L_{r\,0}}} P_{r\,0}$
$P_{i\,0}$	$\sqrt{\dfrac{2\pi\varrho L_{b\,0}}{\epsilon_{in}}} v_{b\,0}$	$\sqrt{\dfrac{\pi\varrho L_{ao\,0}}{C_{c\,ao}}} v_{ao\,0}$	$\sqrt{\dfrac{\pi\varrho L_{r\,0}}{\epsilon_b}} v_{r\,0}$	10^4
$L_{i\,0}$	$t_{ao\,0}\sqrt{\dfrac{\pi}{2\varrho}} \xi_{in\,0} R_{in\,0}$	L_{ao}	$t_{ao\,0}\sqrt{\dfrac{\pi}{2\varrho}} \xi_{b\,0} R_{b\,0}$	$t_{ao\,0}\sqrt{\dfrac{\pi}{2\varrho}} \xi_{r\,0} R_{r\,0}$

with $t_{ao\,0} := \sqrt{\frac{2\varrho}{\pi}} \frac{L_{ao\,0}}{\xi_{ao\,0} R_{ao\,0}}$, and $P_{source\,0} := P_{r\,0}$. After substitution, System 7.43 becomes

$$\begin{cases} \partial_t \hat{\varphi}_i + \hat{\xi}_i \partial_s(\hat{R}_i \hat{v}_i) = 0, \\ \partial_t v_i + \dfrac{a_{i\,0}}{2}\Big(2\hat{u}_i \partial_s \hat{v}_i + \hat{v}_i \partial_s \hat{u}_i\Big) + k_i \dfrac{\hat{v}_i}{\hat{R}_i^2} + \hat{R}_i \partial_s(\hat{\xi}_i \hat{\varphi}_i) = 0, \end{cases} \tag{7.49}$$

where $a_{i\,0}$ and k_i are defined as

$$a_{i\,0} := \frac{t_{ao\,0}}{L_{i\,0}} u_{i\,0} \quad k_i = \frac{t_{ao\,i} k_\nu}{\pi R_{i\,0}^2},$$

and System 7.44 now reads

$$\begin{cases} \hat{R}_{in}(0)\hat{\xi}_{in}(0)\hat{\varphi}_{in}(0) = \dfrac{a_{in\,0}}{2}\hat{u}_{in}(0)\hat{v}_{in}(0) - c_{vp\,0}\hat{R}_{in}(0)\hat{\nu}_{in}, \\ \hat{R}_{in}(\hat{L}_{in})\hat{\xi}_{in}(\hat{L}_{in})\hat{\varphi}_{in}(\hat{L}_{in}) = -\dfrac{a_{in\,0}}{2}\hat{u}_{in}(\hat{L}_{in})\hat{v}_{in}(\hat{L}_{in}) + c_{vp\,1}\hat{R}_{in}(\hat{L}_{in})\hat{P}_{x\,in}, \\ c\hat{R}_{ao}(0)\hat{\xi}_{ao}(0)\hat{\varphi}_{ao}(0) = \dfrac{a_{ao\,0}}{2}\hat{u}_{ao}(0)\hat{v}_{ao}(0) - c_{vp\,2}\hat{R}_{ao}(0)\hat{P}_{x\,in}, \\ \hat{R}_{ao}(\hat{L}_{ao})\hat{\xi}_{ao}(\hat{L}_{ao})\hat{\varphi}_{ao}(\hat{L}_{ao}) = -\dfrac{a_{ao\,0}}{2}\hat{u}_{ao}(\hat{L}_{ao})\hat{v}_{ao}(\hat{L}_{ao}) + c_{vp\,3}\hat{R}_{ao}(\hat{L}_{ao})\hat{P}_{c\,ao} \\ + c_{bo\,ao}\hat{R}_{ao}^2(\hat{L}_{ao})\hat{v}_{ao}(\hat{L}_{ao}), \\ \hat{R}_b(0)\hat{\xi}_b(0)\hat{\varphi}_b(0) = \dfrac{a_{b\,0}}{2}\hat{u}_b(0)\hat{v}_b(0) - c_{vp\,4}\hat{R}_b(0)\hat{P}_{x\,in}, \\ \hat{R}_b(\hat{L}_b)\hat{\xi}_b(\hat{L}_b)\hat{\varphi}_b(\hat{L}_b) = -\dfrac{a_{b\,0}}{2}\hat{u}_b(\hat{L}_b)\hat{v}_b(\hat{L}_b) + c_{vp\,5}\hat{R}_b(\hat{L}_b)\hat{P}_{x\,ar}, \\ \hat{R}_r(0)\hat{\xi}_r(0)\hat{\varphi}_r(0) = \dfrac{a_{r\,0}}{2}\hat{u}_r(0)\hat{v}_r(0) - c_{vp\,6}\hat{R}_r(0)\hat{P}_{x\,ar}, \\ \hat{R}_r(\hat{L}_r)\hat{\xi}_r(\hat{L}_r)\hat{\varphi}_r(\hat{L}_r) = -\dfrac{a_{r\,0}}{2}\hat{u}_r(\hat{L}_r)\hat{v}_r(\hat{L}_r) + c_{vp\,7}\hat{R}_r(\hat{L}_r)\hat{P}_{c\,r} + c_{bo\,r}\hat{R}_r^2(\hat{L}_r)\hat{v}_r(\hat{L}_r), \end{cases} \tag{7.50}$$

where the coefficients are defined as

$c_{vp\,0} := \dfrac{t_{ao\,0}}{L_{in\,0}} \dfrac{1}{\varrho} \dfrac{R_{in\,0}}{v_{in\,0}} P_{source\,0}$	$c_{vp\,1} := \dfrac{\pi t_{ao\,0}}{\varepsilon_{in}} \dfrac{R_{in\,0} v_{in\,0}}{P_{in\,0}}$
$c_{vp\,2} := \dfrac{\pi t_{ao\,0}}{\varepsilon_{in}} \dfrac{R_{ao\,0} v_{ao\,0}}{P_{in\,0}}$	$c_{vp\,3} := \dfrac{\pi t_{ao\,0}}{C_{cao}} \dfrac{R_{ao\,0} v_{ao\,0}}{P_{ao\,0}}$
$c_{vp\,4} := \dfrac{2\pi t_{ao\,0}}{\varepsilon_{in}} \dfrac{R_{b\,0} v_{b\,0}}{P_{in\,0}}$	$c_{vp\,5} := \dfrac{\pi t_{ao\,0}}{\varepsilon_{b}} \dfrac{R_{b\,0} v_{b\,0}}{P_{b\,0}}$
$c_{vp\,6} := \dfrac{2\pi t_{ao\,0}}{\varepsilon_{in}} \dfrac{R_{r\,0} v_{r\,0}}{P_{b\,0}}$	$c_{vp\,7} := \dfrac{\pi t_{ao\,0}}{C_{cr}} \dfrac{R_{r\,0} v_{r\,0}}{P_{r\,0}}$
$c_{bo\,ao} := \dfrac{\pi t_{ao\,0} R_{c\,ao}}{\varrho L_{ao\,0}} R_{ao\,0}^2$	$c_{bo\,r} := \dfrac{\pi t_{ao\,0} R_{c\,r}}{\varrho L_{r\,0}} R_{r\,0}^2$

Moreover, the pressures read

$$\begin{cases} \dot{\hat{P}}_{x\ in} = c_{vp\,1} \hat{R}_{in}(\hat{L}_{in}) \hat{v}_{in}(\hat{L}_{in}) - c_{vp\,2} \hat{R}_{ao}(0) \hat{v}_{ao}(0) - c_{vp\,4} \hat{R}_{b}(0) \hat{v}_{b}(0), \\ \dot{\hat{P}}_{c\,ao} = c_{vp\,3} \hat{R}_{ao}(\hat{L}_{ao}) \hat{v}_{ao}(\hat{L}_{ao}) - c_{pp\,ao} \hat{P}_{ao}, \\ \dot{\hat{P}}_{x\,ar} = c_{vp\,5} \hat{R}_{b}(\hat{L}_{b}) \hat{v}_{b}(\hat{L}_{b}) - c_{vp\,6} \hat{R}_{r}(0) \hat{v}_{r}(0), \\ \dot{\hat{P}}_{c\,r} = c_{vp\,7} \hat{R}_{r}(\hat{L}_{r}) \hat{v}_{r}(\hat{L}_{r}) - c_{pp\,r} \hat{P}_{r}, \end{cases} \tag{7.51}$$

where $c_{pp\,ao} := t_{ao\,0}^{-1}(C_{c\,ao} R_{per\,ao})$ and $c_{pp\,r} := t_{ao\,0}^{-1}(C_{c\,r} R_{per\,r})$.

7.5.3 Iterative pseudo-linearization

The complete formulation of the arm, although simplified by the adimensionalization, remains non-linear. The idea is to follow the same strategy described in Section 7.4.3 to achieve the pseudo-linearized formulation to employ in the iterative process. Clearly, the intermediate variables of each of the one-dimensional segment of the model configuration follows the behavior prescribed for $\hat{R}$, $\hat{\xi}$ and $\hat{u}$ in the aortic test-case presented before. This leads to, for all $t \geq 0$ and $k \geq 1$

$$\begin{cases} \partial_t \hat{\varphi}_{i\,k} + \hat{\xi}_{i\,k-1} \partial_s (\hat{R}_{i\,k-1} \hat{v}_{i\,k}) = 0, \\ \partial_t \hat{v}_{i\,k} + \dfrac{a_{i\,0}}{2} \Big(2\hat{u}_{i\,k-1} \partial_s \hat{v}_{i\,k} + \hat{v}_{i\,k} \partial_s \hat{u}_{i\,k-1} \Big) + k_i \dfrac{\hat{v}_{i\,k}}{\hat{R}_{i\,k-1}^2} + \hat{R}_{i\,k-1} \partial_s (\hat{\xi}_{i\,k-1} \hat{\varphi}_{i\,k}) = 0, \end{cases} \tag{7.52}$$

while, at the boundary

$$
\begin{cases}
\hat{R}_{in\,k-1}(0)\hat{\xi}_{in\,k-1}(0)\hat{\varphi}_{in\,k}(0) = \dfrac{a_{in\,0}}{2}\hat{u}_{in\,k-1}(0)\hat{v}_{in\,k}(0) - c_{vp\,0}\hat{R}_{in\,k-1}(0)\hat{\nu}_{in\,k},\\
\hat{R}_{in\,k-1}(\hat{L}_{in})\hat{\xi}_{in\,k-1}(\hat{L}_{in})\hat{\varphi}_{in\,k}(\hat{L}_{in}) = -\dfrac{a_{in\,0}}{2}\hat{u}_{in\,k-1}(\hat{L}_{in})\hat{v}_{in\,k}(\hat{L}_{in}) + c_{vp\,1}\hat{R}_{in\,k-1}(\hat{L}_{in})\hat{P}_{x\,in\,k},\\
\hat{R}_{ao\,k-1}(0)\hat{\xi}_{ao\,k-1}(0)\hat{\varphi}_{ao\,k}(0) = \dfrac{a_{ao\,0}}{2}\hat{u}_{ao\,k-1}(0)\hat{v}_{ao\,k}(0) - c_{vp\,2}\hat{R}_{ao\,k-1}(0)\hat{P}_{x\,in\,k},\\
\hat{R}_{ao\,k-1}(\hat{L}_{ao})\hat{\xi}_{ao\,k-1}(\hat{L}_{ao})\hat{\varphi}_{ao\,k}(\hat{L}_{ao}) = -\dfrac{a_{ao\,0}}{2}\hat{u}_{ao\,k-1}(\hat{L}_{ao})\hat{v}_{ao\,k}(\hat{L}_{ao}) + c_{vp\,3}\hat{R}_{ao\,k-1}(\hat{L}_{ao})\hat{P}_{c\,ao\,k}\\
+c_{bo\,ao}\hat{R}^2_{ao\,k-1}(\hat{L}_{ao})\hat{v}_{ao\,k}(\hat{L}_{ao}),\\
\hat{R}_{b\,k-1}(0)\hat{\xi}_{b\,k-1}(0)\hat{\varphi}_{b\,k}(0) = \dfrac{a_{b\,0}}{2}\hat{u}_{b\,k-1}(0)\hat{v}_{b\,k}(0) - c_{vp\,4}\hat{R}_{b\,k-1}(0)\hat{P}_{x\,in\,k},\\
\hat{R}_{b\,k-1}(\hat{L}_{b})\hat{\xi}_{b\,k-1}(\hat{L}_{b})\hat{\varphi}_{b\,k}(\hat{L}_{b}) = -\dfrac{a_{b\,0}}{2}\hat{u}_{b\,k-1}(\hat{L}_{b})\hat{v}_{b\,k}(\hat{L}_{b}) + c_{vp\,5}\hat{R}_{b\,k-1}(\hat{L}_{b})\hat{P}_{x\,ar\,k},\\
\hat{R}_{r\,k-1}(0)\hat{\xi}_{r\,k-1}(0)\hat{\varphi}_{r\,k}(0) = \dfrac{a_{r\,0}}{2}\hat{u}_{r\,k-1}(0)\hat{v}_{r\,k}(0) - c_{vp\,6}\hat{R}_{r\,k-1}(0)\hat{P}_{x\,ar\,k},\\
\hat{R}_{r\,k-1}(\hat{L}_{r})\hat{\xi}_{r\,k-1}(\hat{L}_{r})\hat{\varphi}_{r\,k}(\hat{L}_{r}) = -\dfrac{a_{r\,0}}{2}\hat{u}_{r\,k-1}(\hat{L}_{r})\hat{v}_{r\,k}(\hat{L}_{r}) + c_{vp\,7}\hat{R}_{r\,k-1}(\hat{L}_{r})\hat{P}_{c\,r\,k}\\
+c_{bo\,r}\hat{R}^2_{r\,k-1}(\hat{L}_{r})\hat{v}_{r\,k}(\hat{L}_{r}),
\end{cases}
\tag{7.53}
$$

$$
\begin{cases}
\dot{\hat{P}}_{x\ in\,k} = c_{vp\,1}\hat{R}_{in\,k-1}(\hat{L}_{in})\hat{v}_{in\,k}(\hat{L}_{in}) - c_{vp\,2}\hat{R}_{ao\,k-1}(0)\hat{v}_{ao\,k}(0) - c_{vp\,4}\hat{R}_{b\,k-1}(0)\hat{v}_{b\,k}(0),\\
\dot{\hat{P}}_{c\,ao\,k} = c_{vp\,3}\hat{R}_{ao\,k-1}(\hat{L}_{ao})\hat{v}_{ao\,k-1}(\hat{L}_{ao}) - c_{pp\,ao}\hat{P}_{ao\,k},\\
\dot{\hat{P}}_{x\,ar\,k} = c_{vp\,5}\hat{R}_{b\,k-1}(\hat{L}_{b})\hat{v}_{b\,k}(\hat{L}_{b}) - c_{vp\,6}\hat{R}_{r\,k-1}(0)\hat{v}_{r\,k}(0),\\
\dot{\hat{P}}_{c\,r\,k} = c_{vp\,7}\hat{R}_{r\,k-1}(\hat{L}_{r})\hat{v}_{r\,k}(\hat{L}_{r}) - c_{pp\,r}\hat{P}_{r\,k}.
\end{cases}
\tag{7.54}
$$

The energy stability

We now show the semi-discrete variational formulation of System 7.52 in order to prove the energy stability. We apply the midpoint time-scheme and we retrieve

$$
\begin{cases}
\left(\dfrac{\hat{\varphi}^{n+1}_{i\,k} - \hat{\varphi}^{n}_{i\,k}}{\tau_a}, \tilde{\hat{\varphi}}\right) + \left(\partial_s(\hat{R}^{n+\frac{1}{2}}_{i\,k-1}\hat{v}^{n+\frac{1}{2}}_{i\,k}), \tilde{\hat{\varphi}}\hat{\xi}^{n+\frac{1}{2}}_{i\,k-1}\right) = 0,\\
\left(\dfrac{\hat{v}^{n+1}_{i\,k} - \hat{v}^{n}_{i\,k}}{\tau_a}, \tilde{\hat{v}}\right) + a\left(\tilde{\hat{v}}, \hat{v}^{n+\frac{1}{2}}_{i\,k}, \hat{u}^{n+\frac{1}{2}}_{i\,k-1}\right) + k_{adim}\left(\dfrac{\hat{v}^{n+\frac{1}{2}}_{i\,k}}{\hat{R}^{n+\frac{1}{2}}_{i\,k-1}}, \dfrac{\tilde{\hat{v}}}{R^{n+\frac{1}{2}}_{i\,k-1}}\right)\\
\qquad +(\partial_s(\hat{R}^{n+\frac{1}{2}}_{i\,k-1}\,\tilde{\hat{v}}), \hat{\varphi}^{n+\frac{1}{2}}_{i\,k}\hat{\xi}^{n+\frac{1}{2}}_{i\,k-1})\hat{R}^{n+\frac{1}{2}}_{k-1} = -c_{vp}\hat{R}^{n+\frac{1}{2}}_{i\,k-1}\,\tilde{\hat{v}}(P_i - P_{ext})\Big|^{outlet}_{inlet},
\end{cases}
\tag{7.55}
$$

with $a\left(\tilde{\hat{v}}, \hat{v}^{n+\frac{1}{2}}_{i\,k}, \hat{u}^{n+\frac{1}{2}}_{i\,k-1}\right)$ that reads

$$
a\left(\tilde{\hat{v}}, \hat{v}^{n+\frac{1}{2}}_{i\,k}, \hat{u}^{n+\frac{1}{2}}_{i\,k-1}\right) := \frac{a_{i\,0}}{2}\int_{inlet}^{outlet}\left(2\tilde{\hat{v}}\hat{u}^{n+\frac{1}{2}}_{i\,k-1}\partial_s\hat{v}_{i\,k} + \hat{v}^{n+\frac{1}{2}}_{i\,k}\tilde{\hat{v}}\hat{u}^{n+\frac{1}{2}}_{i\,k-1}\right)ds - \frac{a_{i\,0}}{2}\tilde{\hat{v}}\hat{v}^{n+\frac{1}{2}}_{i\,k}\hat{u}^{n+\frac{1}{2}}_{i\,k-1}\Big|^{outlet}_{inlet}.
$$

The choice of the test functions – $\tilde{\hat{v}}$ and $\tilde{\hat{\varphi}}$ – is specific to each segment and allows us to prove, within each iteration, the preservation of an energy density. In particular, for each vessel i we pick $\tilde{\hat{v}} = \hat{v}^{n+\frac{1}{2}}_{i\,k}$ and $\tilde{\hat{\varphi}} = \hat{\varphi}^{n+\frac{1}{2}}_{i\,k}$ and we retrieve

$$\begin{cases} \dfrac{||\hat{\varphi}_{i\,k}^{n+1}||^2 - ||\hat{\varphi}_{i\,k}^{n}||^2}{\tau_a} + \Big(\partial_s(\hat{R}_{i\,k-1}^{n+\frac{1}{2}}\hat{v}_{i\,k}^{n+\frac{1}{2}}), \hat{\varphi}_{i\,k}^{n+\frac{1}{2}}\hat{\xi}_{i\,k-1}^{n+\frac{1}{2}}\Big) = 0, \\ \dfrac{||\hat{v}_{i\,k}^{n+1}||^2 - ||\hat{v}_{i\,k}^{n}||^2}{\tau_a} + a\Big(\hat{v}_{i\,k}^{n+\frac{1}{2}}, \hat{v}_{i\,k}^{n+\frac{1}{2}}, \hat{u}_{i\,k-1}^{n+\frac{1}{2}}\Big) + k_{adim}\left(\dfrac{\hat{v}_{i\,k}^{n+\frac{1}{2}}}{\hat{R}_{i\,k-1}^{n+\frac{1}{2}}}, \dfrac{\hat{v}_{i\,k}^{n+\frac{1}{2}}}{R_{i\,k-1}^{n+\frac{1}{2}}}\right) \\ \qquad +(\partial_s(\hat{R}_{i\,k-1}^{n+\frac{1}{2}}\,\hat{v}_{i\,k}^{n+\frac{1}{2}}), \hat{\varphi}_{i\,k}^{n+\frac{1}{2}}\hat{\xi}_{i\,k-1}^{n+\frac{1}{2}})\hat{R}_{i\,k-1}^{n+\frac{1}{2}} = -c_{vp}\hat{R}_{i\,k-1}^{n+\frac{1}{2}}\,\hat{v}_{i\,k}^{n+\frac{1}{2}}(P_i - P_{ext})\Big|_{inlet}^{outlet}. \end{cases} \tag{7.56}$$

Then, we perform some algebraic manipulation and obtain

$$\frac{||\hat{\varphi}_{i\,k}^{n+1}||^2 - ||\hat{\varphi}_{i\,k}^{n}||^2}{\tau_a} + \frac{||\hat{v}_{i\,k}^{n+1}||^2 - ||\hat{v}_{i\,k}^{n}||^2}{\tau_a} + k_{adim}\left(\frac{\hat{v}_{i\,k}^{n+\frac{1}{2}}}{\hat{R}_{i\,k-1}^{n+\frac{1}{2}}}, \frac{\hat{v}_{i\,k}^{n+\frac{1}{2}}}{R_{i\,sk-1}^{n+\frac{1}{2}}}\right) = \text{boundary terms}.$$

The energy densities read

$$\begin{aligned} &\mathcal{E}_{i-vessel}^{n} = ||\hat{\varphi}_{i\,k}^{n}||^2 + ||\hat{v}_{i\,k}^{n}||^2, \quad \mathcal{E}_{bc\,in}^{n} = (\hat{P}_{x\,in\,k}^{n})^2, \quad \mathcal{E}_{bc\,ao}^{n} = (\hat{P}_{c\,ao\,k}^{n})^2, \\ &\mathcal{E}_{bc\,ar}^{n} = (\hat{P}_{x\,ar\,k}^{n})^2, \quad \mathcal{E}_{bc\,r}^{n} = (\hat{P}_{c\,r\,k}^{n})^2, \end{aligned}$$

where $\mathcal{E}_{i-vessel}^{n}$ is the energy density at the present time for each i, corresponding to any 1D segment of the model configuration, while $\mathcal{E}_{bc\,ao}^{n}$ and $\mathcal{E}_{bc\,r}^{n}$ are the energy densities of the lumped-parameter models at the outlet of the aortic segment and the radial one, respectively, and $\mathcal{E}_{bc\,in}^{n}$ and $\mathcal{E}_{bc\,ar}^{n}$ takes into account the energy density of the outlet penalization contribution for the inlet and the first upper limb segment. Actually, $\mathcal{E}_{bc\,in}^{n}$ is also the inlet energy density for the aortic and first arm segment while $\mathcal{E}_{bc\,ar}^{n}$ is the inlet coupling energy for the radial segment. We also have some dissipation contributions that read

$$\begin{aligned} &\mathcal{D}_{i-vessel}^{n+\frac{1}{2}} = k_i\left|\left|\frac{\hat{v}_{i\,k}^{n+\frac{1}{2}}}{\hat{R}_{i\,k-1}^{n+\frac{1}{2}}}\right|\right|^2, \quad \mathcal{D}_{bc\,ao}^{n+\frac{1}{2}} = c_{bo\,ao}(\hat{R}_{ao\,k-1}^{n+\frac{1}{2}}(\hat{L}_{ao})\hat{v}_{ao\,k}^{n+\frac{1}{2}}(\hat{L}_{ao}))^2 + c_{pp}(\hat{P}_{c\,ao\,k}^{n+\frac{1}{2}})^2, \\ &\mathcal{D}_{bc\,r}^{n+\frac{1}{2}} = c_{bo\,r}(\hat{R}_{r\,k-1}^{n+\frac{1}{2}}(\hat{L}_r)\hat{v}_{r\,k}^{n+\frac{1}{2}}(\hat{L}_b))^2 + c_{pp}(\hat{P}_{c\,r\,k}^{n+\frac{1}{2}})^2, \end{aligned}$$

where $\mathcal{D}_{i-vessel}^{n+\frac{1}{2}}$ takes into account the dissipative contributions of each term of the 1D formulations, while $\mathcal{D}_{bc\,ao}^{n+\frac{1}{2}}$ and $\mathcal{D}_{bc\,r}^{n+\frac{1}{2}}$ the dissipative terms of the two Windkessel models that close the circuit. Finally, the energy conservation property reads, for all $n \in \mathbb{N}$

$$\begin{aligned} &\frac{\mathcal{E}_{i-vessel}^{n+1} - \mathcal{E}_{i-vessel}^{n}}{\tau_a} + \frac{\mathcal{E}_{bc\,in}^{n+1} - \mathcal{E}_{bc\,in}^{n}}{\tau_a} + \frac{\mathcal{E}_{bc\,ao}^{n+1} - \mathcal{E}_{bc\,ao}^{n}}{\tau_a} + \frac{\mathcal{E}_{bc\,ar}^{n+1} - \mathcal{E}_{bc\,ar}^{n}}{\tau_a} + \frac{\mathcal{E}_{bc\,r}^{n+1} - \mathcal{E}_{bc\,r}^{n}}{\tau_a} \\ &+\mathcal{D}_{i-vessel}^{n+\frac{1}{2}} + \mathcal{D}_{bc\,ao}^{n+\frac{1}{2}} + \mathcal{D}_{bc\,r}^{n+\frac{1}{2}} = \pi\hat{R}_{in\,k-1}^{n+\frac{1}{2}}(0)\hat{v}_{in\,k}^{n+\frac{1}{2}}(0)\hat{\nu}_{in\,k}^{n+\frac{1}{2}}, \end{aligned}$$

at the right hand side we find the input source term $\hat{\nu}_{in\,k}^{n+\frac{1}{2}}$.

7.6 Results and discussion

7.6.1 Numerical results

In order to observe the behavior of our iterative 4D-Var strategy we perform a simulation, defined as 'identical twin experiment' in [Lawless et al., 2005a], using some synthetic data of peripheral aortic pressure – with the upper thoracic aorta test-case – and of radial pressure

– with the model configuration including the upper limb circulation – as observations for the inverse problem. These data were obtained from a simulation of the direct problem described in the previous sections at convergence. Finally, we show preliminary results obtained by using real clinical data of pressure recorded invasively *in vivo* by using a catheter, collected at the Lariboisière Hospital by F. Vallée, F. Kimmig and I.

Synthetic observations In Figure 7.4 and Figure 7.5 we show the results obtained by running the inverse problem, respectively with the aortic test case and the upper limb model, using synthetic data as observations. With this simulation we want to test the behavior of the iterative strategy proposed in this chapter. We can observe that the estimations of the inlet total pressure converge after few 'outer' iterations ($k = 3$) of the inverse problem. Moreover, it highlights the advantage of the iterative method, seeing that the estimations get closer to the target source, being the total pressure used as input for the forward simulation that produced the synthetic observations.

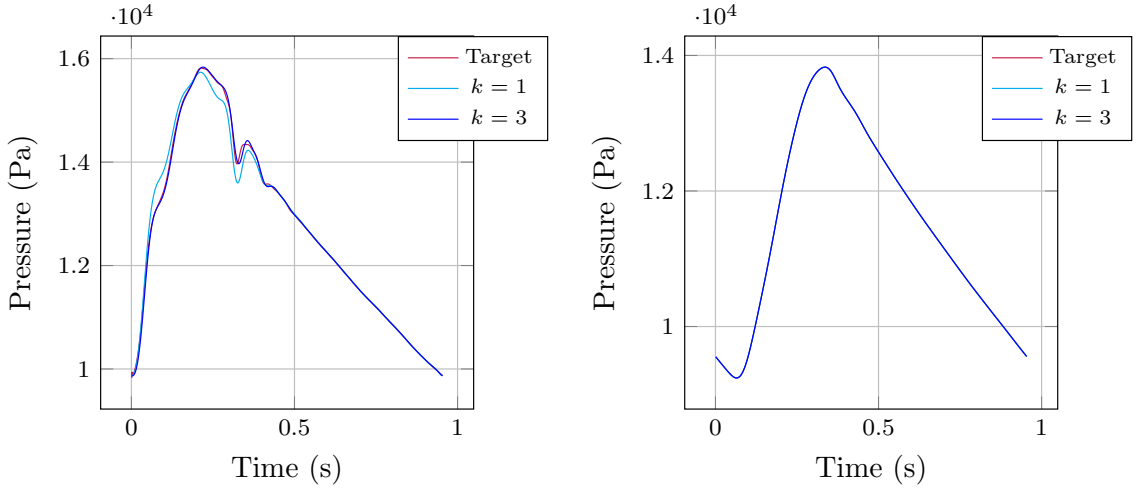

Figure 7.4 – Pressure waves estimated using synthetic peripheral aortic pressure observations previously obtained with a direct simulation of the iterative pseudo-linear model at convergence. The inlet source (on the left), being the total pressure, and the peripheral aortic pressure (on the right) are plotted: at the first iteration (light blue curve) and at convergence (dark blue curve), and compared to the expected results (in red) being respectively the input given for the direct simulation and the synthetic observations.

Real *in vivo* observations In this paragraph we show some preliminary results obtained with some *in vivo* record of peripheral pressure. First, in Figure 7.6 we give a schematic representation of the surgical set-up to collect the data we employed as observation for the upper thoracic aorta test-case. In this figure the observation and the total pressure estimated at convergence are shown. However, the central pressure records were not exploitable. For this reason, in Figure 7.7 ,we compare to the *in vivo* data of flux and pressure the results obtained for the blood flow inside the vessel at the measurements site and the outlet peripheral pressure, at the first iteration (light blue curve) and at convergence (dark blue curve). It is possible to observe that the computed flow presents a back flow while the measurements do not. However, it is hard to comment on this aspect as the measurements of velocity (used to derive the flow by means of the measured diameter of the vessel) are very noisy and do not show any negative curve, even if its presence is physiologically alike. Then, in Figure 7.8 we represent qualitatively the surgical set-up where the pressure data were collected within the arterial circulation of the left arm, that we used

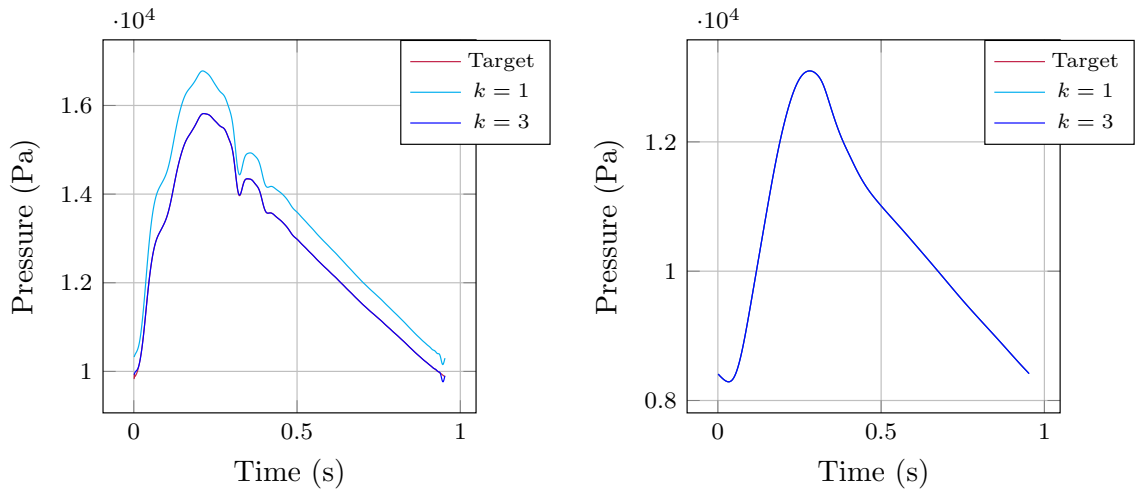

Figure 7.5 – Pressure waves estimated using synthetic peripheral radial pressure observations previously obtained with a direct simulation of the iterative pseudo-linear model at convergence. The inlet source (on the left), being the total pressure, and the peripheral radial pressure (on the right) are plotted: at the first iteration (light blue curve) and at convergence (dark blue curve), and compared to the expected results (in red) being respectively the input given for the direct simulation and the synthetic observations.

as observations for the inverse problem applied to the model configuration including the upper limb arteries. These data provided exploitable central pressure record, and we were able to compare the estimation of the total pressure, as shown in Figure 7.9 on the left, to the real data. Although these results represent a preliminary step towards a validation against *in vivo* data, the estimations obtained at convergence of our strategy are promising. Moreover, the inverse problem is shown to be capable of reproducing physiological estimation of the central pressure and it presents a good behavior when dealing with real noise coming from the *in vivo* measurements.

Acknowledgment

We are very grateful to Fabrice Vallée for providing us with the data for the upper thoracic aorta test and for giving F. Kimmig and I the possibility to participate to the collection of the data employed for the test with the model of the arm arteries.

7.6.2 Discussion

In this chapter we have presented a new method to deal with non-linear physical system of the form of Eq. (7.1) in data assimilations problems. In particular, we reduce the problem to an iterative method involving – at each iteration – linear operators, and that shows to reproduce, at convergence, non-linear behaviors. The outcomes of the simulations performed with synthetic pressure data support the suitability of the iterative inverse problem to retrieve a proper estimation. Moreover, the results obtained when dealing with real measurements of pressure as observations are promising. However, the parametrization plays an important role and affects extensively the estimation. In order to obtain the results shown in Figure 7.7 and Figure 7.9 the parametrization has been performed by hand, taking into account patients characteristics (e.g. sex, age etc.). Though, this is not suitable for real clinical applications as it is general and user-dependent. For this reason, this strategy should be coupled with a parameter estimation method, for instance in two steps, to be

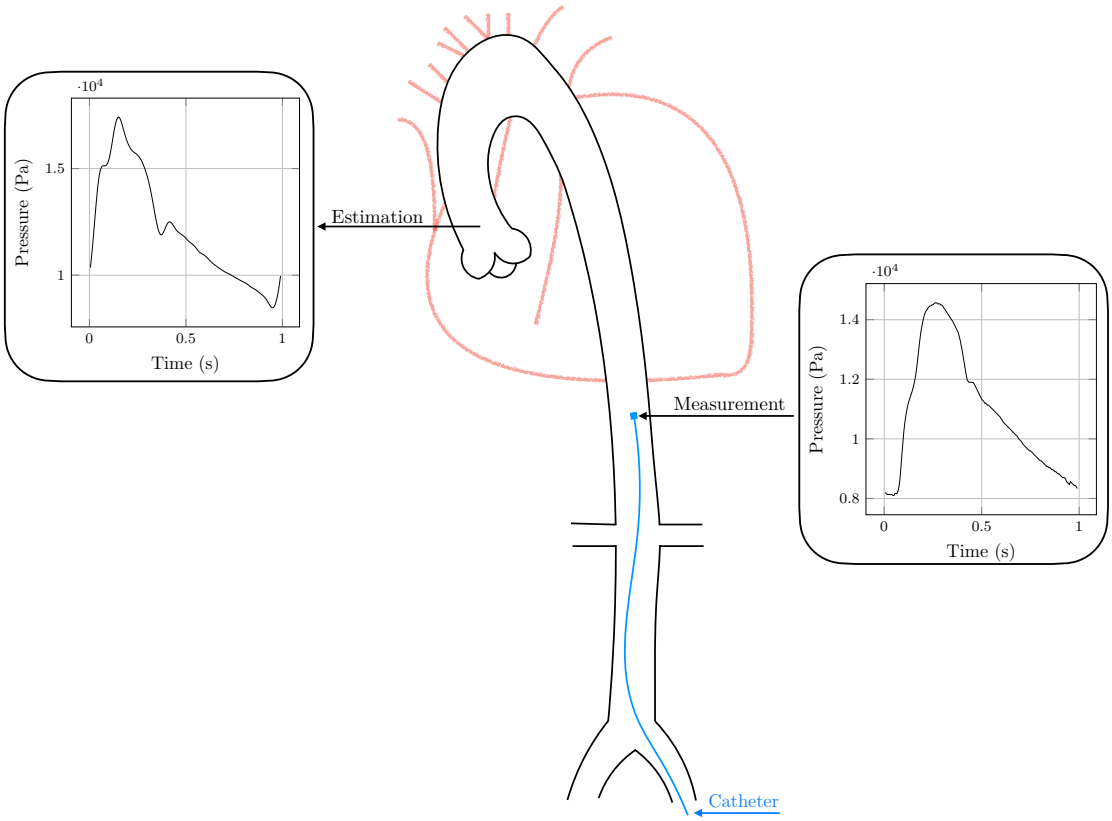

Figure 7.6 – Qualitative representation of an aortic vessel with the measurement site highlighted by a flesh and the recorded peripheral pressure wave used as observation, on the right. The central point corresponding to the input source estimated gives rise to a flesh, on the left side of the vessel, that points out the inlet total pressure estimated by using the iterative method. The position of the catheter is indicated by the blue line entering from the aortic lower limb bifurcation.

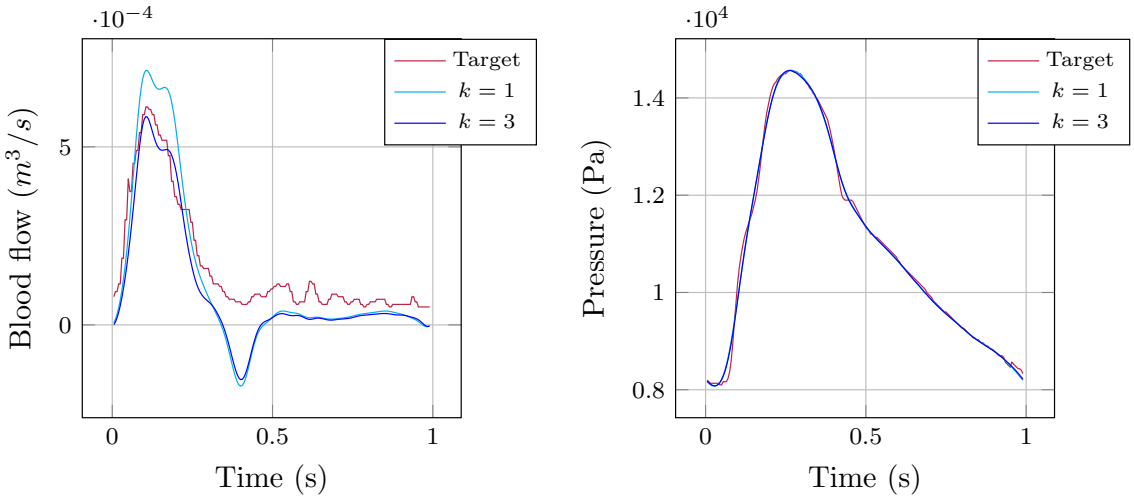

Figure 7.7 – Results obtained using real *in vivo* peripheral aortic pressure data as observations, registered through a intra-aortic catheter. The blood flow inside the aorta (on the left) and the peripheral aortic pressure (on the right) are plotted: at the first iteration (light blue curve) and at convergence (dark blue curve), and compared to the expected results (in red) being respectively the flow derived from the recorded velocity and the peripheral pressure wave used as observation.

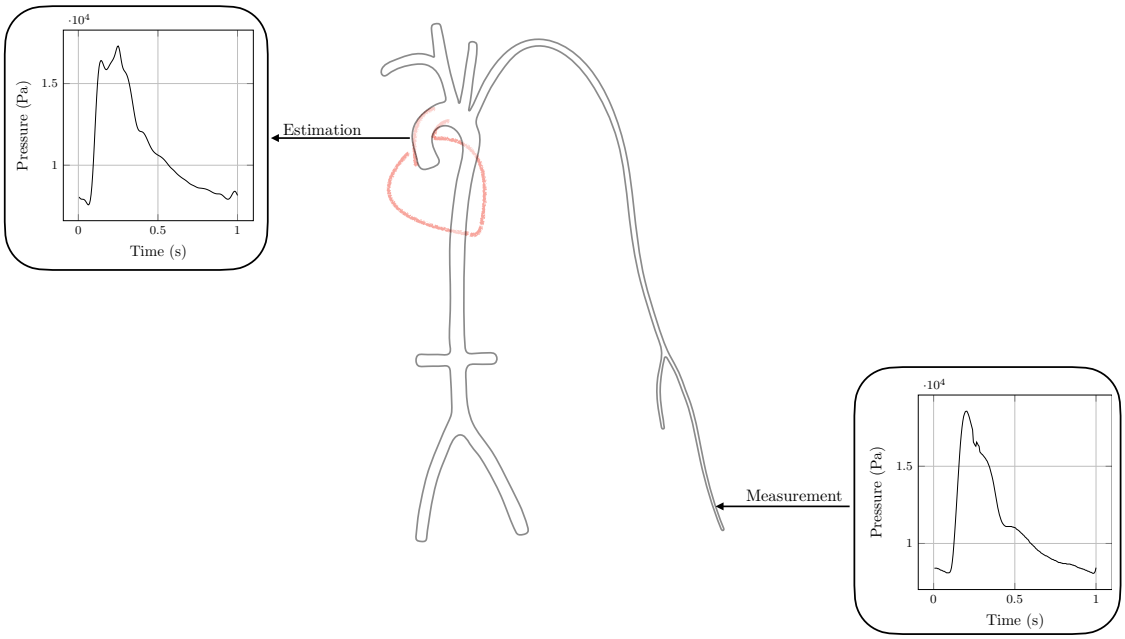

Figure 7.8 – Qualitative representation of the arterial circulation including the aortic vessel and the main arteries of the left arm, with the measurement site highlighted by a flesh and the recorded radial pressure wave used as observation, on the right. The central point corresponding to the input source estimated gives rise to a flesh, on the left side of the vessel, that points out the inlet total pressure estimated by using the iterative method.

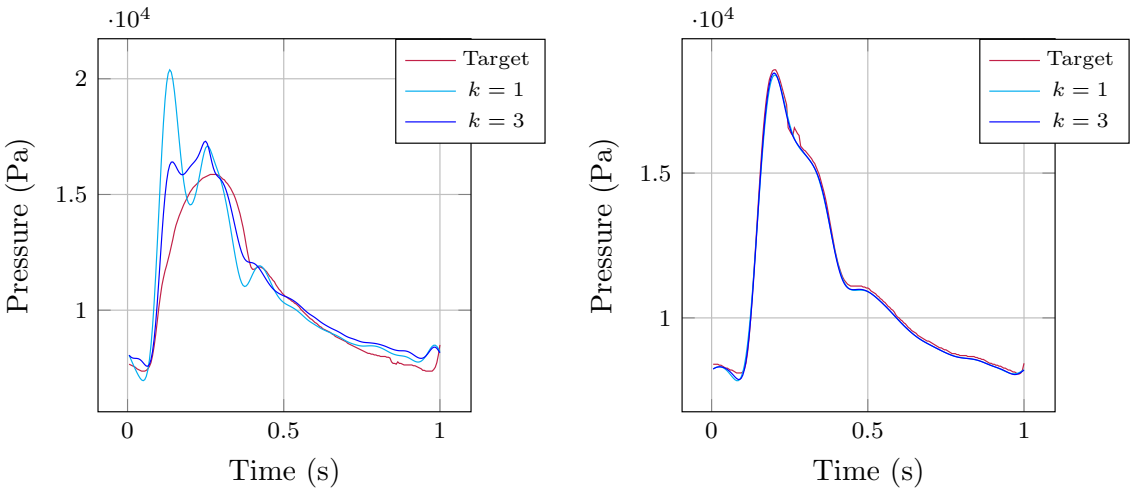

Figure 7.9 – Results obtained using real *in vivo* peripheral radial pressure data as observations, registered through a catheter. The inlet total pressure (on the left) and the peripheral radial pressure (on the right) are plotted: at the first iteration (light blue curve) and at convergence (dark blue curve), and compared to the expected results (in red) being respectively the central pressure and the peripheral pressure wave used as observation.

able to tune the model according to the patient before using it to retrieve central circulation informations, see the next chapter for further details. Finally, this method would require a more complete validation, this could be achieved by using more real clinical data after proper parametrization.

Bibliography

Chen, C.-H., Nevo, E., Fetics, B., Pak, P. H., Yin, F. C., Maughan, W. L., and Kass, D. A. (1997). Estimation of central aortic pressure waveform by mathematical transformation of radial tonometry pressure. *Circulation*, 95(7):1827–1836.

Gratton, S., Lawless, A. S., and Nichols, N. K. (2007). Approximate gauss–newton methods for nonlinear least squares problems. *SIAM Journal on Optimization*, 18(1):106–132.

Joachim, J., Vallée, F., Gall, A. L., Matéo, J., Lenck, S., Millasseau, S., Houdart, E., Mebazaa, A., and Gayat, E. (2017). Velocity–pressure loops for continuous assessment of ventricular afterload: influence of pressure measurement site. *Journal of Clinical Monitoring and Computing*, 32(5):833–840.

Karamanoglu, M. and Feneley, M. P. (1996). Derivation of the ascending aortic-carotid pressure transfer function with an arterial model. *American Journal of Physiology-Heart and Circulatory Physiology*, 271(6):H2399–H2404.

Karamanoglu, M. and Feneley, M. P. (1997). On-line synthesis of the human ascending aortic pressure pulse from the finger pulse. *Hypertension*, 30(6):1416–1424.

Laroche, S. and Gauthier, P. (1998). A validation of the incremental formulation of 4d variational data assimilation in a nonlinear barotropic flow. *Tellus A: Dynamic Meteorology and Oceanography*, 50(5):557–572.

Lawless, A., Gratton, S., and Nichols, N. (2005a). Approximate iterative methods for variational data assimilation. *International journal for numerical methods in fluids*, 47(10-11):1129–1135.

Lawless, A., Gratton, S., and Nichols, N. (2005b). An investigation of incremental 4d-var using non-tangent linear models. *Quarterly Journal of the Royal Meteorological Society*, 131(606):459–476.

Manganotti, J., Caforio, F., Kimmig, F., Moireau, P., and Imperiale, S. (2021). Coupling reduced-order blood flow and cardiac models through energy-consistent strategies: modeling and discretization. *Advanced Modeling and Simulation in Engineering Sciences*, 8(1):1–37.

Ortega, J. M. and Rheinboldt, W. C. (2000). *Iterative solution of nonlinear equations in several variables*. SIAM.

Pauca, A. L., O'Rourke, M. F., and Kon, N. D. (2001). Prospective evaluation of a method for estimating ascending aortic pressure from the radial artery pressure waveform. *Hypertension*, 38(4):932–937.

Robert, C., Durbiano, S., Blayo, E., Verron, J., Blum, J., and Le Dimet, F.-X. (2005). A reduced-order strategy for 4d-var data assimilation. *Journal of Marine Systems*, 57(1-2):70–82.

Tikhonov, A. N. (1963). Solution of incorrectly formulated problems and the regularization method. *Soviet Math.*, 4:1035–1038.

CHAPTER 8

Conclusions and perspectives

Sometimes attaining the deepest familiarity with a question is our best substitute for actually having the answer.
— Brian Greene, *The Elegant Universe*

The content of this chapter includes a work realized in collaboration with François Kimmig.

Contents

8.1 Conclusion

The work presented in this thesis is at the intersection between biomechanical modeling, numerical methods and clinical application. In particular, it places itself in the context of general anesthesia, with a focus on a key matter for this field: cardiovascular monitoring. The subject of this thesis originates from the strong collaboration between the Inria team MΞDISIM and the anesthesiologists of the Lariboisière Hospital, and it aims to employ cardiovascular modeling and inverse problem techniques to develop a method that could be used to enhance the cardiovascular monitoring.
More precisely, we have set ourselves the goal to derive a strategy to exploit peripheral pressure measurements to retrieve central pressure and flow waves. In order to do that, we needed a model to link the data and the quantities to estimate and a data assimilation method to use the measurements with the model and obtain the informations of interest. First of all, we developed a one-dimensional model of the arterial vessels between measurements and estimation site (see Part I). The one-dimensional blood flow model relies on energy-preserving time-discretization [Chapelle et al., 2012] that leads to an energy compliant discrete formulation [Manganotti et al., 2021]. Moreover, this model is completed by a coupling with a cardiac model [Caruel et al., 2013] enriched with a rheological model that links deformation and contraction [Kimmig et al., 2019]. The coupling strategy pursued was that of deriving a model satisfying the desired energy properties. This provides good stability properties that are suitable for the application of inverse problem strategies. In what concern the data assimilation method, we decided to rely on a variational approach [Le Dimet and Talagrand, 1986] (see Part I) and we solved an optimal control problem by means of iterative non-tangent methods [Lawless et al., 2005].
Finally, we were able to develop a strategy that put the bases for the use of data assimilation strategies applied on reduced cardiovascular model in real clinical applications, such as the cardiovascular monitoring during general anesthesia.

8.2 Perspectives

The inverse problem strategy presented in this part allows us to estimate the central pressure of a model representing the arterial circulation between the heart and the wrist, by using some peripheral observations, namely the radial pressure measurements. This means that the circulatory informations close to the heart become accessible, as well as the pressure and flow in every site of the network included in the spatial domain of the model. However, it is well known that in order to foresee real clinical applications, models parameters have to be chosen patient-specifically [Caiazzo et al., 2017]. More precisely, we have seen that the parametrization of the model is crucial to obtain reliable input pressure corresponding to central pressure waves. Moreover, in clinical applications there is a need to adapt the model to each patient and move towards patient-specific parametrizations. This could be achieved enhancing the inverse problem developed in this work with a parameter estimations techniques. The tuning of parameters can be reached by means of different techniques, which in our context would depend on the number of measurement sites available during surgeries and the type of recording (continuous during the surgical procedure, available only before the surgery or just for few cardiac cycles etc.), that also determines the identifiability of the required quantities [Perasso, 2009]. For example we could imagine a two-steps procedure where the parameters of the upper limb model are adapted to the patient before the source estimation problem is actually performed. Further details on this idea and other possibilities are addressed below.

8.2.1 Two-steps procedure: separate parameters and source estimations

The arm arteries parameters of the model presented in Chapter 7 could be parametrized by reducing the model domain to the upper limb and by taking an input inlet pressure from continuous measurements obtained non-invasively through a brachial cuff (such as the one described in the patent of Pfeiffer et al. [2015]). With a real pressure input and with the peripheral radial data used as observations, we could apply either variational or sequential methods (see Chapter 5) to estimate the parameters of interest, determined after an identifiability analysis. This procedure could be performed before the application of the inverse problem for the source estimation or, if the cuff-derived pressure is accessible during surgery, at small time intervals to check on the modifications of the circulatory parameters for example due to drugs. However, this method would not allow anesthesiologists to have a real time monitoring of the cardiovascular state of the patient. In order to move towards real time augmented monitoring, a sequential approach that involves the estimation of both the parameters and the state at the same time has to be employed. In the following section we present an on-going work which would represent an alternative to the above mentioned method, in case additional measurements are available continuously during surgery, namely the aortic flow and the electrocardiogram to tune the cardiac electric activation.

8.2.2 Real time procedure: the augmented state

A real time monitoring can be achieved by applying sequential data assimilation techniques, such as the Kalman filter (see Chapter 5 and references therein). A preliminary attempt is presented in this section, where the model described in Chapter 3 is used and we apply an Unscented Kalman Filter (UKF), previously derived in the team and parametrized by François Kimmig, to set-up a parameters estimation problem that uses pressure and flow measurements available during surgeries and which is able to retrieve cardiac and circulatory parameters, as well as the model state. In the context of general anesthesia, we use the *in vivo* data available during surgeries: namely peripheral pressure, aortic blood velocity and cardiac electrical signal to adapt the atrial pressure input. We focus on the estimation of those parameters that show a higher inter- and intra-person variability. They are indeed of primary importance to define the cardiovascular status of the patient.

8.2.2.1 Model set-up

In this section we will present some preliminary numerical results obtained with the application of the UKF on a model of the heart coupled with the thorax and upper limb circulation. The configuration of the model is similar to the one described in Chapter 3, which involves the zero-dimensional left ventricle model, the one-dimensional model of the upper thoracic aorta and the upper limb arteries and the lumped-parameter model of the heart valves, that are slightly modified. More in details, an inductance is added to each valve represented by a lumped-parameter model and a backward flow trough the aortic valve is included. The inductance are added to improve the regularization of the flux and to have the blood flow as a state variable in the formulation, which simplify the use of aortic flow observations. The formulation now reads

$$\begin{cases} C_{mi}\dfrac{d}{dt}P_v = -Q_{ar} - Q_v + Q_{at}, \\ L_{at}\dfrac{d}{dt}Q_{at} = -(K_{at}|Q_{at}|_+ - K_{iso}|Q_{at}|_-) - P_v + P_{at}, \\ L_{ar}\dfrac{d}{dt}Q_{ar} = -(K_{ar}|Q_{ar}|_+ - K_{back}|Q_{ar}|_-) - P_{ar} + P_v. \end{cases}$$

where P_v, P_{at} and P_{ar} are respectively the pressure inside the ventricle, the atrial pressure and the pressure at the beginning of the arterial circulation, and Q_v, Q_{at} and Q_{ar} are the corresponding flow of blood. Finally, K_{at} and K_{ar} are the resistance of the valve to the forward flow and K_{iso} and K_{back} to the backward one. The modified valve configuration is shown in Figure 8.1

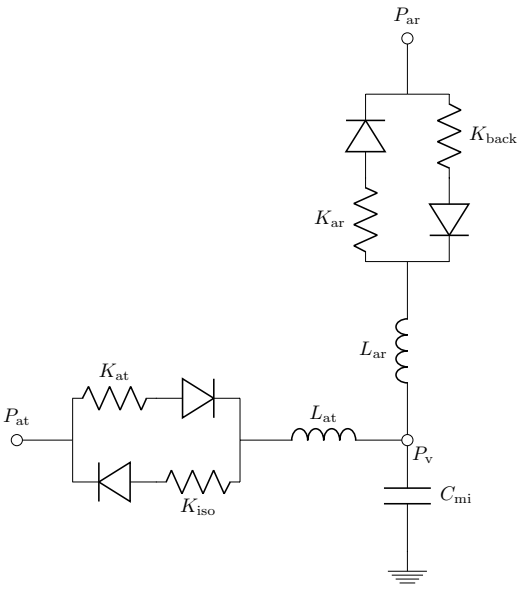

Figure 8.1 – Configuration of the lumped-parameter model representing the mitral and aortic valve, with the addition of the inductance and the aortic back flow.

8.2.2.2 Kalman filter strategy

To perform the parameter estimation we rely on an Unscented Kalman Filter (UKF) [Julier et al., 1995] (see Chapter 5) as we are dealing with the non-linear dynamics described in [Manganotti et al., 2021]. More precisely, we apply the UKF with an augmented state [Moireau et al., 2008], $\hat{z} = (\theta, z)$, where θ represents the parameters to estimate and has a null dynamics – $\dot{\theta} = 0$ – and z is the state of the model.

8.2.2.3 Preliminary results

The results we present in this section are obtained by using synthetic data, generated from a forward simulation where the input atrial pressure and the electrical activation are given, based on physiological knowledge [Le Gall et al., 2020]. The data used are the distal radial pressure – the pressure in the last element of the one-dimensional radial segment – and the aortic flow – being the flow in the lumped-parameter model of the valves that exits the heart through the aortic valve and enters the arterial circulation – previously obtained with a forward simulation. First, we estimate three parameters: the contractility of the myocardium, arm vessel wall elasticity and the peripheral impedance of the upper thoracic aorta. The results are shown in Figure 8.2. It is possible to observe that the filter is able to reproduce a state that matches the data after few cardiac cycle and the value of the parameters gets close to the target value (which is known since the data are synthetic). Then, we add an additional parameter, namely the peripheral impedance for the radial artery. The results of this simulation, shown in Figure 8.3, suggests that the four

parameters chosen cannot be accurately estimated by using two observations. In fact, even if the estimated state, contractility and peripheral resistance of the aortic vessel are similar to those of Figure 8.2, the estimation of the radial stiffness and of the radial peripheral resistance diverge from the target value. However, further simulations are necessary to have a better understanding of the functioning of the filter.

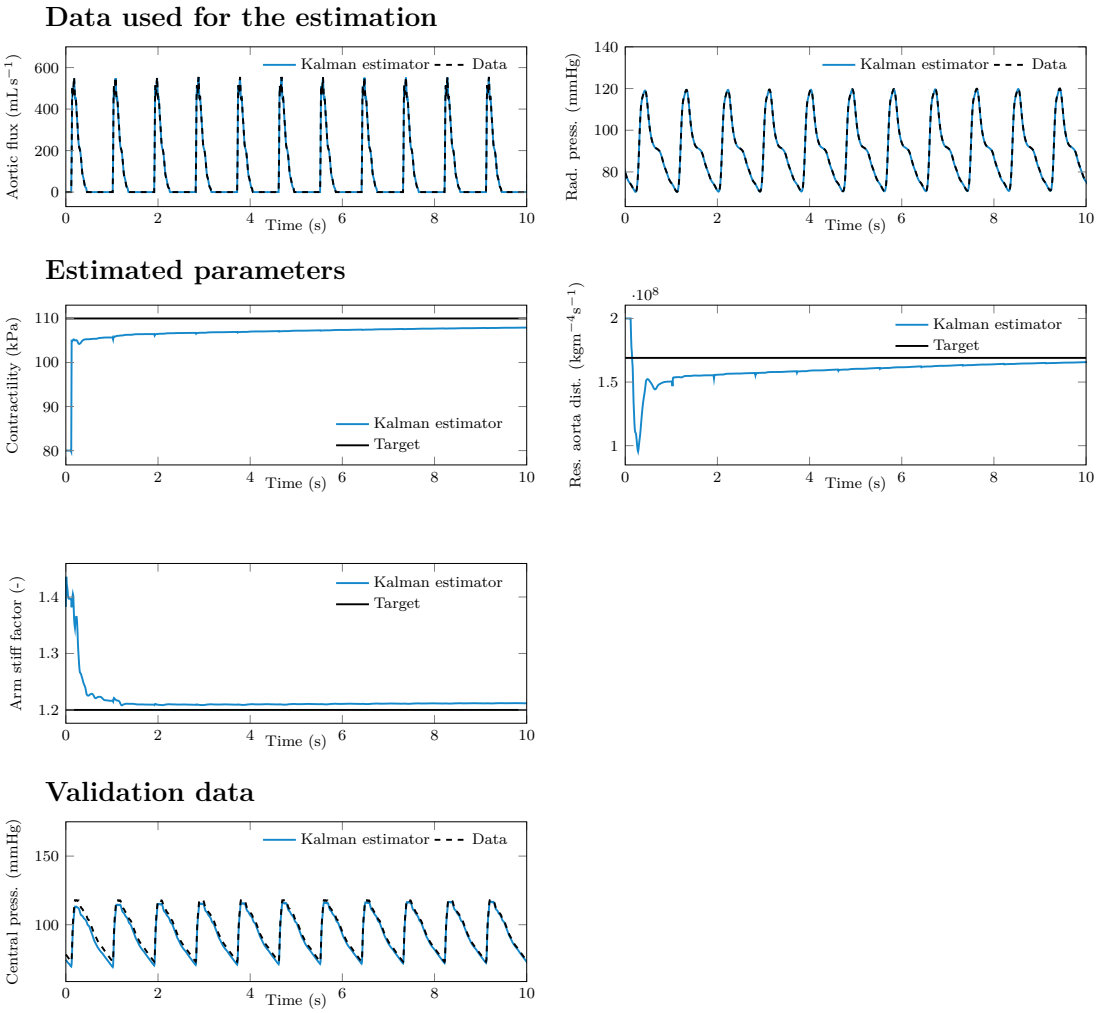

Figure 8.2 – Comparison between observations (dashed black line) and estimated with the KF (blue line) aortic flow (top left) and radial pressure (top right) over time. The estimated parameters are shown over time and compared to the target value (black line) in the second row and third row. The estimation involved the contractility of the heart (second row on the left), the peripheral resistance of the upper thoracic aorta model (second row on the right) and a factor that multiplies the Young modulus of the radial model (on the third row). At the bottom left the estimated central pressure (blue line) is compared to the target central pressure (dashed black line).

8.2.2.4 Discussion

The results presented above for the UKF are promising, however when real data are employed the estimations obtained are not reliable. Additional analysis on the parameters identifiability are required according to the available measurements. Besides, the sequential strategy presented above is designed to rely on the permanent availability of the aortic flow, which is strongly affected by noise when the surgeon uses the electric scalpel. One

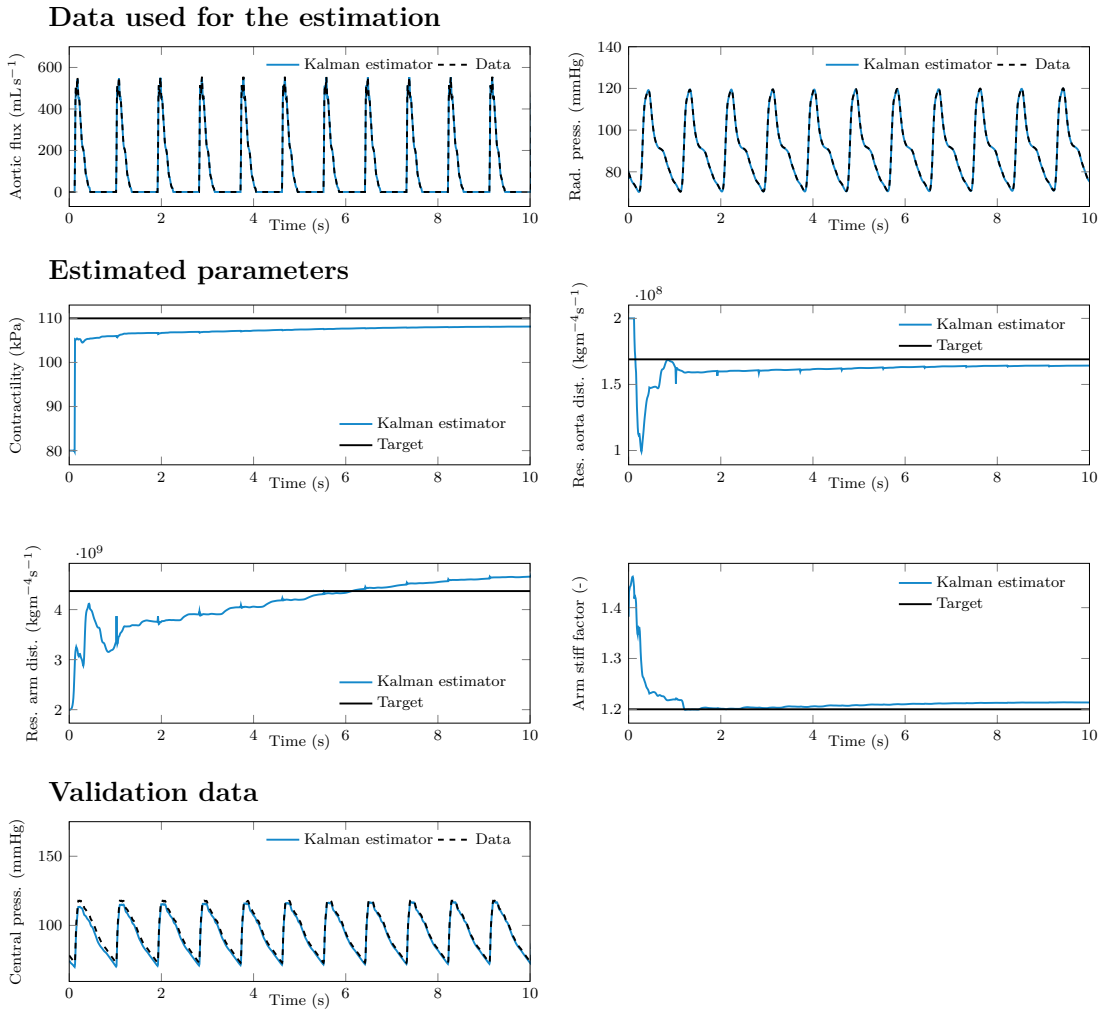

Figure 8.3 – Comparison between observations (dashed black line) and estimated with the KF (blue line) aortic flow (top left) and radial pressure (top right) over time. The estimated parameters are shown over time and compared to the target value (black line) in the second row and third row. The estimation involved the contractility of the heart (second row on the left), the peripheral resistance of the upper thoracic aorta model (second row on the right), the peripheral resistance of the radial model (third row on the left) and a factor that multiplies the Young modulus of the radial model (third row on the right). At the bottom left the estimated central pressure (blue line) is compared to the target central pressure (dashed black line).

solution would be to couple the filter with the variational method described in Chapter 7 in a 'parallel' fashion. When the flow and the peripheral pressure are available simultaneously, the Kalman filter could be used to retrieve both parameters and the state of the model. Then, when and if the aortic flow measurement becomes inaccessible, the variational inverse problem could take over until the flow signal comes back. Moreover, the method described in Chapter 7 could be used to define a 'patient-based' cardiac output or central pressure, which would serves as an additional derived-measurement to contribute to the filter estimations.

Data-driven estimations An alternative way to estimate parameters and state in a single step could be data-driven methods, which have recently been used in cardiovascular estimation problems [Arzani and Dawson, 2021; Bikia et al., 2020; Carson et al., 2019; Chiarelli et al., 2019; Regazzoni et al., 2021]. Among the positive aspects of the neural network is the absence of a model that requires 'a priori' calibration, which is usually a limitation of model-driven methods. However, the lack of 'physical knowledge' is also a weakness of data-driven methods, especially when the physics of the phenomena is well known and described by detailed models validated against real clinical data. This leads to uncertainty regarding the efficiency of these methods. A possible solution could be to 'empower' neural networks with a physical model to guide the learning process [Lucor et al., 2021]. However, the major limitation for neural networks in clinical applications is the amount of data required for training, as the mass collection of these data raises ethical issues [Bikia et al., 2020] and complicates access to them.

8.2.3 Validation against transfer function estimations

We have seen that we can provide central pressure estimations by using peripheral pressure data by means of the variational method presented in Chapter 6 and Chapter 7, and through Kalman filter techniques as shown in the previous section if aortic flow measurements are available. Nevertheless, in the introduction we have seen that the central pressure estimation is usually retrieved by means of a transfer function [O'Rourke, 1970]. One way to test the outcomes of the methods described in Part II would be to compare the central aortic pressure estimations obtained with a transfer function, for example the one used in Joachim et al. [2017], to those derived with the combined method described above.

Bibliography

Arzani, A. and Dawson, S. T. (2021). Data-driven cardiovascular flow modelling: examples and opportunities. *Journal of the Royal Society Interface*, 18(175):20200802.

Bikia, V., Papaioannou, T. G., Pagoulatou, S., Rovas, G., Oikonomou, E., Siasos, G., Tousoulis, D., and Stergiopulos, N. (2020). Noninvasive estimation of aortic hemodynamics and cardiac contractility using machine learning. *Scientific Reports*, 10(1):1–17.

Caiazzo, A., Caforio, F., Montecinos, G., Müller, L. O., Blanco, P. J., and Toro, E. F. (2017). Assessment of reduced-order unscented kalman filter for parameter identification in 1-dimensional blood flow models using experimental data. *International journal for numerical methods in biomedical engineering*, 33(8):e2843.

Carson, J., Lewis, M., Rassi, D., and Van Loon, R. (2019). A data-driven model to study

utero-ovarian blood flow physiology during pregnancy. *Biomechanics and modeling in mechanobiology*, 18(4):1155–1176.

Caruel, M., Chabiniok, R., Moireau, P., Lecarpentier, Y., and Chapelle, D. (2013). Dimensional reduction of cardiac models for effective validation and calibration. In *Functional Imaging and Modeling of the Heart*, pages 259–267. Springer Berlin Heidelberg.

Chapelle, D., Le Tallec, P., Moireau, P., and Sorine, M. (2012). Energy-preserving muscle tissue model: formulation and compatible discretizations. *Journal for Multiscale Computational Engineering*.

Chiarelli, A. M., Bianco, F., Perpetuini, D., Bucciarelli, V., Filippini, C., Cardone, D., Zappasodi, F., Gallina, S., and Merla, A. (2019). Data-driven assessment of cardiovascular ageing through multisite photoplethysmography and electrocardiography. *Medical engineering & physics*, 73:39–50.

Joachim, J., Vallée, F., Gall, A. L., Matéo, J., Lenck, S., Millasseau, S., Houdart, E., Mebazaa, A., and Gayat, E. (2017). Velocity–pressure loops for continuous assessment of ventricular afterload: influence of pressure measurement site. *Journal of Clinical Monitoring and Computing*, 32(5):833–840.

Julier, S. J., Uhlmann, J. K., and Durrant-Whyte, H. F. (1995). A new approach for filtering nonlinear systems. In *Proceedings of 1995 American Control Conference-ACC'95*, volume 3, pages 1628–1632. IEEE.

Kimmig, F., Chapelle, D., and Moireau, P. (2019). Thermodynamic properties of muscle contraction models and associated discrete-time principles. *Advanced Modeling and Simulation in Engineering Sciences*, 6(1):6.

Lawless, A., Gratton, S., and Nichols, N. (2005). An investigation of incremental 4d-var using non-tangent linear models. *Quarterly Journal of the Royal Meteorological Society*, 131(606):459–476.

Le Dimet, F.-X. and Talagrand, O. (1986). Variational algorithms for analysis and assimilation of meteorological observations: theoretical aspects. *Tellus A: Dynamic Meteorology and Oceanography*, 38(2):97–110.

Le Gall, A., Vallee, F., Pushparajah, K., Hussain, T., Mebazaa, A., Chapelle, D., Gayat, E., and Chabiniok, R. (2020). Monitoring of cardiovascular physiology augmented by a patient-specific biomechanical model during general anesthesia. A proof of concept study. *PLoS ONE*, 15(5):e0232830.

Lucor, D., Agrawal, A., and Sergent, A. (2021). Physics-aware deep neural networks for surrogate modeling of turbulent natural convection. *arXiv preprint arXiv:2103.03565*.

Manganotti, J., Caforio, F., Kimmig, F., Moireau, P., and Imperiale, S. (2021). Coupling reduced-order blood flow and cardiac models through energy-consistent strategies: modeling and discretization. *Advanced Modeling and Simulation in Engineering Sciences*, 8(1):1–37.

Moireau, P., Chapelle, D., and Le Tallec, P. (2008). Joint state and parameter estimation for distributed mechanical systems. *Computer methods in applied mechanics and engineering*, 197(6-8):659–677.

O'Rourke, M. F. (1970). Influence of ventricular ejection on the relationship between central aortic and brachial pressure pulse in man. *Cardiovascular Research*, 4(3):291–300.

Perasso, A. (2009). *Identifiabilité de paramètres pour des systèmes décrits par des équations aux derivées partielles. Application à la dynamique des populations*. PhD thesis, Université Paris-Sud XI.

Pfeiffer, U., Kisban, S., Thomamueller, T., Uhlitz, A.-L., and Knoll, R. (US Patent 2015/0359446 A1, Dec. 17, 2015). Blood pressure measuring system comprising a kinking-proof shell. Technical report, UP-MED GMBH.

Regazzoni, F., Chapelle, D., and Moireau, P. (2021). Combining data assimilation and machine learning to build data-driven models for unknown long time dynamics—applications in cardiovascular modeling. *International Journal for Numerical Methods in Biomedical Engineering*, 37(7):e3471.

Where we came forth, and once more
saw the stars.
– Dante Alighieri

DOCTORAL SCHOOL

Titre : Modélisation et problèmes inverses en hémodynamique : vers un monitorage cardiovasculaire augmenté

Mots clés : modèles réduits, problèmes inverses, modélisation cardiaque, monitorage cardiovasculaire

Résumé : Ce projet est un travail à l'interface entre la biomécanique et les mathématiques appliquées dans un contexte clinique. Plus précisément, le contexte clinique est l'anesthésie générale, qui est une procédure à haut risque, car elle peut induire un comportement circulatoire non physiologique. Pour cette raison, une surveillance étroite de l'état cardiovasculaire du patient près du cœur est cruciale. Cependant, cela nécessite des mesures invasives qui ne sont pas toujours accessibles et, par conséquent, les anesthésistes s'appuient généralement sur des mesures périphériques, par exemple la pression radiale. L'objectif de ce travail est de fournir, au moyen d'un modèle de flux sanguin couplé à un modèle cardiaque et de techniques d'assimilation de données, une stratégie pour estimer l'état cardiovasculaire en utilisant ces mesures périphériques. Notre point de départ est un modèle de flux sanguin unidimensionnel capable de reproduire les phénomènes de propagation des ondes qui caractérisent la circulation artérielle. Le modèle repose sur une nouvelle formulation discrète préservant l'énergie qui permet un couplage numériquement stable avec un modèle d'ordre réduit du ventricule gauche proposé précédemment. Ce modèle couplé est capable de simuler, étant donné une pression atriale, des résultats physiologiques et est complété pour prendre en compte les artères reliant la sortie cardiaque au site des mesures. Ensuite, une partie importante du travail est consacrée à la construction et à l'analyse de stratégies de problèmes inverses qui, une fois appliquées sur le modèle de flux sanguin, permettent d'estimer des marqueurs cardiovasculaires centraux à partir des mesures périphériques de pression. La stratégie proposée est basée sur une approche 4D-variationnelle itérative qui s'appuie sur une méthode de Gauss-Newton approchée, adaptée pour la résolution de problèmes de contrôle optimal appliqués sur des formulations non linéaires. Le problème inverse est analysé dans sa version linéarisée autour de l'état stationnaire, qui correspond à la première étape de la procédure itérative. Notre stratégie d'inversion nous permet de reproduire le débit et la pression d'entrée et montre des résultats prometteurs lorsque des données cliniques réelles sont impliquées.

Title : Modeling and inverse problems in hemodynamics: towards augmented cardiovascular monitoring

Keywords : reduced models, inverse problems, cardiac modeling, cardiovascular monitoring

Abstract : This project is at the interface between biomechanics and applied mathematics in a clinical context. More precisely, the clinical background is general anesthesia, which is a high-risk procedure as it can induce an unphysiological circulatory behavior. For this reason a close monitoring of the cardiovascular status of the patient near the heart is crucial. However, this requires invasive measurements that are not always available and therefore anesthesiologists usually rely on peripheral measurements, for example the radial pressure. The objective of this work is to provide, by means of a blood flow model coupled with a cardiac model and of data assimilation techniques, a strategy to estimate the cardiovascular state by using these distal measurements. We start from a one-dimensional blood flow model that is able to reproduce the wave propagation phenomena that affect the arterial circulation. The model relies on a novel discrete energy-preserving formulation which allows for a numerically stable coupling with a previously proposed reduced-order model of the left ventricle. This coupled model is able to simulate, given an atrial pressure, physiological results and is extended to take into account the pathway that links the cardiac outlet to the measurements site. Then, an important part of the work is dedicated to the construction and analysis of inverse problem strategies that, once applied on the blood flow model, allows to estimate central cardiovascular markers from the distal measurements of pressure. It is based on an iterative 4D-variational approach that relies on an approximated Gauss-Newton method, suitable for the solution of optimal control problems applied on non-linear formulations. The inverse problem is analyzed in its linearized version around a steady state, which corresponds to the first step of the iterative procedure. Our inversion strategy, allows us to reproduce the input flow and pressure and show promising results when real clinical data are involved.

Institut Polytechnique de Paris
91120 Palaiseau, France